IntechOpen

Advances in Glass Science and Technology

Edited by Vincenzo M. Sglavo

ADVANCES IN GLASS SCIENCE AND TECHNOLOGY

Edited by **Vincenzo M. Sglavo**

Advances in Glass Science and Technology
http://dx.doi.org/10.5772/intechopen.69580
Edited by Vincenzo M. Sglavo

Contributors

Kadir Bilisik, Gaye Kaya, Hüseyin Özdemir, Gulhan Erdogan, Mahmut Korkmaz, Jihui Yuan, Uwe Petzold, Montri Suklueng, Hongwei Guo, Josefina Alvarado-Rivera, Carlos Guadalupe Pérez Hernández, María Elena Zayas Saucedo, Mario Alvarez-Ramos, Quanlong He, Pengfei Wang, Min Lu, Bo Peng, Limbraj Spoan Ravangave, Ganesh Devde, Nguyen Van Toan, Naoki Inomata, Masaya Toda, Takahito Ono, Daniel Milanese, Joris Lousteau, Xiushan Zu, Arturo Chavez-Pirson, Nadia G. Boetti, Diego Pugliese, Nasser Peyghambarian

Notice

Statements and opinions expressed in the chapters are these of the individual contributors and not necessarily those of the editors or publisher. No responsibility is accepted for the accuracy of information contained in the published chapters. The publisher assumes no responsibility for any damage or injury to persons or property arising out of the use of any materials, instructions, methods or ideas contained in the book.

We are IntechOpen,
the world's leading publisher of
Open Access books
Built by scientists, for scientists

3,500+
Open access books available

111,000+
International authors and editors

115M+
Downloads

151
Countries delivered to

Our authors are among the
Top 1%
most cited scientists

12.2%
Contributors from top 500 universities

CLARIVATE ANALYTICS
BOOK
CITATION
INDEX
INDEXED

WEB OF SCIENCE™

Selection of our books indexed in the Book Citation Index
in Web of Science™ Core Collection (BKCI)

Interested in publishing with us?
Contact book.department@intechopen.com

Numbers displayed above are based on latest data collected.
For more information visit www.intechopen.com

Meet the editor

Vincenzo M. Sglavo is a professor of materials science and technology at the Department of Industrial Engineering, University of Trento (Italy). He received the Laurea degree "cum laude" in materials engineering from the University of Trento in 1988.

In 1989, he joined the Department of Materials Engineering, University of Trento, as an assistant professor and in 1999 became associate professor. From May 1993 to August 1994, he worked as postdoc fellow at the Department of Materials Science and Engineering, Pennsylvania State University, USA, where he went back as an adjunct professor in 2001. His current research interests include fracture phenomena in glasses and ceramics, strengthening of glass by ion exchange, electrical field-assisted sintering, and materials for solid oxide fuel cells. Author of more than 150 scientific papers and 12 patents, Prof. Sglavo is a member of the American Ceramic Society, the Society of Glass Technology, and the Italian Association of Professional Engineers.

Contents

Preface

Glass, as a man-made material, has been used since about 10,000 BC and has played a major role in the advancement of civilizations. The entire human history has run together with the development of new glass components in the arts, architecture, transportation, medicine and communication.

Today, the rate of glass innovation is continuously accelerating, thanks to deeper understanding of glass physics and chemistry, modern analytic and control technologies and more powerful calculation and simulation tools. Advancements in glass science and technology are helping to solve some of our world's most urgent challenges, such as more effective healthcare, cleaner energy and water and efficient communication leading to the development of innovative applications.

This book includes eleven chapters divided into two sections. In the first one, new findings in the structure and crystallization of innovative glass compositions are reported. In the second one, innovative technologies and applications are described from the use of glass in optical devices and lasers to fibres in composites, micro-patterned components in sensors and microdevices, beads in building walls and sealing in solid oxide fuel cells.

Prof. Vincenzo M. Sglavo
Department of Industrial Engineering
University of Trento
Italy

Advances in Glass Science

The Nature of the Defects in Phosphate-Based Glasses Induced by Gamma Radiation

Quanlong He, Pengfei Wang, Min Lu and Bo Peng

Additional information is available at the end of the chapter

Abstract

Final optics assembly is one of the most important parts in high energy and large-scale laser systems like US National Ignition Facility and SG III in China. Those final optics assembly are facing some severe tests, like the laser-induced damage caused by 3ω (351 nm) laser irradiation. Meanwhile, the irradiation of gamma ray and X-rays, will also cause the changes of optical properties in the investigated multi-component phosphate glasses that have potential use in novel color separation optics in high power laser facilities. These changes of optical properties are associated with the defects induced by gamma radiation. In details, some defects contribute to the absorption in the UV region, which will deteriorate their UV performance. However, some of the induced defects can be eliminated by thermal treatment due to the release and capture of the electrons in conduction band. Besides, the doped Fe, Co, B, Ce and Sb will also affect the defect-state in phosphate-based glasses. In details, gamma radiation resistances of the phosphate glass can be greatly improved by CeO_2 and Sb_2O_3 co-doping, and the introduction of B_2O_3 reduces the connectivity of phosphate chains and thus increases the concentration of PO_3-EC and PO_4-EC defects.

Keywords: defects, phosphate-based glass, gamma radiation, radiation resistance, absorption

1. Introduction

Fluoride-containing phosphate-based glass is considered to be a special case of optical laser glasses that have potential use in color separation optics in high power laser facilities. Thus glasses have received a great deal of interest due to their excellent properties, such as tunable melt viscosity and glass forming ability, high transparency from the ultraviolet to the infrared

region of the optical spectra, relatively lower refractive together with low non-linear refractive indices, etc., which endow them with applications as an attractive candidate for high-performance UV optics and high power laser technology, such as lens system in excimer laser systems, UV microlithography equipment and other special UV optics [1–4]. In this case, the investigations on the glass's micro-structure and micro-defects as well as the corresponding optical and physical properties of various phosphate-based glasses have never stopped in the improvement of their optical properties for developing high performance UV laser glasses.

Absorptive ions-doped phosphate-based laser glasses have exhibited great potential in the area of optical filters in high-energy and large-scale laser facilities like SG III in China and US National Ignition Facility (NIF) [5–8], in which the unconverted fundamental (1ω) and second harmonic frequency (2ω) laser lights should be separated or filtered from the main third harmonic frequency (3ω) laser light as entered into fusion target chamber to avoid the error of laser beam diagnostics for the inertial confinement fusion (ICF) experiments. Compared with silicate glasses, the iron and Co doped 1ω and 2ω absorptive fluoride-containing phosphate-based glass exhibits much lower absorption and higher pulse laser-induced damage thresholds (LIDTs) at 3ω wavelength [8]. Unfortunately, several types defects will form in these phosphate glasses during the glass preparation process and post processing that are harmful for their transmittance and will significantly decrease their LIDTs particular at UV region. And, the nature of the defects in these specific glasses is very complex and still not explicit, especially for the evolutionary mechanism of the produced defects. Therefore, to explore the information about the defects is critical for understanding of their evolutionary mechanism of the produced defects.

In this chapter, we will address the nature of the defects in phosphate-based glasses induced by gamma radiation, by first discussing the properties of most common defects in phosphate-based glasses. Then, we will report details about the effects of gamma radiation on the defects in the phosphate-based glasses. Finally, we will discuss the self-repairing capability of defects induced by gamma radiation during heat treatment process. Furthermore, this chapter will also address the effect of defects in phosphate-based glasses.

2. Properties of various defects in phosphate-based glasses

There are two types of defects that are generated in phosphate-based glasses, intrinsic defects that arise from glass matrix and the raw materials, and extrinsic defects which are caused by impurities or dopants [9]. It is well established that the basic structural unit of phosphate glass is the P-tetrahedra that made up phosphate chains in phosphate-based glass [10]. Modifier cations, glass preparation process including thermal annealing conditions, glass melting, and energetic radiations may influence the above mentioned phosphate chains, which subsequently form several intrinsic defects, such as phosphate-related oxygen hole center (POHC) characterized by an unpaired electron shared between two orbitals of two non-bridging oxygens bound to a phosphorus atom, oxygen-related hole center (OHC), and phosphate-related electron centers (PEC) including PO_2-EC, PO_3-EC and PO_4-EC defects etc. [11, 12] which are common defects in various phosphate glass systems. On the other hand, some unavoidable trace impurities such as iron, cobalt, and other intentionally or unintentionally doped transition metals

could produce numerous extrinsic defects [13], such as Fe^{2+}, Fe^{3+}, Co^{2+} which have large absorption in the UV-VIS range. In addition, it is well established that the absorption bands of holes defects lie in the low energy region, and several bands connected with electrons defects are positioned near the high energy region.

3. Defects induced by gamma radiation in phosphate-based glasses

High-power UV laser irradiation, with potential use of the series of fluoride containing phosphate-based glasses in megajoule class lasers as NIF and SG III will also suffer from the irradiation of the gamma rays and X-rays in the experimental chamber [14]. So, gamma radiation is a general tool to investigate the nature of the defects in phosphate-based glasses.

Various defects are formed during the gamma radiation process, which determines obvious absorption in the visible range, as shown by the gradually deepened maroon color as the total gamma radiation dose increases as shown in **Figure 1**. The details can also be found in the transmission spectra (**Figure 2**). Gamma radiation causes several defects in phosphate-based glass that have large absorption in the region of UV-VIS spectrum range, as shown by the decreased transmittance in **Figure 2**. By increasing the total radiation dose, the transmittance decreases further, especially for the absorption bands at around 385 and 530 nm which is related to the POHC defects and PO_3-EC defects [15], respectively. This suggests that more PO_3-EC and POHC defects are generated during the irradiation process with increasing total dose. Besides, it can be found that the UV absorption edges of these glass samples gradually red-shifts with the increase of irradiation dose, which is ascribed to the increased defects concentration of both Fe^{3+} and PO_3-EC [13]. To better illustrate the absorption characteristics of these defects, one of the absorption spectra was fitted and separated into multi Gaussian peaks, as shown in **Figure 3**. It can be found that the positive charged hole center defects lie in the low energy region i.e. POHC at 2.36 eV and OHC at 4.28 eV, while several negative charged electron center defects are positioned near the high energy region such as PO_3-EC at 5.94 eV and PO_4-EC at 5.17 eV [16]. Besides, the band of the two positive charged hole center defects at around 3.22 eV are also related to the PO_3-EC, which corresponds to the large absorption at 385 nm as shown in **Figure 2**.

Figure 1. Photographs of a series of phosphate-based glasses with different radiation doses (20k, 100k, 250k, 500k and 1000k rad (Si)).
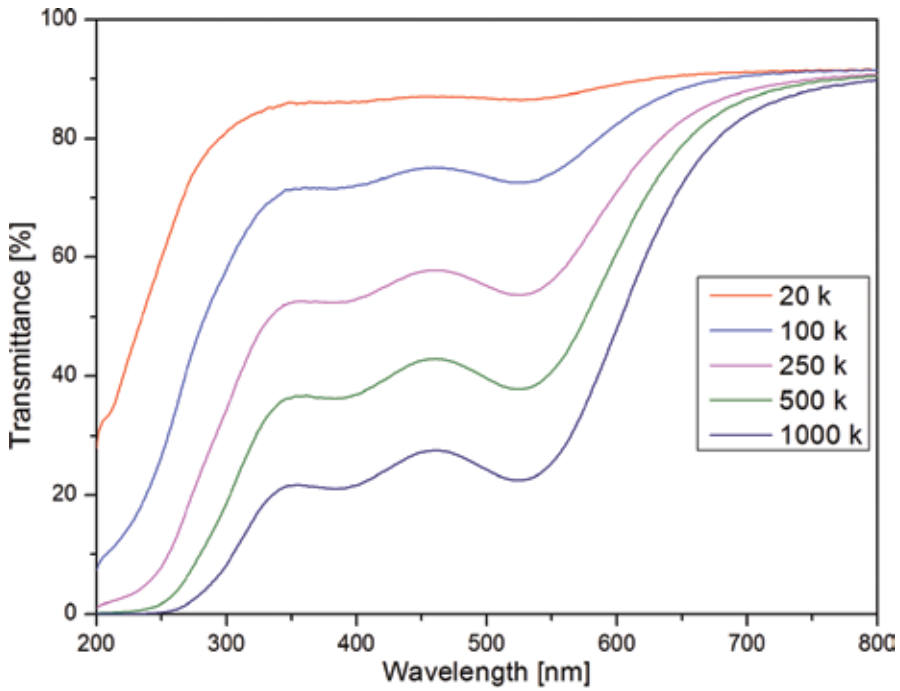
Figure 2. Transmission spectra of the series of phosphate-based glasses with different radiation doses (20k, 100k, 250k, 500k and 1000k rad (Si)).
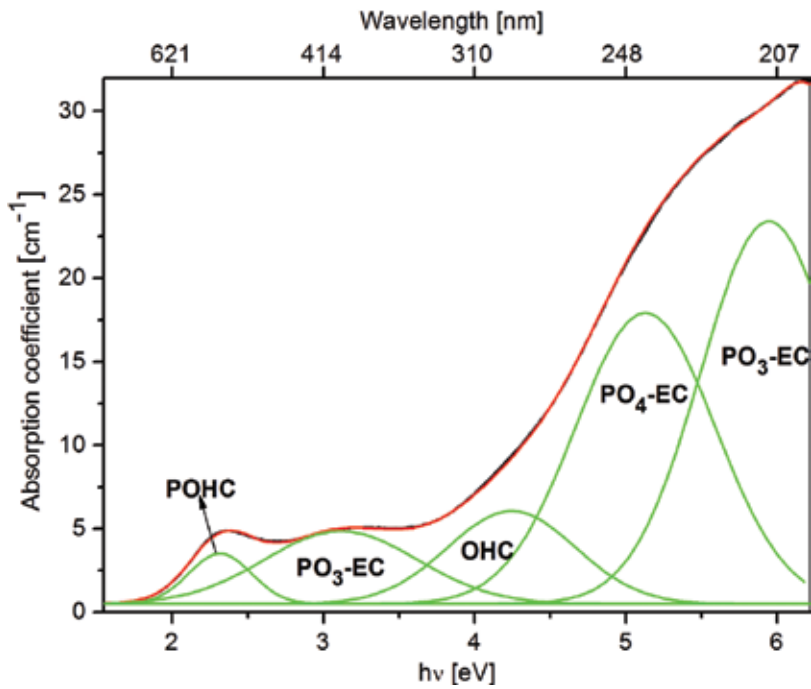
Figure 3. Separation of radiation induced absorption band for the phosphate-based glasses [14].
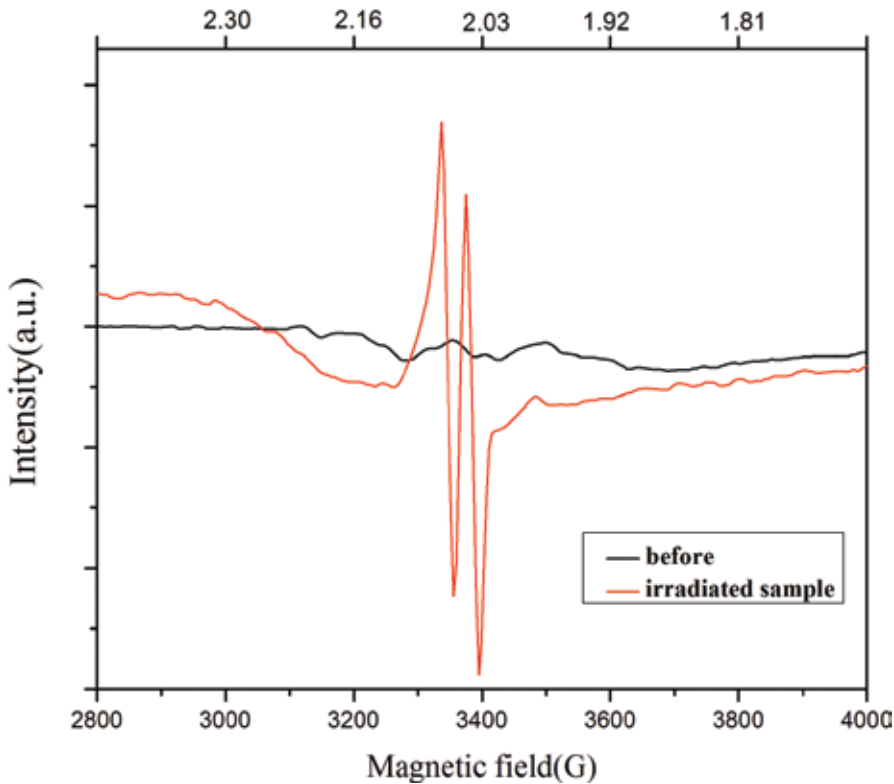
Figure 4. The EPR spectra of the samples before and after gamma radiation.

Typical EPR spectra of phosphate-based glass before and after gamma radiation are shown in **Figure 4**. All EPR spectra are dominated by the signals of intrinsic defects. The main signal is the POHC defects with the g-value around 2.06 [17]. After gamma irradiation, this signal becomes significant. Another signal located close to the POHC signal can also be found in the irradiated samples, which is associated with the OHC defects caused by gamma radiation. It can be noticed that the signals of PO_3-EC and PO_4-EC are enhanced if compared with that of the un-irradiated samples. These results suggest that gamma irradiation causes much more defects in glass.

Gamma irradiation causes the increase of various defects in the phosphate-based glasses, resulting in an obvious decline of the transmittance in the UV and visible range, indicating that more color centers are generated in these glasses.

4. The influence of heat treatment on the defects in the fluoride-containing phosphate-based glasses

Post heat treatment is an effective method to investigate the information of the defects and reveal their evolutionary mechanism [9]. Post heat treatment can remove the defects caused by gamma radiation in phosphate-based glasses. In order to illustrate the changes of the main defects concentration in these phosphate-based glasses upon the post heat treatment, **Figures 5** and **6** present

the relations between the absorption-peak's area of the corresponding defects and the post heat treatment temperatures. As one can see, the POHC concentration is significantly higher in Co-doped than that in FP sample (made in air atmosphere). With the increase of radiation doses, POHC defects concentration increased, while their concentration decreases with the increase of post heat treatment temperature as shown in **Figure 5a**. In **Figure 5b**, it is obvious that the concentrations of OHC defects decrease with the increase of post heat treatment temperature. Besides, the corresponding decrease tendency is obvious although at low heat treatment temperature. It was also found that the OHC concentration level increases relatively slow in the FP and Co doped samples when increase the total gamma radiation doses. The variations in the phosphate-based glasses irradiated with different radiation dose and heat treated at different temperatures are shown in **Figure 5c**. In details, the FP:Fe sample maintains the highest FD defect concentration level, and the concentration levels could be described as an order of FP:Fe > FP (air) > FP > FP:Co.
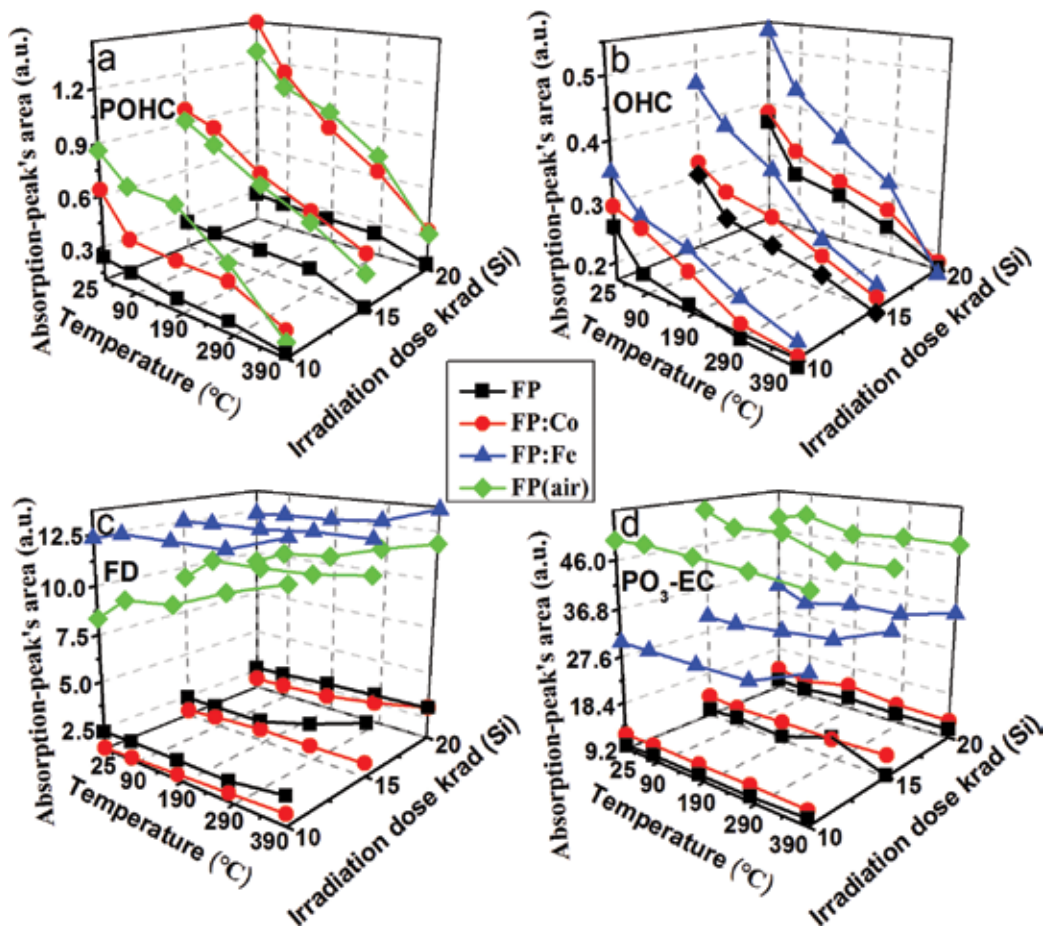
Figure 5. Line chart displaying the absorption-peak's area of corresponding intrinsic defects (a: POHC, b: OHC, c: FD, d: PO$_3$-EC) in the FP, FP: Co, FP: Fe and FP (air) samples irradiated with different radiation dose and heat treated at different temperatures [9].
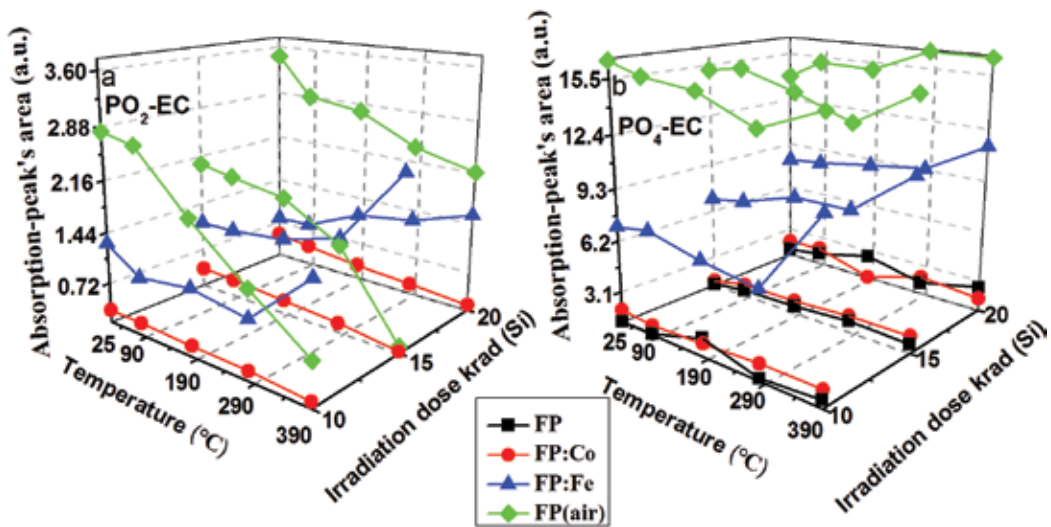
Figure 6. Line chart displaying the absorption-peak's area of PEC defects (a (PO_2-EC), b (PO_4-EC)) in the FP, FP: Co, FP: Fe and FP (air) samples irradiated with different radiation dose and heat treated at different temperatures [9].

In addition, the concentration levels of FD defects in Fe-doped sample is much higher than others, indicating that Fe is likely contributing to the generation the FD defects in these phosphate-based glass. Similarly, the FD defect is insensitive to the total gamma radiation doses, and its concentration increases slowly at low temperature i.e. ≤190°C, but with further increase their post heat treatment temperature, its concentration increases apparently. As seen in **Figure 5d**, the concentration level of PO_3-EC defect in these phosphate-based glasses is higher than other defects, and their concentration is insensitive to the total gamma radiation dose and the post heat treatment temperature, this is due to the PO_3-EC defects is the main defect in these glass, and their structure is like to the glass's network. The same phenomenon can also be observed in **Figure 6b**. This might be because PO_3-EC and PO_4-EC defects are mainly associated with the skeleton structure of these phosphate-based glasses. Meanwhile, phosphate contents dominate the glass composition and therefore, PO_3-EC will be the main defects in these phosphate-based glasses, thus its concentration level is much higher than others. And their concentration is relatively stable in the investigated phosphate-based glasses. Based on the above-mentioned results, we can infer that OHC and POHC defects are mainly ascribed to gamma radiation in our experiments, and these defects could be reduced in the considered phosphate-based glasses by post heat treatment near their glass transition temperatures.

Thermal energy at room temperature may induce the release of trapped electrons in the gamma radiated samples, and post heat treatment can accelerate this process. In details, part of the trapped electrons in PO_3-EC, PO_4-EC and PO_2-EC defects recombines with POHC defects through the conduction band to form Q^3 units under thermal energy. Meanwhile, some free electrons are captured by OHC defects to form Q^0 units under air atmosphere, which result in the decreased OHC defect. Heat treatment is effective way to remove the gamma radiation-caused defects by recombination of HC with EC defects in the considered phosphate-based glasses.

5. Factors that affect the defects in phosphate-based glasses

5.1. Influence of Ce and Sb doping on the defect-state in phosphate-based glass

As we all know, the induced transmittance decrease in optical glasses is mainly due to the absorption by color centers in glass matrix [18]. The radiation resistance [19], i.e. the suppression of the decreased transmittance in optical losses, of the optical components including optical glasses, color-separation gratings and protective filters can be improved by doping of cerium [20, 21]. Cerium ions have two valence states, Ce^{3+} and Ce^{4+} in these phosphate-based optical glasses. Trivalent ions can be converted into tetravalent ions by capturing the radiation-induced holes, thus inhibiting the generation of hole centers. And tetravalent ions inhibit the formation of electrons centers resulting from trapped electrons, which prevents to some extent the formation of color centers that have large absorption in the visible range [22].

Figure 7 shows the O1s XPS spectra of Ce doped samples. These bands located at the higher and lower binding energy are ascribed to bridging oxygen (BO) and non-bridging oxygen [23] (NBO), respectively. It can be found that NBO (the ratios of the peak's area of NBO to the sum peak's area) in Ce-doped sample decrease from 58.7 to 54.6%, while BO increase, compared with the Ce-free sample. This indicates that NBO bond can be destroyed by Ce-doping
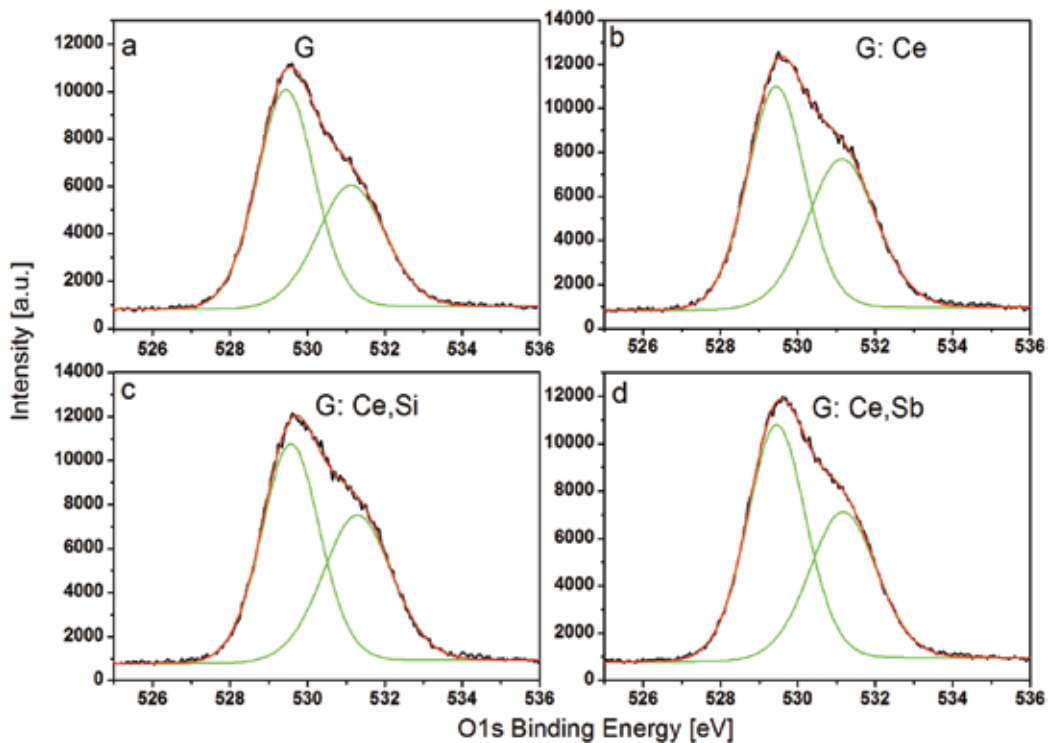
Figure 7. Measured O1s XPS spectra of G (a), G: Ce (b), G: Ce,Si (c) and G: Ce,Sb (d) glasses with Gaussian peak fittings [18].

in these types of phosphate-based glasses. Nevertheless, as for these co-doped samples, the ratio of NBO in the Ce and Sb co-doped sample increase from 55.1 to 57.6% and BO decrease compared with that of Ce and Si co-doped sample. This suggests that the trend of breaking NBO bond can be suppressed by doping of Si or Sb in these Ce-containing phosphate glasses.

Figure 8a shows that more color centers are generated in these phosphate-based glasses when exposed to the gamma radiation. These color centers have large absorption in the UV and visible region as shown by the transmittance decline. By increasing the total radiation doses, the transmittance further decreases, especially at around 385 and 525 nm, which is ascribed to POHC and PO_3-EC defects [15]. Under gamma radiation with the total dose of 250k rad(Si), the radiation resistance (transmittance ratio of the irradiated to that of the non-irradiated sample at certain wavelength) of cerium-doped glass is improved from 56.4 to 61.9% at 385 nm, and from 57.39 to 73.9% at 525 nm. This radiation resistance can be further enhanced in co-doped samples, especially for the Sb co-doped sample, i.e. their radiation resistance increases to 92.4% at 525 nm. This is in accordance with the changes of glass color in **Figure 8** (inset). These results indicate that the radiation resistance of gamma radiation can be significantly improved by doping Sb^{3+} in Ce-containing phosphate glasses. As we further increase the
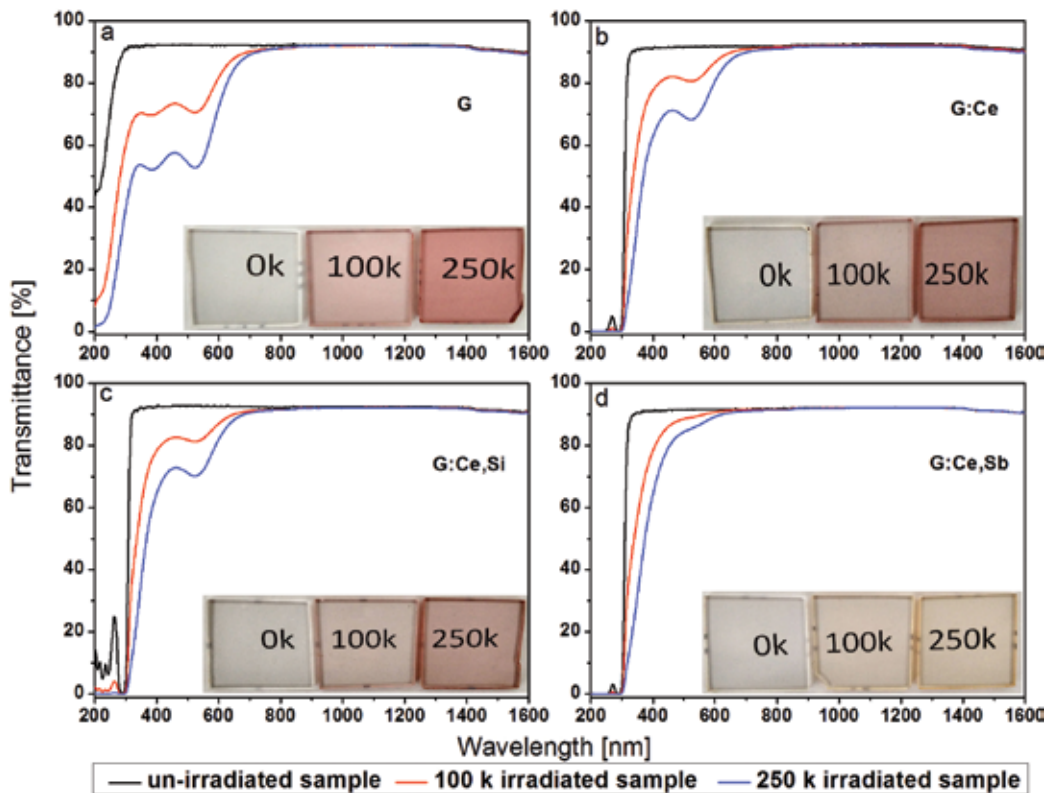
Figure 8. Measured transmission spectra and (inset) photograph of G (a), G: Ce (b), G: Ce,Si (c) and G: Ce,Sb (d) glasses before and after gamma radiation (100k and 250k rad (Si), respectively) [18].

content of cerium (to 0.66 wt% (0.75 mol%)) in the Ce, Sb co-doped sample, its radiation resistance further increases to 82.5% at 385 nm and 99.3% at 525 nm, the corresponding transmission spectra being shown in **Figure 9**. In details, the absorption at around 385 and 525 nm are 0.95 and 0.035 cm^{-1}, respectively. This result is better than that reported by Heng X, et al. [24].

Figure 10 compares the EPR spectra of these Ce-doped and Ce-free samples before and after gamma radiation with total dose of 250k rad(Si). The EPR spectra of these samples before irradiation are dominated by the signals with the magnetic field in the range of 3100–3500 G and around at 3355 G and are associated with PO_3-EC and POHC defects [17], respectively, especially for the Ce-free samples. It is obvious that PO_3-EC's signals decrease when CeO_2 was doped into these glasses; this is ascribed to the decreasing NBO associated with the precursors of PO_3-EC defects in the considered phosphate-based glass. Co-doped with Si in these samples, these signals become apparent. It can be found that these POHC defects signals are significantly enhanced when exposing to gamma radiation, as shown the red line in **Figure 10**. This is associated with the increase of POHC defects caused by gamma radiation. However, this signal becomes weaker in co-doped samples, i.e. Ce, Sb co-doped glasses (their defects signals significant decrease when compared with others). These results suggest that co-doping with Si and Sb can efficiently decrease the POHC defects in these Ce-containing phosphate glasses, especially for Sb ions.

It is well known that cerium ions in these phosphate-based glasses exists as Ce^{4+} that can be converted to Ce^{3+} by capturing the electrons caused by gamma radiation, thus decreasing the PO_3-EC defects. Therefore, Ce-doping causes the concentration decrease of NBO bonds,
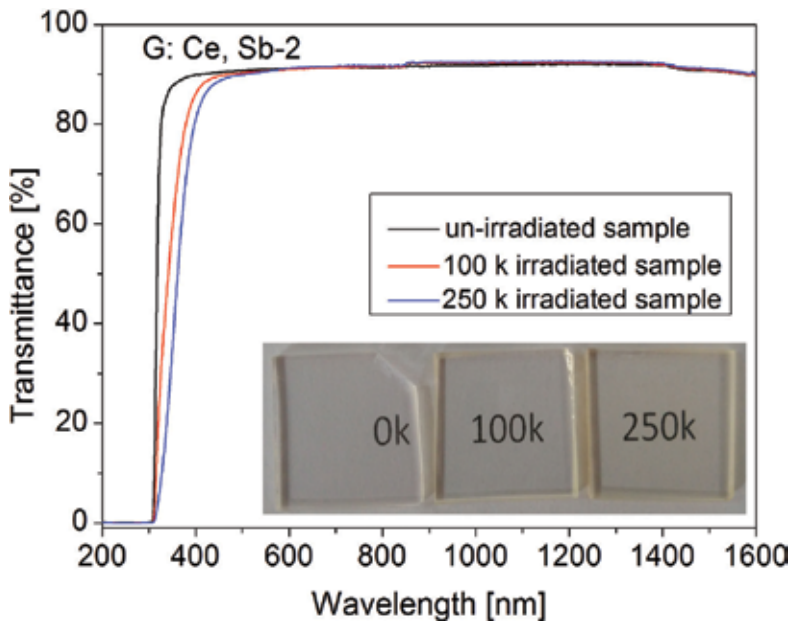
Figure 9. Measured transmission spectra and (inset) photographs of G: Ce, Sb-2 (higher Ce doping concentration) glasses before and after gamma radiation (100k, 250k rad (Si), respectively) [18].
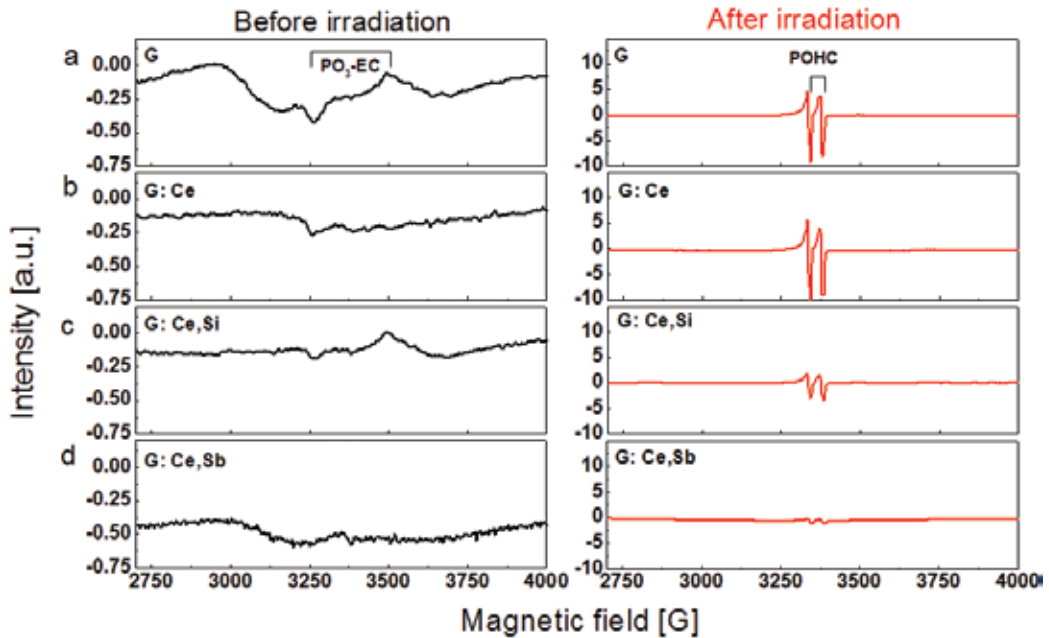
Figure 10. Measured EPR spectra of a (G), b (G: Ce), c (G: Ce,Si) and d (G: Ce,Sb) glasses before and after gamma radiation (250k rad (Si)) [18].

resulting in more limited POHC and PO_3-EC defects precursors. Besides, some Ce^{3+} ions are converted to Ce^{4+} by capturing the holes induced by gamma radiation and then suppress the generation of POHC defects. Although doping by Sb ions in Ce-containing phosphate glasses can increase the precursors concentration of POHC defects, Sb^{3+} can be easily photo-oxidized to Sb^{4+} by capturing the gamma radiation induced holes when exposed to the gamma radiation. Besides, to improve their stability, Sb^{4+} can be converted to Sb^{5+} by further capturing these induced holes. Therefore, the concentration of gamma radiation induced electrons and holes decreases in the considered phosphate-based glasses.

5.2. Influence of H_3BO_3 addition on the defect-state of phosphate-based glass

It is known that B_2O_3 addition can decrease the melting point and the crystallization temperature of the host glass, further depressing the volatilization of phosphorus and fluorine, but also improving their chemical durability and thermal stability [25, 26]. Therefore, the effects of B_2O_3 addition on the defects is critical for understanding the change of the property for the considered phosphate-based glasses.

Figure 11 presents the Raman spectra of phosphate glass samples [25]. It can be found that the peaks at around 1262 cm^{-1} decrease with the increase of B_2O_3 content, and the small peak almost disappears when the H_3BO_3:SiO_2 ratio reaches 7.5:2. Meanwhile, the intensity of the peaks located at about 666 cm^{-1} increase, which is related to the increase of B_5O_8 units [27]. The intensity of bands at around 590 cm^{-1} decrease as the H_3BO_3:SiO_2 ratio became larger, this
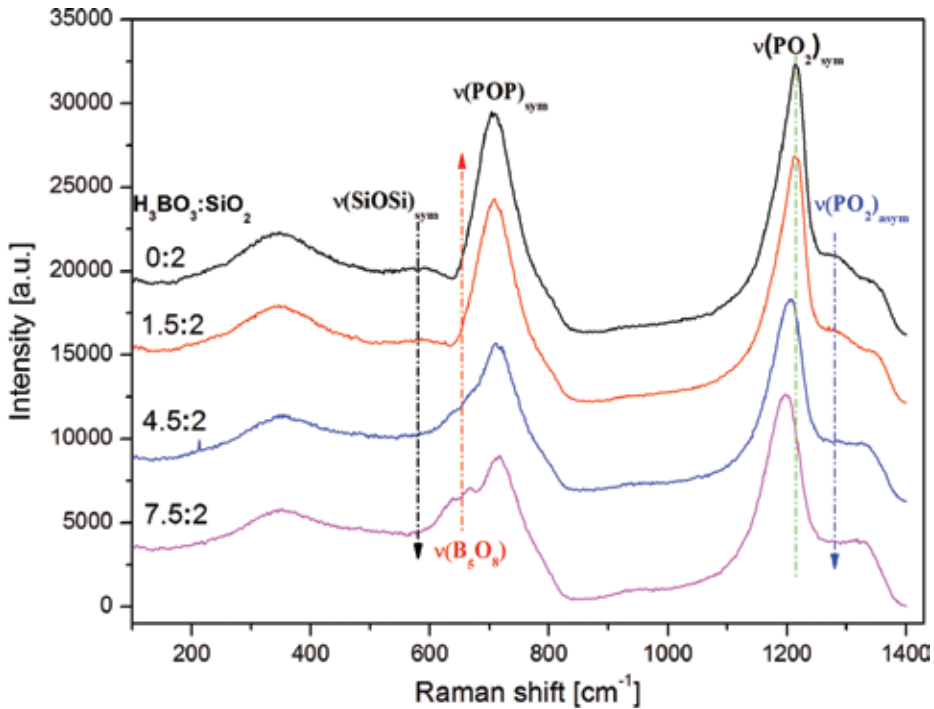
Figure 11. The Raman spectra of the series of phosphate-based glasses with different H_3BO_3: SiO_2 ratio (0:2, 1.5:2, 4.5:2 and 7.5:2, respectively) [25].

being associated with the increase of B_2O_3 and corresponding decrease of SiO_2 concentration in the final glasses. The existence of bands involving B_5O_8, together with the Rajbhandari's results [28] indicate that B_5O_8 units do not form mechanically isolated network units but rather they are bonded to each other to form a vitreous networks.

Figure 12 shows the O1s XPS spectra for different B_3O_3 content. The peaks near the lower (at around 529.5 eV) and higher (at around 531.5 eV) binding energy are assigned to NBO and BO, respectively [23]. With the introduction of B_2O_3, the non-bridging oxygens decrease, whereas the bridging oxygens increase. This is in agreement with the changes in Raman spectra in **Figure 11**.

It is interesting that the absorption of Fe^{3+} increase with B_2O_3 addition. And with further increase of B_2O_3 content, the absorption of Fe^{3+} is nearly invariant. As we all know, iron is one of the undesirable transition metal impurities that is very easily introduced through raw materials. Herein, the concentration of iron ions in the phosphate-based glasses is almost the same due to the same raw materials and preparation process. Besides, the introduction of B_2O_3 will cause the breakage of phosphate chains (**Figure 13d**) and contribute to form PO_3-EC defects. However, further increase the content of B_2O_3 in the considered phosphate-based glass, B_2O_3 could enter the glass network structure (**Figure 13e**) and form B_5O_8 units that will enhance the connectivity of these long phosphate chains, and decrease the concentration of PO_3-EC defects.
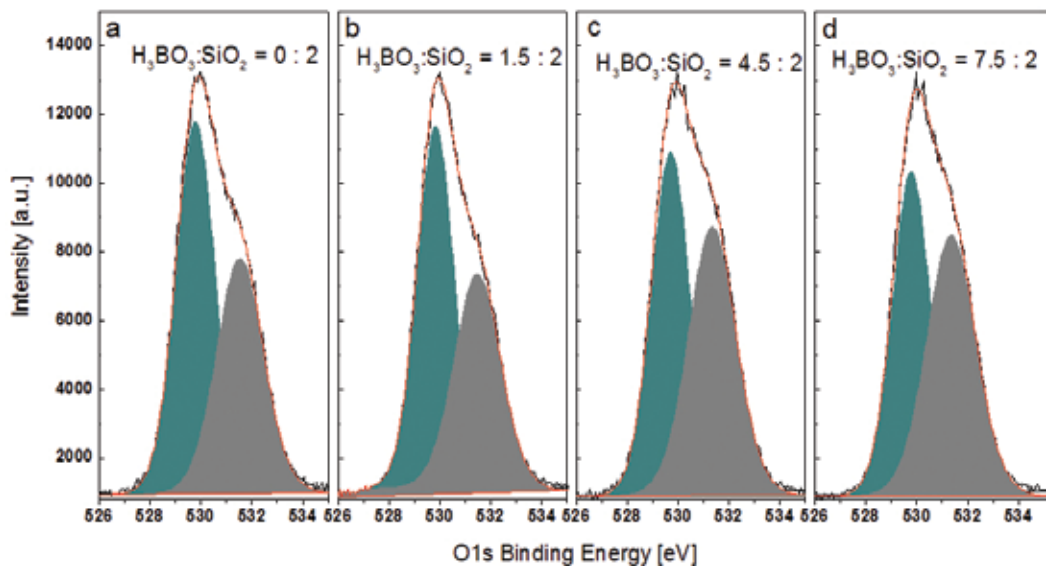
Figure 12. XPS spectra of the series of phosphate-based glasses with different H_3BO_3: SiO_2 ratio (a (0:2), b (1.5:2), c (4.5:2) and d (7.5:2)) [25].
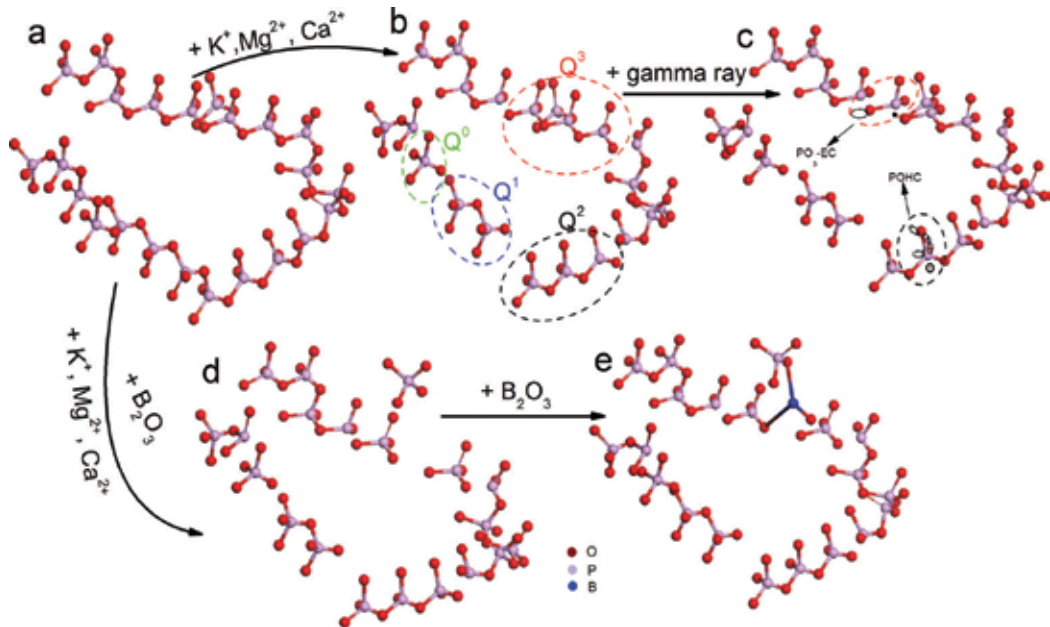
Figure 13. Schematic representations the changes of phosphate glasses network (a (the structure of basic glass), b (the structure with doped R^+ and R^{2+}), c (the structure after gamma radiation), d (the structure with doped SiO_2 and B_2O_3) and e (the structure with doped more B_2O_3)) caused by alkali (R^+), alkaline earth metal cations (R^{2+}) and B_2O_3 as well as gamma irradiation (oxygen atoms (red), phosphorus atoms (pink), boron atoms (blue)) [25].

By increasing B_2O_3, the tendency of the transmittance to decrease in the UV-VIS region is gradual until a critical H_3BO_3:SiO_2 ratio (4.5:2), when exposed to gamma radiation with high dose. By further increasing the content of B_2O_3, this trend becomes weak. These results suggest that the formed B_5O_8 can suppress the formation of PO_3-EC and POHC defects. The results provide evidence for enhanced gamma radiation resistances in the considered multicomponent phosphate glasses. Therefore, B_2O_3-doped phosphate glasses could be used as a new type of host materials for applications in space exploration and radioactive wastes treatments.

5.3. Influence of iron and cobalt on the defect-state of phosphate-based glass

Many types of doping ions together with unwanted impurities, as extrinsic defects, also influence the UV absorption and damage property of the considered glass optics [29]. Iron and cobalt-doped phosphate-based glasses show a various degree of red-shift (**Figure 14**) as compared with un-doped glass, which is dominated by the charge-transfer transition of Fe^{3+} and the absorption of cobalt, respectively [3, 13]. According to Ref. [30], the low transmittance at around 215 and 250 nm is dominated by the charge-transfer absorption of Fe^{2+} and Fe^{3+}, respectively. And the two bands between 1.9 and 2.4 eV are related to the cobalt ions [3].
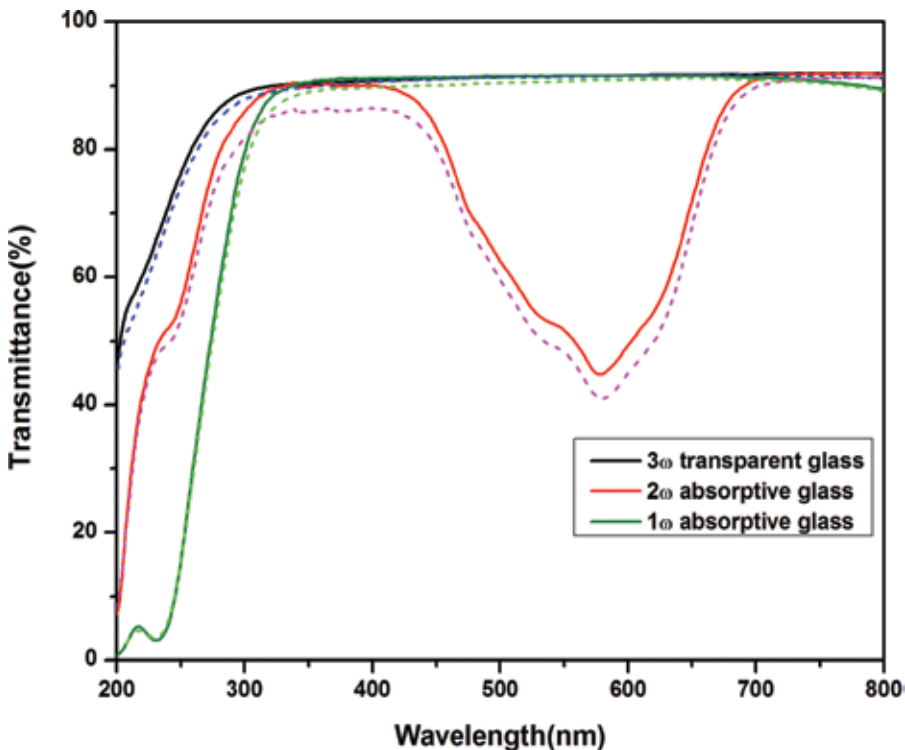
Figure 14. The UV/VIS transmission spectra of the series of fluoride-containing phosphate-based glass samples before (solid line) and after (short dash line) thermal treatment in H_2 atmosphere [29].
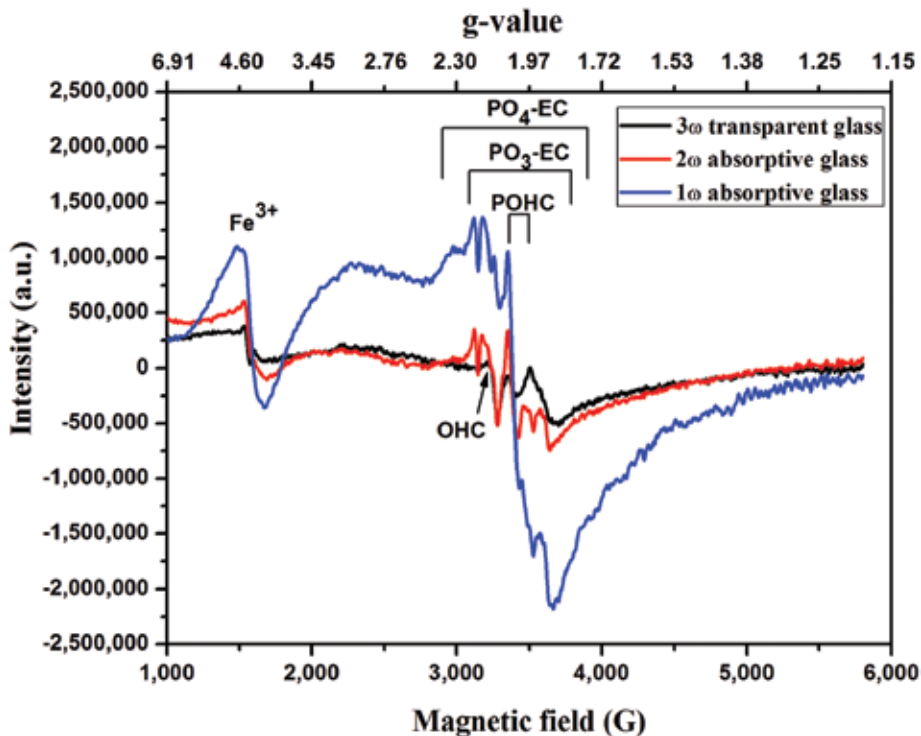
Figure 15. The ESR spectra of 1ω absorptive, 2ω absorptive and 3ω transparent glasses [29].

ESR measurements give direct evidence of the paramagnetic color centers in glasses. The ESR intensity of Fe^{3+} (g-value around at 4.3) [31] shows an order of 3ω, 2ω and 1ω glass, which is in agreement with the changes of the UV absorption edge as shown in **Figures 14** and **15**. The signals of PO_3-EC, PO_4-EC, POHC defects become apparent after doping with iron or cobalt ions, indicating that cobalt and iron contribute to form these defects. No obvious cobalt signal was found in 2ω absorptive glasses. The absence of Co^{2+} signal might be associated with the distortion of their complexes, which signal could only be detected at the practical laboratory temperature (77 K) [32].

To our best knowledge, the heat treatment in reducing atmosphere leads to the shift of the Fe^{3+} ↔ Fe^{2+} equilibrium in the glasses toward the right side. Thus, it is reasonable to put forward that Fe^{3+} are favorable to form POHC defects. On the other hand, the presence of Fe^{2+} and Co^{2+} favors the formation of FD center defects, which have a large absorption cross section at ~5.50 eV. It is known that Co^{2+} is the main valence state [33, 34], in the weak basicity host glass, like phosphate-based glass; therefore, these results indicate that Co^{2+} suppresses the formation of POHC defects in this types phosphate-based glasses.

Doping with iron and cobalt shows significant impact on the transmittance of these two absorptive glasses, especially for the UV transmission edges, by influencing the concentration of other defects. The results indicate that Fe^{3+} suppress the formation of FD defects, while promotes the

formation of POHC defects. Besides, Co^{2+} inhibits the formation of POHC and PO_4-EC defects, and Fe^{2+} promotes the formation of POHC defects.

6. Summary

In this chapter, we outlined some of the basic properties of the common defects in phosphate-based glasses. Gamma radiation was employed to investigate the influence of dopants on the nature of defects in phosphate-based glasses. And the evolutionary mechanism of defects associated with the post heat treatment was also discussed.

Author details

Quanlong He[1,2], Pengfei Wang[1]*, Min Lu[1] and Bo Peng[1]

*Address all correspondence to: pfwang@opt.ac.cn

1 State Key Laboratory of Transient Optics and Photonics, Xi'an Institute of Optics and Precision Mechanics, Chinese Academy of Sciences (CAS), Xi'an, P.R. China

2 University of Chinese Academy of Sciences (UCAS), Beijing, P.R. China

References

[1] Ehrt D, Seeber W. Glass for high performance optics and laser technology. Journal of Non-Crystalline Solids. 1991;**129**(1-3):19-30. DOI: 10.1016/0022-3093(91)90076-I

[2] Brow RK. The structure of simple phosphate glasses. Journal of Non-Crystalline Solids. 2000;**263**:1-28. DOI: 10.1016/S0022-3093(99)00620-1

[3] Möncke D, Ehrt D. Radiation-induced defects in CoO- and NiO-doped fluoride, phosphate, silicate and borosilicate glasses. Glass Science and Technology. 2002;**75**:243-253

[4] Ehrt D, Ebeling P, Natura U, et al. Redox equilibria and ultraviolet radiation induced defects in glasses. International Congress on Glass. 2001;**1**:84

[5] Moses EI, Campbell JH, Stolz CJ, et al. Optical engineering at the Lawrence Livermore National Laboratory. In: Sato PT, Lane MA, editors. Proceedings of SPIE-The International Society for Optical Engineering. Vol. 5001. Bellingham, WA: SPIE–International Society for Optical Engineering; 2003. p. 1

[6] Honig J, Adams JJ, Carr CW, et al. Optics Performance at 1ω, 2ω and 3ω: Final Report on LDRD Project 03-ERD-071. Livermore, CA: Lawrence Livermore National Laboratory (LLNL); 2006

[7] John LE, William FK, William WS, et al. NIF Technology Review, from Technology Resource Group of the NIF Council; Nov. 4, 1999

[8] Wang P, Lu M, Gao F, et al. Luminescence in the fluoride-containing phosphate-based glasses: A possible origin of their high resistance to nanosecond pulse laser-induced damage. Scientific Reports. 2015;**5**:8593. DOI: 10.1038/srep08593

[9] Wang P, He Q, Lu M, et al. Evolutionary mechanism of the defects in the fluoride-containing phosphate based glasses induced by gamma radiation. Scientific Reports. 2016;**6**:18926. DOI: 10.1038/srep18926

[10] Fletcher LB, Witcher JJ, Troy N, et al. Femtosecond laser writing of waveguides in zinc phosphate glasses [Invited]. Optical Materials Express. 2011;**1**:845-855. DOI: 10.1364/OME.1.000845

[11] Ebeling P, Ehrt D, Friedrich M. X-ray induced effects in phosphate glasses. Optical Materials. 2002;**20**:101-111. DOI: 10.1016/S0925-3467(02)00052-6

[12] Feng DD, He Q, Lu M, et al. Investigations on the photoluminescence spectra and its defect-related nature for the ultraviolet transmitting fluoride-containing phosphate-based glasses. Journal of Non-Crystalline Solids. 2015;**425**:130-137. DOI: 10.1016/j.jnoncrysol.2015.06.009

[13] Ehrt D. UV-absorption and radiation effects in different glasses doped with iron and tin in the ppm range. Comptes Rendus Chimie. 2002;**5**:679-692. DOI: 10.1016/S1631-0748(02)01432-7

[14] He Q, Xue Y, Wang P, et al. Natural healing behavior of gamma radiation induced defects in multicomponent phosphate glasses used for high energy UV lasers. Optical Materials Express. 2017;**7**(9):3284-3293. DOI: 10.1364/OME.7.003284

[15] Fan S, Yu C, He D, et al. Gamma rays induced defect centers in phosphate glass for radio-photoluminescence dosimeter. Radiation Measurements. 2011;**46**(1):46-50. DOI: 10.1016/j.radmeas.2010.09.002

[16] Ebeling P, Ehrt D, Friedrich M. Study of radiation-induced defects in fluoride-phosphate glasses by means of optical absorption and EPR spectroscopy. Glass Science and Technology. 2000;**73**(5):156-162

[17] Möncke D, Ehrt D. Radiation-induced defects in CoO- and NiO-doped fluoride-phosphate glasses. Glass Science and Technology. 2001;**74**:65-73

[18] He Q, Wang P, Sun M, et al. Significant improvement of gamma radiation resistance in CeO_2 doped phosphate glass by co-doping with Sb_2O_3. Optical Materials Express. 2017;**7**(3):1113-1121. DOI: 10.1364/OME.7.001113

[19] Speit B, Rädlein E, Frischat GH, et al. Radiation resistant optical glasses. Nuclear Instruments and Methods in Physics Research Section B: Beam Interactions with Materials and Atoms. 1992;**65(**1-4):384-386. DOI: 10.1016/0168-583X(92)95071-X

[20] Stroud JS. Color centers in a cerium-containing silicate glass. The Journal of Chemical Physics. 1962;**37**(4):836-841. DOI: 10.1063/1.1733170

[21] Engholm M, Jelger P, Laurell F, et al. Improved photodarkening resistivity in ytterbium-doped fiber lasers by cerium codoping. Optics Letters. 2009;**34**(8):1285-1287. DOI: 10.1364/OL.34.001285

[22] Jetschke S, Unger S, Schwuchow A, et al. Role of Ce in Yb/Al laser fibers: Prevention of photodarkening and thermal effects. Optics Express. 2016;**24**(12):13009-13022. DOI: 10.1364/OE.24.013009

[23] Wagner CD, Riggs WM, Davis LE, et al. Handbook of X-ray Photoelectron Spectroscopy. Minnesota: Perkin-Elmer Corporation, Physical Electronics Division; 1978

[24] Heng X, Qian Q, Chen X, et al. Reduced radiation damage in a multicomponent phosphate glass by Nb^{5+} or Sb^{3+} doping. Optics Materials Express. 2015;**5**(10):2272-2280. DOI: 10.1364/OME.5.002272

[25] He Q, Wang P, Sun M, et al. Effects of doping B_2O_3 on the defects-state in SiO_2-containing phosphate based glasses. Optical Materials Express. 2017:**7**(8):2697-2705. DOI: 10.1364/OME.7.002697

[26] Karabulut M, Yuce B, Bozdogan O, et al. Effect of boron addition on the structure and properties of iron phosphate glasses. Journal of Non-Crystalline solids. 2011;**357**(5):1455-1462. DOI: 10.1016/j.jnoncrysol.2010.11.023

[27] Konijnendijk WL, Stevels JM. The structure of borosilicate glasses studied by Raman scattering. Journal of Non-Crystalline Solids. 1976;**20**(2):193-224. DOI: 10.1016/0022-3093(76)90132-0

[28] Rajbhandari P, Montagne L, Tricot G. Doping of low-T_g phosphate glass with Al_2O_3, B_2O_3 and SiO_2: Part I-effect on glass property and stability. Materials Chemistry and Physics. 2016;**183**:542-550. DOI: 10.1016/j.matchemphys.2016.09.013

[29] He Q, Wang P, Lu M, et al. Investigations on the photoluminescence of the iron and cobalt doped fluoride-containing phosphate-based glasses and its defects-related nature. Journal of Alloys and Compounds. 2016;**685**:153-158. DOI: 10.1016/j.jallcom.2016.05.253

[30] Zou X, Toratani H. Radiation resistance of fluorophosphate glasses for high performance optical fiber in the ultraviolet region. Journal of Applied Physics. 1997;**81**(8):3354-3362. DOI: 10.1063/1.365029

[31] Srinivasulu K, Omkaram I, Obeid H, et al. Use of Fe^{3+} ion probe to study the structural coordination in sodium–lead borophosphate glasses by utilizing electron paramagnetic resonance and optical spectroscopy. Journal of Alloys and Compounds. 2013;**546**:208-215. DOI: 10.1016/j.jallcom.2012.08.054

[32] Griscom DL. Electron spin resonance in glasses. Journal of Non-Crystalline Solids. 1980;**40**(1): 211-272. DOI: 10.1016/0022-3093(80)90105-2

[33] ElBatal FH, Ouis MA, Morsi RMM, et al. Interaction of gamma rays with some sodium phosphate glasses containing cobalt. Journal of Non-Crystalline Solids. 2010;**356**(1):46-55. DOI: 10.1016/j.jnoncrysol.2009.09.030

[34] Abdelghany AM, ElBatal FH, ElBatal HA, et al. Optical and FTIR structural studies of CoO-doped sodium borate, sodium silicate and sodium phosphate glasses and effects of gamma irradiation - A comparative study. Journal of Molecular Structure. 2014;**1074**:503-510. DOI: 10.1016/j.molstruc.2014.06.011

Structure and Physical Properties of $59B_2O_3$–$10Na_2O$–$(30 - x)CdO$–$xZnO$–$1CuO$ $(0 \leq x \leq 30)$ Glass System

L.S. Ravangave and G. N. Devde

Abstract

A series of stable and transparent glasses with the composition $59B_2O_3$–$10Na_2O$–$(30 - x)$ CdO–$xZnO$–$1CuO$ $(0 \leq x \leq 30)$ (where x = 0, 7.5, 15, 22.5, and 30 mol%) were prepared by conventional melt-quenching technique. These glasses were characterized using X-ray diffraction (XRD), Fourier-transform infrared (FTIR) and Raman spectroscopes, differential scanning calorimetry (DSC), optical absorption, and electron paramagnetic resonance (EPR). XRD and DSC analysis confirmed the glassy nature of the prepared samples. The physical properties such as density (ρ), molar volume (V_m), oxygen packing density (OPD), and the molar volume of oxygen (V_o) were calculated and discussed. FTIR and Raman studies showed that the glass network consists of BO_3 and BO_4 units in various borate groups. From DSC, it was found that the glass transition temperature (T_g) varies nonlinearly with the addition of ZnO content in place of CdO. Both EPR and optical absorption results have confirmed that the Cu^{2+} ions are in octahedral coordination with a strong tetrahedral distortion. The changes in various spectroscopic properties of Cu^{2+} ions in the glasses such as spin-Hamiltonian parameters ($g_{\parallel}$, $g_{\perp}$ and $A_{\parallel}$) and bonding coefficients (α^2, β_1^2, and β^2) were understood with the help of FTIR and Raman studies.

Keywords: glasses, DSC, Raman, FTIR, EPR

1. Introduction

Alkali borate systems are attractive materials from a fundamental point of view as well as technological point of view [1]. From the literature, it has been observed that certain borate glasses are of greater interest and relevance because of their suitability in the progress of waveguides, electro-optic switches and modulators, magneto-optic materials, and solid-state

laser materials [2]. B_2O_3–ZnO glass has a high transparent window in the region from 370 nm to 2.2 µm, and these glasses are attractive host materials to incorporate rare earth elements for optoelectronics and optical fibers [3, 4]. The properties of B_2O_3 glass can often be altered by the addition of network modifiers. The most commonly used network modifiers are the alkali (Li_2O, Na_2O, and K_2O) and alkaline earth oxides (MgO, CaO, SrO, and BaO) [5, 6]. When mixed with these glass modifiers, its internal structure is rearranged due to the formation of non-bridging oxygen [7]. In particular, the addition of alkali oxide to pure B_2O_3 causes a progressive change of the boron atom coordination number (CN), from 3 (BO_3) to 4 (BO_4), and results in the formation of various borate units (diborate, triborate, tetraborate groups, etc.) [1].

From the literature, it was found that with the presence of ZnO or CdO in B_2O_3 glass matrix, UV transmission ability could be enhanced [8]. Therefore the authors have selected Na_2O, CdO, and ZnO as network modifiers. The addition of Cd and Zn oxides also results in the large glass formation domain [9]. When zinc oxide is introduced to borate glasses, there are two ways in which zinc ion can get incorporated into the glass. Zinc oxide may act as a network modifier by disrupting the bonds connecting neighboring $[BO_3]$ and $[BO_4]$ groups. On the other hand, zinc oxide can be incorporated into the glass as $[ZnO_4]$ structural units. Besides Cu^{2+} ions have been chosen in the present study as an EPR probe due to its EPR spectrum being sensitive enough to detect minute changes in the structure of the glasses [10]. Therefore in this article, authors have been presented the structural changes of Cu^{2+} ions-doped B_2O_3–Na_2O–CdO–ZnO glass induced by addition of ZnO into B_2O_3 glass matrix at 10 mol% Na_2O content. The various literature surveys show no evidences on structural study using FTIR, Raman spectroscopy, EPR, and optical absorption. Therefore the authors have planned to investigate the structural, optical, and physical changes in the Cu^{2+} ions-doped B_2O_3–Na_2O–CdO–ZnO glass system. The authors have also studied the spin-Hamiltonian parameters and site symmetry around Cu^{2+} ions in these glasses using EPR and optical absorption studies. The variations in the thermal properties and other physical properties in terms of structural changes of glasses have been discussed [6].

2. Experimental

2.1. Glass preparation

Glasses with compositional formula $59B_2O_3$–$10Na_2O$–$(30 − x)CdO$–$xZnO$–$1CuO$ (where x = 0, 7.5, 15, 22.5, and 30 mol%) were prepared using melt-quenching technique, and a series of glasses along with their codes are given in **Table 1**. All the chemicals used were of 99% purity from well-known companies (sd-fine, Merck, and Loba Chemie).

Appropriate amounts of H_3BO_3, Na_2CO_3, ZnO, and CdO were ground with a mortar and pestle and thoroughly mixed. About 1 mol% CuO was added as a spin probe and was melted in a platinum crucible at 1000°C for 30 min in an Autoset electric furnace; a similar technique was employed by Devde et al. [6].

Sample code	Composition (mol%)
BNCZ1	59B$_2$O$_3$–10Na$_2$O–30CdO
BNCZ2	59B$_2$O$_3$–10Na$_2$O–22.5CdO–7.5ZnO
BNCZ3	59B$_2$O$_3$–10Na$_2$O–15CdO–15ZnO
BNCZ4	59B$_2$O$_3$–10Na$_2$O–7.5CdO–22.5ZnO
BNCZ5	59B$_2$O$_3$–10Na$_2$O–30ZnO

Table 1. Glass compositions of 59B$_2$O$_3$–10Na$_2$O–(30 − x)CdO–xZnO–1CuO (0 ≤ x ≤ 30 mol%) glass system.

During the melting the crucible with homogeneous mixture was covered with a lid to avoid the volatility of the powder compounds or contamination from the furnace. Melts were stirred frequently to promote homogeneity, and the liquids were rapidly poured into a mold made with a stainless steel which was maintained at 200°C and pressed with another stainless steel plate maintained at the same temperature. The prepared glass samples were then transferred to another furnace and annealed at 300°C for 6 h to relieve thermal stress and strains of the glass samples. The prepared samples were examined, and it was found that the samples are clear, bubble free, and transparent.

2.2. Physical properties

Archimedes' method using xylene as immersion liquid was employed for the measurement of densities of the prepared glasses at room temperature. An average of three samples of each glass code was used. Obtained density values were used to calculate the molar volume using relation $V_m = M/\rho$, where M and ρ are the average molecular weight and density of the glasses, respectively. Oxygen packing density (OPD) was calculated using the relation $OPD = \Sigma x_i n_i / V_m$, where x_i is the molar fraction of an oxide $R_m O_n$ and n_i is the number of oxygen atoms of this oxide [6]. The molar volume of oxygen (V_o) is the volume of glass in which 1 mole of oxygen is contained. These values were calculated using the relation $V_o = (V_m)(1/\Sigma x_i n_i)$.

Various spectroscopic techniques were employed for structure investigation of present glass system.

2.3. XRD

X-ray diffraction patterns of the glass samples were recorded from Philips diffractometer (PANalytical X-pert PRO model) with Cu K$_\alpha$ (1.54 Å) source at room temperature.

2.4. FTIR studies

The infrared transmission spectra of all glasses were recorded at room temperature in the wave number range 400–1800 cm^{-1} by a Shimadzu FTIR-8001 Fourier-transform computerized infrared spectrometer. The IR transmission measurements were made using the KBr pellet technique.

2.5. Raman studies

Raman spectra of all prepared glasses were recorded at room temperature in the range 200–1800 cm^{-1} using a He–Ne excitation source (632.81 nm) coupled with Jobin Yvon Horiba (LABRAM HR-800) micro Raman spectrometer equipped with a 50× objective lens to focus the laser beam. The incident laser power was focused in a diameter of ~1–2 μm, and a notch filter was used to suppress Rayleigh light. Samples used for the measurement were of 1 mm thickness and 1 cm in diameter. Raman shifts are measured with a precision of ~0.3 cm^{-1}, and the spectral resolution is of the order 1 cm^{-1}; a similar characterization was studied by Upender et al. [11].

2.6. DSC studies

Differential scanning calorimetry of the prepared glass powders was carried out at temperatures up to 850°C at the rate of 10°C/min using a SETARAM instrument (Model LABSYS EVO DSC; SETARAM Instrumentation, Caluire, France) to determine the thermal properties of the glasses [6].

2.7. EPR studies

JEOL-JES FE 3X EPR spectrometer was employed for recording EPR spectra of the glass samples in the X-band at room temperature with 100 kHz field modulation. Polycrystalline diphenyl picryl hydrazyl (DPPH) was used as the standard "g" marker for the determination of magnetic field; a similar technique was employed by G. Upender et al. for invention of structure of WO_3–GeO_2–TeO_2 glasses [12].

2.8. UV-Visible absorption studies

UV-Visible absorption spectra of prepared borate-based glasses were recorded by using LABINDIA Analytical UV-3092 spectrophotometer in the wavelength range 350–900 nm at room temperature. The precision of wavelength measurement is about ±1 nm [12].

3. Results and discussion

3.1. Basic glass properties

The physical parameters of the present glasses are presented in **Table 2**. It is observed that the density (ρ) decreases from 3.334 to 2.815 g/cm^3 with the addition of ZnO content from 0 to 30 mol% at the expense of CdO content. This could be due to the lower molecular weight of ZnO (81.38 g/mol) in comparison with CdO (128.4 g/mol). This could also be due to the lower density of ZnO (ρρ = 5.606 g/cm^3) than that of CdO (ρ ρ= 6.95 g/cm^3).

The molar volume (V_m) increases from 25.972 to 26.224 cm^3/mol with ZnO content up to 15 mol% then V_m starts decreasing from 26.224 to 25.995 and then to 25.749 with further

Parameter	x = 0	x = 7.5	x = 15	x = 22.5	x = 30
*AMW (g/mol)	86.589	83.062	79.536	76.009	72.483
ρ (g/cc) (±0.005)	3.334	3.181	3.033	2.924	2.815
$^{\dagger}V_m$ (cm^3/mol)	25.972	26.112	26.224	25.995	25.749
OPD (mol/l)	83.936	83.487	83.129	83.862	84.663
V_o (cm^3/mol)	11.914	11.978	12.029	11.924	11.812

*AMW: average molecular weight.

†Error in V_m is ±0.005.

Table 2. Physical parameters of 59B$_2$O$_3$–10Na$_2$O–(30 − x)CdO–xZnO–1CuO (0 ≤ x ≤ 30 mol%) glass system.

addition of ZnO up to 30 mol% at the expense of CdO. This could be due to the difference between cation radii of Cd^{2+} ion (1.03 Å) and Zn^{2+} ion (0.83 Å). The nonlinear variation in V_m also suggests the dual role of ZnO content as in the present system ZnO up to 15 mol%, it plays a modifier role, and beyond it plays a glass former role. It is also observed that the oxygen packing density (OPD) decreases from 83.936 to 83.129 mol/l, while oxygen molar volume (V_o) increases from 11.914 to 12.029 cm^3/mol with ZnO content up to 15 mol%. But OPD increases from 83.129 to 84.663, while V_o decreases from 12.029 to 11.812 with ZnO addition up to 30 mol%. The nonlinear variation in OPD and V_o values with the increase in ZnO content from 0 to 30 mol% could be due to the variation in density (ρ) and the dual role of ZnO in the present glass system, while the number of oxygen atoms in the glass network remains the same according to the ratio 1:1.

3.2. XRD

The obtained XRD patterns of BNCZ glass system are shown in **Figure 1**. It is clear that a broad hump is repeatedly observed in all the samples and is the characteristic of glass, and there is no evidence of crystallization. Hence it is confirmed that the prepared samples possess glassy nature.

3.3. FTIR studies

The IR transmission spectra of all the glasses were recorded in the wave number range 1600–400 cm^{-1} and are shown in **Figure 2**. The band positions and their assignments are given in **Table 3**.

In the BNCZ glass system, significant bands are observed at about ~474, 694, 970–1040, 1250–1260, and 1360–1375 cm^{-1}. These bands assigned to B$_2$O$_3$ and about 80% of the boron atoms are present in the boroxol rings, B$_3$O$_6$, that are interconnected by independent BO$_3$ groups. The vibrational modes of the vitreous borate network are mainly active in three infrared regions. The IR features located in the first region that ranges between 1200 and 1600 cm^{-1} [13]. The second region ranges between 800 and 1200 cm^{-1}, and the third region ranges between 600 and 800 cm^{-1}. From **Figure 2** it is evidently seen that the structure of the glass network formed
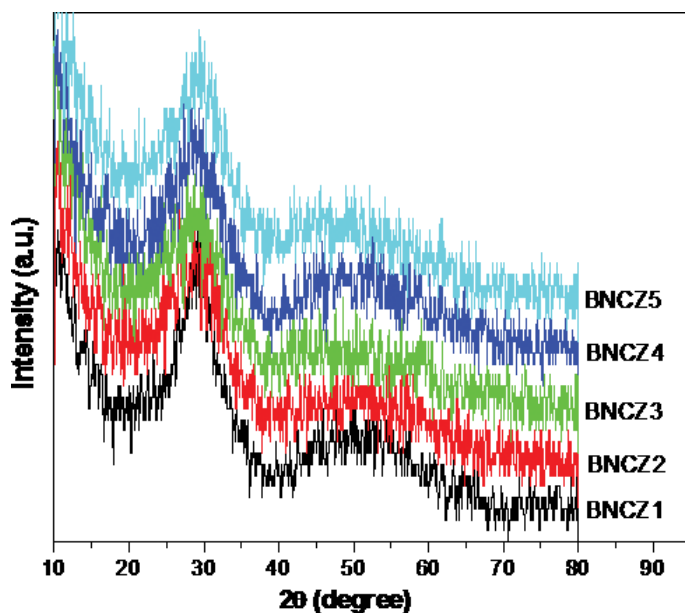
Figure 1. XRD patterns of $59B_2O_3$–$10Na_2O$–$(30 − x)CdO$–$xZnO$–$1CuO$ (0 = x = 30 mol%) glass system.
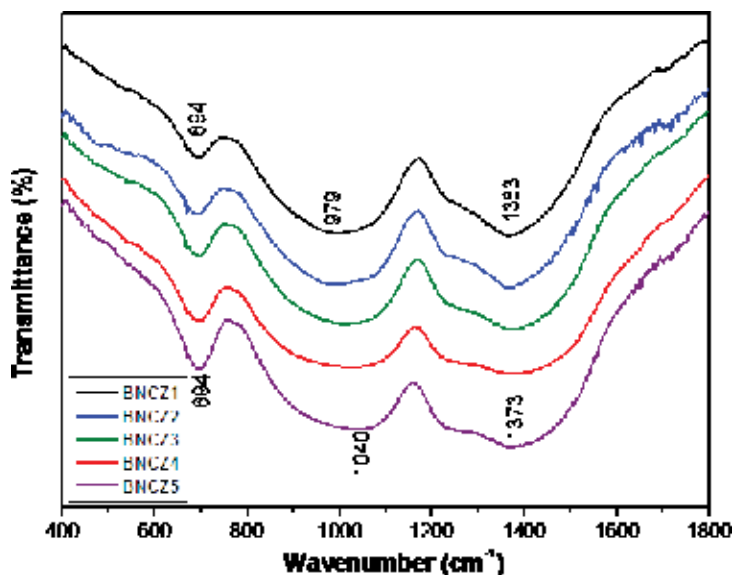
Figure 2. IR spectra of $59B_2O_3$–$10Na_2O$–$(30 − x)CdO$–$xZnO$–$1CuO$ (0 = x = 30 mol%) glass system.

by boron ions is significantly changed with the incorporation of ZnO at the expense of CdO content. The absence of IR band at ~806 cm^{-1} indicates that the boroxol rings are not formed in the present glass system, and hence the structure of the glasses consists of borate groups other than the boroxol rings. The weak band observed at ~474 cm^{-1} in all the glasses is attributed to the vibration of metal cations in their oxygen sites (RO_4 groups where R = Cd, Zn) [16].

Band positions	Assignment
1360–1375	Symmetric stretching vibrations of B–O bonds of trigonal $(BO_3)^{3-}$ units in Meta, Pyro and ortho borates
1260	Symmetric stretching vibrations of B–O of $(BO_3)^{3-}$ units in meta and Ortho Borates
1040	B–O stretching vibrations of BO_4 units in tri, tetra and penta borate groups
970	B–O asymmetric stretching of BO_4 units of diborate groups
690	Bending vibrations of B–O–B linkages in borate network

Table 3. Band positions and assignments of IR bands of $59B_2O_3$–$10Na_2O$–$(30 - x)CdO$–$xZnO$–$1CuO$ $(0 \leq x \leq 30$ mol%) glass system.

The bands observed around 694 cm^{-1} could be attributed to the bending vibration of B–O–B linkages of various borate groups [17]. The bands near 979 cm^{-1} are assigned to B–O asymmetric stretching of BO_4 units of diborate groups [18]. This band shifts to higher wave number side, i.e., from 979 to 1040, while the intensity of this band significantly decreased with the increase of ZnO content up to 30 mol%. The bands observed at around 1040 cm^{-1} are due to B–O stretching vibrations of BO_4 units in tri-, tetra-, and pentaborate groups [12, 19, 20]. The bonds that appeared in the range of 1260 cm^{-1} are assigned to B–O symmetric stretching vibrations of $(BO_3)^{3-}$ units in metaborate and orthoborates [21]. The intensity of this band is unaffected with the addition of ZnO content up to 30 mol%. The bands at around 1363–1375 cm^{-1} could be attributed due to symmetric stretching vibrations of B–O bonds of trigonal $(BO_3)^{3-}$ units in meta-, pyro-, and orthoborates [21, 22]. The broadness of these bands was found to be more with the substitution of ZnO content up to 30 mol%. The B_2O_3 is built up of BO_3 triangles, and upon adding ZnO, the coordination number of the boron changes from SP^3 tetrahedral BO_4 to form SP^2 planar BO_3, preserving the B–O bonding without the creation of non-bridging oxygen ions. It means that the introduction of ZnO causes a significant formation of the BO_3 groups with a lower coordination number. Therefore, the progressive increase in ZnO content makes the IR bands observed at about 1040 and 1373 cm^{-1} more pronounced. This means that the BO_3 groups and hence the bridging oxygen contents are increased with increasing of ZnO content on the expenses of CdO content.

3.4. Raman studies

Figure 3 shows the Raman spectra of the present glass system in the spectral range 200–1800 cm^{-1} consisting of sharp, broad peaks and shoulders.

The Raman peak positions are summarized in **Table 4**.

The Raman spectrum of vitreous B_2O_3 is dominated by a strong peak centered at ~804 cm^{-1}. The ~804 cm^{-1} peak is assigned to the boroxol ring breathing vibration involving little motion of boron [23–25]. The desired peak at ~ 804 cm^{-1} was not appeared and therefore boroxol rings are absent in the present glass system. Therefore, boroxol ring is absent in these glasses. The Raman peak at around 447–470 cm^{-1} is assigned to pentaborate and diborate groups [26]. The weak Raman peak appearing at ~697 cm^{-1} is due to metaborate/$(BO_3)^{3-}$ vibrations [27, 28]. The strong peak at around ~770 cm^{-1} is assigned to symmetric breathing vibrations of six-membered
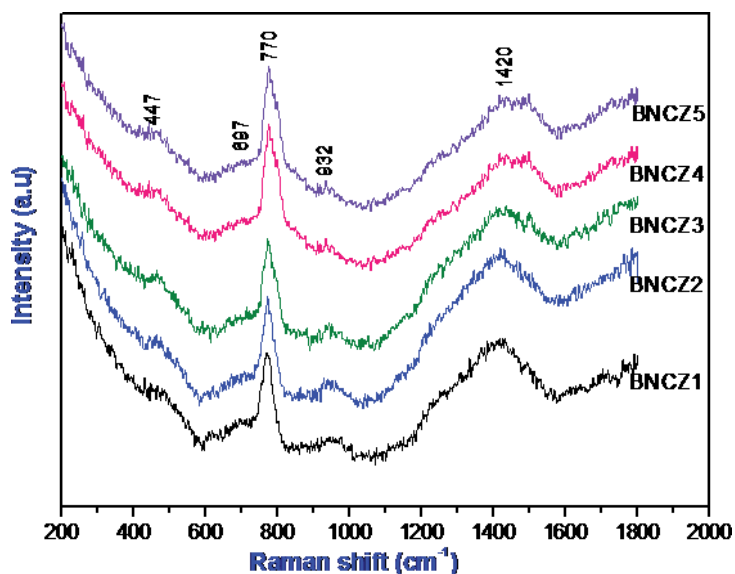
Figure 3. Raman spectra of $59B_2O_3$–$10Na_2O$–(30 − x)CdO–xZnO–1CuO (0 = x = 30 mol%) glass system.

Sample code	Raman peaks (cm⁻¹)				
BNCZ1	470	697	770	948	1420
BNCZ2	464	697	770	943	1420
BNCZ3	464	697	770	942	1420
BNCZ4	457	697	770	935	1420
BNCZ5	447	697	770	932	1420

Table 4. Raman peak positions of $59B_2O_3$–$10Na_2O$–(30 − x)CdO–xZnO–1CuO ($0 \le x \le 30$ mol%) glass system, with error ±1 cm⁻¹.

rings with both BO_3 triangles and BO_4 tetrahedra (tri-, tetra-, or pentaborate groups) [29, 30]. The intensity of this peak is significantly increased with the addition of ZnO content up to 30 mol%. This observation suggests more number of BO_3 units instead of BO_4 units in six-membered rings. No Raman peaks appeared at around ~ 834 cm⁻¹ in any of the glass, and it indicates that there are no pyroborate groups ($B_2O_5^{4-}$) present in these glasses. The pentaborate and tetraborate groups were assigned by the peaks observed in the range ~930–950 of Raman spectrum. The broad band around 1420 cm⁻¹ was assigned to the B–O⁻ bonds attached to the large number of borate groups [31, 32]. The decrease in intensity of the peak at ~1420 cm⁻¹ is due to increase of ZnO content up to 30 mol%. This shows that significant formation of Zn^{2+}-B–O⁻ bonds by reducing the number of non-bridging oxygen's (NBO's) similar finding was recorded by Upentre et al. for the glass system (90–x)TeO2–10GeO2–xWO 3 (7.5 ≤ x ≤ 30) doped with Cu^{2+} ions [33]. The observed slight decrease in intensity and shift in the peak ~470 toward lower wave number (447 cm⁻¹) indicates the decrease of penta- or diborate groups in the glasses. The intensity of the peak at ~940 cm⁻¹ decreases while shifts to lower wave number

from 948 to 943, 942, 935, and then 932 with increase in ZnO content. This may indicate the presence of less number of pentaborate groups and bond lengths of B–O bonds of pentaborate groups could be increased. The above results suggest the presence of more BO$_3$ units in the glasses with the addition ZnO as Zn^{2+} establishes the linkages of NBOs with BO$_4$ units.

3.5. Differential scanning calorimetry (DSC)

The DSC thermograms of the present glasses are shown in **Figure 4**. Glass transition tempera-ture (T$_g$) is always visible, and this result is in agreement with the result of XRD data as both the techniques confirm the glassy nature of the samples.

The values of glass transition temperature (T$_g$) are given in **Table 5**.

From this table it is observed that T$_g$ decreases from 497 to 488°C with gradual increase in ZnO content up to 15 mol% at the expense of CdO, and thereafter T$_g$ increases from 488 to 492 and then to 496°C with further addition of ZnO up to 30 mol%. This behavior sug-gests that T$_g$ varies nonlinearly with the addition of ZnO content in place of CdO. It is well known that a higher cation radius of Cd^{2+} (1.03 Å) replaced with a lower cation radius of Zn^{2+} (0.83 Å) decreases the overall cation polarizability (polarizability is proportional to the cation size); as a result, T$_g$ should decrease linearly with ZnO content. On the contrary to this, the bond strength of Zn–O (151 kJ/mol) is more than that of Cd–O (101 kJ/mol) [33]; as a result, T$_g$ should increase linearly. But none of the reasons are suitable in this case. Therefore, the observed nonlinear variation in T$_g$ with ZnO content can be understood in the following way: As it was observed clearly from FTIR and Raman that more numbers of BO$_4$ units are present up to 15 mol% of ZnO, then with further addition of ZnO in place of CdO up to 30 mol%,
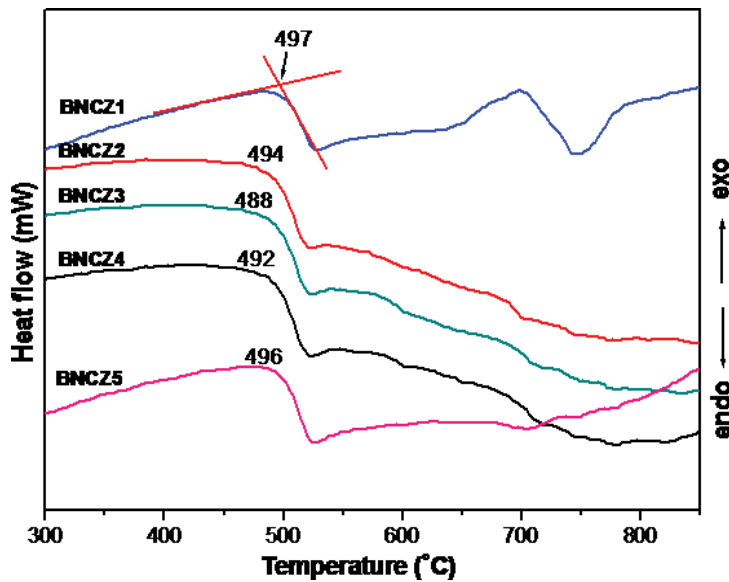
Figure 4. DSC curves of 59B$_2$O$_3$–10Na$_2$O–(30 − x)CdO–xZnO–1CuO (0 = x = 30 mol%) glass system. Heating rate was 10°C/min.

Sample code	Glass Transigirían temperature T_g (°C)
BNCZ1	497
BNCZ2	494
BNCZ3	488
BNCZ4	492
BNCZ5	496

Table 5. Glass Transigirían temperature T_g (°C) for compositions of $59B_2O_3–10Na_2O–(30 − x)CdO–xZnO–1CuO$ ($0 \leq x \leq 30$ mol%) glass system.

most of BO_4 units are converted to BO_3 units. The bond strength of BO_4 units (373 kJ/mol) is smaller than BO_3 units (498 (kJ/mol%) [34]. Hence, T_g decreases up to 15 mol% of ZnO and then starts increasing with further addition of ZnO up to 30 mol%. Besides this the higher field strength of Zn^{2+} ions (0.53 cm^{-2}) than that of Cd^{2+} ions (0.38 cm^{-2}) in the glass network also causes to increase the T_g [34]. However, the ionicities of both Zn–O (51%) and Cd–O (51%) are the same, and its role could be neglected. From **Figure 4** it is clearly seen that except in BNCZ1 the onset crystallization temperature (T_o) is not prominently observed with the incorporation of ZnO content. This indicates that the increase of ZnO in place of CdO has a tendency to prevent crystallization. Thus, the present glasses are more thermally stable against crystallization.

3.6. EPR studies

The electron paramagnetic resonance spectra of Cu^{2+}-doped BNCZ series are shown in **Figure 5**. It is essential to dope the glass samples with Cu^{2+} ions as this gives resonance signals; a similar work is reported in earlier literature [35–37]. The copper ions with spin 1/2 gives a nuclear spin $I = 3/2$ for ^{63}Cu and ^{65}Cu and therefore results in $(2I + 1)$ hyperfine components, i.e., four parallel and four perpendicular components.

The spectra recorded for prepared glass series exhibit three parallel components in the lower field region and one parallel component which is overlapped with the perpendicular component. The EPR spectra of copper ions in all the glass samples have been analyzed using an axial spin-Hamiltonian in which the quadrupole and nuclear Zeeman interaction terms are ignored.

$$H = g_{\parallel} \beta H_z S_z + g_{\perp} \beta (H_x S_x + H_y S_y) + A_{\parallel} S_z I_z + A_{\perp} (S_x I_x + S_y I_y) \qquad (1)$$

The symbols have their usual meaning.

The solution to the spin-Hamiltonian gives the expressions for the peak positions related to the principal values of g and A tensor as follows [35–37].

For parallel hyperfine peaks,

$$h\nu = g_{\parallel} \beta H_{\parallel} + m A_{\parallel} + (15/4 - m^2) A_{\perp}^2 / 2 g_{\parallel} \beta H_{\parallel} \qquad (2)$$
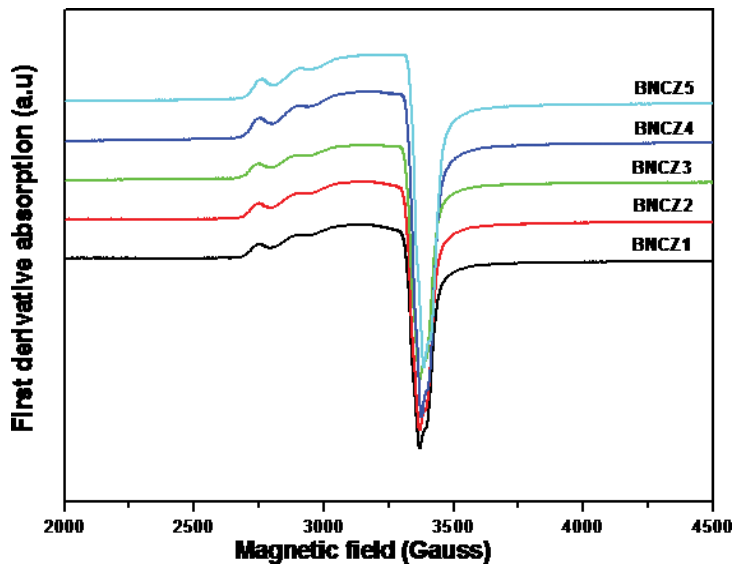
Figure 5. EPR spectra of 59B_2O_3–10Na_2O–(30 – x)CdO–xZnO–1CuO (0 = x = 30 mol%) glass system at room temperature.

For perpendicular hyperfine peaks,

$$h\nu = g_\perp \beta H_\perp + mA\perp + (15/4 - m^2)(A\perp^2 + A_\parallel^2)/4g_\perp \beta H_\perp \tag{3}$$

The symbols have the usual meaning. Using Eqs. (2) and (3), the spin-Hamiltonian parameters of all the glasses have been calculated and are tabulated as shown in **Table 6** [12].

From **Table 6**, the $g_\parallel$, $g_\perp$ and $A_\parallel$ values are found to be dependent on the glass composition. It is found that $g_\parallel > g_\perp > g_e$ (where g_e = 2.0023 is free electron g-value). Therefore from the g values and shape of the EPR spectra, it can be concluded that the ground state of the Cu^{2+} is d_{x2-y2} orbital $^2B_{1g}$ state, the Cu^{2+} ions are located in tetragonally distorted octahedral sites [35–37]. The changes in the spin-Hamiltonian parameters with varying ZnO content in the place of CdO content are attributed to the change in electron cloud density around the Cu^{2+} ions in the glass network. The change in electron cloud density can be understood in the following way: From FTIR and Raman structural analysis, it was observed that the structure of the glasses changed with the incorporation of ZnO content from 0 to 30 mol%. The increasing ZnO content from 0 to 30 mol% to B_2O_3 glass network leads to change the coordination number of certain boron atoms from 4 to 3. Thus it is understood that every glass composition of the glass system is composed of both triangular (BO_3) and tetrahedral (BO_4) units. Therefore, some of the Cu^{2+} ions are surrounded by these groups containing NBOs which may present varied electron cloud density around Cu^{2+} site in the form of CuO_6 and hence the variations in the spin-Hamiltonian parameters as observed in the present glass system. The variations in EPR parameters not only depend on the above said reasons but also depend on the differences in the field strengths of various cations (B^{3+} (1.39 cm^{-2}), Na^+ (0.18 cm^{-2}), Cd^{2+} (0.38 cm^{-2}), and Zn^{2+} (0.53 cm^{-2})) as well as the cation polarizabilities of Na^+ ions

Glass code	$g_{\parallel}$	$g_{\perp}$	$A_{\parallel} (\times 10^{-4}\ cm^{-1})$
BNCZ1	2.323	2.064	147
BNCZ2	2.322	2.068	147
BNCZ3	2.325	2.066	148
BNCZ4	2.327	2.069	146
BNCZ5	2.326	2.068	147

Table 6. Spin-Hamiltonian parameters (SHP) of $59B_2O_3$–$10Na_2O$–$(30 - x)CdO$–$xZnO$–$1CuO$ ($0 \leq x \leq 30$ mol%) glass system.

(0.181 Å^3), Zn^{2+} ions (0.283 Å^3), Cd^{2+} ions (1.087 Å^3), and B^{3+} ions (0.002 Å^3) [6] that cause the fluctuations in the ligand field around Cu^{2+} ions, and this in turn varies the spin-Hamiltonian parameters as observed.

3.7. Optical absorption studies

The UV-Visible absorption spectra of prepared glass series were displaced in **Figure 6**.

The observed absorption band around ~765 nm in BNCZ1 is assigned to the $^2B_{1g} \rightarrow {}^2B_{2g}$ transition (ΔE_{xy}) of Cu^{2+} ion in octahedral coordination with a strong tetrahedral distortion, and the EPR results were found to be in agreement with this assumption [36]. From **Figure 6**, it was found that the absorption peak firstly blueshifted, i.e., from 764 to 760 and then to 756 nm with the addition of ZnO up to 15 mol%, and then redshifted, i.e., from 756 to 760 to 763 nm with the further addition of ZnO from 15 to 30 mol%. This result is consistent with the observations made in FTIR, Raman, and DSC. As pointed out by Raman and IR analysis, the major structural changes in the present glass take place with the addition of divalent ZnO. This consequence suggests that ZnO enters the glass system in the form of network modifier. Hence, all the observations are clearly from tetragonal (BO_4) to trigonal (BO_3) units with the incorporation of ZnO content at the expense of CdO content.

The variation in peak position with ZnO doping in glass system BNCZ (30 mol%) indicates the change in the ligand field around paramagnetic Cu^{2+} ions. This could be due to higher field strength of Zn^{2+} ions (0.53 cm^{-2}) than that of Cd^{2+} ions (0.38 cm^{-2}) [33]. The change in polarizability of oxygen ions surrounding the Cu^{2+} may also change the peak position [6]. This can be understood as follows. As ZnO content substitutes CdO content from 0 to 30 mol%, from IR and Raman structural analysis, it was observed that ZnO has played the dual role. Thus, during the modifier role of ZnO (up to 15 mol%), weak bonds Zn^{2+}–O–B were formed in the place of B–O–B or Cd–O–B, whereas during the former role of ZnO (from 15 to 30 mol%), strong Zn–O–B bonds were formed. Thus the oxygen ions in Zn^{2+}–$^-$O–B bonds are less tightly bound than in B–O–B or Cd–O–B bonds. Thus the oxygen ions can be treated as NBOs in which electrons are loosely bound to the nucleus, and hence these NBOs are more polarized than the oxygen ions in B–O–B or Cd–O–B. These NBOs are decreased during the conversion of BO_4 units into BO_3 units when ZnO started playing the former role above 15 mol%. Similar observations
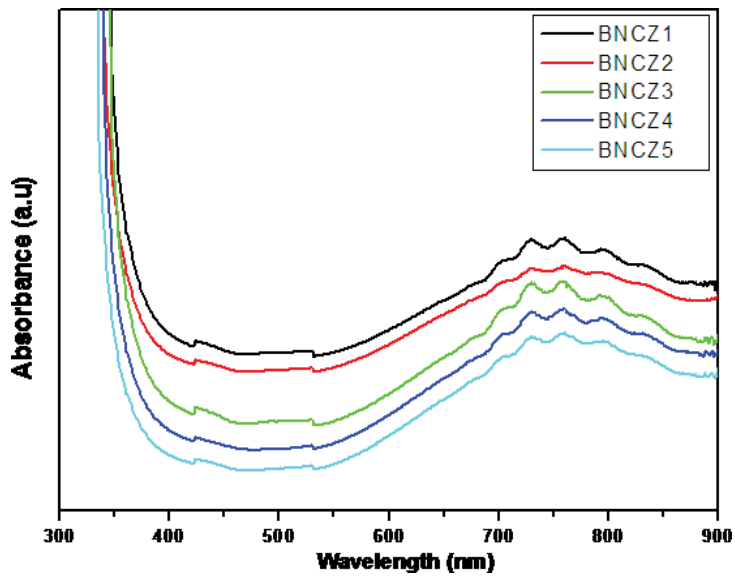
Figure 6. Optical absorption spectra of 59B$_2$O$_3$–10Na$_2$O–(30 − x)CdO–xZnO–1CuO.

were reported by other authors [37]. With the conversion of four coordination boron atoms [BO$_4$] into three coordination boron atoms [BO$_3$], the excess of oxygen converts some of Zn^{2+} ions into tetrahedra [ZnO$_4$] where the structural modification in the glass network could be reason for the variation of the ligand field strength of Cu^{2+} ions. This may be the reason why the optical absorption maximum has showed the nonlinear variation with ZnO content.

3.7.1. Cu^{2+}-ligand bonding nature

The data of EPR and optical absorption can be correlated to understand the environment around Cu^{2+} ions in the present glass network; in connection to this, the bonding parameters were evaluated using EPR and optical data by the following equations [6].

$$g_{\parallel} = 2.0023(1\text{-}4\lambda\alpha^2\beta_1^{\,2}/\Delta E_{xy}) \tag{4}$$

$$g_{\perp} = 2.0023(1\text{-}\lambda\alpha^2\beta^2/\Delta E_{xz,yz}) \tag{5}$$

where ΔE_{xy} and $\Delta E_{xz,yz}$ are the energies corresponding to the transitions of $^2B_{1g} \rightarrow {}^2B_{2g}$ and $^2B_{1g} \rightarrow {}^2E_g$, respectively, and λ is the spin-orbit coupling constant (= −828 cm^{-1}) and the bonding coefficients α^2, $\beta_1^{\,2}$, and β^2 (≈1.00) characterize in-plane σ bonding 16 between the d orbital of Cu^{2+} and the p orbital of ligand, in-plane π bonding between the d orbital of Cu^{2+} and p orbital of ligand and out-of-plane π bonding between the d orbital of Cu^{2+} and p orbital of ligand in the glasses respectively [6]. Besides the values of ΔE_{xy} and $\Delta E_{xz,yz}$ are also calculated and presented in **Table 7**. In the present glasses, the bonding parameters α^2, $\beta_1^{\,2}$, and β^2 were evaluated using the following equations [38, 39] and are displayed in **Table 7**.

Parameter	x = 0	x = 7.5	x = 15	x = 22.5	x = 30
λ (nm) ($\pm$1)	764	760	756	760	763
ΔE_{xy} (cm^{-1})	13,089	13,158	13,228	13,158	13,106
$\Delta E_{xz,yz}$ (cm^{-1})	20,666	19,408	20,017	19,117	19,408
α^2	0.798	0.799	0.804	0.802	0.803
β^2	0.964	0.963	0.957	0.959	0.958
β_1^2	0.793	0.794	0.801	0.803	0.797
Γ_π (%)	41.4	41.2	39.8	39.4	40.6
Γ_σ (%)	37.33	37.15	36.22	36.59	36.41

Table 7. Bonding parameters of 59B$_2$O$_3$–10Na$_2$O–(30 − x)CdO–xZnO–1CuO (0 ≤ x ≤ 30 mol%) glass system.

$$\alpha^2 = \left| A_\parallel/P \right| + (g_\parallel\text{-}2) + 3/7(g_\perp\text{-}2) + 0.04 \tag{6}$$

$$\beta_1^2 = [(g_\parallel/g_e) - 1]\Delta E_{xy}/4\lambda\alpha^2 \tag{7}$$

$$\beta^2 = [(g\perp/g_e) - 1]\Delta E_{xz,yz}/\lambda\alpha^2 \tag{8}$$

Here P is dipolar hyperfine coupling parameter (=0.036 cm^{-1}). From Eqs. (4) and (5), in order to determine Cu^{2+} bonding coefficients, besides the EPR parameters, the energy positions of the absorption bands of Cu^{2+} which indicate the values of ΔE_{xy} and $\Delta E_{xz,yz}$ are required. Since one absorption band corresponding to $^2B_{1g} \rightarrow {^2B_{2g}}$ transition (ΔE_{xy}, are presented in **Table 7**) was observed, the position of the second band can be estimated by using the following equation [39] and the values are presented in **Table 7**.

$$\Delta E_{xz,yz}(^2B_{1g}\rightarrow{^2E_g}) = 2K^2\lambda/2.0023 - g_\perp \tag{9}$$

where K^2 is the orbital reduction factor (K^2 = 0.77) and λ is the spin-orbit coupling constant.

The normalized covalency of the Cu^{2+}–O in-plane bonding of σ and π symmetry is expressed in terms of bonding coefficients α^2 and β_1^2 as follows:

$$\Gamma_\sigma = 200(1\text{-}S)\ (1\text{-}\alpha^2)/(1\text{-}2S)\% \tag{10}$$

$$\Gamma_\pi = 200(1\text{-}\beta_1^2)\% \tag{11}$$

where S is the overlapping integral (S$_{oxy}$ = 0.076). The values of Γ_σ and Γ_π are given in **Table 6**. It is clear from **Table 7** that both of these values are varied with addition of ZnO content to B$_2$O$_3$ network. This could be due to variation of structural changes within the glasses. In

general if α^2 have smaller values, then the greater the covalent nature of the bonding. The calculated values of α^2 for prepared glass series (the range 0.798–0.803) suggest that the in-plane σ bonding in the glasses is moderately covalent in nature, whereas the values of β_1^2 (0.793–0.803) obtained for various glasses indicate that the in-plane π bonding is significantly ionic in nature.

The changes in this parameter can be attributed to the changes in O–X bonds (where X = B, Cd, and Zn) because it reflects the competition in the Cu^{2+}–O–X bonds, between the cupric ion and its neighboring X cations for attracting the lone pairs of the intervening oxygen ions. In the present system, the values of β^2 were found to be close to unity, and it suggests that out-of-plane π bonding is more ionic in nature and the magnitudes of all bonding parameters are comparable to those found for Cu^{2+} in other glasses [6].

4. Conclusions

Transparent glasses with composition 59B$_2$O$_3$–10Na$_2$O–(30 − x)CdO–xZnO–1CuO (where x = 0, 7.5, 15, 22.5, and 30 mol%) were prepared by melt-quenching technique. It was observed that the density (ρ) decreases, while OPD, molar volume (V$_m$), and oxygen molar volume (V$_o$) are nonlinearly varying with the addition of ZnO content from 0 to 30 mol% at the expense of CdO content. From FTIR studies, it is found that the glasses are composed of [BO$_4$] and [BO$_3$] units in various borate groups. FTIR and Raman studies revealed that more numbers of BO$_4$ units are present up to 15 mol% of ZnO, and then with further addition of ZnO in place of CdO up to 30 mol%, most of BO$_4$ units are converted to BO$_3$ units. The non-linear variation in T$_g$ is due to the dual role of ZnO. From EPR results, it was found that 채 > 弘 and the changes in spin-Hamiltonian parameters are primarily due to the ligand field variations around Cu^{2+} ions. It is found that 의 > 토 for the present glass system. This suggests that the Cu^{2+} ions in the present glasses are coordinated by six ligands (CuO$_6$ chromophore) which form an octahedron elongated along the z-axis and also suggests that the ground state of Cu^{2+} ions is the d$_{x2–y2}$ orbital (^{2}B$_{1g}$ state). From the optical absorption studies, it was found that broad absorption maximum is due to ^{2}B$_{1g}$ → ^{2}B$_{2g}$ transition of Cu^{2+} ion. The change in polarizability of oxygen ions surrounding the Cu^{2+} could be the reason for the variation of the peak position. The optical absorption results also suggested that there is covalency for the in-plane σ-bonding and that the in-plane π-bonding is significantly ionic in nature in Cu^{2+}–O bonds.

Author details

L.S. Ravangave* and G. N. Devde

*Address all correspondence to: lsravangave@gmail.com

Department of Physics, Shri Sant Gadge Maharaj College, Nanded, Maharashtra, India

References

[1] Cormier L, Majerus O, Neuville DR, Calas G. Temperature-induced structural modification between alkali borate glasses and melts. Journal of the American Ceramic Society. 2006;**89**:13

[2] Yue YL, Yu XJ, Wu HT, Chen XJ. Dielectric properties of quaternary calcium aluminoborosilicate system glasses. Materials Research Innovations. 2009;**13**:129

[3] Shelby JE. Introduction to Glass Science and Technology. Cambridge: The Royal Society of Chemistry; 2005

[4] Abdel-Baki M, El-Diasty F. Role of oxygen on the optical properties of borate glass doped with ZnO. Journal of Solid State Chemistry. 2011;**184**:2762

[5] Hecht HG, Johnston TS. Study of the structure of nickel in soda-boric oxide glasses. The Journal of Chemical Physics. 1967;**46**:23

[6] Devde GN, Upender G, Chandra Mauli V, Ravangave LS. Structure,thermal and spectroscopic properties of Cu^{2+} ions doped $59B_2O_3$-$10K_2O$-$(30-x)ZnO$-$xBaO$-$1CuO$ ($0 \leq x \leq 30$ mol%) glass system. Journal of Non-Crystalline Solids. 2016;**432**:319-324

[7] Saddeek, Latif LAE. Effect of TeO_2 on the elastic moduli of sodium borate glasses. Physica B. 2004;**348**:475

[8] Naresh V, Buddhudu S. Structural, thermal, dielectric and ac conductivity properties of lithium fluo-borate optical glasses. Ceramics International. 2012;**38**:2325

[9] Bale S, Rahmana S, Awasthi AM, Sathe V. Role of Bi_2O_3 content on physical, optical and vibrational studies in Bi_2O_3-ZnO-B_2O_3 glasses. Journal of Alloys and Compounds. 2008;**460**:699

[10] Siegel I, Lorence JA. Paramagnetic Resonance of copper in Amorphous and polycrystalline GeO_2. The Journal of Chemical Physics. 1966;**45**:2315

[11] Upender G, Vardhani CP, Suresh S, Awasthi AM, Chandra Mouli V. Structure, physical and thermal properties of WO_3-GeO_2-TeO_2 glasses. Materials Chemistry and Physics. 2010;**121**(1-2):335-341

[12] Upender J, Babu C, Chandra Mouli V. Chandra Mouli,Structure,glass transition temperature and spectroscopic properties of $10LiO_2$-xP_2O_5-$(89-x)TeO_2$-CuO ($5 \leq x \leq 25$ mol%) glass system. Spectrochimica Acta Part A. 2012;**89**:39

[13] Kamitsos EI, Karakassides MA, Chryssikos GD. Vibrational spectra of magnesium-borate glasses. 2 Raman and mid-infrared investigation of the network structure. Journal of Physical Chemistry. 1987;**91**:1073-1079

[14] Tarte P. In: Prins IA, editor. The determination of cation co-ordination in glasses by infrared spectroscopy. Physics of Non Crystalline Solids. Amsterdam: Elsevier; 1964. p. 549

[15] Condrate RA. The fractography of Glass. In: Pye LD, Stevens HI, Lacourse WC, editors. Introduction to Glass Science. New York: Plenum Press; 1972

[16] Condrate RA. Vibrational spectra of structural units in glass. Journal of Non-Crystalline Solids. 1986;**84**:26

[17] Nelson BN, Exarhos GJ. Vibrational spectroscopy of cation-site interactions in phosphate glasses. Chemical Physics. 1979;**71**:2739

[18] Fayon F, Bessada C, Coutures JP, Massiot D. High Resolution, Double-Quantum 31P MAS NMR Study of the Intermediate-Range order in crystalline and Glass lead phosphate. Inorganic Chemistry. 1999;**38**:5212

[19] El-Damrawi G, El-Egili K. Characterization of novel CeO₂-B₂O₃ glasses. Structure and Properties Physics B. 2001;**299**:180

[20] Abo-Naf M, Azooz MA. Charecterization of some glasses in the system SiO₂-Na₂ORO by infrared spectroscopy. Materials Chemistry and Physics. 2002;**77**:846

[21] Ardelean I, Cora S, Lucacel RC, Hulpus O. EPR,FT-IR, Spectroscopic studies of B₂O₃-Bi₂O₃-MnO glasses. Solid State Sciences. 2005;**7**:1438

[22] Gaafar MS, Saddeek YB, Abd El-Latif L. Ultrosonic studies on alkali borate tungstate glasses. Journal of Physics and Chemistry of Solids. 2009;**70**:173

[23] El-Egili K. Infrared studies of Na₂O-B₂O₃-SiO₂ and Al₂O₃-B₂O₃-SiO₂ glasses. Physica B. 2003;**325**:340

[24] Yiannopoulos YD, Chryssikos GD, Kamitsos EI. Structure and properties of alkaline earth borate glasses. Physics and Chemistry of Glasses. 2001;**42**:164

[25] Dwivedi BP, Rahman MH, Kumar Y, Khanna BN. Raman scattering study of lithium borate glasses. Journal of Physics and Chemistry of Solids. 1993;**54**:621

[26] Furukawa T, White WB. Structure and crystallization of glasses in Li₂O-Si₂O₅-TiO₂ system determined by Raman spectroscopy. Physics and Chemistry of Glasses. 1982;**21**:85

[27] Meera BN, Ramakrishnan J. Raman spectral studies of borate glasses. Journal of Non-Crystalline Solids. 1993;**159**:1

[28] Devde GN, Ravangave LS. Raman, FTIR, DSC, EPR and optical properties of 59B₂O₃-10K₂O-(30-x)ZnO-xLi₂O-1CuO glass system doped with Cu²⁺ ions. IJEST. 2015;**7**(12):407-417

[29] Rejisha SR, Anjana PS, Gopakumar N, Santha N. Synthesis and characterization of strontium and barium bismuth borate glass-ceramics. Journal of Non-Crystalline Solids. 2014;**388**:68

[30] Subhadra M, Kistaiah P. Effect of Bi2O3 content on physical and optical properties of 15Li₂O-15K₂O-xBi₂O₃-(65-x)B₂O₃-5V₂O₅ glass system. Vibrational Spectroscopy. 2012;**62**:23

[31] Sekiya T, Mochida N, Ohtsuka A, Soejima A. Raman spectra of BO3/2-TeO2 glasses. Journal of Non-Crystalline Solids. 1992;**151**:222

[32] Ciceo-Lucacel R, Ardelean I. FT-IR and Raman study of silver lead borate-based glasses. Journal of Non-Crystalline Solids. 2007;**353**:2020

[33] Upendre G, Chandramouli VC, Prasad M. Vibrational, EPR and Optical Spectroscopy of Cu^{2+} doped glasses with$(90-x)TeO_2$-$10GeO_2$-$xWO_3$$(7.5 \leq x \leq 30$ mol%) composition. Journal of Non-Crystalline Solids. 2011;**357**(3):903-909

[34] Dimitrov V, Komatsu T. An interpretation of optical properties of oxides and oxide glasses interms of electronic ion polarizability and average single bond length. Journal of Chemical Technology and Metallurgy. 2010;**45**:219

[35] Volf B. Chemical Approach to Glass. New York: Elsevier; 1984

[36] Ramesh Kumar V, Rao JL, Gopal NO. EPR and optical absorption studies of Cu^{2+} ions in alkaline earth alumino borate glasses. Material Research Bulletin; 2005;**40**:1256-1269

[37] Srinivasulu K, Omkaram I, Obeid H, Suresh Kumar A, Rao JL. Spectral studies of Cu^{2+} ions in sodium-lead borophosphate glasses. Physica B. 2012;**407**:4741

[38] Kivelson D, Neiman R. ESR Line shapes in glasses of copper complexes. The Journal of Chemical Physics. 1961;**35**:145

[39] Abdel-Baki M, Abdel-Wahab FA, El-Diasty F. One-Photon band gap engineering of borate glass doped with ZnO for photonic application. Journal of Applied Physics. 2012;**111**. DOI: 073506

Nanocrystallization of the $Cd_3Al_2Ge_3O_{12}$ Garnet in Glasses of the CdO-TeO_2-GeO_2 System

Josefina Alvarado Rivera,
Carlos Guadalupe Pérez Hernández,
María Elena Zayas and Enrique Álvarez

Additional information is available at the end of the chapter

Abstract

In this study, a series of glasses of the system $xCdO$-$10TeO_2$-$(90–x)GeO_2$ were fabricated, varying the modifier oxide content from 10 to 80 wt%. According to XRD analysis, partial crystallization occurred for the glass $60CdO.10TeO_2.30GeO_2$ presenting the formation of GeO_2 and $CdTeO_3$; the $70CdO.10TeO_2.20GeO_2$ glass shows sharp diffraction peaks corresponding to the $Cd_3Al_2Ge_3O_{12}$ garnet crystalline phase. Transmission electron microscopy showed that the garnet crystals have sizes below 20 nm. At the highest concentration of CdO (80 wt%), a transparent orange glass can be obtained, and this sample can be identified as an inverted glass where CdO participates as a network former. The optical band gap of the glasses decreases as CdO content increases from 3.91 to 3.0 eV. In general, all glasses show a typical broad emission when excited with UV light (325 nm); chromatic coordinates were calculated and pointed out the presence of emissions in the white, green, and yellow regions. In summary, the obtained glasses are a promising material for IR technologies, nonlinear optics, and design of solid state lighting devices.

Keywords: tellurite, germanates, nanocrystals, photoluminescence, inverted glasses

1. Introduction

As technology keeps evolving, particularly in the optics and telecommunication applications, materials with very special properties and capabilities like specific spectral operation ranges, high refractive index, and low phonon energy are needed [1]. Herein, silicon oxide (SiO_2), germanium oxide (GeO_2), tellurium oxide (TeO_2), vanadium pentoxide (V_2O_5), cadmium sulfide (CdS), to name a few, have been used to fabricate special glasses with optical

properties adequate to their final application. The main characteristic of the mentioned compounds is that they are glass network formers, and alkali oxides (Na_2O, CaO, K_2O, and MgO) and metallic oxides (like ZnO and Fe_2O_3) are network modifiers. Tellurium oxide is a special case of a glass former; it has been proved that the structural unit that constitutes the network is of octahedral coordination nature, which deviates from the classical structural model of tetrahedral coordination. Zachariasen postulated through empirical observation that cations surrounded by four oxygens in a tetrahedral geometry could form glass [2]. However, it has been found by several authors that some glasses (including TeO_2-based glasses) do not follow this rule. Goldschmidt [3] pointed out the important role of the radius ratio for glass-forming oxides, which is the ratio between the ionic radius of the cation and oxygen atoms, r_C/r_O, and it has values of 0.2–0.4 for tetrahedral coordination. Afterwards, Zachariasen took these concepts as a base to develop a model for glass formation, where tetrahedral units share oxygen atoms at the corners constructing a continuous glass network. The SiO_2 glass is formed by a tridimensional network of $(SiO_4)^{4-}$ connected through oxygen atoms at the corners, where at least three corners participate in the irregular network, which does not have translational periodicity. That network is "interrupted" where other cations from modifier compounds (X) are added to glass, forming Si—O—X bonds terminating the connectivity. Some cations can participate forming either as the glass network or as modifiers like Al, Be, Zr, Zn, Cd, and Pb, and this change in behavior will depend on their concentration and their interaction with other components in the glass [4].

For decades, continuous research of new glass systems has led to modify the rules of the classic glass model. Lead orthosilicate glass ($PbSiO_4$) is a glass that does not follow Zachariasen's rules since Pb^{2+} has an octahedral coordination and a large ionic radius (r = 132 pm). In addition, it is possible to fabricate borate glasses with low concentration of B_2O_3, which forms rutile-like octahedral units [5]. The term "inverted glasses" first appeared in the work of Stevels [6] regarding a metasilicate glass formed by three isolated coupled SiO_4 units instead of a continuous network. Thus, a glass that does not follow the classical model and whose network is formed by polyhedra of modifier cations in their majority is called an inverted glass. Some examples are tellurites in which Te ions with a six-fold coordination number form distorted octahedra interconnected between oxygens at the corners [2]. As it is the case of $CaO–Na_2O–MgO–P_2O_5$ glasses with a concentration of MgO higher than 60% mol, Mg—O coordination number changes from ~6 to ~5, which is lower than that of its crystalline form, allowing MgO to change its role to that of a glass former [7].

Finally, applications of inverted glasses will depend on the chemical composition of each vitreous system, and there is a variety of them. For example, for vitreous systems with network modifiers like CdO, ZnO, PbO, and MgO, among others, in high proportions, they are characterized by their good optical properties, and these glasses are attractive for optical devices and laser designs [7]. Furthermore, the introduction of rare earth oxides to germanate tellurite glasses together with their transparency in the infrared region makes them interesting for multiband amplifiers [8].

In this work, the effect of high contents of CdO on the crystallization and formation of inverted glasses of the $CdO-TeO_2-GeO_2$ system was studied. It was expected that as the

modifier oxide increases, devitrification of the glasses will very likely occur. However, as Cd^{2+} cations can coordinate in octahedral units, it is possible that its role as modifier can change to that of an intermediate. Furthermore, the energy band gap of the glasses was calculated from optical absorption spectra. For possible applications in solid state lighting, photoluminescence under UV light excitation of amorphous and crystallized samples was studied.

2. Experimental procedure

2.1. Glass fabrication

A series of eight glasses with a concentration of xCdO-10TeO$_2$-(100−x)GeO$_2$, with x values from 80 to 10 wt%, was fabricated. This series of glasses is localized in the rich GeO$_2$ region of the ternary system diagram as is depicted in **Figure 1**. All oxide powders were purchased by Sigma Aldrich with a >98% purity and were used without further purification (see **Table 1**). The appropriate amount of powders was mixed and homogenized with acetone and then left overnight to dry at room temperature. Afterwards, the batches were melted at 1350°C for 20 min in alumina crucibles, and then the melts were quenched in bronze molds. The density of the glasses was determined using Archimedes' principle estimating the difference between the body weight and the apparent immersed weight. All these measurements were carried out at room temperatures, and distilled water was used as reference immersion liquid.
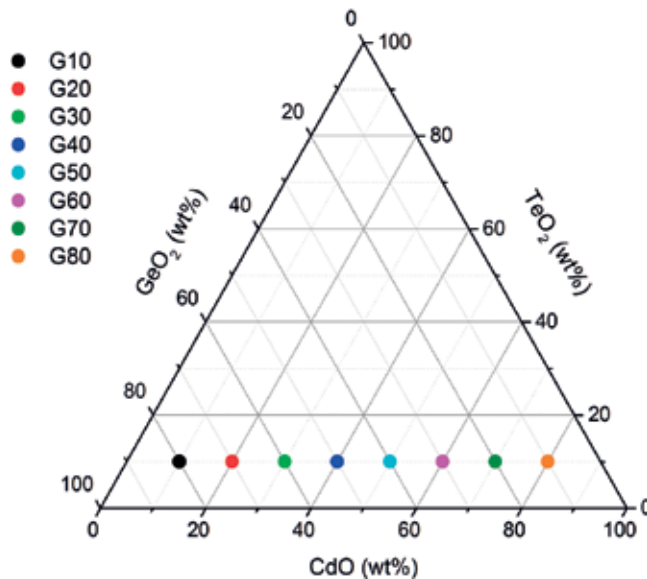
Figure 1. Nominal composition of the studied glass series displayed on the CdO-TeO$_2$-GeO$_2$ ternary diagram.

Label	CdO (wt%)	TeO$_2$ (wt%)	GeO$_2$ (wt%)	Obtained glasses
G10	10	10	80	
G20	20	10	70	
G30	30	10	60	
G40	40	10	50	
G50	50	10	40	
G60	60	10	30	
G70	70	10	20	
G80	80	10	10	

Table 1. Nominal compositions of the glass series.

2.2. Material characterization

The fabricated glasses were characterized by several techniques to study their structural, thermal, and photoluminescent properties. Differential thermal analysis (DTA) was performed in a TA Instrument SDT2960; the samples were heated in an alumina crucible at a rate of 10°C/min from ambient temperature to 1200°C. X-ray diffraction (XRD) was carried out by a Bruker D8 ADVANCE diffractometer. Raman spectroscopy was performed using a 632 nm laser in a Horiba Jobin-Yvon LABRAM HR800 spectrometer. Fourier transform infrared (FTIR) was measured in a Perkin-Elmer model spectrum two spectrometer in the range of 4000 to 500 cm^{-1}. X-ray photoelectron spectroscopy (XPS) of selected samples was also performed

in a Perkin Elmer PHI 5100 spectrometer with a dual Al/Mg anode, Al kα X-ray of 1436 eV excitation radiation was used for the samples characterization, and charge displacement of the samples was corrected using C 1 s peak position at 284.8 eV. Sample G70, which showed a great devitrification, was characterized by transmission electron microscopy to observe the size of the crystalline phase formed in the glass matrix. Photoluminescence of the glasses was monitored in a Horiba Jobin-Yvon FluoroLog-3 spectrofluorometer using different excitation wavelengths in the UV region.

3. Results and discussion

The obtained glasses were of yellowish transparent color (**Table 1**) and for concentrations of CdO of 60 and 70 wt% presented devitrification, at 80 wt% CdO, an orange transparent glass was obtained, and it can be considered an inverted glass. Formation of glass at greater proportions of the modifier oxide was not expected according to Zachariasen's rules. Instead, the formation of a crystalline phase rich in Cd was the most plausible outcome. However, it was possible to obtain a partially devitrified glass, a transparent glass, and a crystalline sample. It can be seen that at 60 wt% CdO, devitrification at the top of the sample is visible, and a white crystalline phase was formed.

3.1. Density and thermal properties

Density, glass transition (T_g), crystallization (T_c), and melting (T_m) temperature values for each glass are shown in **Table 2**. In general, density increases with CdO content, except for samples C20 and C30 where an anomaly is observed (**Figure 2a**). At 30 wt% CdO, the glass density reaches a minimum value and then increases steadily up to 80 wt%. This behavior is consistent with the "germanate anomaly" in alkali germanate glasses where at a certain concentration of alkali oxides, the increment in nonbonding oxides (NBO) affects the glass density [9, 10]. At higher concentrations of CdO, an increase in density occurs probably because of the large Cd ion; such behavior has been previously reported in glasses, crystals, and solutions

Glass	E$_g$ (eV)	CdO (wt%)
C10	3.90	10
C20	3.93	20
C30	3.88	30
C40	3.84	40
C50	3.77	50
C60	3.74	60
C70	3.61	70
C80	3.01	80

Table 2. Optical energy band gap, E$_g$, of the glasses.
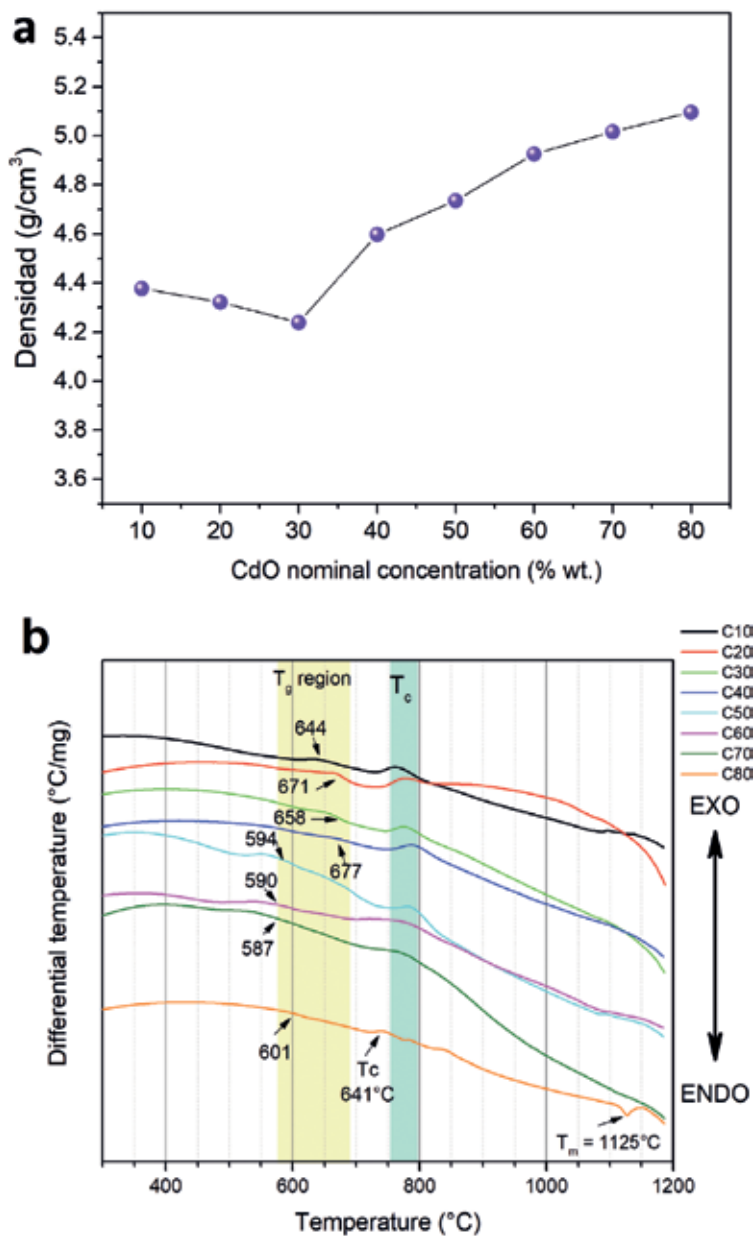
Figure 2. (a) The density of the glasses as a function of CdO concentration and (b) DTA curves of the analyzed glasses.

[11, 12]. DTA curves of the fabricated glasses are presented in **Figure 2b**; the exothermal peaks are associated to T_g or T_c, and there is one endothermic peak for glass C80, which corresponds to a melting point. The samples below 50 wt% GeO_2 have the highest values of T_g and T_c and decrease for the glasses with a higher concentration of CdO; sample C80 is the only one, in the range of analysis, that presents a melting temperature at 1125°C.

3.2. Structural characterization

3.2.1. XRD

Diffraction patterns of all samples are shown in **Figure 3**, and they are separated into three parts. Samples that showed a broad band without diffraction peaks indicating their amorphous nature are exhibited in **Figure 3a**, which were the glasses richest in GeO$_2$ up to 50 wt%, and C80 sample presented with the highest concentration of CdO. Thus, we obtained an inverted glass where CdO changes its role from modifier to glass network former together with GeO$_2$ and TeO$_2$; only a few systems have shown this behavior [7, 13]. Sample G30 (**Figure 3b**) presented a diffraction peak at 2θ = 23.3° related to the orthorhombic phase $Al_6Ge_2O_{13}$. On the other hand, C60 (**Figure 3b**) presented several defined diffraction peaks overlapped with the glassy matrix broad band, and it corresponds with a cadmium aluminum germanate ($Cd_3Al_2Ge_3O_{12}$), which has a garnet crystalline structure. Aluminum incorporation into the glass has its origin from the high-alumina crucible corrosion during the melting process at 1350°C. Furthermore,
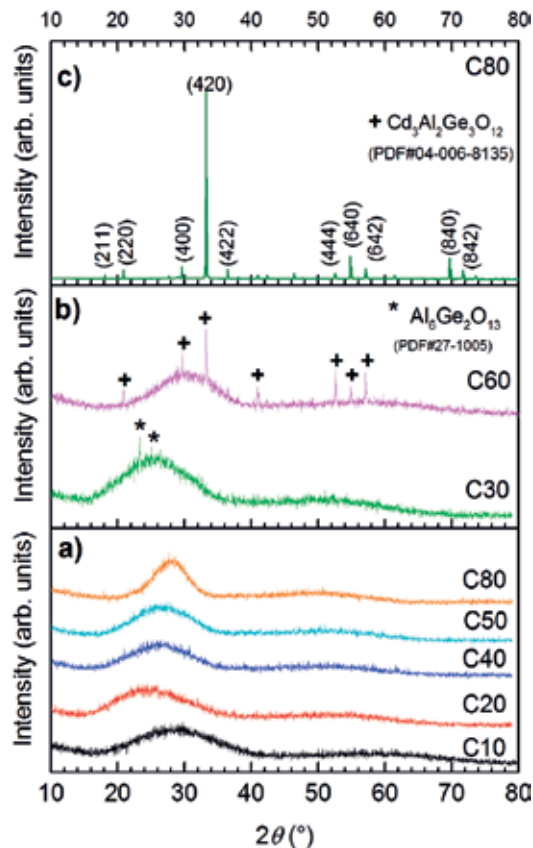
Figure 3. Diffraction patterns of (a) samples that show the characteristic broad diffraction band of amorphous materials, (b) C30 and C60 glasses with phase crystallization, and (c) sample C70 evidencing a complete devitrification and formation of $Cd_3Al_2Ge_3O_{12}$.

sample C70 evidenced well-defined sharp diffraction peaks assigned to the $Cd_3Al_2Ge_3O_{12}$ garnet. It is interesting that both crystalline phases found in the glasses have aluminum in their chemical composition, and phases with only the glasses original constituents (like $CdTeO_3$ or $CdGeO_3$) were not detected.

3.3. Raman spectra

Evolution of the glass structure was explored using Raman spectroscopy, and the spectra are presented in **Figure 4**. Samples C60 and C70 were fabricated a second time to confirm if it was possible to obtain glasses with those compositions, and two yellowish transparent glasses were obtained. The bands related to Ge—O—Ge bonds, GeO_4 and GeO_6 structural units, and Te—O—Te bonds appear in the 400–600 cm^{-1} region [10, 14]. As the concentration of GeO_2 reduces, this broad band changes its intensity until it vanishes for samples C70 and C80. The band within the range of 600 to 900 cm^{-1} exhibits changes in intensity as GeO_2 decreases in content. In the same region, bands for both Ge—O—Ge and Te—O—Te bonds can be found. The maximum shift toward lower wavenumber values from 740 to 760 cm^{-1} is associated with Te—O^- bonds in TeO_{3+1}/TeO_3 groups for the C70 and C80 samples [14–16]. As for glasses C10 to C60, a shift toward 792 cm^{-1} occurs, and in this region, absorption bands related to NBOS from GeO_4 groups are found. Thus, GeO_4 groups can be distinguished in two types, Q^3 (1 NBO) and Q^2 (2 NBOs) units, and the absorption bands related to them appear at ~790 and ~870 cm^{-1}, respectively [10]. Henderson [9] studied the evolution of Q^3 and Q^2 units as a function of the increment in the concentration of alkali oxides; results show that the absorption
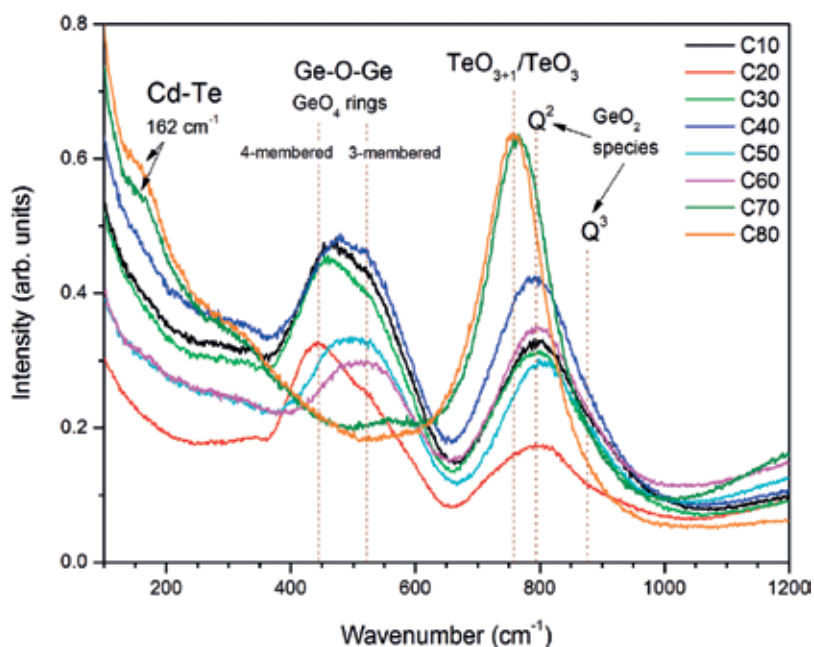
Figure 4. Raman spectra of the glasses; two main broad bands dominate the spectra features and are related to GeO_4 and TeO_{3+1}/TeO_3 structural units present in the glass network.

band of Q^3 units is more intense at higher contents of the modifiers, and a less intense band of Q^2 units is also detected. Thus, Cd^{2+} ions are introducing a larger amount of NBO oxides, as a consequence of its high coordination number, and then at concentrations of 70 and 80 wt%, the network is "inverted" as CdO becomes the glass former.

A third small band at lower wavenumber values (162 cm⁻¹) only appears for samples C70 and C80, and it is related to Cd—Te bonds [17, 18]. However, no crystalline formation of CdTe was identified by XRD. Then, we can only infer that in those rich CdO samples part of Cd^{2+} ions are still participating as modifiers and are also coordinated with Te in TeO_{3+1}/TeO_3 groups due to the lone pair of electrons of Te atoms.

3.4. Infrared spectra

FTIR spectra of the glasses under study (**Figure 5**) show a very broad band in the range of 600–900 cm⁻¹ in which Ge—O—Ge and Te—O—Te bond vibrations are found. As it was observed from Raman spectra, CdO induces a change in coordination of germanium ions from four to six, and absorption bands of GeO_4 and GeO_6 units appear around ~880 and ~715 cm⁻¹, respectively [1, 10, 19, 20]. CdO induces a change in coordination number of Ge from four to six, GeO_4 groups disappear at higher concentrations of the modifier (C70, C80), and only a small and smooth band of GeO_6 remains [1, 21]. Te—O—Te bonds in TeO_4 network absorption band appears around 780 cm⁻¹, and NBOs in Te—O⁻ or Te=O from TeO_{3+1}/TeO_3 units are located at 820 cm⁻¹ [21]. For glasses C70 and C80, a very small band at 763 cm⁻¹ is still visible, and it
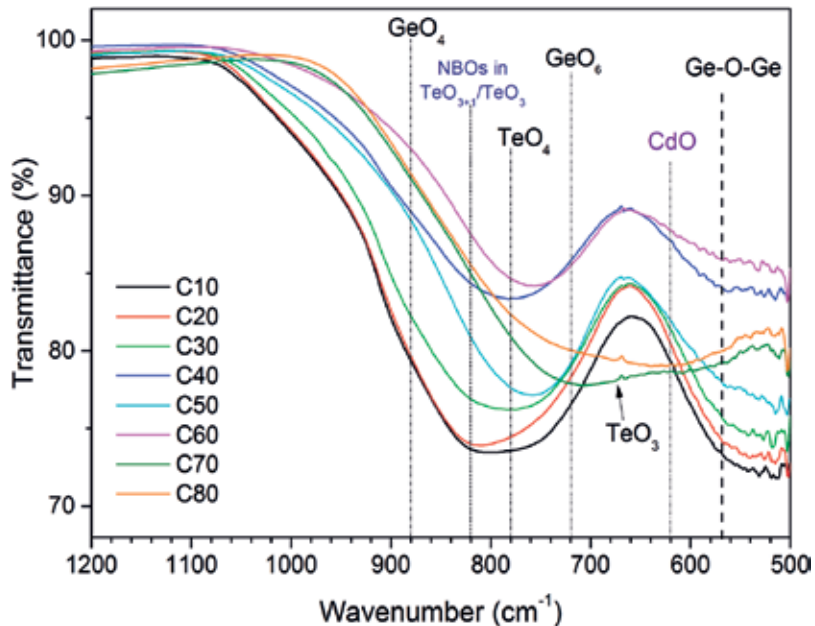
Figure 5. FTIR spectra of all CdO-TeO₂-GeO₂ glasses showing two broad bands at 700–900 and 500–650 cm⁻¹. The former is composed of the bands related to GeO_4, GeO_6, and Te—O—Te bonds in TeO_4 and TeO_{3+1}/TeO_3 groups; the latter corresponds to Ge—O—Ge of Ge ions in six-fold and four-fold coordination.

corresponds to TeO_3 groups, this band does not appear for lower CdO concentrations [1]. It is difficult to determine the band's positions ought to the overlapping of both Te—O—Te and Ge—O—Ge bonds absorption bands. Thus, a position shift probably occurs as the concentration of GeO_2 and CdO changes. At this respect, absorption bands of Cd-O bonds in CdO are reported to appear at 620 cm^{-1} which is visible only for samples C79 and C80 [22]. In the low wavenumber region, around 500–600 cm^{-1}, there is an absorption band of symmetric stretching vibrations of Ge—O—Ge at 566 cm^{-1} [23]. From this analysis, we can confirm that Cd—O bonds constitute the glass structure of the inverted glasses and there are some remaining GeO_6 and TeO_3 groups.

3.5. XPS

At this point, we have established that CdO has a very important role in the structural change of the glass network. High-resolution XPS analysis was performed on C10, the lowest in CdO concentration, and C60, C70, and C80, Cd 3d, Te 3d, Ge 3d, and Al 2p photoelectron lines spectra are presented in **Figure 6**. In the case of Cd 3d spin-orbit doublet (**Figure 6a**), peak positions are presented in 405.3, 405.4, 405.1, 405.15 and 412.1, 412.05, 411.9, 412 eV, respectively, for sample C10, C60, C70, and C80. Those values can be referred to Cd^{2+} ions as it was reported by Moholkar [24], confirming that the above 60 wt% of CdO changes its role to that of a glass former. **Figure 6b** presents Te $3d_{5/2}$ and Te $3d_{3/2}$ doublet in which each photoelectron lines are composed of two well-defined peaks, evidencing that Te ions are chemically bonded in two distinct species. It is noticeable that the peak positions do not shift in binding energy for all analyzed compositions, and they are at 572.5, 575.8 and 583, 586.3 eV for Cd $3d_{5/2}$ and $3d_{3/2}$, respectively. Previous XPS analysis on tellurite glasses showed that Te $3d_{5/2}$ position is in the range of 575.6–576.9 eV and is associated to Te^{4+} [25–27]; the peak intensity varies with CdO concentration. It is the least intense at 60 wt% and then increases for samples richest in CdO. The peaks at 572.5 and 583 eV (Cd $3d_{5/2}$ and $3d_{3/2}$) are related to CdTe [27], and for glasses, C70 and C80, a band related to CdTe was found in Raman analysis. A shift toward lower energy values of the core level peak indicates that Cd^{2+} undergoes an increment in its charge distribution sphere, and this is a very polarizable cation. It is worth to notice that the peaks related to CdTe are more intense for the sample C10 (only 10 wt% of CdO) than those for rich CdO glasses. Thus, Cd^{2+} ions do not participate as a traditional modifier oxide, only interacting with oxygen in Ge—O^- and Te—O^- terminal bonds. It could be possible that cadmium ions are attracted to the lone pair of electrons of Te in TeO_{3+1}, and TeO_3 groups, forming O—Te—Cd complexes in which Cd ions are interrupting the network connectivity. Further analysis is needed to perform to understand how Cd^{2+} ions are interacting and changing the glass network and affecting the optical properties of the glasses in this system.

Ge 3d core-level peak spectra of the analyzed glasses are displayed in **Figure 6c**. A shift toward lower binding energy values (from 32.15 to 30.9 eV) as CdO concentration increases can be distinguished, and it is associated with Ge coordination change from four to six [28]. Al 2p photoelectron line is shown in **Figure 6d** for C60, C70, and C80 glasses only, and no aluminum incorporation was detected for sample C10. Aluminum was not detected in Raman or FTIR

spectroscopies; Al 2p peak position is 73.9 eV for C60 and C70 samples and corresponds to Al—O bonds in Al_2O_3 [29]. For C80 glass, the peak shifts toward 72.6 eV, which is related to Al^0, and this indicates that aluminum is probably not participating in glass network formation.
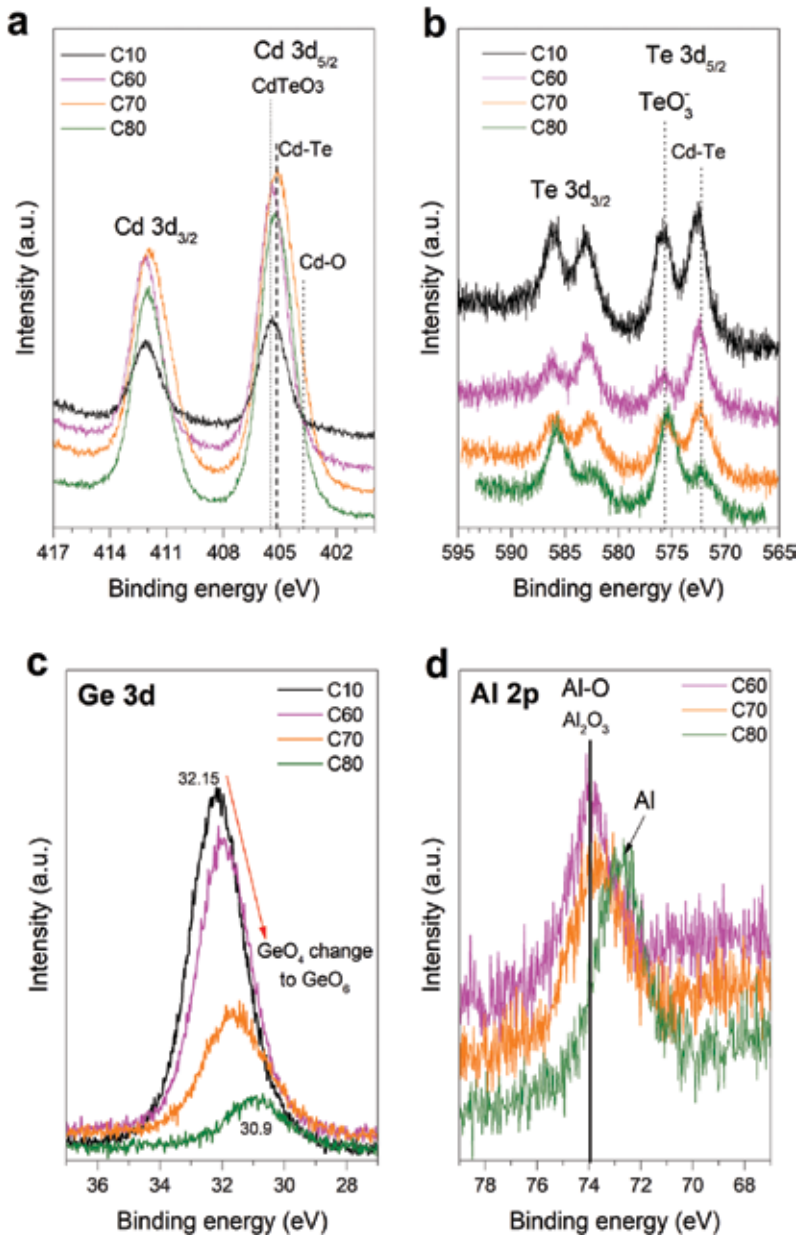
Figure 6. High-resolution XPS spectra of samples C10, C60, C70, and C80 of Ge 3d and Al 2p peaks; and Cd 3d and Te 3d spin-orbit doublets.

3.6. UV-Vis

Optical absorption of the glasses is shown in **Figure 7** and energy band gap by Tauc's method by plotting $(h\nu\alpha)^n$ vs. $(h\nu - E_g)$ was estimated; $h\nu$ is the photon energy, α is the absorption coefficient, and $n = 1/2$ is the amorphous materials. The determined values for E_g are listed in **Table 3**. As it is seen, CdO has a significant effect on the energy band gap of the glasses that decreases as the content of the modifier oxide increases, from 3.90 to 3.01 eV for 10 and 80 wt% of CdO, respectively. This behavior can be related to CdO semiconductor properties that modify the dielectric constant of the host material; previous investigations show that Cd ions can exhibit such significant decrease in E_g values [30, 31].

3.7. Photoluminescence

Glass photoluminescence (PL) was monitored using a 370 nm UV excitation light; this wavelength was selected according to the emission of commercial chips used as UV pumps in LEDs, which is in the range of 360–375 nm. PL emission spectra of the glasses show a broad band emission covering the visible spectral range (400–700 m) and are presented in **Figure 8**. The effect of CdO concentration on the glass structure and, therefore, in the light emission of the glasses is evident; the spectral features show variations through all concentrations. Luminescence in glasses has its origin in "defects" from a chemical standpoint because a glass structure lacks periodicity and symmetry operations. Emission spectra of $CdO\text{-}TeO_2\text{-}GeO_2$ glasses are very complex as a consequence of the several components and related defects that constitute their glass structure.
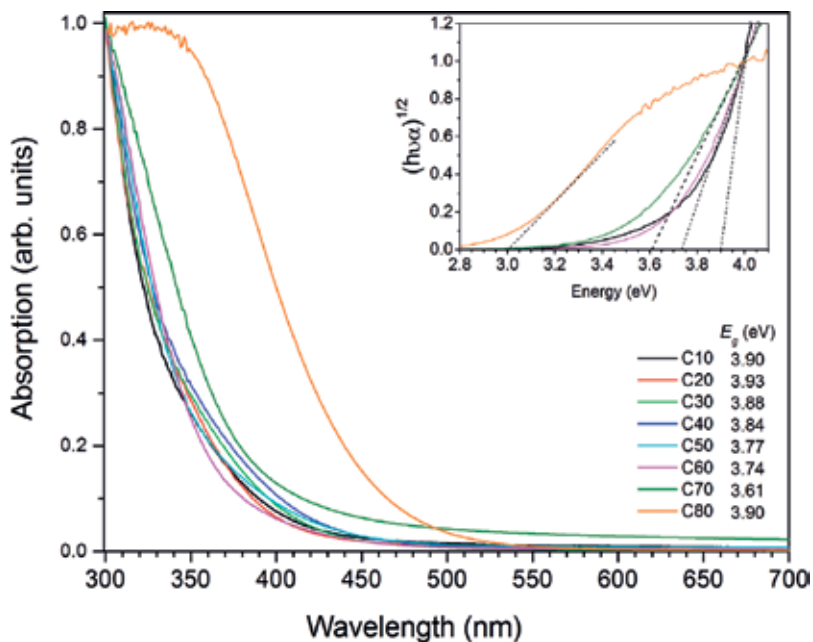
Figure 7. UV–Vis absorption spectra of the glasses; the inset shows $(h\nu\alpha)^n$ vs. $(h\nu - E_g)$ of some samples and their corresponding tangent line to the point of inflection of the curve to the $h\nu$ at the point of intersection.

Glass	E_g (eV)	CdO (% wt.)
C10	3.90	10
C20	3.93	20
C30	3.88	30
C40	3.84	40
C50	3.77	50
C60	3.74	60
C70	3.61	70
C80	3.01	80

Table 3. Estimated energy band gap, E_g, of the CdO-TeO$_2$-GeO$_2$ glasses.

In general, all sample spectra show a band maximum that gradually shifts from 555 to 585 nm as CdO content increases. At lower wavelengths, C10 and C40 show a distinct shoulder around 449 nm, and for sample C20, shifts to 455 nm and its intensity decrease. C50 and C60 do not show a shoulder, only a broad band at 571 and 576, respectively, indicating that the glass structure did change and the defect causing that feature disappeared. Sample C70 has a band shoulder at 476 nm, as it was mentioned above, and at this composition, the structure starts to invert from a GeO$_2$ to a CdO network. Sample C30 shows a small emission band at 415 nm, and C80 presents a structured band with two maxima at 422 and 434 nm, and it is more intense than the main broad band in other glasses.
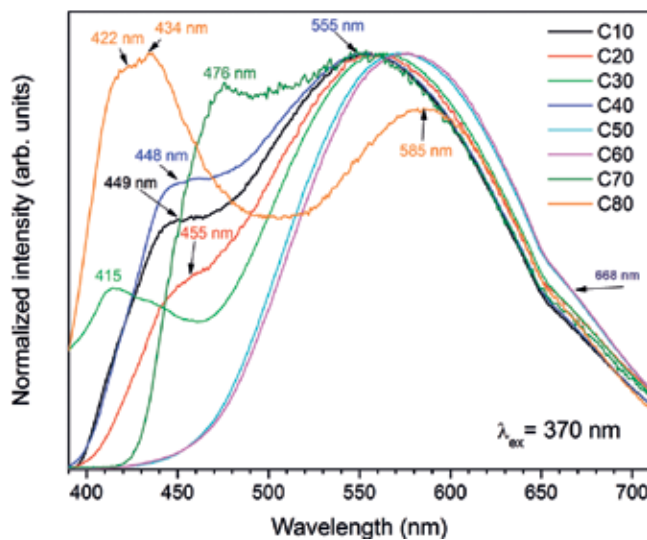
Figure 8. PL emission spectra of the glasses monitored using an excitation wavelength of 370 nm.

It has been thoroughly studied that in GeO_2 glasses, the Ge^{2+} emission center (defect) presents two emission bands at 300 and 395 nm under UV light (254 and 330 nm), which is from the $S_1 \rightarrow T_0$ and $T_1 \rightarrow T_0$ transitions [32]. However, those bands related to GeO_2 glass do not appear in the range of analysis, and it seems that, for samples C30 and C80, emission spectra extend beyond the monitored range toward UV region. Tikhomirov et al. [33] reported that the intrinsic luminescence of Na_2O-ZnO-TeO_2 glasses is associated to bi-coordinated Te and Te—Te bond defects, showing a broad emission with a maximum at 670 nm using a 478 nm excitation light. Thus, defects associated to TeO_2 in the glasses under study are also to be considered. Another aspect of the emission in these glasses can be related to the change in CdO role from a modifier to a glass former. In the literature, cadmium oxide in its crystalline form presents oxygen vacancies and interstitial Cd^{2+}, and these defects increase when the oxide is doped with other metallic ions [24]. On the other hand, Cd ions modify the field strength of Te and Ge due to its polarizability effect and the Cd d^{10} configuration [24]. Therefore, further photoluminescence emission and excitation characterization together with decay times are needed to understand the origin of CdO-TeO_2-GeO_2 glass emission.

To explore possible applications of the fabricated glasses, chromatic coordinates (**Table 4**) were calculated and are depicted in the CIE 1931 chromaticity diagram in **Figure 9**. Global emission of the glasses covers a wide range of colors from sample C10 to C70 that are in the yellow and orange region and C80 that has a white light emission with chromatic coordinates of x = 0.3299 and y = 0.3158, closer to the ideal x = 0.33 and y = 0.33. According to these results, CdO-TeO_2-GeO_2 glasses could be doped with rare earth ions and be potentially used as phosphors for solid state lighting devices.

3.8. $Cd_3Al_2Ge_3O_{12}$ garnet characterization

It is worth to mention that garnets are complex crystal structures with an $A_3B_2(XO_4)_3$ formula, where A is a divalent cation with dodecahedral coordination, B is a trivalent cation of octahedral coordination, and X is a tetravalent cation (Si^{4+}, Ge^{4+}) in tetrahedral coordination.

Sample	x	y
C10	0.3444	0.3961
C20	0.3678	0.4235
C30	0.3755	0.4221
C40	0.3373	0.3851
C50	0.4440	0.4979
C60	0.4993	0.4953
C70	0.3414	0.4089
C80	0.3299	0.3158

Table 4. Estimated chromatic coordinates of the glasses as a function of CdO content.
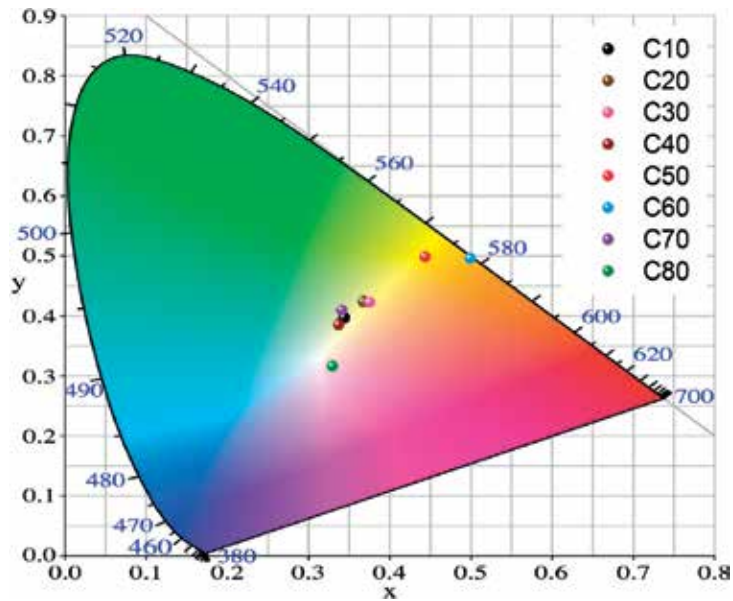
Figure 9. Chromatic coordinates of the glass emission on the CIE 1931 chromaticity diagram where the emission color of the glasses varies along the white, yellow, and yellowish-orange region.

Silicate garnets are found in nature and have a variety of colors depending on the divalent and trivalent cations that constitute the crystal. There are also nonsilicate garnets like the yttrium aluminum garnet (YAG), $Y_3Al_5O_{12}$, and Ce^{3+} doped YAG has a red emission under blue light excitation and is used for lasers [34]. Thus, garnet crystals have potential to be used as phosphors because of their photoluminescence properties as it was previously reported for Ce^{3+} and Mn^{2+} doped silicate and germanate glasses [25]. In a previous Section 3.2.1 in **Figure 3**, the diffraction pattern of C70 glass exhibited the crystalline nature of the sample, and we confirmed the formation of a $Cd_3Al_2Ge_3O_{12}$ garnet. In this section, transmission electron microscopy (TEM) and PL characterization of this crystalline sample are presented.

3.9. TEM

TEM micrographs at different magnifications where phase separation with a droplet distribution in the glass matrix are displayed in **Figure 10a** and **b**. Those droplets are nanocrystals, and at higher magnification, a periodic arrangement is visible in **Figure 10c**. The measured interplanar distance is 2.75 Å that corresponds to the (420) plane in $Cd_3Al_2Ge_3O_{12}$. As a comparison, the Laue diffraction pattern of the nanocrystals overlapped with XRD diffraction pattern is presented in **Figure 10d**, showing the matching of the most intense diffraction peaks related to (420), (422), and (444) Miller indexes of the $Cd_3Al_2Ge_3O_{12}$ garnet. Thus, sample C70 is a nanostructured material composed by the garnet nanocrystals embedded in a glassy matrix.
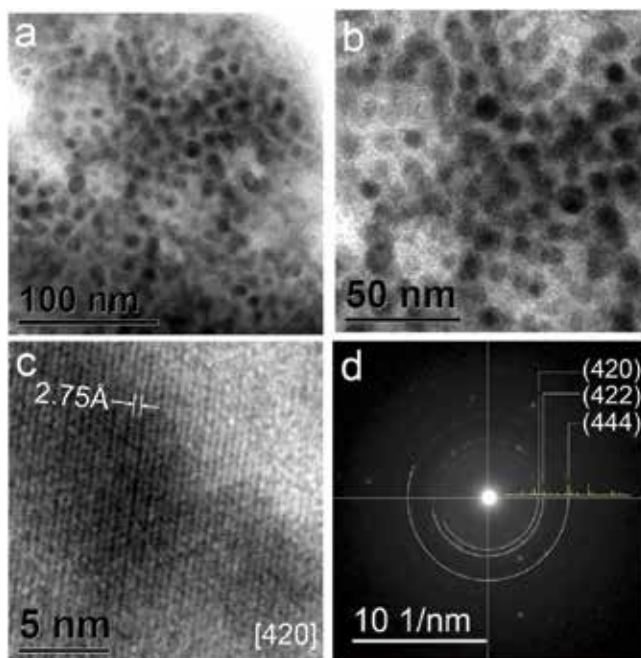
Figure 10. (a and b) Micrographs of sample C80 showing phase separation with a droplet distribution of the nanocrystals, (c) HR-TEM micrograph of the nanocrystals and measuring of the interplanar distance, (d) Laue diffraction pattern comparison with XRD diffraction pattern of sample C70.

3.10. Photoluminescence

Lui et al. [35] have previously reported the synthesis of $Cd_3A_{12}Ge_3O_{12}$ doped with Dy^{3+} ions and its afterglow properties. In their work, emission of the doped garnet under a 254 nm excitation light shows a broad band overlapped with the $^4F_{9/2} \rightarrow {}^6H_{15/2}$ and $^4F_{9/2} \rightarrow {}^6H_{13/2}$ emission transitions of Dy^{3+} at 485 and 580 nm, respectively. Then, as comparison, our sample was excited with the same wavelength, the same wavelength to excite our crystallized sample was used, and the resulting spectrum is displayed in **Figure 11a**. The spectrum consists of a very broad band in the visible spectral range (400–750 nm) with a maximum at 526 nm. In the previous report, the emission band maximum of the Dy doped garnet is located at ~430 nm. The authors proposed two possible origins of the intrinsic garnet emission: the formation of Cd^{2+} vacancies during processing and the presence of $(GeO_4)^{4+}$ tetrahedral groups [35, 36]. However, $(GeO_4)^{4+}$ group emission is around 310 nm as it was reported for the $Ca4ZrGe_3O_{12}$ garnet [37]. Moreover, the GeO_2 emission is in the UV range and it was discussed previously. It is reported that germanate compounds like $SrGeO_3:Eu^{3+}$, $NaLa_9(GeO_4)_6O_2$, and rare earth doped garnets like ${\{Ca(Tb)\}}_3Ga_2Ge_3O_{12}$ and $Sr_3[Y(Tb)]_2Ge_3O_{12}$ are of interest to be employed as red-light phosphors for near-ultraviolet-white light emitting diodes and field-emission displays (NUV-WLEDs and FEDs) [38–40]. Chromaticity coordinates of the intrinsic luminescence of cadmium aluminum germanate were estimated (x = 0.3267, y = 0.4795) and are presented in the CIE 1931 color space in **Figure 11b**, as it can be seen that the emission color is in the yellowish-green region.
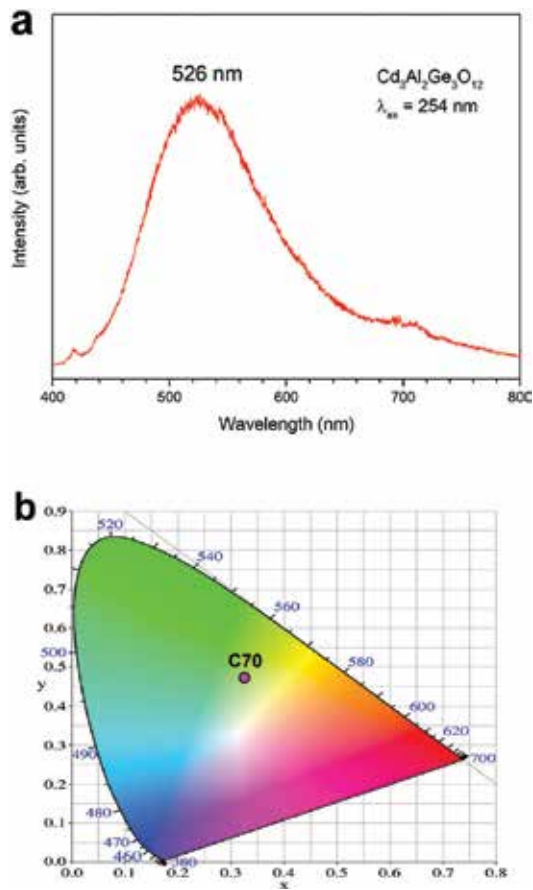
Figure 11. (a) Emission spectra of the C70 crystallized sample monitored using a 254 nm laser. (b) Chromatic coordinates of C70 light emission on the CIELAB 1931 color space, which are in the yellowish-green region.

4. Summary

A series of yellowish transparent glasses of the CdO-TeO$_2$-GeO$_2$ system were obtained even at high CdO content. Thus, CdO changes its role from modifier to network former. Incorporation of aluminum through crucible corrosion leads to the formation of the Cd$_3$A$_{12}$Ge$_3$O$_{12}$ garnet at 60 and 70 wt% of CdO. The glasses were structurally characterized by XRD, Raman, and XPS spectroscopies demonstrating that their structure is complex and undergoes several changes as the CdO content increases, and this behavior affects the energy band gap values. Luminescence of the glasses demonstrates several structural changes that the samples undergo with concentration variation, showing a very broad structured emission band in the range of visible light monitored with a 370 nm excitation wavelength. The defects that cause the emission of the glasses are yet to be understood and studied. Chromatic coordinates show that emission color of the glasses varies in the range of yellow to orange. The glass with CdO 80 wt% global emission lies in the white light region of the CIE 1931 chromaticity diagram with x = 0.3299 and

y = 0.3158 values. Thus, these series of glasses are good candidates for optoelectronic devices or as rare earth ion hosts. The $Cd_3Al_2Ge_3O_{12}$ garnet is nanostructured as it was determined by TEM analysis, and PL measurements shows a broad emission centered at 526 nm with calculated chromatic coordinates of x = 0.3267, y = 0.4795, which lies in the yellowish-green region of the CIE 1931 chromatic diagram. Previous reports in the literature show that garnet structures doped with rare earth ions, especially germanates, are of interest for their applications as phosphors in optoelectronic devices. Further research is needed to fully understand the structure and hence the optical properties of glasses of the $CdO-TeO_2-GeO_2$ system.

Acknowledgements

Author details

Josefina Alvarado Rivera[1]*, Carlos Guadalupe Pérez Hernández[2], María Elena Zayas[3] and Enrique Álvarez[2]

*Address all correspondence to: josefina.alrive@gmail.com

1 CONACYT-University of Sonora, Hermosillo, Sonora, Mexico

2 Physics Department, University of Sonora, Hermosillo, Sonora, Mexico

3 Physics Research Department, University of Sonora, Hermosillo, Sonora, Mexico

References

[1] Rachkovskaya GE, Zakharevich GB. IR spectra of tellurium germanate glasses and their structure. Journal of Applied Spectroscopy. 2007;**74**(1):86-89. DOI: 10.1007/s10812-007-0013-z

[2] El-Mallawany RAH. Handbook of Tellurite Glasses—Physical Properties and Data. CRC Press: USA; 2011

[3] Goldschmidt VM. Skriffer Norke Videnskaps Akad. Oslo I, Mathematisch-Naturwiss. Klasse. 1926;**1**:7

[4] Carter CB, Norton MG. Ceramic Materials Science and Engineering. New York: Springer; 2007

[5] Tcheivili L. Un vidrio de fluoruro de plomo (A lead fluoride glass). Boletín de la Sociedad Española de Cerámica. 1968;Agosto-Julio:461-473

[6] Stevels JM. The glass considered as a polymer. Glass Industry. 1954;**35**(2):69-72

[7] Walter G, Vogel J, Hoppe U, Hartmann P. The structure of CaO-Na$_2$O-MgO-P$_2$O$_5$ invert glass. Journal of Non-Crystalline Solids. 2001;**296**(3):212-223. DOI: 10.1016/S0022-3093 (01)00912-7

[8] Feng X, Tanabe S, Hanada T. Spectroscopic properties and thermal stability of Er^{3+} doped germanotellurite glasses for broadband fiber amplifiers. Journal of the American Ceramic Society. 2001;**84**(1):165-171. DOI: 10.1111/j.1151-2916.2001.tb00625.x

[9] Henderson S. The germanate anomaly: What do we know? Journal of the Non-Crystalline Solids. 2007;**353**(18-21):1695-1704. DOI: 10.1016/j.jnoncrysol.2007.02.037

[10] Alvarado-Rivera J, Rodríguez-Carvajal DA, Acosta-Enríquez MC, Manzanares-Martínez MB, Álvarez E, Lozada-Morales R, Díaz GC, et al. Effect of CeO$_2$ on the glass structure of sodium germanate glasses. Journal of the American Ceramic Society. 2014;**97**(11):3493-3500. DOI: 10.1111/jace.13202

[11] Sreenivasulu V, Upender G, Mouli VC, Prasad M. Structural, thermal and optical properties of TeO$_2$-ZnO-CdO-BaO glasses doped with VO^{2+}. Spectrochimica Acta Part A: Molecular and Biomolecular Spectroscopy. 2015;**148**:215-222. DOI: 10.1016/j.saa. 2015.03.085

[12] Grado-Caffaro MA, Grado-Caffaro M. A quantitative discussion on band-gap energy and carrier density of CdO in terms of temperature and oxygen partial pressure. Physics Letters A. 2008;**372**(27-28):4858-4860. DOI: 10.1016/j.physleta.2008.04.068

[13] Brady GW. Structure of tellurium oxide glass. Journal of Chemical Physics. 1957;**27**:300. DOI: 10.1063/1.1743690

[14] Upender G, Vardhani CP, Suresh S, Awasthi AM, Mouli VC. Structure, physical and thermal properties of WO$_3$-GeO$_2$-TeO$_2$ glasses. Materials Chemistry and Physics. 2010;**125** (1-2):335-341. DOI: 10.1016/j.matchemphys.2010.01.050

[15] Ersundu AE, Çelikbilek M, Solak N, Aydin S. Glass formation area and characterization studies in the CdO-WO$_3$-TeO$_2$ ternary system. Journal of the European Glass Ceramic Society. 2011;**31**(15):2775-2781. DOI: 10.1016/j.jeurceramsoc.2011.07.027

[16] Yang Z, Xu S, Yang J, Hu L, Jiang Z. Thermal analysis and optical transition of Yb^{3+}, Er^{3+} co-doped lead-germanium-tellurite glasses. Journal of Materials Research. 2004;**19**(6):1630-1637. DOI: 10.1557/JMR.2004.0226

[17] Ma L, Chen Y, Wei Z, Cai H, Zhang F, Wu X. Facile method to prepare CdS nanostructure bases on the CdTe films. Applied Surface Science. 2015;**349**(15):740-745. DOI: 10.1016/j. apsusc.2015.05.024

[18] Dzhagan V, Lokteva I, Himcinschi C, Jin X, Kolny-Olesiak J, Zahn DR. Phonon Raman spectra of colloidal CdTe nanocrystals: Effects size, non-stoichiometry and ligand exchange. Nanoscale Research Letters. 2011;**6**(1). DOI: 10.1186/1556-276X-6-79

[19] Rachokoskaya GE, Zakharevich GB. Germanate lead-tellurite glasses for optical light filters. Glass and Ceramics. 2012;**68**(11-12):385-388. DOI: 10.1007/s10717-012-9396-2

[20] Culea E, Pop L, Bosca M, Rusu T, Pascuta P, Rada S. FTIR spectroscopic study of some lead germanate glasses. Journal of Physics: Conference Series. 2009;**182**(1):012061

[21] Monteiro G, Santos LF, Pereira JCG, Almeida RM. Optical and spectroscopic properties of germanotellurite glasses. Journal of Non-Crystalline Solids. 2011;**357**(14):2695-2701. DOI: 10.1016/j.jnoncrysol.2010.12.062

[22] Tripathi R, Dutta A, Das S, Kumar A, Sinha TP. Dielectric relaxation of CdO nanoparticles. Applied Nanoscience. 2016;**6**(2):175-181. DOI: 10.1007/s13204-015-0427-5

[23] Lucacel RC, Marcus C, Ardelean I. FTIR and Raman spectroscopic studies of copper doped $2GeO_2.PbO.Ag_2O$ glasses. Journal of Optoelectronics and Advanced Materials. 2007;**9**(3):747-750

[24] Moholkar AV, Agawane GL, Sim KU, Kwon YB, Choi DS, Rajpure KY, Kim JH. Temperature dependent structural, luminescent and XPS studies of CdO:Ga thin films deposited by spray pyrolysis. Journal of Alloys and Compounds. 2010;**506**(2):794-799. DOI: 10.1016/j.jallcom.2010.07.072

[25] Salim MA, Khattak GD, Tabet N, Wenger LE. X-ray photoelectron spectroscopy (XPS) studies of copper-sodium tellurite glasses. Journal of Electron Spectroscopy and Related Phenomena. 2003;**128**(1):75-83. DOI: 10.1016/S0368-2048(02)00214-1

[26] Lim JW, Jain H, Toulouse J, Marjanovic S, Sanghera JS, Miklos R, Aggarwal ID. Structure of alkali tungsten tellurite glasses by X-ray photoelectron spectroscopy. Journal of Non-Crystalline Solids. 2004;**349**:60-45. DOI: 10.1016/j.jnoncrysol.2004.08.263

[27] Castro-Rodríguez R, Iribarren A, Bartolo-Pérez P, Peña JL. Obtaining of polycrystalline $CdTeO_3$ by reactive pulse laser deposition. Thin Solid Films. 2005;**484**(1):100-103. DOI: 10.1016/j.tsf.2005.02.011

[28] Mekki A, Holland D, Ziq KA, McConville CF. Structural and magnetic properties of sodium iron germanate glasses. Journal of Non-Crystalline Solids. 2000;**272**(2):179-190. DOI: 10.1016/S0022-3093(00)00235-0

[29] Moulder FJ. X-Ray Photoelectron Spectroscopy: A Reference Book of Standard Spectra for Identification and Interpretation of XPS Data. Eden Prairie, Minnesota: Physical Electronics Division, Perkin-Elmer Corporation; 1992

[30] Gowrishankar S, Balakrishnan L, Gopalakrishnan N. Band gap engineering in Zn(1−x)CdxO and Zn(1−x)MgxO thin films by RF sputtering. Ceramics International. 2014;**40**(1):2135-2142. DOI: 10.1016/j.ceramint.2013.07.130

[31] Duman S, Turgut G, Özçelik FŞ, Gurbulak B. The synthesis and characterization of sol-gel spin coated CdO thin films: As a function of solution molarity. Materials Letters. 2014;**126**:232-235. DOI: 10.1016/j.matlet.2014.04.063

[32] Wada N, Mayu I, Kojima K. Glass composition dependence of luminescence due to Ge^{2+} center in germanate glasses. Journal of Non-Crystalline Solids. 2006;**352**(23):2657-2661. DOI: 10.1016/j.jnoncrysol.2006.02.073

[33] Tikhomirov VK, Ronchin S, Montagna M, Ferrari M, Furniss D. Intrinsic defect related photoluminescence in TeO$_2$-based glasses. Physica Status Solidi A. 2001;**187**(11):R4-R6. DOI: 10.1002/1521-396X(200109)187:1<R4::AID-PSSA99994>3.0.CO;2-6

[34] He X, Liu X, Li R, Yang B, Yu K, Zeng M, Yu R. Effects of local structure of Ce^{3+} ions on luminescent properties of Y$_3$Al$_9$O$_{12}$:Ce nanoparticles. Scientific Reports. 2016;**6**:22238. DOI: 10.1038/srep22238

[35] Lui Z, Liu Y. Afterglow energy transfer in Cd$_3$Al$_2$Ge$_3$O$_{12}$:Dy. Physica Status Solidi A. 2005;**202**(9):1814-1817. DOI: 10.1002/pssa.200420034

[36] Blasse G, Bril A. Fluorescence of Eu^{3+} activated-garnets containing pentavalent vanadium. Journal of Electrochemistry. 1967;**114**(3):250-252. DOI: 10.1149/1.2426560

[37] Blasse G, De Blank J, IJdo DJW. The luminescence of the garnet Ca$_4$ZrGe$_3$O$_{12}$. Materials Research Bulletin. 1995;**30**(7):845-850. DOI: 10.1016/0025-5408(95)00068-2

[38] Wang T, Xu X, Zhou D, Qiu J, Yu X. Luminescent properties of SrGeO$_3$:Eu^{3+} red emitting phosphors for field emission displays. ECS Journal of Solid State Science and Technology. 2014;**3**(8):R139-R143. DOI: 10.1149/2.0081408jss

[39] Cao Y, Zhu G, Wang Y. Synthesis, structure and luminescence characteristics of a novel red phosphor NaLa$_9$(GeO$_4$)$_6$O$_2$:Eu^{3+} for light emitting diodes and field emission displays. RSC Advances. 2015;**5**(81):65710-65718. DOI: 10.1039/C5RA10435A

[40] Avouris P, Chang IF, Duvgneaud PH, Giess EA, Morgan TN. Luminescence of germanate garnets with terbium on dodecahedral and octahedral lattices sites. Journal of Luminescence. 1982;**26**(3):213-225. DOI: 10.1016/0022-2313(82)90049-7

Crystallization Kinetics of Bi_2O_3-SiO_2 Binary System

Hongwei Guo

Abstract

The Bi_2O_3-SiO_2 glasses were prepared by the melt cooling method. The non-isothermal crystallization kinetics and phase transformation kinetics of the BS glasses were analyzed by the Kissinger and Augis-Bennett equations by means of differential scanning calorimetry (DSC) and X-ray diffraction (XRD). The results show that three main crystal phases, namely $Bi_{12}SiO_{20}$, Bi_2SiO_5, and $Bi_4Si_3O_{12}$ are generated sequentially in the heat treatment process. The corresponding activation energy is 150.6, 474.9, and 340.3 kJ/mol. The average crystallization index is 2.5, 2.1, and 2.2. The crystal phases generated by volume nucleation grow in a one-dimensional pattern, and the metastable Bi_2SiO_5 can be transformed into $Bi_4Si_3O_{12}$, which is in a more stable phase.

Keywords: differential scanning calorimetry, glass-ceramics, non-isothermal, kinetics

1. Crystallization kinetics of Bi_2O_3-SiO_2 binary system

1.1. The structure of bismuth glass and Bi_2O_3-SiO_2 system glass-forming characteristics and structure

Pure Bi_2O_3 cannot form glass, but a small amount of glass formers such as B_2O_3, P_2O_5, and SiO_2 can be used to obtain a melt that condenses into a glassy state [1].

Bismuth ions, similar to lead ions, can enter the network structure of the glass (Bi atom has a similar atomic weight, ionic radius, and electronic configuration as lead atom, both having 2S-electrons on the outer layer). As a glass former, the influence of bismuth on the linear expansion coefficient is not so great if compared to barium and strontium. The glass-forming region of this system is relatively large [1], where the Bi_2O_3/B_2O_3 ratio can reach 2/1 or more. Therefore, when the content of Bi_2O_3 is high enough, it may play a role as a glass former.

The literature [2] studied the formation area of B_2O_3-Tl_2O-Bi_2O_3, B_2O_3-PbO-Bi_2O_3, B_2O_3-CdO-Bi_2O_3 system glass. Glass was melted in a metal crucible, melting amount 2–4 g. This kind of glass is melted in kerosene furnace at 800–900°C for 10–30 min. The resulting glass B_2O_3 content is not high. This proves that the other components act as glass-forming bodies, including Bi_2O_3, PbO, CdO, and Tl_2O. **Figure 1** shows the glass structure of Bi_2O_3-B_2O_3 system at Bi_2O_3 60 mol%. When the concentration of Bi_2O_3 is 75 mol%, the structure is shown in **Figure 2**. It is noteworthy that a more complex structure appears when adding lead oxide to bismuth borate glass, as shown in **Figure 3**. This is because the bismuth ions undergo a severe polarization and deform under the action of an external electric field, thus promoting the formation of asymmetric radicals.

Figure 4 shows the phase diagram of the Bi_2O_3-SiO_2 system [3–5]. By analyzing it, we could found that the Bi_2O_3-SiO_2 system has the properties of forming glass at the molar ratio Bi_2O_3: SiO_2 = 1:1. According to the report by Fei et al. [6, 7], the Bi_2O_3-SiO_2 system glass can be prepared by the conventional glass preparation process at a molar ratio of Bi_2O_3:SiO_2 = 1:1.

Similar to PbO, Bi_2O_3 in the glass structure can significantly reduce the viscosity, increase the density, and can also act as a flux. Bi is a heavy metal element but its field strength is very
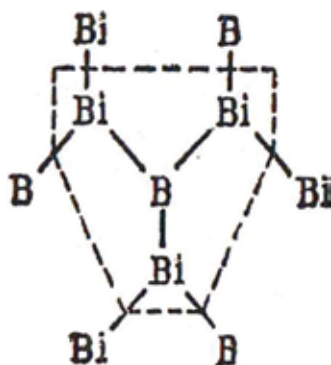
Figure 1. Glass structure of Bi_2O_3-B_2O_3 system at Bi_2O_3 60 mol%.
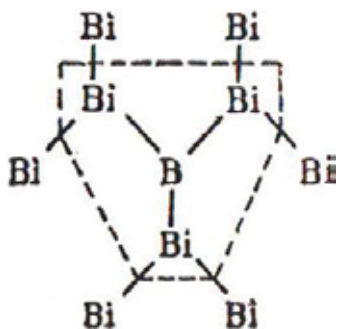
Figure 2. Glass structure of Bi_2O_3-B_2O_3 system at Bi_2O_3 75 mol%.
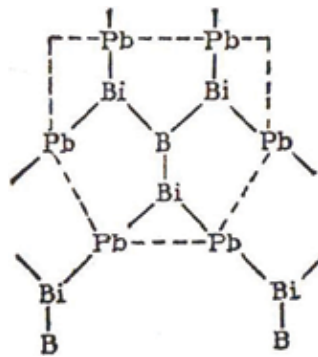
Figure 3. Glass structure of B₂O₃-PbO-Bi₂O₃ system.
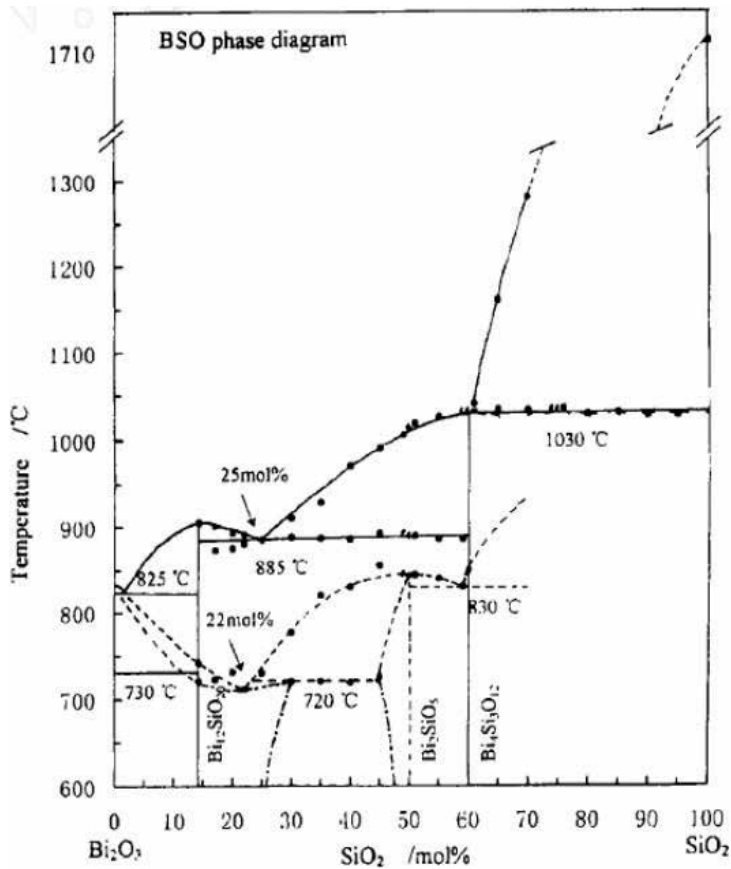
Figure 4. Equilibrium phase diagrams of the Bi₂O₃-SiO₂ system.

small, the bond strength of the Bi-O bond is much stronger than that of the Si-O bond. Therefore, Bi cannot form glass alone but the Bi₂O₃-SiO₂ system glass may have a broad glass-forming region. That is to say the amount of Bi₂O₃ added in this system can be large.

When the mole fraction of Bi_2O_3 is greater than 50%, it is necessary to partially form the glass after water quenching.

Figure 5 shows the XRD patterns of Bi_2O_3-SiO_2 base glasses with a molar ratio of 1:1. The preparation process was as follows: Bi_2O_3 and SiO_2 with a molar ratio of 1:1 were ground for 3 h with absolute ethanol as grinding medium and dried for 1 h. Then, the batch was poured into 200 ml corundum crucible, placed in the box-type electric furnace for melting at 1100°C. Since Bi_2O_3 is volatile, the corundum crucible was capped.

After casting, annealing was carried out at 400°C for 1 h. The annealed glass samples were reddish brown. A part of the samples were ground down to 200 mesh powder.

XRD analysis was carried out. The test conditions were CoK_α radiation, tube voltage 40 kV and current 4 mA, step 0.02°, scanning speed 6°/min, scanning range 10–80°. **Figure 5** shows the typical steamed bun peak. Due to the strong glass forming ability of SiO_2, the Bi_2O_3-SiO_2 system glass is easy to be obtained when the molar ratio of Bi_2O_3/SiO_2 is less than 1.

1.2. Separation of Bi_2O_3-SiO_2 binary system glass

Phase separation, that is, liquid–liquid immiscibility, is a common phenomenon in glass-forming systems [1, 2, 8, 9].

It has been proven that the size of the cationic potential of the network has a decisive effect on phase separation of the oxide glass: when the cation potential $Z/r > 1.4$ (ion potential refers to the ionic charge number Z and ionic radius r ratio), the system produces liquid–liquid immiscible region above the liquidus temperature. When the value of Z/r is between 1.0 and 1.4, the liquidus is S-type, and there is a metastable immiscible region below the liquidus; when the value of $Z/r < 1.0$, the phase separation will not happen [2, 8, 9].
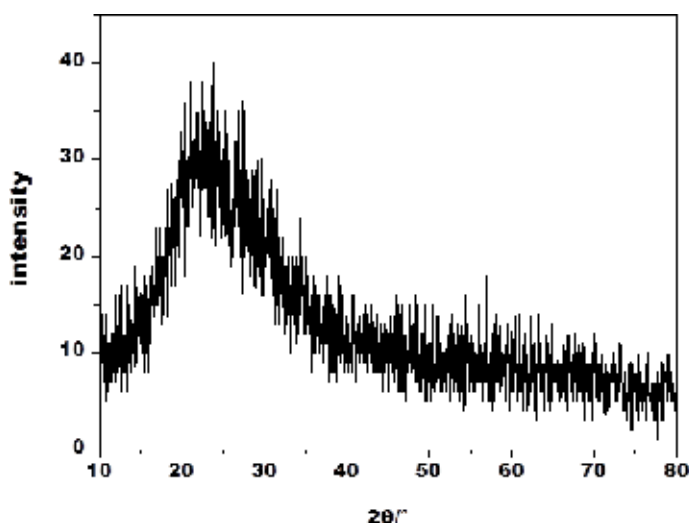
Figure 5. XRD patterns of the Bi_2O_3-SiO_2 system glass.

The cation potential of Bi is Z/r = 3/1.03 > 1.4, which makes it clear that the liquid–liquid immiscible region is generated in the Bi$_2$O$_3$-SiO$_2$ system above the liquidus temperature. Bi is in the seventh main group, and it can expand the phase separation area. Therefore, it is argued that phase separation occurs during the melting of the Bi$_2$O$_3$-SiO$_2$ system glass, resulting in a silicon-rich phase and a bismuth-rich phase. The phase separation in the glass leads to the appearance of new phases, providing favorable nucleation sites and phase separation results in a larger atomic mobility of one of the two liquid phases, which facilitates uniform nucleation. It can be seen that the separation in the Bi$_2$O$_3$-SiO$_2$ system favors the precipitation of crystals in the system.

1.3. Non-isothermal crystallization of Bi$_2$O$_3$-SiO$_2$ (Bi$_2$O$_3$:SiO$_2$ = 1:1) system glass

Figure 6 shows the DSC curves of Bi$_2$O$_3$-SiO$_2$ system glass at different heating rates. There are three distinct crystallization exothermic peaks. At the same time, the temperature of the crystallization peak tends to be stable at heating rate of 10°C/min. In this chapter, a 10 K/min heating rate curve was chosen to determine the heat treatment system of Bi$_2$O$_3$-SiO$_2$ system glass.

From the curves with the heating rate of 10°C/min in **Figure 6**, the three obvious crystallization exothermic peaks were at 564, 659, and 793°C. The heat treatment of the Bi$_2$O$_3$-SiO$_2$ system glass is shown in **Table 1**. Among them, p0 is the basic glass control group, and p1, p2, and p3 correspond to three crystallization peaks from low to high, respectively. Based on the basic glass processing conditions, better crystals can be formed and the type of precipitated crystals can be determined by XRD phase analysis.

The XRD analysis was performed on the samples maintained at different temperatures according to the above heat treatment system. The results are shown in **Figure 7**. Through the
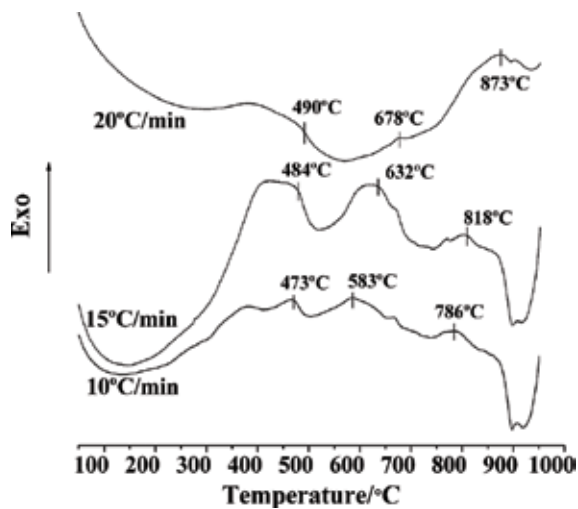
Figure 6. DSC curves of different heating rates of the Bi$_2$O$_3$-SiO$_2$ system (Bi$_2$O$_3$:SiO$_2$ = 1:1).

Heat treatment system	Sample no			
	P0	p1	p2	p3
Nucleation temperature/°C	—	530	630	659
Nucleation time/h	0	1	1	1
Crystal growth temperature/°C	—	564	659	793
Crystal growth time/h	0	3	3	3

Table 1. Heat treatment of the Bi_2O_3-SiO_2 system.
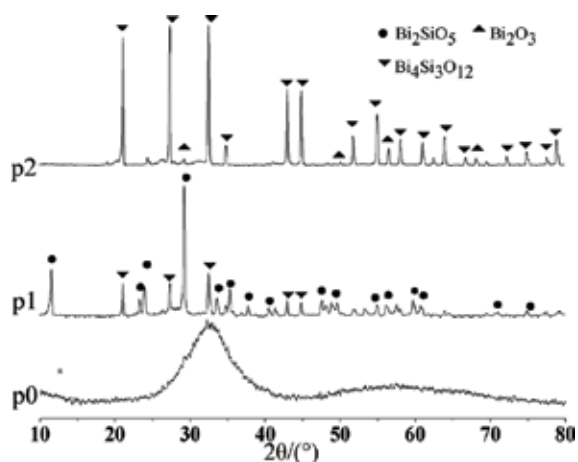
Figure 7. XRD patterns of the samples for different holding time.

comparison with the standard PDF card, it can be seen that the main crystal phase of the p1 sample corresponding to the first crystallization peak on the DSC curve is $Bi_{12}SiO_{20}$, and the minor phase is SiO_2; the main crystal phase of the p2 sample corresponding to the second crystallization peak is Bi_2SiO_5, the secondary crystal phase is $Bi_{12}SiO_{20}$; the main crystal phase of the p3 sample corresponding to the third crystallization peak is $Bi_4Si_3O_{12}$. The results show that the base glass is amorphous, and a diffuse diffraction peak appears in the spectrum. The peak position corresponds to the characteristic peaks of the other three main crystal phases, indicating that there is a short-range ordered structure in the glass, which is considered to be the basis for the separation of the glass [2, 8].

Zhereb et al. divided the liquid state range of the equilibrium diagram of the Bi_2O_3-SiO_2 system into three temperature zones: low-temperature region A, medium-temperature zone B, and high-temperature zone C [3, 5, 10, 11]. Zhereb et al. [5, 12–14] argue that the main crystal phase precipitated in the low-temperature zone A is $Bi_{12}SiO_{20}$, the main crystal phase precipitated in the medium-temperature zone B is Bi_2SiO_5, and the main crystal phase precipitated in the low temperature zone C is $Bi_4Si_3O_{12}$. The abovementioned experimental results are consistent with the conclusions given by Zhereb et al.

1.4. Estimation of thermodynamic properties of Bi$_2$O$_3$-SiO$_2$ melt

At present, no report has been found which focuses on the thermodynamic properties of Bi$_2$SiO$_5$ and Bi$_{12}$SiO$_{20}$. Therefore, it is necessary to estimate the required unknown data for the analysis.

1. c_p:

The heat capacity of the solid compound can be approximated as the weighted sum of the solid atomic heat capacity.

$$c = \sum n_i c_i \tag{1}$$

where n_i is the number of i atoms in the compound molecule; and c_i is the atomic heat capacity of the i atom. The atomic heat capacities of Bi, Si and O are shown in **Table 2**.

According to Eq. (1) and **Table 2**, we can calculate that:

$$
\begin{aligned}
c_p(\text{ Bi}_2\text{SiO}_5) &= 2 \times c_p(\text{Bi}) + c_p(\text{Si}) + 5 \times c_p(\text{O}) \\
&= (2 \times 3.6 + 6.4 + 5 \times 4.0) \text{ cal g}^{-1}\text{ K}^{-1} \\
&= 33.6 \text{ cal g}^{-1}\text{ K}^{-1} = 140.64 \text{ J g}^{-1}\text{ K}^{-1}
\end{aligned}
$$

$$
\begin{aligned}
c_p(\text{ Bi}_{12}\text{SiO}_{20}) &= 12 \times c_p(\text{Bi}) + c_p(\text{Si}) + 20 \times c_p(\text{O}) \\
&= (12 \times 3.6 + 6.4 + 20 \times 4.0) \text{ cal g}^{-1}\text{ K}^{-1} \\
&= 129.6 \text{ cal g}^{-1}\text{ K}^{-1} = 542.5 \text{ J g}^{-1}\text{ K}^{-1}
\end{aligned}
$$

From the abovementioned calculation, we know that the c_p of solid Bi$_2$SiO$_5$ is 33.6 cal g^{-1} K^{-1} (140.64 J g^{-1} K^{-1}).

Generally, the specific heat of the liquid material is 0.4–0.5 cal g^{-1} K^{-1}, and the material with high specific heat can be taken as large. For example, the specific heat of water can be approximately 1 cal g^{-1} K^{-1}. Therefore, the liquid Bi$_2$SiO$_5$ and Bi$_{12}$SiO$_{20}$ c are taken as 1 cal g K, that is, 4.186 J g^{-1} K^{-1}.

2. ΔH_{fus}

Beijing Institute of Nonferrous Metals Research and Beijing University of Science and Technology Department of Physics and Chemistry jointly proposed to use binary phase diagram calculation system to get the thermodynamic properties [15, 16]. Biostatic equilibrium phase diagram of Bi$_2$O$_3$-SiO$_2$ system can be seen in **Figure 4**. It can be seen that the metastable phase

Atom	Bi	Si	O
c_i	3.6	6.4	4.0

Table 2. Atomic heat capacity (cal·g^{-1}·K^{-1}).

diagram is more complex, including a peritectic reaction and a eutectic reaction. The reaction of precipitating crystals from the liquidus is:

$$A\,(L) + B(L) = C(S) \tag{2}$$

The coefficients of A and B are denoted as p and q. At the beginning of the reaction, the liquid phase composition can be expressed as $\zeta_A + \zeta_B$, at this time $\zeta_C = 0$. At the end of the reaction, $\zeta'_A = \zeta_A - p\zeta_C$, $\zeta'_B = 0$, $\zeta'_C = \zeta_C$. $x_A = \zeta_A/(\zeta_A + \zeta_B)$, $x_B = \zeta_B/(\zeta_A + \zeta_B)$; $x'_A = (\zeta_A - p\,\zeta_C)/[\zeta_A-(p-1)\,\zeta_C]$. Then, we can get, $x_c = \zeta_B/[q\,\zeta_A-(p-1)\,\zeta_B]$, So $x_c/x_B = 1/[q-(p+q-1)\,x_B]$.

Then, through further calculations, the following equation can be obtained:

$$\frac{dx_c}{dT} = \frac{(p+q)^2}{q}\,\frac{dx}{dT}$$

$$\Delta H_{fus} = \frac{-RT_f^2}{p/(p+q)^2}\,\frac{dT}{dx_B^l} \tag{3}$$

where R is the gas constant.

The following equation can be obtained by calculated from Eq. (3):

$$\Delta H_{fus}(\mathrm{Bi_2SiO_5}) = \frac{1}{4}\left(-8.314 \times 845^2\right) \times \frac{(-1.5)}{526} = 69.716\ \mathrm{kJ\ g^{-1}}$$

$$\Delta H_{fus}(\mathrm{Bi_{12}SiO_{20}}) = \frac{6}{49}\left(-8.314 \times 900^2\right) \times \frac{(-1.402)}{2856} = 26.995\ \mathrm{kJ\ g^{-1}}$$

So, $\Delta H_{fus}\ (\mathrm{Bi_2SiO_5}) = 69.716\ \mathrm{kJ\ g^{-1}}$, $\Delta H_{fus}\ (\mathrm{Bi_{12}SiO_{20}}) = 26.995\ \mathrm{kJ\ g^{-1}}$.

1.5. Crystallization thermodynamics of Bi$_2$SiO$_5$ and Bi$_{12}$SiO$_{20}$ in Bi$_2$O$_3$-SiO$_2$ system

The thermodynamic theory shows that under isothermal pressure:

$$\Delta G = \Delta H - T\Delta S \tag{4}$$

when $\Delta G = 0$, $\Delta H - T\Delta S = 0$,

$$\Delta S = \Delta H/T_0 \tag{5}$$

where T_0 is the equilibrium temperature of the phase change.

If there is a phase change under unbalanced condition of any temperature T,

$$\Delta H - T\Delta S \neq 0 \tag{6}$$

If ΔH and ΔS do not change with temperature, the following equation can be obtained by taking Eq. (5) into Eq. (6):

$$\Delta G = \Delta H - T\frac{\Delta H}{T_0} = \Delta H \frac{T_0 - T}{T_0} = \Delta H \frac{\Delta T}{T_0}. \tag{7}$$

From Eq. (7), it can be seen that only when $\Delta G < 0$ ($\Delta H \Delta T/T < 0$), the phase change will occur spontaneously. When the phase change is a crystallization exothermic process, $\Delta H < 0$ ($\Delta T > 0$), T_0-T < 0. This indicates that the system must be subcooled during the crystallization process.

In this chapter, the enthalpy and entropy change of the crystallization process are calculated at the equilibrium temperature of the system. The enthalpy change and entropy change of the crystallization process are calculated by the irreversible process [17]. Where T is the actual phase transition temperature, T is the equilibrium temperature of the phase change
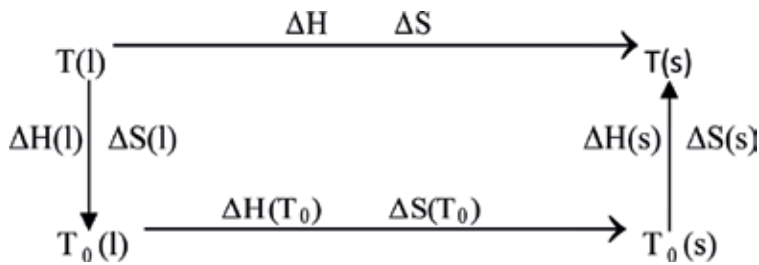
According to this process,

$$\Delta S = \Delta S(l) + \Delta S(s) + \Delta S(T_0) \tag{8}$$

$$\Delta H = \Delta H(l) + \Delta H(s) + \Delta H(T_0) \tag{9}$$

$$\Delta S(l) = \int_T^{T_0} \frac{C_p(l)}{T} dT \tag{10}$$

$$\Delta S(s) = \int_{T_0}^T \frac{C_p(S)}{T} dT \tag{11}$$

$$\Delta S(T_0) = \frac{-\Delta_{fus} H(T_0)}{T_0} \tag{12}$$

$$\Delta H(l) = \int_T^{T_0} c_p(l) dT \tag{13}$$

$$\Delta H(s) = \int_{T_0}^T c_p(s) dT \tag{14}$$

$$\Delta H(T_0) = -\Delta_{fus} H(T_0) \tag{15}$$

T_0 for Bi$_2$SiO$_5$ is obtained from the phase diagram at 845°C, 1118.15 K. Substituting the T_0, c_p, ΔH_{fus} of Bi$_2$SiO$_5$ into Eqs. (8)–(15) are calculated as follows:

$$\Delta S(\text{Bi}_2\text{SiO}_5) = \Delta S(l) + \Delta S(s) + \Delta S(T_0) = \int_T^{T_0} \frac{c_p(l)}{T}dT + \int_{T_0}^T \frac{c_p(s)}{T}dT - \frac{\Delta_{fus}H(T_0)}{T_0} \tag{16}$$

$$\Delta S(\text{Bi}_2\text{SiO}_5) = (140.64 - 4.186) \times (\ln T - \ln 1118.15) - \frac{69.716 \times 10^3}{1118.15}$$

$$\Delta S(\text{Bi}_2\text{SiO}_5) = 136.454 \ln T - 1020.18 \tag{17}$$

$$\Delta H(\text{Bi}_2\text{SiO}_5) = \Delta H(l) + \Delta H(s) + \Delta H(T_0)$$

$$= \int_T^{T_0} c_p(l)dT + \int_{T_0}^T c_p(s)dT - \Delta_{fus}H(T_0)$$

$$\Delta H(\text{Bi}_2\text{SiO}_5) = (140.64 - 4.186) \times (T - 1118.15) - 69.716 \times 10^3$$

$$\Delta H(\text{Bi}_2\text{SiO}_5) = 136.454\,T - 222292.04$$

The above calculated ΔS and ΔH are taken into Eq. (7), $\Delta T = 145$ K, $\Delta G = -7.478$ kJ < 0. This indicates that the process of precipitating Bi_2SiO_5 from the base glass can be carried out spontaneously when the temperature $T = T_0\text{-}\Delta T = 973.15$ K.

The same method is used to calculate $\text{Bi}_{12}\text{SiO}_{20}$, and T for $\text{Bi}_{12}\text{SiO}_{20}$ was obtained from the phase diagram at $900°$C, that is, 1173.15 K:

$$\Delta S(\text{Bi}_{12}\text{SiO}_{20}\text{Bi}_{12}\text{SiO}_{20}) = \Delta S(l) + \Delta S(s) + \Delta S(T_0) = \int_T^{T_0} \frac{c_p(l)}{T}dT + \int_{T_0}^T \frac{c_p(s)}{T}dT - \frac{\Delta_{fus}H(T_0)}{T_0} \tag{18}$$

$$\Delta S(\text{Bi}_{12}\text{SiO}_{20}) = (542.50 - 4.186) \times (\ln T - \ln 1173.15) - \frac{26.995 \times 10^3}{1173.15} \Delta S(\text{Bi}_{12}\text{SiO}_{20})$$

$$= 538.314 \ln T - 3804.506 \quad \Delta H(\text{Bi}_{12}\text{SiO}_{20}) = \Delta H(l) + \Delta H(s) + \Delta H(T_0) \tag{19}$$

$$= \int_T^{T_0} c_p(l)dT + \int_{T_0}^T c_p(s)dT - \Delta_{fus}H(T_0)$$

$$\Delta H(\text{Bi}_{12}\text{SiO}_{20}) = (538.314 - 4.186) \times (T - 1173.15) - 26.995 \times 10^3$$

$$\Delta H(\text{Bi}_{12}\text{SiO}_{20}) = 1538.314\,T - 658518.069$$

The above calculated ΔS and ΔH are taken into Eq. (7), $\Delta T = 300$ K, $\Delta G = -29.579$ kJ < 0. This indicates that the process of precipitating $\text{Bi}_{12}\text{SiO}_{20}$ from the base glass can be carried out spontaneously when the temperature $T = T_0\text{-}\Delta T = 873.15$ K.

It should be noted that, in the abovementioned analysis, c and ΔH values are all estimated. T_0 is obtained from the phase diagram, but the phase diagram of the system has not been fully analyzed, The liquidus in the figure cannot be completely determined, so T_0 and the actual value may also have some error. The calculated value in this chapter can only be used to qualitatively determine how spontaneous the crystallization process is at a certain temperature, not for the precise calculation of crystallization temperature.

1.6. Bi$_2$O$_3$-SiO$_2$ (Bi$_2$O$_3$:SiO$_2$ = 1:1) system glass non-isothermal crystallization kinetics

1.6.1. Crystallization kinetics

Crystallization activation energy E and crystal growth index n are two important parameters to research the crystallization kinetics of glass. The process where glass gradually transforms into the crystal state needs a certain activation energy to overcome the structural rearrangement barrier. The higher is the potential barrier, the greater is the activation energy. Therefore, to a certain extent, the crystallization activation energy reflects the degree of crystallization ability. The crystal growth index n can reflect the nucleation and growth mechanism during the crystallization process.

1.6.2. Crystallization activation energy

In non-isothermal transition, the exothermic peak temperature T_p of the glass on the DSC curve is affected by the heating rate β. When the heating rate is slow, the transition time is sufficient and the process can be carried out at lower temperature, so T_p is lower, and the instantaneous transition rate is small, and the crystallization peak is gentle; when the heating rate is faster, the exothermic peak temperature T_p is correspondingly increased, the instantaneous transition rate is large, and the crystallization peak is sharper [18]. In this chapter, the DSC curves of the samples at the heating rates 5, 10, 15, and 20°C/min were measured. The Kissinger and Ozawa methods were used to calculate the crystallization activation.

(1) Kissinger method to calculate the crystallization activation energy

The kinetics of glass crystallization by DSC method is based on the Johnson-Mehl-Avrami (JMA) equation. Assuming that the reaction mechanism function is f(x) = (1-x)^n, the corresponding equation is:

$$\frac{dx}{dt} = K(1-x)^n \tag{20}$$

where n is the reaction order, that is, the crystal growth index, x the phase transition fraction, and K the crystallization rate constant.

The reaction rate constant K follows the Arrhenius relation [19]:

$$K = K_0^{-E/RT} \tag{21}$$

where K_0 is the effective frequency factor, E the crystallization activation energy, R the gas constant, and T the absolute temperature.

By the JMA equation, the glass non-isothermal crystallization kinetics can be expressed by the Kissinger Equation [18–20]:

$$\ln\left[\frac{T_p^2}{\beta}\right] = \frac{E}{RT_p} + \ln\left[\frac{E}{R}\right] - \ln K_0 \tag{22}$$

where T_p is the crystallization temperature of the DSC curve and β is the heating rate.

The DSC curves of the Bi_2O_3-SiO_2 system glass at different heating rates are shown in **Table 3**.

According to the Kissinger equation, $\ln(T_p \beta)$ and $1/T_p$ is plotted and linearly fitted to obtain the slope E/R. **Figure 8** shows the $\ln(T_p/\beta)$-1/T relationship for the Bi_2O_3-SiO_2 system glass.

From **Figure 8**, the activation energies of the three crystals precipitated in the Bi_2O_3-SiO_2 system glass are: E_{p1} = 150.6 kJ/mol, E_{p2} = 474.9 kJ/mol, and E_{p3} = 340.3 kJ/mol.

(2) Ozawa method to calculate the crystallization activation energy

The Ozawa equation for non-isothermal crystallization of glass can be expressed as:

$$\ln\beta = \frac{-E}{RT_p} + C \tag{23}$$

where E is the crystallization activation energy, T_p the DSC curve crystallization exothermic peak temperature, and C is a constant related to the reaction mechanism function.

A graph of $\ln\beta$ versus $1/T_p$ is made (**Figure 9**), and a straight line with slope of E/R can be obtained. Then we can calculate the crystal activation energy E.

Heating rate (°C/min)	5	10	15	20
Crystalline peak temperature (°C)	547.2	564.0	586.8	593.4
	653.7	659.0	669.3	672.3
	785.2	793.0	812.3	818.1

Table 3. The DSC crystallization peak temperature of Bi_2O_3-SiO_2 system at different heating rates.
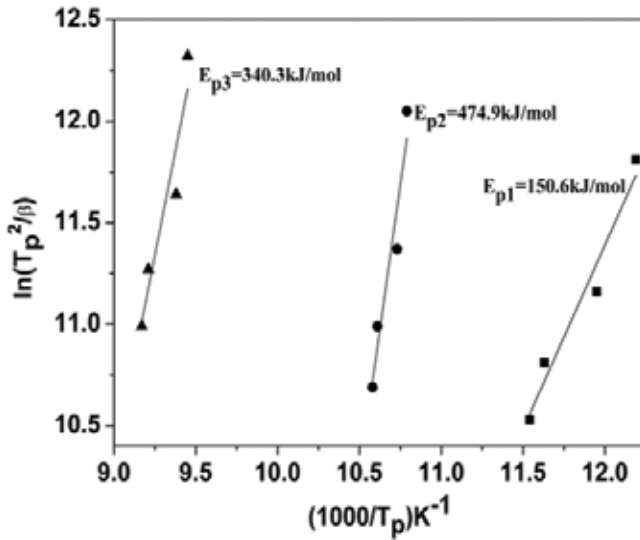
Figure 8. $\ln(T_p^2/\beta)$-1/T_p diagram of Bi_2O_3-SiO_2 glass-ceramics.
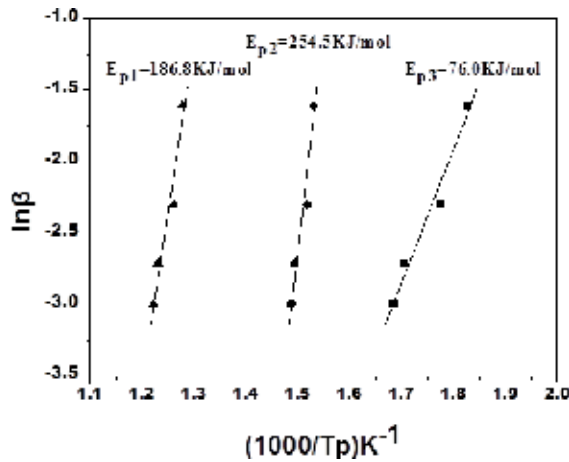
Figure 9. lnβ-1/T_p diagram of Bi$_2$O$_3$-SiO$_2$ glass-ceramics.

From **Figure 9**, the activation energies of the three crystals precipitated in the glass of Bi$_2$O$_3$-SiO$_2$ system are: E$_{p1}$ = 76.0 kJ/mol, E$_{p2}$ = 254.5 kJ/mol, and E$_{p3}$ = 186.8 kJ/mol.

Although the Kissinger method and the Ozawa method generate different activation energy values, the trend is the same. It can be seen that the crystallization ability of Bi$_{12}$SiO$_{20}$ corresponding to the first crystallization peak (in the low temperature region A) is the strongest, the crystallization ability of the second crystal-forming peak (in the middle-temperature region B) is the weakest, and the crystallization ability of the third crystal-forming peak (in the high-temperature region C) is between the first two peaks.

1.6.3. Crystal growth index

Under the condition that the crystallization activation energy has been determined by the Kissinger method, the crystal growth index n can be obtained by the Augis-Bennett Equation [21, 22]:

$$n = \frac{2.5}{\Delta T} \times \frac{RT_p}{E} \tag{24}$$

where ΔT is the temperature at which the DSC is exothermic at half maximum.

According to the theory of solid phase transition, when n = 4, the way of crystal growth is volumetric nucleation and growth is in three-dimensional space; when n = 3, the way of crystal growth is volumetric nucleation and growth is in two-dimensional space; when n = 2, the way of crystal growth is volumetric nucleation and growth is in one-dimensional direction; when n = 1, the way of crystal growth is surface nucleation, crystals grow in one-dimensional direction on the surface [21, 22].

Table 4 shows the crystal growth indices of the three crystals precipitated in the glass of Bi$_2$O$_3$-SiO$_2$ system at different heating rates. The average growth indices of the three crystals precipitated by the Bi$_2$O$_3$-SiO$_2$ system were $\overline{n}_{p1}$ = 2.5, $\overline{n}_{p2}$ = 2.1, $\overline{n}_{p3}$ = 2.2.

Sample No	Heating rate/(K·min^{-1})				Average crystal growth index
	5	10	15	20	
p1	3.1	2.9	2.1	1.9	2.5
p2	3.0	2.2	1.6	1.5	2.1
p3	2.4	2.1	2.2	2.2	2.2

Table 4. Crystallization index of BS glass-ceramics under different heating rates.

The crystal growth index n can be expressed as

$$n = a + bc \tag{25}$$

where *a* corresponds to the nucleation rate, and when *a* = 0, the nucleation rate is zero; when *a* > 1, the nucleation rate increases; when *a* < 0, the nucleation rate decreases. *b* reflects the crystallization mechanism, *b* = 0.5, indicating that the crystallization by the diffusion mechanism control; *b* = 1, the crystallization by the interface control. *C* represents the grain growth dimension and *c* = 1, 2, and 3 represent one-dimensional, two-dimensional and three-dimensional growth, respectively.

As we can see, C = 1, b = 0.5, a > 1; therefore, the value of *a* is the smallest when the crystallization temperature is in the middle temperature region B, and the value of n is shown in **Table 4**. When the crystallization temperature is in the low-temperature zone A, the value of *a* is the largest. This is consistent with the crystallization ability of the three crystal phases. In the process of melting of Bi_2O_3-SiO_2 system glass, the phase separation occurs, which leads to the emergence of new phase boundary, which in turn provides favorable nucleation sites for nucleation. Therefore, the crystallization process is mainly controlled by diffusion.

The abovementioned analysis shows that the way of Bi_2O_3-SiO_2 glass system crystallization is volumetric nucleation and growth is in one-dimensional space. The crystallization process is mainly affected by diffusion, and the nucleation rate is the highest when the crystallization temperature is in the low-temperature zone A and the lowest when the crystallization temperature is in the medium-temperature zone B.

2. Summary

1. Bi_2O_3-SiO_2 system glass and metastable crystal Bi_2SiO_5 were prepared by high-temperature melt cooling method. During the heat treatment, three main crystal phases were produced in this order: $Bi_{12}SiO_{20}$, Bi_2SiO_5, and $Bi_4Si_3O_{12}$. There are three distinct crystallization exotherms in the DSC curve.

2. The crystallization kinetics of $Bi_{12}SiO_{20}$ and Bi_2SiO_5 were calculated and analyzed. The results show that the crystallization process can be carried out spontaneously at 873 and 973 K, respectively.

3. The Kissinger equation was used to calculate the crystallization activation energy of the base glass and the results are E_{p1} = 150.6 kJ/mol, E_{p2} = 474.9 kJ/mol, and E_{p3} = 340.3 kJ/mol. The Ozawa equation was used to calculate the crystallization activation energy of the base glass and the results are E_{p1} = 76.0 kJ/mol, E_{p2} = 254.5 kJ/mol, and E_{p3} = 186.8 kJ/mol. The calculation results of the two methods show that the crystal phase Bi$_{12}$SiO$_{20}$ in the low-temperature zone A has the strongest crystallization ability and the crystal phase Bi$_2$SiO$_5$ in the medium-temperature zone B has the weakest crystallization ability. The average crystallization index of three kinds of crystals was calculated by Augis-Bennett equation and the results are $\bar{n}_{p1}$ = 2.5, $\bar{n}_{p2}$ = 2.1, and $\bar{n}_{p3}$ = 2.2, respectively. The crystallization process is mainly affected by diffusion.

Author details

Hongwei Guo[1,2]*

*Address all correspondence to: 03guohongwei@163.com; guohongwei@sust.edu.cn

1 Glass Physics and Chemistry, China Electronic Glass Association, China

2 Shaanxi University of Science and Technology, Material Science and Engineering Academy, Xian, China

References

[1] Chen SS. Fusible Glass. China Building Industry Press; 1975:31-60

[2] Nie CS. Practical Glass Components. Tianjin Science and Technology Press; 2001:424-428

[3] Zhereb VP, Skorivo VM. Metastable states in bismuth-containing oxide systems [J]. Inorganic Materials. 2003;**39**(2):121-145

[4] Pastukhov EA, Istomin SA, Belousova NV, et al. Physicochemical properties of Bi$_2$O$_3$-Fe$_2$O$_3$ and Bi$_2$O$_3$-V$_2$O$_5$ melts. Rasplavy. 2000;**1**:8-13

[5] Zhereb VP, Skorivo VM. Metastable states in bismuth-containing oxides systems. Inorganic Materials. 2003;**39**(2):25-121

[6] Fei YD, Fan SJ. Research progress of phase relationship and behaviors of Bi$_2$O$_3$-SiO$_2$ system. Journal of Inorganic Materials. 1997;**l2**(4):469-476

[7] Fei YD, Fan SJ, Sun RY. Phase diagram of Bi$_2$O$_3$-SiO$_2$ system. Journal of Inorganic Materials. 1998;**13**(6):798-802

[8] Hu ZQ. Inorganic Materials Science Basic Tutorial. Chemical Industry Press. 2004;**232**:84-86

[9] Zhao YZ, Yin HR. Glass Technology. Chemical Industry Press. 2006;**64**(61):9-10

[10] 刘超, 张昌龙, 周卫宁, Liu C, Zhang CL, Zhou WN. Hydrothermal method to generate colorless BSO crystals. Journal of Synthetic Crystals. 2009;**38**(2):291-295

[11] Cai MQ, Yin Z, Zhang MS, et al. First-principles study of ferroelectric and nonlinear optical property in bismuth titanate. Chemical Physics Letters. 2005;**401**(4-6):405-409

[12] Zhereb VP, F Kargin Y, Skorikov VM. Structural model of Bi_2O_3-AO_2 (a= Si, Ge) melts, Izv. Akad. Nauk SSSR, Neorganicheskie Materialy. 1978;**14**(11):2029-2031

[13] Zhereb VP. Physicochemical study of metastable range phase equilibrium in the systems Bi_2O_3-AO_2 (A=Si, Ge, Ti). Cand. Sci. (Chem.) Dissertation, Moscow: Kurnakov Institute of General and Inorganic Chemistry, Russian Academy of Sciences; 1980

[14] Zhereb VP, Skorivo VM. Effect of metastable phases on the structural perfection of single crystals of stable bismuth oxide compounds. Inorganic Materials. 2003;**39**(11):1365-1372

[15] QB Wang, GY Guo. Liquid and solid matter heat capacity estimation and simple determination method [J]. Contemporary chemical industry. 1985;(4):21-24

[16] Sun GR, Li WC. Prediction of rare earth oxide heat of fusion by binary phase diagram. Chinese Journal of Rare Earths. 1991;**9**(2):117-121

[17] Wang ZL, Zhou YP. Physical Chemistry. Higher Education Press; 2001. 120-122

[18] Lu JS, Dong W. Crystallization dynamics and heat treatment process of LiAlSi based transparent glass [J]. Journal of Nanchang Hangkong University. 2009;**23**(3):5-12

[19] Kissinger HE. Reaction kinetics in differential thermal analysis [J]. Analytical Chemistry. 1957;**29**(11):1702-1706

[20] Lu JS, Dong W. Crystallization behavior and properties of ternary nucleating agent Li_2O-Al_2O_3-SiO_2 system glass. Functional Materials. 2006;**37**(2):156-159

[21] Augis JA, Bennett JE. Calculation of the avrami parameters for heterogeneous solid state reaction using a modification of the Kissinger method. The Journal of Analysis. 1978;**13**:283-292

[22] Yin HR, Lv CZ, Li H. Phase transformation kinetics of LAS transparent glass—Ceramic with zero phosphorus expansion [J]. Functional Materials. 2009;**40**(1):92-96

Advances in Glass Technology

Optical Glass: A High-Tech Base Material as Key Enabler for Photonics

Uwe Petzold

Abstract

Optical glass is the base material for the fabrication of spherical lenses, aspheres, prisms, beam splitters, optical fibers, axicons, or other optical components. The photonic industry relies on such components and so on optical glass. Photonics is a key enabling technology for many market segments and applications. The requirements for optical glass are the highest transmission and tight tolerances of not only the optical properties such as refraction and dispersion but also the mechanical properties such as sufficient size and low stress content. In order to achieve the above mentioned specification, a sophisticated melting technology, hot forming processes, annealing procedure, and measurement devices are required. This chapter discusses the most relevant information of these processes.

Keywords: optical glass, photonic, index of refraction, abbe number, refractometer, homogeneity

1. Introduction

Photonics is a key enabling technology for many market segments and applications. This becomes visible by looking on current trends like [1–3]:

- Augmented and virtual reality for consumer and even more relevant for industrial applications.

- Assisting systems in automotive as rear/side view cameras, LED/laser lighting, lidar, night vision support, head-up displays, etc.

- Industry 4.0 with connected individual productions and substitution of humans in mechanical and electric production lines by robots requires exact three-dimensional imaging, object recognition, bar code scanning, quality inspection, distance control, and absolute optical measurements.

- Continuous development of displays with higher resolutions or trends like "internet of things" needs lithographic production lines with accurate positioning that relies on interferometric measurement and recording devices with precisely imaging objectives.

- Enlarged usage of laser technology for cutting, engraving, or welding.

- Use of cameras for security and defense applications or in drones.

- Three-dimensional printing requires also three-dimensional imaging.

Due to these trends, the overall optics and photonics market will grow significantly above 600 billion USD until 2020 (see **Figure 1**). Taking their relevance on further products and services into account, its impact is even bigger.

All these photonic products have in common that they rely on optical glass. Optical glass is the raw material for the fabrication of spherical lenses, aspheres, prisms, beam splitters, optical fibers, axicons, or other optical components (see **Figure 2**).

Optical engineers use components out of various optical glasses to optimize their designs concerning resolution, aberrations, stray light, etc. Such applications take advantage of the essential combination of material features of optical glass like high light transmission, large variety but also precise light deflection (index of refraction and dispersion), high uniformity of light deflection, and sufficient environmental resistance.

Today, most of the optical glasses are melted in continuous tank technology. In order to melt optical glass, it is essential to keep the process parameter like composition and temperatures within tight tolerances and further control the optical features like refractive index and Abbe
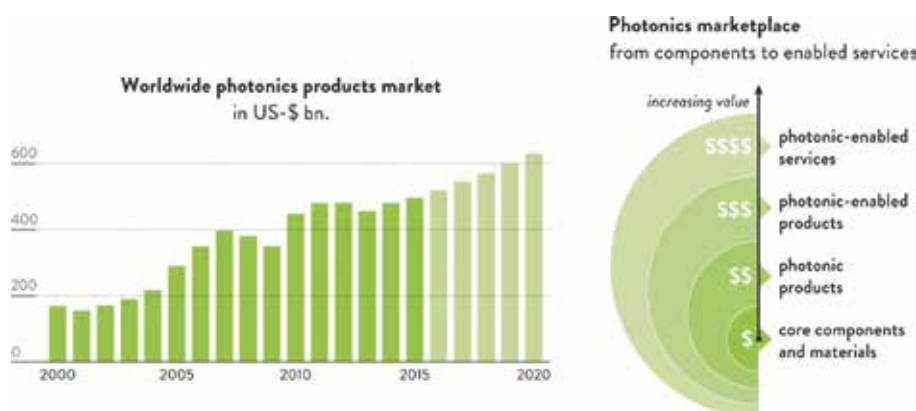
Figure 1. Development of the global market size of photonic products (left). The impact on the global economy is due to products and services that rely on photonic products significantly bigger as indicated by the right diagram [4].

Figure 2. Fabricated optical components out of raw strips and blocks of optical glass (left) [5]. Profile of a digital single-lens reflex camera (Leica S) showing several components made of optical glass (right) [6].

number in adequate loops. Right after the casting, an annealing lehr cools down the glass to avoid cracks due to mechanical stress caused by temperature gradient between inner and outer parts of the glass. This process is called coarse annealing. The composition of the glass defines the first three digits of the refractive index, but even simple optical designs require more precise refraction values. The velocity of the annealing process has an influence on the internal structure of the glass matrix and so on the optical properties. Therefore, an additional fine annealing procedure defines the final optical features. This is necessary because applications like interferometric measurements are sensitive to variations in the sixth digit of the index of refraction. While the melting of the optical glass takes in the order of magnitude of 1 day, the fine annealing procedure could take from several days (small dimensions) up to several months (large dimensions). Cold processing steps like sawing, cutting, grinding, lapping, and polishing convert the fine annealed raw glass into the required optical components to enable the optical functionalities as described above.

This chapter provides a brief overview about the variety of optical glasses and their production procedure including melting, coarse, and fine annealing. Further, the author introduces the definition of the Abbe number. This value describes the dispersion and defines together with the refractive index the optical position. The Abbe diagram depicts the optical position of various optical glasses. This diagram explains the naming conventions of optical glasses. Finally, the measurement techniques in an industrial environment for the main properties of optical glasses are explained.

2. What is optical glass?

Glass has many unique properties. For each application mentioned in this book, the supplying industry breeds special glass types with adapted features to serve the requirements of their application. The most obvious feature of optical glass for a human eye is the high transparency as indicated in **Figure 3**. Compared to window glass, the optical path in optical glass is more than 30 times longer for achieving the same transmission, which is a huge difference.
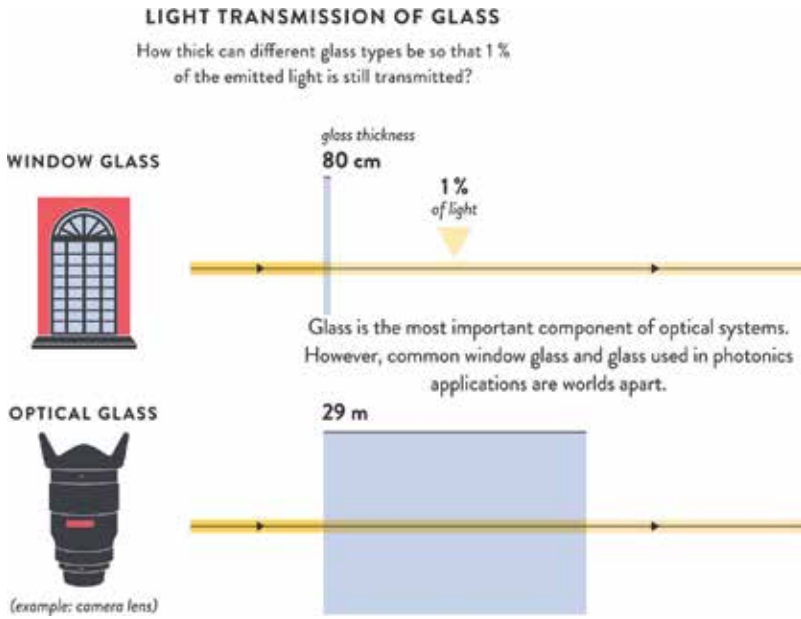
Figure 3. Comparison of the light transmission through window glass and optical glass [4].

In order to achieve such high grades of transmission, the requirements on the purity of the ingredients, the haze level, the number of bubbles, and the inclusions are significantly stronger than for window glass. **Figure 4** shows the internal transmittance over the visible spectrum and the near-infrared regime.
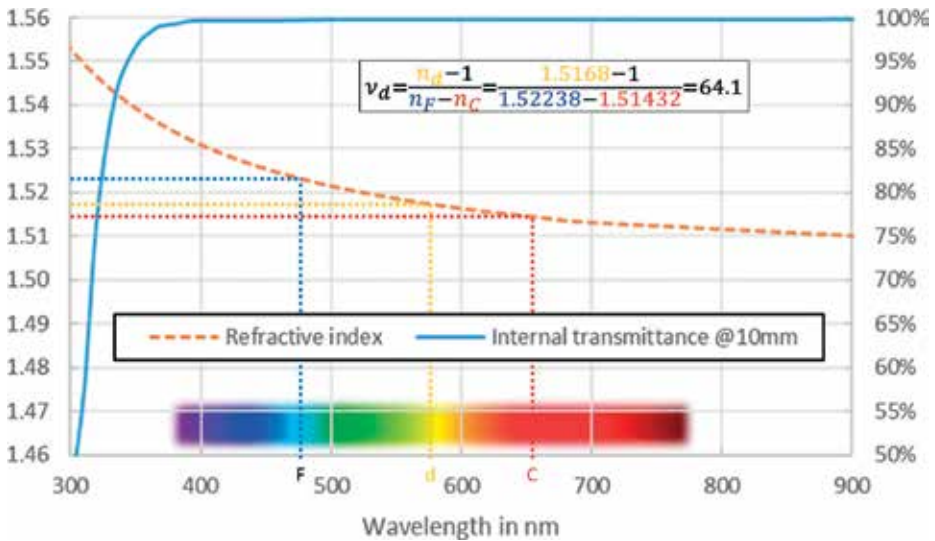
Figure 4. Spectral development of the internal transmittance and refractive index of an optical glass (e.g., SCHOTT N-BK7®). (Data taken from [7]).

In contrast to the transmission, the optical position of an optical glass is not obvious for a human eye. Hereby, the refractive index at a specific wavelength and the Abbe number describing the dispersion define the optical position.

The graphic in **Figure 4** shows the decrease of the refractive index starting from the ultraviolet over the visible spectrum to the near-infrared regime. Dispersion is the name of this spectral refractive index development. The Abbe number v_d as defined in the upper box of **Figure 4** is a measure for the dispersion. The value n_d at the d-line (587.5618 nm) is typically the reference for the refractive index. These two values n_d and v_d define the optical position and exhibit the main distinctive features of optical glass types.

This dispersion is one of the main reasons why we need optical glasses and high sophisticated lens systems for the photonic products at all. If a single lens focuses a blue light ray (e.g., the F-line at 486.1327 nm) and a red light ray (e.g., the C-line at 656.2725 nm), both rays experience different deflections due to the varying refractive index. Therefore, the focus position of both colors differs. If an optical designer combines a flint and a crown glass lens in a proper way, the designer achieves that the focus of the blue and the red ray overlaps. This doublet is an achromatic system. Unfortunately, the focus position of other colors still varies. Therefore, a further chromatic correction and other aberrations require a complex multi-lens design as depicted in **Figures 5** and **2** (right) [8]. Such lens system design relies on a broad portfolio of optical glass that spread widely in their optical position.

Figure 6 shows a n_d– v_d diagram, also called Abbe diagram. This diagram maps the different optical glass types by using the refractive index and Abbe number as coordinates. The left part of the diagram corresponding to high Abbe numbers contains the crown glasses indicated with the letter "K" in the end. The right part of the diagram corresponding to low Abbe numbers contains the flint glasses as indicated with the letter "F" in the end. Besides the rough differentiation between crowns and flints, the map shows further areas of similar chemical composition, e.g., the region of barium flints with the label "BAF" or the area of lanthanum crowns with the label "LAK" [9]. According to their position in the diagram, the glasses get their labels, e.g., F2 is located in the "F" regime. The number at the very end of the glass-type label is without any further information and counts of the developments in the relevant area (seldom followed by a letter indicating a new version). The prefix "N-" indicates that no lead and arsenic are contained in the glass [8]. Then, the prefix "P-" types are special

Figure 5. Exploded view on a lens system consisting of 10 different lenses made of different optical glass types. This depicts the complexity of such setups [5].
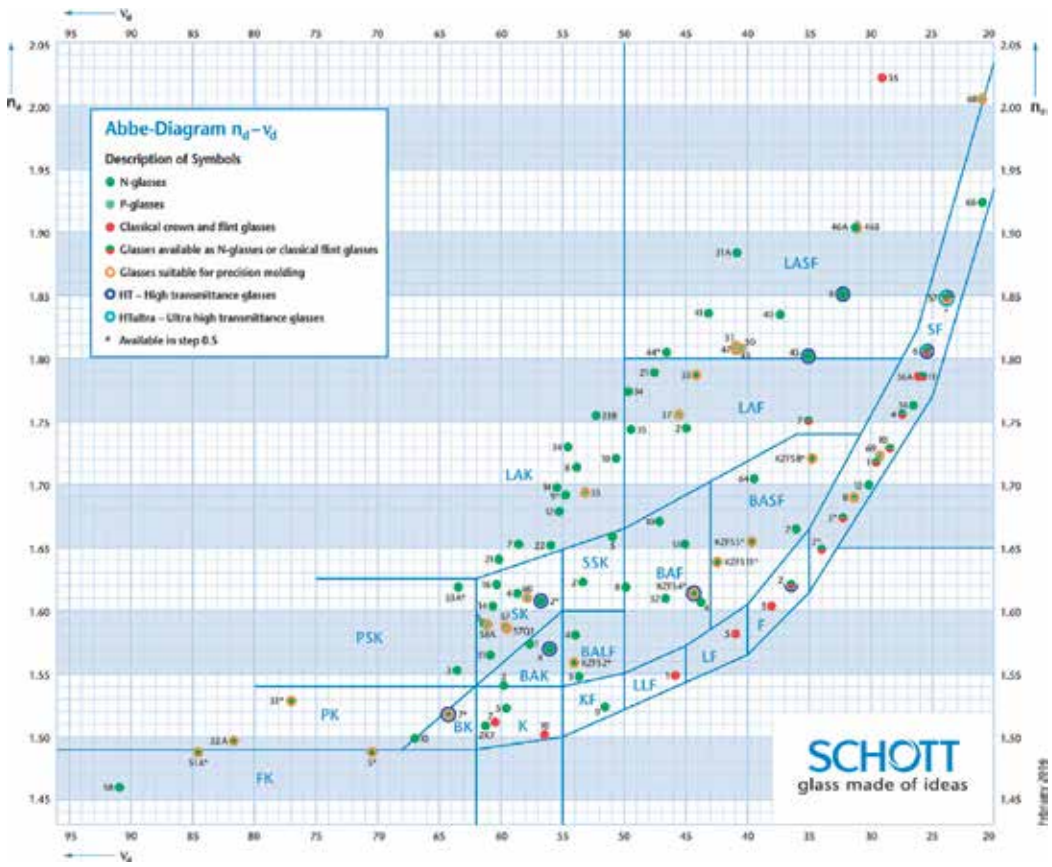
Figure 6. The $n_d - v_d$ diagram, also called Abbe diagram, displaying the optical position of the various glass types [11].

glasses that are environment friendly as well but additionally show a low transformation temperature to enable precise molding process [10]. Finally, the suffix "HT" or "HTultra" defines special versions of the glass type with high or even ultrahigh transmittance. All explanations are valid for the optical glass manufacturer SCHOTT as a reference but are in general transferable to other manufactures as well.

3. Production of optical glass

In earlier days, optical glass manufacturer filled pots with the ingredients of the optical glass composition, melted the raw material, reduced the bubble content by refining processes, mixed the liquid composition, casted the glass, and filled up the pot again [12]. The state-of-the-art method is to melt glass in a continuous process in a tank production. **Figure 7** shows a sketch of such a tank. Compared to other glass industries mentioned in this book, the optical glass production is rather tiny. Seldom, the overall volume inside such tank exceeds more than 5 tons.
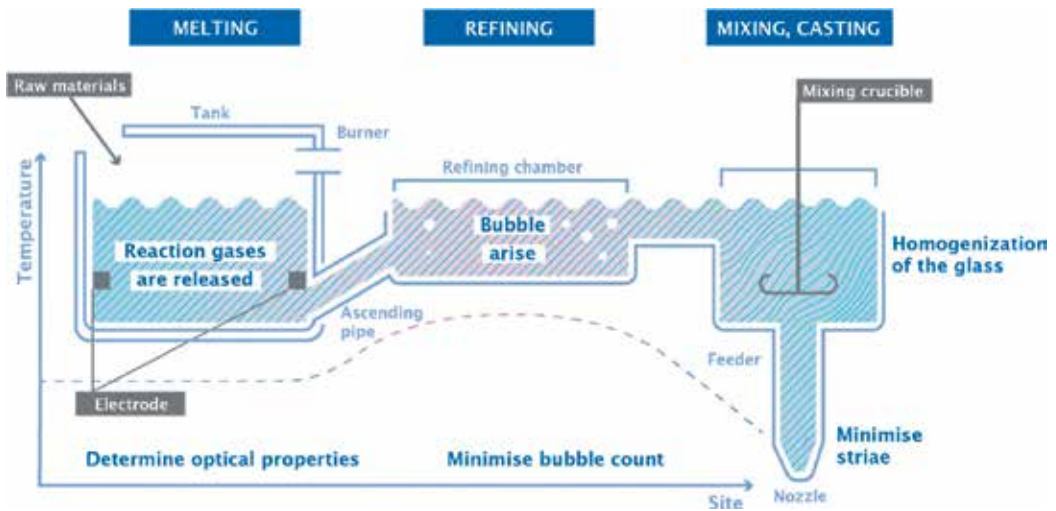
Figure 7. Sketch of a melting tank for optical glasses including the spatial temperature profile. The overall time consumption from the raw material melting to the casting takes several hours (with courtesy of SCHOTT).

A glass manufacturer feeds continuously the ingredients into the melting chamber. Gas burners and electrodes heat up and finally melt the ingredients. The picture in **Figure 8** shows some still solid raw material on the liquid surface in the melting chamber.

The melted material contains some bubbles due to residual air inside the raw material and due to chemical reactions between the ingredients. Just driven by convection, the liquefied material flows into the neighboring refining chamber. The increased temperature in the refining chamber leads to growing gas bubbles and so to a larger buoyancy. Additionally, the higher temperature, the reduced viscosity of the melt supports this upthrust, and the gas bubbles vanish. Afterward, the melted material flows into the mixing chamber. A mechanical stirrer homogenizes the melt by rotational motion. The decreased temperature in the mixing chamber and feeder increases the
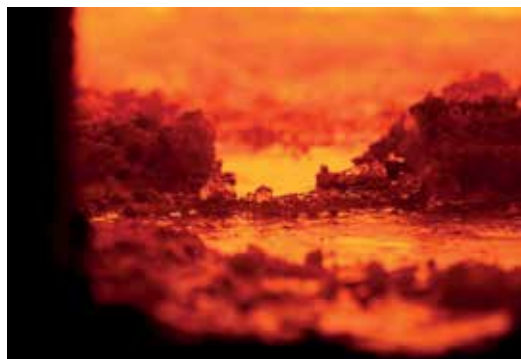
Figure 8. View inside the melting chamber with some still solid raw material on the surface of the melted material (with courtesy of SCHOTT).

viscosity of the melt in order to enable a proper hot forming during the casting. Typically, glass manufacturer produces an endless strip (width ~160 mm, height ~40 mm); sometimes the glass manufacturer uses molds to produce one block after another (length ~200 mm, width ~200 mm, height ~200 mm). **Figure 9** shows the hot forming process of a strip production. The glass is not yet frozen and still glowing red due to black body radiation.

As glass has a rather low heat conductivity (~ 1 W/(m × K)), a fast cooling process results in a high value of stress. The outer part is already frozen, but the inner part of a strip is still liquid. So, the volume change during the freezing of the inner part cannot be compensated by the already solid outer part. If this stress exceeds a certain threshold, some cracks or breakage occurs. With increasing thickness of a strip, this risk of damage rises. Therefore, a controlled cooling process is necessary for optical glass. An annealing lehr of several meter lengths after the casting minimizes the risk of damage. At the hot end of the annealing lehr has a similar temperature as the feeder and at the other end a few hundred degrees. **Figure 10** shows a view through such an annealing lehr with an endless strip of optical glass inside.

After the coarse annealing in the lehr, the glass manufacturer breaks or saws the glass strip into manageable length depending on the final application. Actually, the annealing rate has a significant impact on the optical position of the glass. Controlling the chemical composition tightly is mandatory to hit the target values of the refractive index and the Abbe number. The order of magnitude of the accuracy required is 10^{-4} to 10^{-6} in the refractive index depending on the application. By keeping the chemical composition constant, the glass manufacturer can control the refractive index within an accuracy of 10^{-3} to 10^{-4}. The annealing velocity influences the internal glass structure and so the optical features. The fine adjustment of the refractive index takes place in the so-called fine annealing. Therefore, ovens heat up each piece of glass again. At a target temperature around the glass-type specific transformation temperature, the stress inside the glass relaxes. By cooling the glass with a constant rate, the glass manufacturer can control the refractive index with the required precision of 10^{-4} and 10^{-6}. **Figure 11** shows the influence of the annealing rate on the optical position. The red cross in the center of the diagram corresponds to the target value that is mentioned, e.g., in a catalog or a data sheet [5, 9]. The figure also contains the preferred tolerance steps for refractive index and Abbe number from ISO 12123 that specifies raw optical glass (bluish boxes) [14].
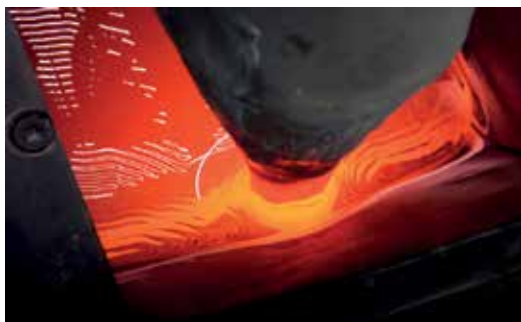
Figure 9. Hot forming process to produce an endless strip of width 160 mm and height 40 mm. The still liquid glass is glowing due to the black body radiation [13].

Figure 10. View through an annealing lehr of roughly 12 m length that cools down the endless strip slowly to avoid stress and cracks. This procedure takes several hours (with courtesy of SCHOTT).
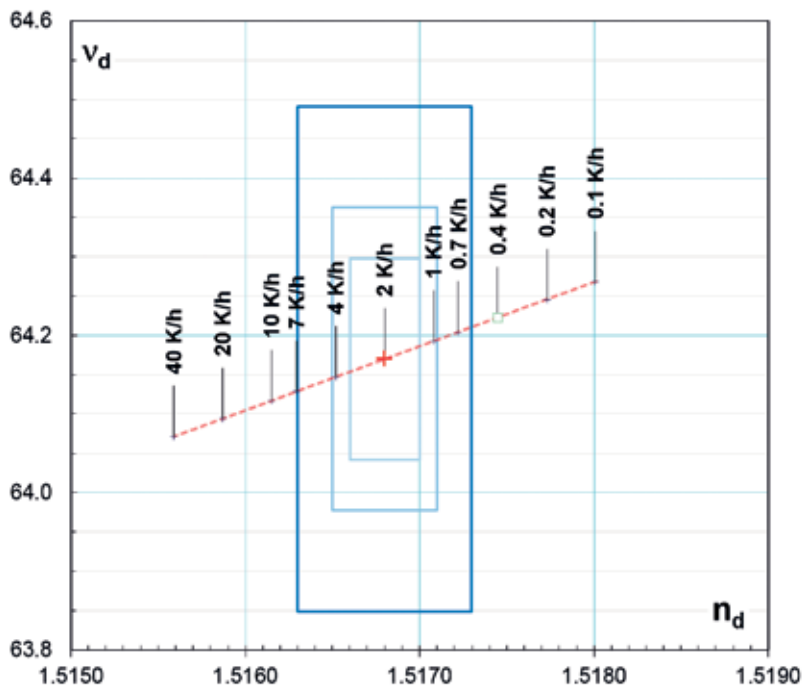
Figure 11. Close-up of v_d − n_d diagram that indicates the required precision and the impact of the annealing rate on the optical position. Data shows SCHOTT N-BK7® based on data taken from [15].

The green square depicts a piece of glass, which was annealed with a cooling rate of 0.4 K/h. Obviously, the optical position is not within the accepted maximum tolerance range (dark blue box). This piece of glass could be annealed again (reversible process) with a higher annealing rate along the annealing line inside the tolerance range [12]. So, the refractive index

and Abbe number are fine-tuned by the annealing process. In this example, an annealing with 2 K/h would adapt the optical position to the target value. The printed annealing line is constant for a specific glass type but differs significantly from one glass type to another. Unfortunately, there are boundaries to the annealing rate. Below a glass-type specific annealing rate, the piece of glass tends to crystallize, which would lead to significant haze. Above a certain threshold, which depends on the glass type and the smallest dimension, stress birefringence gets significant. In general, glass is an isotropic media so there is no preferred direction inside the glass system. Nevertheless, if the glass is annealed with a high cooling rate, the inner and the outer parts of a glass blank experience a different temperature gradient (low heat conductivity ~1 W/(m × K)). This leads to mechanical stress. This mechanical stress leads to a preferred direction and so to a refractive index that depends on the polarization orientation of the transmitted light. This effect is called stress-induced birefringence or in short stress birefringence. Besides the mechanical stress, the spatially different temperature rates also influence the regional refractive index (see **Figure 11**). The homogeneity is the feature that summarizes the result of stress birefringence and regional refractive index variation. An interferometer measures the grade of the homogeneity. Therefore, a plane wave travels through the plane-parallel polished glass blank and overlaps afterward with an undisturbed plane wave. The space-resolved intensity distribution depicts the two-dimensional wave front distortion in false color illustration caused by the glass blank (see, e.g., **Figure 12**).

The maximum difference of the wave front distortion divided by the blank thickness (peak-to-valley value PV = 0.47×10^{-6}) defines the homogeneity grade. The tightest homogeneity tolerance in ISO 12123 is a peak-to-valley value below 10^{-6}, which is roughly four times smaller than the width of the green square in **Figure 11**. Especially for larger dimensions, this requires a very sophisticated technology of tight controlling of the chemistry and the hot forming process to avoid bubbles, inclusion, or striae. Further, experienced knowledge of the fine annealing procedure to reduce stress birefringence and regional refractive index variation to a minimum is necessary.

Typically, a V-block refractometer measures the optical position of the optical glass in order to monitor an accurate production [17]. **Figure 13** schematically illustrates the underlying principle.

The glass manufacturer prepares out of the produced and annealed glass a cuboidal sample with dimensions of about $20 \times 20 \times 5$ mm^3. This sample fits in a V-shaped glass block with a precisely known refractive index $n_{V-block}$. An immersion oil between the V-block and the sample decreases the surface quality requirements to the scale of 1 mm in flatness. The glass manufacturer measures the deflection angle θ from optical axis of a light ray that propagates through the setup as depicted in **Figure 13**. The refractive index of the sample n_{sample} for the color of the light ray (wavelength λ) results to [18]

$$n_{sample}^2 = n_{V-block}^2 - n_{air} \cdot \sin(\theta) \cdot \sqrt{n_{V-block} - n_{air} \cdot \sin^2(\theta)} \qquad (1)$$

with the refractive index of the surrounding air n_{air}. Although the accuracy of this method is lower than for the minimum angle deviation method [19], the V-block refractometer is the much faster and cheaper approach. Therefore, the V-block refractometer is the ideal tool to monitor the quality of an optical glass production economically.
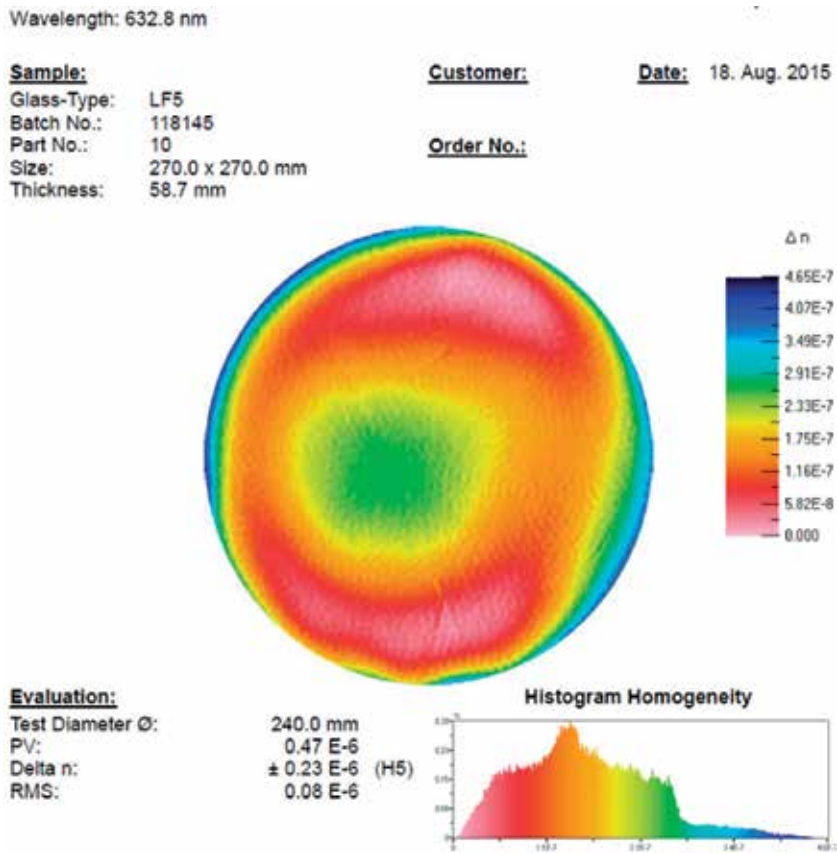
Figure 12. False color illustration of an interferometric wave front distortion of a round LF5 glass blank [16].
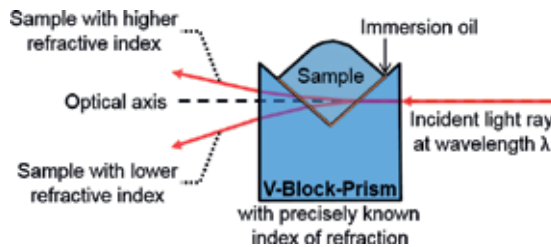
Figure 13. Sketch of the principal setup of a V-block refractometer [17].

Even though the manufacture of optical glass is volume wise, the smallest production of all the productions that are mentioned in this book, it has a significant impact on almost all industries. As indicated in the introduction due to a broad variety of market trends, the worth of this key enabling product is still increasing. On the other hand, only a few companies globally still master the rather complex and highly sophisticated production of optical glass that requires a lot of knowledge and experience [20].

4. Conclusion

Even though optical glass is a base material with quite some history, it will remain a relevant key enabler for the entire photonic industry. As the market for photonics is globally rising over almost all market segments, also the demand for optical glass will increase. High sophisticated optical systems require a broad variety of glass types with tight tolerance of the optical position and high transmission. Such tough requirements need an elaborated melting, annealing, and measurement technology.

Since the late nineteenth century, optical glass manufacturer develop optical glasses. A comparison of the $n_d - v_d$ diagrams of the various optical glass manufacturers shows rather similar portfolios. The optical glass development is limited, e.g., by the relation of refractive index and dispersion (Kramers-Kronig relation) [21]. Therefore, the author expects that the landscape of optical glasses will not change significantly in the future. However, a modified landscape is not necessary as the optical designers in general already have a sufficient portfolio of optical glass types to work with.

The various new market trends and segments like augmented or virtual reality, industry 4.0, autonomous driving, robotic and display development, laser material processing, and 3D printing will evolve quickly with slightly adapted requirements. The outlook for the overall optical glass landscape is therefore that the optical glass manufacturer will marginally improve their portfolio with segment-specific variants of their current portfolio concerning optical positions, low density, high transmittance, high chemical resistance, and extreme thermal behavior.

Author details

Uwe Petzold

Address all correspondence to: uwe.petzold@mail.de

SCHOTT AG, Mainz, Germany

References

[1] VDMA Photonics Forum. Photonics in Germany – Industry Report 2017 [Internet]. 2017. Available from: https://photonik.vdma.org/documents/433966/18769673/VDMA_Photonik-Branchenreport-2017_final_1499938258930.pdf/131364ff-5093-450c-b964-0d8a1820923c [Accessed: Aug 27, 2017]

[2] VDMA Photonics Forum. Photonics in Germany 2017 [Internet]. 2017. Available from: https://photonik.vdma.org/documents/433966/16497924/1492084139120_Photonics%25202017%2520Web.pdf/6b708878-8276-4603-ac7f-966649fdccaa [Accessed: Aug 27, 2017]

[3]   Photonics21 – European Technology Platform. Market Research Study – Photonics 2017 [Internet]. 2017. Available from: http://www.photonics21.org/download/Brochures/Photonics21_Market-Research-Report_charts-second-edition.pdf [Accessed: Aug 27, 2017]

[4]   SPIE & SPECTARIS. Photonics – Technical applications of light [Internet]. 2016. Available from: https://spie.org/Documents/Membership/SPECTARIS_Photonics.pdf [Accessed: Aug 27, 2017]

[5]   SCHOTT AG. Optical Glass 2016 [Internet]. 2016. Available from: https://www.google.de/url?sa=t&rct=j&q=&esrc=s&source=web&cd=2&cad=rja&uact=8&ved=0ahUKEwiY7LmQ6PbVAhVInBoKHQKDA54QFggtMAE&url=http%3A%2F%2Fwww.schott.com%2Fd%2Fadvanced_optics%2Fc36214d9-13c4-468c-bf40-8d438b89f532%2F1.5%2Fschott-optical-glass-pocket-catalog-february-2016-row.pdf&usg=AFQjCNGrby9YGiYmeFvrgxxV9bg8i4gGBQ [Accessed: Aug 27, 2017]

[6]   Leica Camera AG. Leica S-System [Internet]. 2015. Available from: https://de.leica-camera.com/content/download/128506/1601366/version/2/file/Leica+S-System+Catalogue_EN_2015.pdf [Accessed: Aug 27, 2017]

[7]   SCHOTT AG. Optical Glass – Data Sheets [Internet]. 2017. Available from: http://www.schott.com/d/advanced_optics/ac85c64c-60a0-4113-a9df-23ee1be20428/1.1/schott-optical-glass-collection-datasheets-english-17012017.pdf [Accessed: Aug 27, 2017]

[8]   Edmund Optics. Optical Theory Simplified: 9 Fundamentals to Becoming an Optical Genius [Internet]. 2015. Available from: https://www.google.de/url?sa=t&rct=j&q=&esrc=s&source=web&cd=1&cad=rja&uact=8&ved=0ahUKEwiP2aXV5_bVAhXJBBoKHY_EDiMQFggqMAA&url=https%3A%2F%2Fwww.edmundoptics.com%2Fdocument%2Fdownload%2F396295&usg=AFQjCNEijGlCL5yxY7KKUc0Na5oYpoal1g [Accessed: Aug 27, 2017]

[9]   Hartmann P. Optical Glass. 1st ed. Bellingham, Washington, USA: SPIE Press; 2014. 183 p

[10] SCHOTT AG. TIE-40 Optical Glass for Precision Molding [Internet]. 2011. Available from: http://www.schott.com/d/advanced_optics/218a11e2-3bd6-4818-919f-c9cc9b00a1d8/1.1/schott_tie-40_optical_glass_for_precision_molding_us.pdf [Accessed: Aug 27, 2017]

[11] SCHOTT AG. SCHOTT Abbe Diagram Nd Vd [Internet]. 2016. Available from: http://www.schott.com/d/advanced_optics/0387ab58-e80d-4b4d-aa02-324f4bef4c98/1.0/schott-abbe-diagram-nd-vd-february-2016-en.pdf [Accessed: Aug 27, 2017]

[12] Jedamzik R, Reichel S, Hartmann P. Optical Glass with tightest refractive index and dispersion tolerances for high-end optical designs. In: Digonnet MJF, Jiang S, editors. Proc. SPIE 8982, Optical Components and Materials XI, 89821F; Mar 7, 2014. San Francisco CA, USA: SPIE; 2014. DOI: 10.1117/12.2035973

[13] SCHOTT AG. Advanced Optics Goes E-Commerce [Internet]. 2017. Available from: http://www.schott.com/advanced_optics/english/knowledge-center/advanced-optics-live/eshop-trailer.html [Accessed: Aug 27, 2017]

[14] International Organization for Standardization. Optics and Photonics – Specification of Raw Optical Glass [Internet]. 2010. Available from: https://www.iso.org/standard/45848.html [Accessed: Aug 27, 2017]

[15] SCHOTT AG. TIE-29 Refractive Index and Dispersion [Internet]. 2016. Available from: https://www.google.de/url?sa=t&rct=j&q=&esrc=s&source=web&cd=1&cad=rja&uact=8&ved=0ahUKEwj5lLHD6_bVAhVDSRoKHfdOBSEQFggpMAA&url=http%3A%2F%2Fwww.schott.com%2Fd%2Fadvanced_optics%2F02ffdb0d-00a6-408f-84a5-19de56652849%2F1.0%2Ftie_29_refractive_index_and_dispersion_eng.pdf&usg=AFQjCNFGA9IkumI2dahrwflzXzYn7yxIJQ [Accessed: Aug 27, 2017]

[16] Hartmann P. Optical lead flint glasses: Key material in optics since centuries and in future. In: Proceedings of Optical Systems Design 2015: Optical Design and Engineering VI. Vol. 9626. Sep 23, 2015; Jena, Germany: SPIE; 2015. DOI: 10.1117/12.2190326

[17] Petzold U, Jedamzik R, Reichel S, Hartmann P. V-block refractometer for monitoring the production of optical glasses. In: Proc. SPIE 9628, Optical Systems Design 2015: Optical Fabrication, Testing, and Metrology V, 962811; Sep 24, 2015; Jena, Germany: SPIE; 2015. DOI: 10.1117/12.2191218

[18] Pixton BM, Greivenkamp JE. Automated measurement of the refractive index of fluids. Applied Optics. 2008;**47**(10):1504-1509

[19] Tentori D, Lerma JR. Refractometry by minimum deviation: Accuracy analysis. Optical Engineering. 1990;**29**(2):160-168

[20] Hartmann P. Optical glass: Past and future of a key enabling material. Advanced Optical Technologies. 2012;**1**:5-10

[21] Fotheringham U, Baltes A, Fischer P, Höhn P, Jedamzik R, Schenk C, Stolz C, Westenberger G. Refractive index drop observed after precision Molding of optical elements: A quantitative understanding based on the tool–Narayanaswamy–Moynihan model. Journal of the American Ceramic Society. 2008;**91**(3):780-783

Nonsilica Oxide Glass Fiber Laser Sources: Part I

Daniel Milanese, Joris Lousteau, Xiushan Zhu,

Arturo Chavez-Pirson, Diego Pugliese,

Nadia Giovanna Boetti and Nasser Peyghambarian

Additional information is available at the end of the chapter

Abstract

Nonsilica oxide glasses have been developed and studied for many years as promising alternatives to the most used silica glass for the development of optical fiber lasers with unique features and properties. Depending on the glass former of choice, these glasses can offer very distinctive physical properties if compared to silica-based glasses. With regard to the development of photonic fiber devices, these key properties include low phonon energy, high rare-earth ion solubility, high optical nonlinearity and easy handling procedures. This chapter, part I of a detailed study concerning nonsilica oxide glass–based optical fiber laser sources, reviews the main properties of three different nonsilica oxide glass families, namely phosphate, germanate and tellurite. The manufacturing process of an optical fiber using these glass materials is also discussed in Section 3 of this chapter.

Keywords: nonsilica oxide glass, phosphate glass, germanate glass, tellurite glass, rare-earth–doped optical fiber, fiber laser, built-in-casting, suction casting, rod-in-tube, rotational casting

1. Introduction

Inorganic glasses have been playing a key role in the development of optical devices and instruments, thanks to the unique combination of different properties: they are transparent in the visible region, mechanically stiff and resistant, chemically durable and can be easily manufactured into different highly homogenous forms and sizes. Starting from ancient times, transparent glasses were fabricated to make windows and goblets, then later, thanks to the improvement in the glass manufacture brought about by Venetian masters in the Middle Age, stable glass compositions were processed into eyeglasses, lenses and mirrors. High-quality

optical glasses became key player materials for the fabrication of lenses for telescopes and microscopes, thus enabling tremendous development of modern science [1]. Finally, long haul optical fiber–based backbone networks are based on extremely pure and low loss glasses, which then are enabling materials for the internet revolution [2, 3].

Due to their outstanding ultra-low propagation loss and intrinsic thermomechanical properties, silica-based glasses have been the material of choice for most optical fiber–related applications. As passive media, they were crucial in allowing the deployment of long haul fiber networks and found applications even as nonlinear frequency conversion fiber laser sources, despite the low intrinsic nonlinearity of silica. When doped with rare-earth (RE) ions, they have been used for fiber lasers and amplifiers with outstanding performance in the near-infrared wavelength region [4].

Despite its success, however, silica glass possesses several intrinsic limits:

1. The high phonon energy of silica glass around 1100 cm^{-1} [5] permits to exploit only a restricted range of the possible emission wavelengths offered by RE ions. Silica glass fibers have proved to be outstanding for the development of 1, 1.5 and 2 μm laser sources, but numerous applications require alternative wavelengths, in particular in the mid-infrared (mid-IR) wavelength region.

2. The RE doping concentration level is limited in silica glass [6]: both the nature of the silica glass network and the doping process itself limit the doping concentration achievable. Thus, silica glass cannot be used to develop short-length devices that are required for a single-frequency fiber laser and for the development of low-nonlinearity booster amplifier for high peak power lasers.

3. Additionally, the short infrared transmission edge of silica glasses restricts their use for numerous high-impact applications, such as mid-IR laser, chemical sensing and infrared imaging [7].

The so-called soft glasses are based on alternative glass formers exhibiting different nature and structure, which offer alternative phonon energies and transmission characteristics, high RE ion doping levels (up to 10^{21} ions/cm^3) and high optical nonlinearity (orders of magnitude higher than that exhibited by silica glass). Soft glasses include oxide and nonoxide glasses. Nonoxide glass compositions of great interest for laser emission in the mid-IR wavelength region are mainly based on fluoride [8] and chalcogenide [9, 10] glass formers. They provide a wide transmission window extending up to the mid-IR well above 2 μm, but their low chemical stability and poor mechanical properties have so far strongly limited their use for devices in harsh environment. Oxide glasses, although exhibiting shorter wavelength range of operation in the infrared, are suitable for the integration with commercial fiber–based components and demonstrated reliability for the incorporation in operational environment.

In this chapter, we present a detailed overview of the most promising oxide-based soft glass systems, namely phosphate, germanate and tellurite, together with the fabrication of fibers based on these glass families. The synthesis and individual physical properties of these glasses are presented in Section 2 to identify their prospect and range of applications. The engineering

techniques used to manufacture optical fiber preforms out of these glasses and the fiber drawing are then discussed in Section 3.

2. Nonsilica oxide glasses

Engineering a glass for a specific photonic application requires the knowledge of some key parameters that enable its use. In reviewing the main oxide glass system alternative to silica-based compositions, we will focus on the following properties: solubility of RE ions, chemical durability, thermal stability, mechanical reliability, ease of fabrication, fiber drawing ability, nonlinearity and phonon energy. This last property is less familiar outside the community of glass scientists working on active materials for lasers. In studying a suitable material for coherent sources in the mid-IR, a particular effort is required to design hosts that minimize their interaction with the electronic transitions of the ions leading to the emission of photons. High phonon energy glasses cause the decay from an excited state to a lower state to occur via nonradiative emission of heat, in the form of phonons, thus decreasing the overall efficiency of the laser emission [4]. In this section, these properties of phosphate, germanate and tellurite glasses are reviewed.

Table 1 lists the main physical properties of the phosphate, germanate and tellurite glasses reviewed in this chapter and their values compared with silica-based glass [11–18].

2.1. Synthesis of nonsilica oxide glasses

The synthesis of silica glass has been subjected to continuous evolution, with the aim of reducing the causes of extrinsic absorption due to the presence of impurities, namely transition

Glass system	Silica	Phosphate	Germanate	Tellurite
Transmission range (μm)	0.2–2.5	0.2–4.3	0.3–4.0	0.4–5.0
Maximum phonon energy (cm^{-1})	1100	1200	975	800
Glass transition temperature (°C)	1200	400–550	400–450	300–350
Thermal conductivity (Wm^{-1} K^{-1})	1.38	0.57	0.70	1.25
Expansion coefficient (10^{-6}/K)	0.55	13.40	8–11	12–17
Density (g/cm^3)	2.2	2.6	3 ÷ 7.2	5.5
Young's modulus (GPa)	70	47	65	33.6
Refractive index @1.55 μm	1.45	1.56	1.63	1.8–2.3
Abbe number	80	44–82	15–41	10–20
Nonlinear refractive index (m^2/W)	10^{-20}	10^{-20}	10^{-20}	2.5×10^{-19}
Fiber loss (dB/Km)	0.2 @ 1.55 μm	1.5×10^3 @ 1.05 μm	1.2×10^3 @ 1.2 μm	200 @ 1.2 μm
RE solubility (ions/cm^3)	10^{19}	10^{21}	10^{21}	10^{21}

Table 1. Main properties of nonsilica oxide glass systems.

metal ions and water. This led to the development of chemical vapor deposition methods: these synthesis routes utilize chemical precursors in vapor phase as starting reagents, which are transformed into the final oxide components by reaction with oxygen at very high temperatures. These techniques allowed the fabrication of optical fibers capable of providing <0.2 dB/km ultra-low loss in the third telecom window.

Chemical precursors involved in the synthesis of multicomponent nonsilica oxide glasses have very distinct vapor pressures, making high-purity vapor-based fabrication techniques unsuitable for this type of glass compositions. Instead, traditional glass melting techniques must be implemented. Chemical precursors are weighed and batched into a crucible typically made of alumina, silica or a noble metal such as Pt or Au. The glass batch is then melted in a high-temperature furnace for few hours under controlled atmosphere. Typical melting temperatures for the glasses under consideration in this chapter are 800, 1200 and 1300°C for tellurite, germanate and phosphate glasses, respectively. Because of the corrosive nature of some of the chemical precursors involved, this melt casting process leads to an inevitable degree of optical contamination, both related to the initial purity of the chemical precursors but also to possible cross-contamination occurring through the whole preparation process. Crucible material is of prime importance, as some degree of dissolution in the glass can occur during the melting process [19]. Although the final glass material produced through this process does not compete with the purity of standard silica glass preform, yet optical losses below 100 dB/km are readily achievable under meticulous and clean melting conditions.

Moreover, the melt casting process provides the advantage that the glass can be easily shaped using adequate casting mold geometry. This feature is largely exploited when preparing multicomponent glass preforms, as discussed in the following paragraphs.

2.2. Phosphate glasses

Pure phosphate glasses have not been historically as popular as silicate glasses, because of their poor chemical stability and mechanical properties [20], which, however, could be significantly improved by the addition of proper modifier and intermediate ions [21, 22]. Phosphate glasses were mainly used for HF-resistant glasses and for other niche applications [20]. Later on, research works on phosphate glasses were stimulated by the wide range of potential and commercial applications of these materials, from the treatment of hard-water [23] to biomedicine [24] and for the storage of radioactive wastes [25].

Optical quality phosphate glasses, initially developed by Schott and coworkers, were of interest also for their UV transparency [26], but found no significant applications due to their poor stability. However, the need of a suitable gain medium for high-peak power lasers such as the one developed within the framework of the inertial confinement fusion (ICF) research led to a resurge in their employment, after careful engineering of the compositions [27].

2.2.1. Structure

The basic units that constitute the phosphate glass are the P-tetrahedra, with a central phosphorous atom surrounded by four oxygen atoms. These are connected through bridging

oxygen (BO) atoms to give different phosphate anions. The tetrahedra are classified using the Q^i terminology [28], where 'i' represents the number of tetrahedra linked to the unit (shown schematically in **Figure 1**).

Depending on the oxygen to phosphorous ratio, phosphate glasses can be classified into a series of subcategories, from ultra-phosphate (O/P ≤ 3) to ortho-phosphate (O/P = 4).

The O/P ratio in vitreous phosphate (v-P_2O_5) is derived from the stoichiometry of the pure compound and it is equal to 2.5. The basic unit of the structure of the v-P_2O_5 is the Q^3 tetrahedron, which has three covalent bonds via BO atoms with the neighbor tetrahedra and a terminal shorter bond via nonbridging oxygen (NBO) atoms.

The structural strength and chemical durability of the optical phosphate glass can be improved by adding appropriate components, as described in several patents and papers [29–31]. Metal oxides added to v-P_2O_5 can improve the physical properties and chemical stability of the system. In more detail, alkali metal oxides R_2O (R = Li, Na, K, Rb and Cs) can be added to the glass to increase the RE solubility [32]. Network intermediates R_2O_3 (R = B and/or Al) are also added in phosphate glasses to improve their chemical durability and mechanical properties and to decrease the solubility in water. If the amount of R_2O_3 is too low, the glass is water soluble, while if the amount of R_2O_3 is too high, an increase in the glass transition temperature (T_g) and the crystallization temperature occurs [33]. In particular, even a small addition of R_2O_3 can significantly improve the mechanical properties of the phosphate glass. This is due to the particular behavior of R^{3+} ions that can have both tetrahedral and trigonal coordination [33–35]. The presence of alkali-earth oxide MO (M = Mg, Ca, Ba, Sr and Zn) in the glass prevents the devitrification and improves the chemical durability [35]. When the amount of MO is too low, the glass is hygroscopic and has poor chemical durability and poor optical quality; when the amount of MO is too high, the glass tends to devitrify [29].

In conclusion, the addition of various dopants, such as alumina, alkali and earth-alkali oxides, was demonstrated to reinforce the phosphate glass network. Moreover, when RE ions were added, the glasses proved to be suitable materials for lasers, showing an interesting combination of low nonlinear refractive index and high optical gain.

2.2.2. Phosphate glasses as laser material

Phosphate glasses doped with Nd^{3+} ions have proved suitable for the fabrication of large monolithic active material sections constituting the high-peak power laser at Lawrence
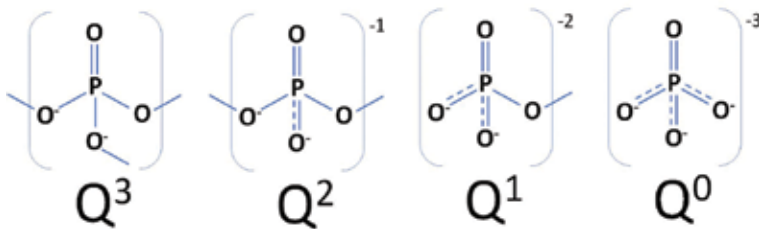
Figure 1. Types of tetrahedral sites occurring in phosphate glasses depending on their composition.

Livermore Laboratories and in other laser ignition facility infrastructures around the world [27]. This was possible by developing compositions with high durability, which displayed a high-emission cross-section, low nonlinear refractive index and high energy storage and extraction characteristics [36]. Besides, phosphate glasses, with respect to silicate glasses, can be fabricated free of Pt inclusions, which may cause catastrophic damage to the optical active material [37].

More recently, the development of high-peak pulsed optical amplifiers asked for materials able to incorporate high amounts of RE ions, and phosphate glasses became an ideal candidate since up to 10^{21} ions/cm^3 of RE can be accommodated without clustering effects [38]. This is important for pulsed optical amplifiers, where nonlinear optical effects must be minimized: phosphate glass allows reducing the length of the amplifier with respect to the silica counterpart. In addition, phosphate glasses are also less susceptible than silica to photodarkening [39] and display cross-sections.

Finally, their mechanical reliability allows the integration of phosphate fibers with commercial silica fibers through cleaving and arc fusion splicing [40].

Phosphate glasses used for lasers in the eye-safe wavelength region usually incorporate erbium (Er^{3+}) as activator ion, with emission centered at around 1550 nm corresponding to the radiative decay from the $^4I_{13/2}$ excited state to the ground state $^4I_{15/2}$ (see **Figure 2**). Like in the case of
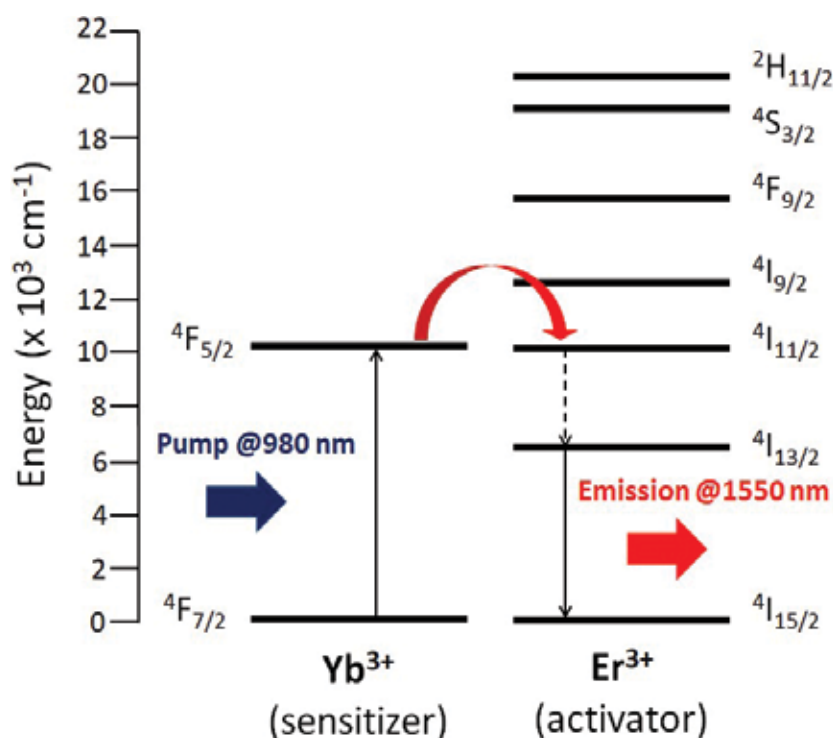
Figure 2. Energy level diagrams of Yb^{3+} and Er^{3+} ions. The main pumping mechanism of the sensitizer-activator scheme is also reported.

Nd^{3+}, also the cross-section of Er^{3+} ions in phosphate host is high: values at peak of around 7.0×10^{-21} cm^2 are reported with respect to values of around 5.5×10^{-21} cm^2 for silica [4, 41]. In order to improve the overall efficiency of the lasing process, ytterbium (Yb^{3+}) ions are often employed as sensitizer in combination with Er^{3+} ions: thanks to the superior absorption cross-section at the pump wavelength (980 nm) of these ions, the excitation from the ground state $^2F_{7/2}$ to the $^2F_{5/2}$ excited state takes place. The energy is then transferred to the $^4I_{11/2}$ excited state of erbium, which decays through the nonradiative $^4I_{11/2} \rightarrow {}^4I_{13/2}$ transition followed by the radiative transition $^4I_{13/2} \rightarrow {}^4I_{15/2}$. This energy transfer reduces the threshold of the laser emission and improves the efficiency of the device [42, 43]. The interplay between ytterbium and erbium ions is depicted in **Figure 2**. Phosphate glass represents, with respect to silica, an ideal host because its high phonon energy allows obtaining transfer efficiencies up to 95% [44].

The lifetime values of the excited state corresponding to the upper laser level provide useful indications of the population inversion ability of the emitter. A higher lifetime value is preferred because that will allow the large population inversion needed for high gain and low noise optical amplifiers. In the case of lasers, high lifetime values will permit lower pump power to reach the laser threshold, with resulting higher efficiency in laser emission and lower heat accumulation in the material. Silica, given the lower oscillator strength of the $^4I_{13/2} \rightarrow {}^4I_{15/2}$ transition, displays generally a higher lifetime value (10.80 ms) than phosphate glass (8.25 ms) [4]. However, phosphate glasses maintain high lifetime values even for high erbium concentrations: values of 7.5 ms are reported for an erbium concentration of 6×10^{20} ions/cm^3 [45].

2.3. Germanate glasses

Pure germanium oxide was obtained in its glassy state around 90 years ago [19], showing similar properties to silica in terms of mechanical strength and chemical stability, although the high cost of the raw materials did not make it an attractive alternative. However, since the Ge━O bond displays a lower energy than Si━O, germanate glasses present a shift to lower wavenumbers in their phonon energy with respect to silica from 1100 to 900 cm^{-1}, thus extending the transparency window up to 4.5 μm [46]. GeO_2 glass was thus proposed as optically transparent material alternative to silica for telecom applications, thanks to the intrinsically low attenuation at the wavelength of 2 μm [47]. Lead germanate glasses [48] were developed and studied in the view of laser beam delivery above 1.5 μm [49]. RE–doped alkali germanate glasses were explored as magneto-optic materials: Faraday angle rotation was measured, providing a linear variation of Verdet constant with the concentration of RE ions [50].

2.3.1. Structure

The structural units of pure germanium dioxide glass are GeO_4 tetrahedra. Binary alkali germanate glasses undergo a change from 4-fold Ge to 6-fold Ge (GeO_6 octahedra), with a corresponding increase in density and refractive index, which reaches a maximum at around 15 mol% of M_2O modifier. Higher values of modifier produce a progressive formation of 4-fold coordinated Ge accompanied by a gradual depolymerization of the network through an increase of nonbridging oxygens. This behavior is also known as the "germanate anomaly" [51, 52].

Lead germanate glasses are made of a mixture of 4- and 6-fold coordinated Ge, which, with increasing the doping level of lead, turns into a predominance of GeO_4 tetrahedral units.

These characteristics, together with high RE solubility, make them very interesting for the development of laser devices operating above 1.5 μm.

2.3.2. Germanate glasses as laser material

Germanate glasses, among oxide soft glasses, are the best in terms of mechanical properties, thanks to the great similarity of GeO_2 with SiO_2. Lead germanate glasses show an outstanding resistance to devitrification [53] and a wide transmission window, while offering a suitable environment for RE ions, thanks to the low phonon energy of 920 cm^{-1}.

For the above-mentioned reasons, the main studies of germanate glasses were focused on those RE ions emitting at wavelengths above 1.5 μm, namely Tm^{3+}, Ho^{3+} and Er^{3+}.

Tm^{3+} ions are of interest for the emission in the mid-IR wavelength region at around 2 μm. A maximum output power of 346 mW and a slope efficiency of 25.6% were obtained when pumping a 1 mol% Tm-doped germanate glass by a 790 nm laser diode [54]. The glass was characterized by good forming ability and chemical durability and exhibited a large emission cross-section of 8.69×10^{-21} cm^2, a high quantum efficiency of the Tm^{3+}: $^3F_4$ level of 71% and a low nonradiative relaxation rate of the $^3F_4 \to {}^3H_6$ transition of 0.09 ms^{-1}.

In view of enhancing the intensity of the 1.8 μm emission of Tm^{3+} ions, the Yb^{3+} ion codoping is commonly adopted due to the large absorption of Yb^{3+} at the diode-pumping wavelength of 980 nm. Among the interesting sensitizers, Yb^{3+} presents the advantage of displaying a simple energy level scheme, which is beneficial for obtaining large absorption and emission cross-sections and for avoiding any undesirable excited state absorption under intense pumping [55]. The radiative characteristics and spectroscopic properties of Yb^{3+}/Tm^{3+}-codoped bismuth germanate glasses with different concentrations of Yb_2O_3 were thoroughly investigated under the excitation of a conventional 980 nm laser diode [56]. The efficient sensitization of Tm^{3+} ions with Yb^{3+} ions was proved by the larger energy transfer coefficient (4.81×10^{-40} cm^6/s) and higher energy transfer efficiency (89%) from Yb^{3+} to Tm^{3+} ions. Moreover, a noticeable peak emission cross-section value of 7.66×10^{-21} cm^2 was calculated based on the emission spectrum.

It is worthwhile noting, however, that the intense upconversion emissions at 480 and 800 nm generated by the strong excited state absorption in the Tm^{3+}/Yb^{3+}-codoped glasses [57] and the lack of flexible pump sources make the sensitization of Tm^{3+} ions with Yb^{3+} ions not always advantageous. To overcome these drawbacks, transition metal (TM) Cr^{3+} ions have been successfully employed as a sensitizer for their two intensive and broad absorption bands from ultraviolet to near-infrared range, which offer a variety of selective pump wavelengths. An enhanced 1.8 μm emission band of Tm^{3+}: $^3F_4 \to {}^3H_6$ in an extremely extended excitation band of 380–900 nm was obtained in fluorogermanate glasses through strong sensitization of Cr^{3+} when pumped by an 808 nm laser diode [58]. An energy transfer efficiency from Cr^{3+} to Tm^{3+} as high as 91.10% was calculated based on experimental data, thus proving that these Cr^{3+}/Tm^{3+}-codoped fluorogermanate glasses are promising matrices for applications in near-infrared eye-safe fiber lasers and amplifiers.
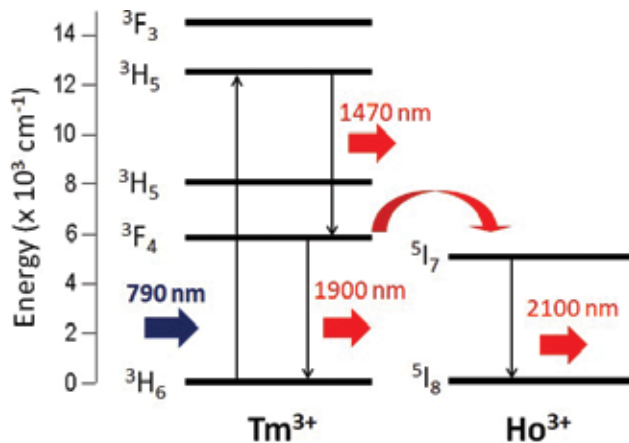
Figure 3. Energy levels of Tm^{3+} and Ho^{3+} ions of interest for the emission in the mid-IR wavelength region.

Besides Tm^{3+}, other promising RE ions in pursuit of the fabrication of high-power and efficient laser sources in the wavelength region around 2 μm are the Ho^{3+} ions. The energy levels of the two ions are reported in **Figure 3**. The emission cross-section of Ho^{3+} is about five times higher than that of Tm^{3+} and, in addition, the fluorescence lifetime of Ho^{3+} is promising in view of developing Q-switched lasers [59]. Unlike Tm^{3+}, Ho^{3+} cannot be pumped directly by using the common commercially available laser diodes operating at 808 or 980 nm for the lack of a suitable absorption band. One intriguing approach to overcome this issue consists in the sensitization of Ho^{3+} ions with other RE ions exhibiting strong absorption bands near the wavelength of existing commercial laser diodes, such as Yb^{3+}, which displays strong absorption bands near 980 nm.

The 2 μm emission properties and energy transfer processes of Ho^{3+}-doped germanate glasses sensitized by up to 12 mol% of Yb^{3+} were deeply investigated with the purpose of manufacturing a near-infrared eye-safe solid-state laser [60]. The emission cross-section of the Ho^{3+}: $^5I_7 \rightarrow \, ^5I_8$ transition near 2 μm was 8.6×10^{-21} cm^3, and the coefficient of the forward energy transfer (Yb^{3+}: $^2F_{5/2} \rightarrow Ho^{3+}$: $^5I_7$) revealed to be 19 times larger than that of the backward transfer (Yb^{3+}: $^2F_{5/2} \leftarrow Ho^{3+}$: $^5I_7$). Interestingly, the glass codoped with 5.0 mol% Yb_2O_3 and 1.0 mol% Ho_2O_3 displayed the highest gain in the 2 μm region.

The mid-infrared emission properties at around 2.85 μm in Ho^{3+}/Yb^{3+}-codoped germanate glasses characterized by a noticeably low OH^- absorption coefficient of 0.24 cm^{-1} and also by a low phonon energy equal to 790 cm^{-1} were reported [61]. The glasses exhibited a large spontaneous transition probability of 36.66 s^{-1}, corresponding to the Ho^{3+}: $^5I_6 \rightarrow \, ^5I_7$ transition, and a broad 2.85 μm fluorescence. Moreover, a peak emission cross-section of 9.2×10^{-21} cm^2 and a predicted maximum gain per unit length at 2.85 μm of 4.3 dB/cm were achieved.

Another interesting research work thoroughly investigated the 2.05 μm emission of Ho^{3+}: $^5I_7 \rightarrow \, ^5I_8$ and the energy transfer mechanisms of Ho^{3+} sensitized by Tm^{3+} and Er^{3+} in novel Ho_2O_3, Tm_2O_3 and Er_2O_3 triply doped germanate glasses [62]. The maximum value of

emission cross-section of Ho^{3+} at around 2.05 µm proved to be 8.003×10^{-21} cm^2, and a noticeable enhancement in the 2.05 µm emission of Ho^{3+}: $^5I_7 \rightarrow {}^5I_8$ was observed when adding the proper amount of Er_2O_3 and Tm_2O_3 under excitation at 808 nm. The maximum value of the Ho^{3+} 2.05 µm emission intensity was obtained at concentrations of Ho_2O_3, Tm_2O_3 and Er_2O_3 equal to 1, 1 and 2 mol%, respectively.

Among the different RE ions able to efficiently emit in the mid-IR wavelength region, a prominent role is played by Er^{3+}, which is an ideal luminescent center for the 2.7 µm emission corresponding to the $^4I_{11/2} \rightarrow {}^4I_{13/2}$ transition and can be directly pumped by using the commercially available and low-cost 808 or 980 nm laser diodes.

For the above-mentioned transition, high spontaneous radiative transition probability of 30.09 s^{-1}, large emission cross-section equal to $(14.84 \pm 0.10) \times 10^{-21}$ cm^2 and superior gain performance were obtained from 1 mol% Er^{3+} activated germanate glasses characterized by good forming ability and thermal stability [63]. Moreover, La_2O_3 and Y_2O_3 modified 1 mol% Er^{3+}-doped germanate glasses with good thermal stability were also synthesized, and their peak emission cross-sections corresponding to the $^4I_{11/2} \rightarrow {}^4I_{13/2}$ transition revealed to be $(14.3 \pm 0.10) \times 10^{-21}$ cm^2 and $(15.4 \pm 0.10) \times 10^{-21}$ cm^2, respectively [64].

2.4. Tellurite glasses

TeO_2 cannot form a noncrystalline solid if quenched rapidly, since the compound does not obey the Zachariasen's rules for glass forming [65]. More stable glasses are obtained when a modifier ion is added, such as BaO, ZnO or Na_2O, the first discovery of glass formation dating back to Berzelius in 1834 [19]. Tellurite glasses have been studied and developed mainly for photonic applications: they offer an interesting alternative to silica mainly because of their high refractive index, good chemical stability and the lowest phonon energy among oxide glasses [12]. They were initially investigated for their potential use as optical amplifiers in the third telecom window. They represent a valid alternative to fluoride glasses as host materials for Tm^{3+} ions operating at the wavelength of 1.47 µm, as part of the thulium-doped fiber amplifier (TDFA). Indeed, tellurite glasses display a wider bandwidth, better depopulation of $^3F_4$ level and higher absorption and emission cross-sections, which increase the efficiency of the amplification [66]. Another interesting feature of tellurite glasses, unique among oxide glasses, is their high refractive index, which opens perspectives for the use of these materials for supercontinuum generation in the mid-IR wavelength region [67]. Faraday angle rotation using both passive and RE–doped tellurite glasses has also been investigated [68].

2.4.1. Structure

Tellurium oxide–based glasses are structured into a predominance of TeO_4 units in trigonal bipyramid arrangement (4-fold coordinated Te, sp^{3}d hybridization), which with the addition of modifier ions change into TeO_3 trigonal pyramids (3-fold coordinated Te, sp^3 hybridization). An intermediate structure of TeO_{3+1} polyhedron was also detected using several types of spectroscopic techniques [69, 70].
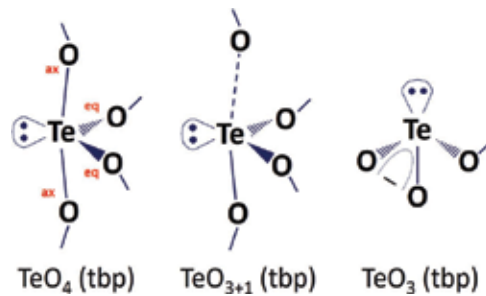
Figure 4. TeO_4, TeO_{3+1} and TeO_3 structural units typical of tellurite glasses.

In tellurite glasses, the TeO_4 trigonal bipyramid (tbp) structural units contain two axial oxygen atoms (O_{ax}) at a distance of 191 pm from the Te atom and two equatorial oxygen atoms (O_{eq}) at the distance of 209 pm. The angles between O_{ax}—Te—O_{ax} and O_{eq}—Te—O_{eq} atoms are 169 and 102°, respectively. With the addition of glass modifiers, the Te—O_{ax} bonds become weaker and longer, which causes the structural change of some TeO_4 units into TeO_{3+1} units and, in a following step, with increasing the amount of glass modifiers, into TeO_3 units. The different structural units are reported in **Figure 4**. Such process is caused by the electron transfer from the glass modifier to a more electronegative $(TeO_4)4\delta$ (where $0 < \delta < 1$ is a parameter representing the ionic character of the Te—O bond) unit [71, 72].

2.4.2. Tellurite glasses as laser material

Tellurite glass has been studied for laser emission since 1978, when the first Nd-doped bulk glass laser was demonstrated [73] by exciting it at the Ar-ion laser emission wavelength of 514.5 nm.

Among oxide glass systems, tellurite glasses are a promising glass host for near-IR and mid-IR lasers thanks to their peculiar properties. The high RE ion solubility (up to ~10^{21} ions/cm^3) within its amorphous matrix allows the realization of highly compact devices. Moreover, tellurite glasses display the lowest phonon energy among all oxide glasses (in the range of 650–800 cm^{-1} depending on the composition), which allows transmission further into the infrared (up to ~5 μm), and high refractive index (~2.0), which means high absorption and emission cross-sections [74, 75]. Tellurite glasses are also more chemically, environmentally and thermally stable than other nonoxide glasses, making them an attractive option for reliable fiber device manufacturing [12].

A drawback of tellurite glasses, like most oxide glasses fabricated from solid-state precursor materials, is the presence of hydroxyl ions (OH^-), which absorb in the mid-IR wavelength region. These ions could decrease the fluorescence intensity and ultimately lead to the deterioration of the laser performance and even inhibit the laser output [75]. In the tellurite glass system, significant results of RE ion emission in the mid-IR region have been reported from Tm^{3+}, Ho^{3+} and Er^{3+} [76–82].

Thulium (Tm) is an ideal choice for the realization of glass lasers in the ~2 μm wavelength range, since it displays one of the broadest fluorescence bands among RE ions [83] due to the transition Tm^{3+}: $^3F_4 \rightarrow {}^3H_6$ that is centered at around 1.8 μm. Tm^{3+} has also the advantage of having an absorption band conveniently located at around 800 nm, which coincides with the output of low-cost and high-power commercial laser diodes. This pumping scheme allows obtaining two ions in the upper laser level for each pumping photon, thanks to a phonon-assisted cross-relaxation process that can potentially result in a laser action with 200% quantum efficiency [84, 85]. It is possible also to pump Tm^{3+} directly into the upper laser level $^3F_4$, which has the potential benefit of a low quantum defect, but has the disadvantage of the lack of convenient low-cost and high-power sources operating in this wavelength range. Possible options that have been demonstrated are an Er^{3+}/Yb^{3+}-codoped tellurite fiber laser [84] and low-power semiconductor laser diodes [86].

Spectroscopic properties of Tm^{3+}-doped TZN (80 TeO_2-10 ZnO-10 Na_2O) and TZNG (75 TeO_2-10 ZnO-10 Na_2O-5 GeO_2) glasses were reported and studied in [76]. The measured full width at half maximum (FWHM) of the Tm^{3+} :$^3F_4$ fluorescence band in TZN glass was 200 μm, compared to 125 nm reported in ZBLAN [87] and 150 nm in silica [88], thus resulting in an enhanced tuning range obtainable in tellurite glass host material. In this work, lasing was also demonstrated in TZNG bulk glass pumped at 793 nm by a Ti:sapphire laser, with a maximum output power of 124 mW and a slope efficiency of 28% with respect to the absorbed pump power. In order to enhance the quantum yield of Tm^{3+} 1.8 μm emission, codoping with Yb^{3+} was proposed [89–91] due to its efficient absorption at 980 nm, which is readily available from InGaAs laser diodes. Moreover, the simple energy level structure of the ytterbium ion offers also an additional benefit by avoiding undesirable excited state absorption (ESA). In [89], an efficient energy transfer between Yb^{3+} and Tm^{3+} was demonstrated, transfer that increases along with Tm^{3+} doping concentration. This study was however limited to low doping concentrations, while in [91] an investigation of the effect of Yb^{3+} codoping on Tm^{3+} ion spectroscopic properties when Yb^{3+} ions content is higher than 2 mol% was conducted with the aim to identify a good candidate active material for short-cavity fiber lasers. This work showed that Yb quenching concentration is of the order of 13 mol% and far larger than Tm quenching concentration, thus allowing to use a Yb:Tm ratio up to 3:1 even for very high Tm concentrations.

The main shortcoming of the widely used TZN tellurite glass as laser material is its low thermal stability, which makes it less durable due to the large amount of heat generated in a laser. To alleviate this problem, a novel Tm^{3+}-doped tungsten tellurite glass composition was developed, with a 50% higher T_g and 36% lower coefficient of thermal expansion (CTE) [92]. The glass was used to demonstrate laser emission in fiber form under excitation through a commercial laser diode operating at 803 nm, although quite a limited slope efficiency (20% with respect to the absorbed pump power) was achieved.

Besides thulium, another RE capable of generating ~2 μm laser emission is holmium (Ho), thanks to the transition Ho^{3+}: $^5I_7 \rightarrow {}^5I_8$. Considering the larger emission cross-section and longer lifetime of the lasing state, Ho^{3+} is suitable for ~2 μm laser, particularly for reducing the laser threshold [93]. However, one of the major shortcomings of Ho^{3+} is the lack of ground state absorption transitions that overlap with convenient high-power pump sources, so

codoping with another RE with a strong absorption band at around 800 or 980 nm, such as Yb^{3+} or Tm^{3+}, is commonly used [76, 79, 94].

In [79], 2.0 μm emission characteristics of Ho^{3+} ions both by direct excitation and by sensitized excitation through energy transfer from Yb^{3+} ions in a codoped barium-tellurite glass are detailed. A fluorescence band of 160 nm and an emission cross-section of 1.45×10^{-20} cm^2 were reported. These values resulted to be higher compared to those previously published for other glass systems. The emission intensity of Ho^{3+}: $^5I_7 \rightarrow {}^5I_8$ was measured to be 8 times higher under the excitation at 980 nm through the energy level $^2F_{5/2}$ of Yb^{3+} ion when compared to the direct excitation of Ho^{3+}. This is due to the high absorption cross-section of Yb^{3+} ion alongside the highly efficient (86%) sensitized energy transfer from Yb^{3+}: $^2F_{5/2}$ to Ho^{3+}: $^5I_6$.

Holmium presents also another interesting mid-IR emission at 2.9 μm from the transition Ho^{3+}: $^5I_6 \rightarrow {}^5I_7$. An extensive investigation of this holmium emitting level in a TZGB glass (74.5 TeO_2-12.2 ZnF_2-6.4 GeO_2-4.2 Bi_2O_3) was conducted in [78]. The result indicates that the main issues with this glass are water incorporation and the low luminescence efficiency of $^5I_6$ level (8%). The reported numerical simulations indicated that the prospect for continuous wave (CW) operation on the $^5I_6 \rightarrow {}^5I_7$ transition in Ho^{3+}-doped tellurite glasses is low.

In [95], the 2.9 μm emission from an Yb^{3+}/Ho^{3+}co-doped tellurite glass (80 TeO_2-15 (BaF_2 + BaO)-3 La_2O_3) is investigated. The FWHM of the emission was 180 nm and the peak emission cross-section was 9.1×10^{-21} cm^2, comparable to other hosts and even better than ZBLAN fluoride glass. The emission intensity increased many folds upon Yb^{3+} excitation at 985 nm compared to direct Ho^{3+} ion excitation, thanks to the high absorption of ytterbium at the pump wavelength followed by the resonant energy transfer from Yb^{3+} to Ho^{3+} ions.

Concerning erbium ion, it is an ideal choice for emission in the mid-IR wavelength range, thanks to its fluorescence at 2.7 μm corresponding to the Er^{3+}: $^4I_{11/2} \rightarrow {}^4I_{13/2}$ transition and the possibility to use 808 or 980 nm laser diodes as pumping source.

The potential of erbium-doped tellurite glass for the realization of compact laser devices at this wavelength was extensively investigated in [82]. In this work, it is shown that the presence of OH^- groups in current state-of the-art Er^{3+}-doped tellurite glass is high enough to suppress the 3 μm emission in the glass, due to a large energy transfer from the excited state to the OH^- radical. Moreover, it was calculated from numerical simulations that in the absence of OH^- impurities, the pumping intensity required for population inversion in an Er^{3+}-doped tellurite CW fiber laser pumped at 976 nm is ~80 kW/cm^2 for Er_2O_3 concentrations ≥ 2.65 mol%. It was also established that a pump ESA process at 976 nm would have a detrimental impact on the performance of the fiber laser.

More recently, a barium tellurite glass host was proposed for obtaining 2.7 μm emission from erbium [80]. This glass possesses higher thermal properties compared to typical TZN glass and lower OH^- content, thanks to the addition of BaF_2. An optical fiber was prepared using the developed glass, and 2.7 μm fluorescence was measured upon excitation through a 980 nm laser diode. The feasibility of an Er^{3+}-doped tellurite fiber laser operating at 2.7 μm based on this novel glass was also theoretically investigated, showing that the barium tellurite fiber is a promising candidate for the development of efficient mid-infrared fiber lasers [80].

3. Nonsilica oxide glass optical fiber fabrication

3.1. Optical fibers

The next paragraphs present the very basic concepts of an optical fiber that are relevant to the understanding of the technological challenges behind the manufacturing of multicomponent oxide glass fibers.

A complete description of the concepts and working principles of the optical fibers is out of the scope of this chapter. For a detailed description, the reader can refer to the excellent textbooks given in [96, 97].

The typical configuration of an optical fiber is shown in **Figure 5**. It consists of a core made of a glass with a refractive index value n_{core} surrounded by a cladding glass layer of refractive index $n_{cladding}$. Although this is not always implemented at the academic level, a thin polymer coating (polyamide or acrylate type polymer) should be applied during the drawing process to strengthen mechanically the fiber and to protect it from long-term moisture degradation or other possible chemical contamination sources.

Electromagnetic radiations are confined in the core provided that the refractive index values of the core and cladding glasses meet the condition $n_{core} > n_{cladding}$.

Under this condition, at least one of the so-called electromagnetic or optical modes can be confined and propagate down the optical fiber core. In first approximation, the modes can be understood as a set of constructive interference patterns along the fiber. For illustration purpose, the intensity profile of the electromagnetic fields of few modes is shown in **Figure 6**.

The number of propagating modes depends on the dimension and the difference of refractive index values between the core and the cladding glasses.

The normalized frequency parameter, *V*, for a step-index optical fiber is given by:

$$V = \frac{2\pi a}{\lambda} \left(n_{core}^2 - n_{clad}^2 \right)^{\frac{1}{2}} \tag{1}$$

where λ is the wavelength in vacuum and *a* is the radius of the fiber core. If $V < 2.4$, the optical fiber can support only one propagating mode in the core. If any power is launched in the other modes at the fiber input, it will leak into the cladding material.
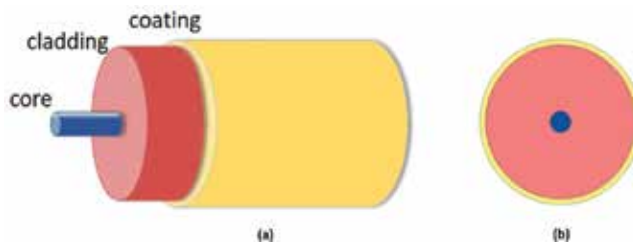
Figure 5. (a) Scheme of a typical optical fiber and (b) cross-section illustration of a typical optical fiber structure.
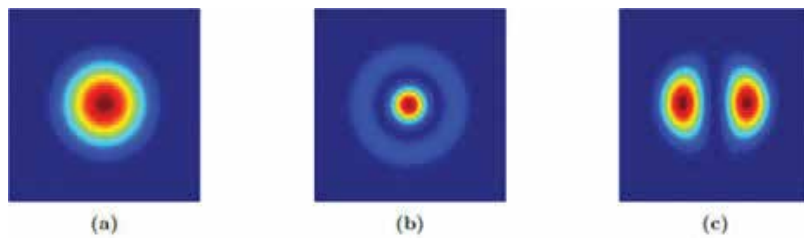
Figure 6. Spatial distribution of the electromagnetic field amplitude of few optical modes in a low numerical aperture multimode fiber: (a) LP_{01} mode or "fundamental mode," (b) LP_{02} mode and (c) LP_{03}.

For numerous applications and in particular for the development of optical coherent sources, single-mode operation is highly desirable. The spatial and temporal properties of the propagating beam in a single-mode fiber can be managed with better control, making this fiber configuration more suitable for the development of high-performance sources.

Typically, a difference value down to 10^{-3} between the refractive index values of the core and the cladding glasses can be achieved. According to equation (1), such refractive index difference value implies that to maintain single-mode operation, a typical core diameter must lay below the values of 15 and 30 µm for wavelengths in the 1 to 2 µm range, respectively

3.2. Double-cladding structure for high-power fiber lasers and amplifiers

The double-cladding strategy was developed to exploit the high pump power available from a laser diode [98]. The structure of the fiber allows to launch high pump power into the first cladding surrounding the core, as reported in **Figure 7**. The pump power is confined within the first cladding, thanks to the second cladding. Along the fiber length, the pump radiation interacts numerous times with the core glass material. At each interaction, the RE ions contained in the core absorb part of the pump power. The excited RE ions subsequently reemit part of the absorbed power by a stimulated emission phenomenon. The reemission being then confined within the core, substantially the double-cladding structure converts low-brightness laser diode power into high-brightness fiber laser.
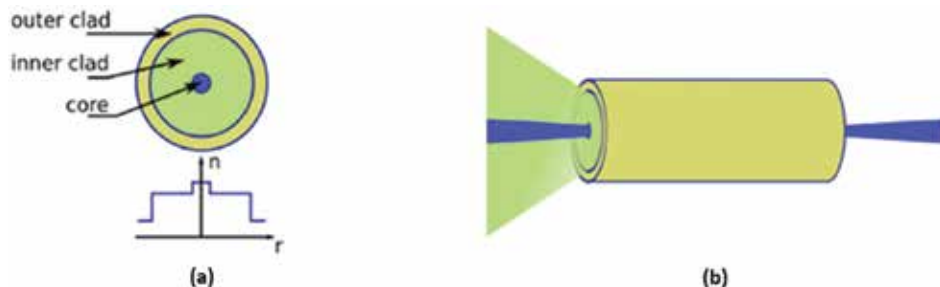
Figure 7. (a) Cross-section image and refractive index profile of a double-cladding fiber for high-power amplifiers and lasers; (b) illustration of the concept of double-cladding structure for a high-power amplifier. Pump laser beam in green, input signal and output amplified signal in blue.

3.3. Preform fiber drawing technique: process and main parameters

The drawing of a soft oxide glass fiber directly from the molten state has been reported [99]; however, the versatility of this approach remains very limited as it requires substantial modification of the drawing facilities in order to change the fiber core/cladding ratio and diameter. Most importantly, the diameter and fiber structural control is difficult to achieve while glass crystallization often occurs at the edges of the crucible walls, impairing both the optical property transmission of the optical fiber due to the presence of scattering crystals and the fiber mechanical robustness.

Actually, as for the advanced silica glass fiber technology, the most employed technique for drawing multicomponent glass fibers is the preform drawing [100]. In this approach, the so-called preform, which is a "macroscopic" version of the fiber, is first manufactured using one of the procedures described in Section 2.1. For multicomponent oxide glass fibers, the typical dimensions of the preform range from 10 to 20 mm in diameter and few cm to 20 cm in length.

The preform is then placed in a drawing tower where it is heated up until the glass reaches a viscosity of about 10^5 Pa s. A schematic illustration of a drawing tower is shown in **Figure 8**. Under the combined effect of gravity and surface tension forces, the softened part of the preform drops down and thins down into a fiber, which is then pulled either using a capstan or attached directly onto a rotating drum at the bottom of the tower. The control of the dimension at the mm scale of the preform and the relatively high tensions, typically 0.1–1 N, of the drawing process allows for a very precise control of the final fiber dimensions and geometry.

The control of the fiber diameter is achieved by tuning the speed at which the preform is being fed into the furnace and the speed at which the fiber is being drawn from the preform. For an

Figure 8. (a) Schematic illustration of a fiber drawing tower, which implements the preform drawing approach; (b) photography of an in-house developed drawing tower installed at Politecnico di Torino.

incompressible liquid, mass conservation considerations lead to the following equation for the fiber diameter d_{fiber}:

$$d_{fiber} = d_{preform}\left(\frac{v_{preform}}{v_{fiber}}\right)^{\frac{1}{2}} \tag{2}$$
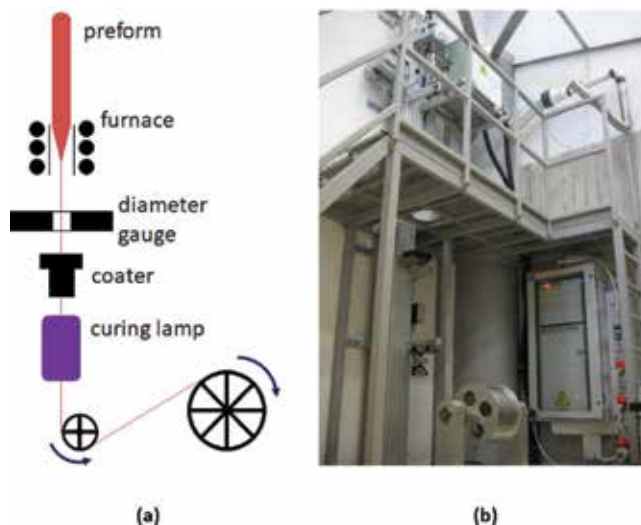
where $d_{preform}$ is the preform diameter and $v_{preform}$ and v_{fiber} are, respectively, the preform feed speed and the pulling speed.

3.3.1. Drawing tower facilities

Commercial towers for soft glasses can be acquired from several specialized manufacturers; however, a cost-effective drawing tower can be developed in-house and leads to similar results in terms of fiber diameter fluctuations, which are typically of ± 1 μm over few tens of meters of fiber. For multicomponent oxide glasses, the main source of fluctuations/contaminations in the final fiber arises at the production stage of the preform, not during the drawing process itself.

The fiber drawing process of a multicomponent glass preform is carried out at a typical speed ranging from few m/min to 30 m/min at most. This is in contrast to the very high drawing speed used to produce telecom silica glass optical fiber, which reaches up to 20 m/s [100]. Because of this slow drawing speed, automated diameter adjustment through a diameter monitor feedback can be rather inefficient, especially in the academic field where very often one fiber is different from the next in terms of its glass composition or structure. As such, the furnace configuration and the feeding procedure of the preform into the furnace become crucial to ensure the diameter stability during the drawing process. Beside obvious parameters such as the temperature stability of the furnace, ensuring a steady laminar flow around the preform during the drawing procedure is key. The choice of the gas used N_2/O_2, Ar or N_2 depends strongly on the glass composition. The low gas content in H_2O is however necessary to avoid any detrimental effects, optical or mechanical, on the drawn fiber.

The furnace can be based on either resistive elements or an induction head where the susceptor consists of a simple metal or graphite ring. The latter approach offers the possibility to tailor easily and cost-effectively the hot zone by simply changing the susceptors.

3.4. Preform fabrication

3.4.1. Rod-in-tube

In the rod-in-tube technique, the preform consists, in its most simple form, of a rod of core glass inserted into a cladding glass tube. When heated up inside the drawing tower furnace, the cladding tube collapses around the core rod under the effect of gravity and surface tension forces. The two glass materials are then drawn together as a single concentrically structured fiber. For the process to take place in a controlled manner and to avoid excessive residual stress within the fiber, several important material aspects need to be taken into consideration. The two glasses must match in terms of thermomechanical properties: glass working temperature, glass transition temperature and thermal expansion values of the two glasses should match as

much as possible. In practice, these constrains imply that the two glasses have similar compositions, which in turn limit the upper range of the refractive index difference value achievable.

It is also preferable that both the tube inner diameter and the rod diameter match each other closely to avoid structural deformation of the core or trapped air at the interface between the two glasses. The latter issue can be addressed by applying vacuum on the top part of the preform.

As illustrated in **Figure 9**, to achieve a small diameter core dimension or manufacture the double-cladding structure, the preform preparation consists in an intermediate step where a core/cladding preform is thinned down into a cane, which is then inserted into another cladding tube to form a new preform. This process can be repeated several times depending on the thermal stability against crystallization of the glass compositions involved. This cane drawing process is carried out in the drawing tower but at higher viscosity and under higher tension than the fiber drawing process.

3.4.2. Core glass rod manufacture

The core glass rod arises from a single bulk glass casted into either a cylindrical- or rectangular-shaped mold. In the latter case, the bulk can then be machined into a cylindrical rod of the desired dimension. In both cases, the core glass rod needs to be polished preferably using a nonaqueous cooling liquid so as not to impair the optical transmission of the fiber.
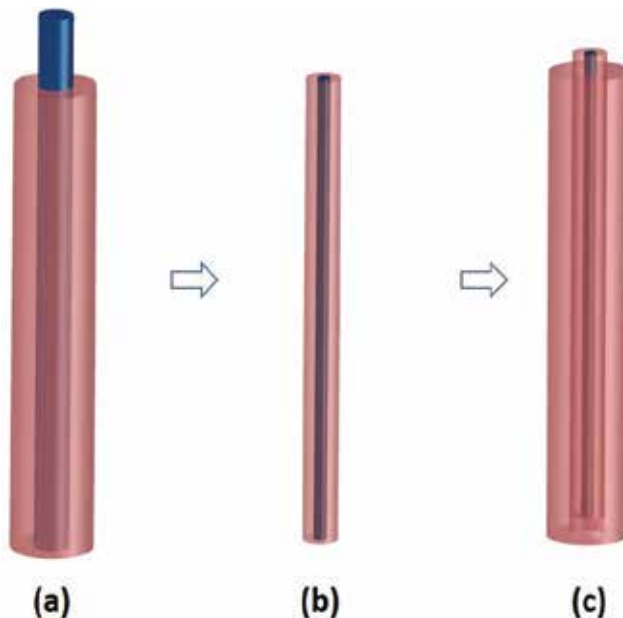
Figure 9. (a) Implementation of an optical fiber preform using the rod-in-tube technique. Core glass rod in blue, cladding glass tube in red; (b) glass cane with a core/cladding structure obtained by drawing the preform shown in (a); (c) implementation of a small core/cladding diameter ratio preform by inserting the rod shown in (b) into an additional cladding glass tube.

3.4.3. Cladding glass tube

3.4.3.1. Drilling

The cladding tube can be manufactured through different techniques. Drilling is carried out either using an ultrasonic drilling setup and/or using specialized diamond drilling bits. This approach allows for machining tubes reliably and with a great precision, making possible a precise control of the fiber dimensions through the drawing process. In addition, the glass does not go through a heating cycle, which could favor crystallization tendency.

There are, however, a number of drawbacks. Because of the brittleness of the glass, this is a slow and therefore time-consuming process. Drilling small diameter holes cannot be achieved over long lengths due to the mechanical flexibility of the drill bit itself. Thin wall tubes are also difficult to manufacture. Adding to the processing time, following drilling, the tube must undergo an additional polishing process not only to smoothen the wall roughness but also to clean up the walls from free glass particles that can be prone to crystallization during the drawing process.

3.4.3.2. Extrusion

An overview of the overall procedure and equipment of the extrusion process is given in [101–102]. In the extrusion process, a bulk glass, typically 30 mm in diameter and 30–50 mm high, is loaded into a furnace apparatus open on top and bottom. A scheme of the process is reported in **Figure 10**. The glass is heated up to a temperature corresponding to a viscosity of 10^8 Pa s. On the top part, a press ram applies a force on the glass bulk. The soften glass exits through the
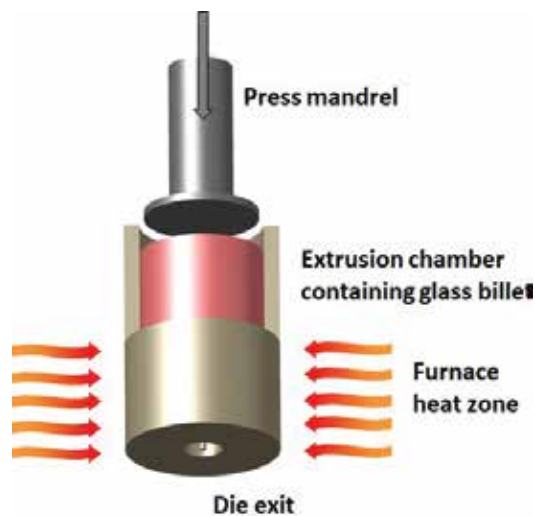
Figure 10. Schematic of the extrusion process for manufacturing glass tubes. A glass billet (in red) is heated up until the glass reaches a viscosity of typically 10^8 Pa s. A high pressure is then applied onto the top billet surface through a mandrel. The softened glass is then slowly pushed out of the die through the bottom orifice of this latter. The orifice arrangement with a pin in its center allows for producing a glass tube.

bottom part of the apparatus, which consists of a funnel shape die where a spider setup allows for a pin to be held in the center of the die.

Typically, the pressure applied ranges from 1 to 6 GPa. For multicomponent oxide glasses, the dies can be manufactured out of standard stainless-steel material, although less reactive (more stable and inert) metals such as Inconel are sometimes preferable depending on the temperatures and glass compositions involved. The die surface finish plays an important role onto the surface quality finish of the extruded glass tube itself. Indeed, it is possible to extrude very high-quality surface finish tubes also because the process is carried out at a range of viscosity where surface tension is still effective.

Some swelling effect can occur and tends to distort the preform and modify its dimensions with respect to the die dimension. However, this effect can be limited through pertinent die design and temperature of operation. If compared to the drilling technique, the main disadvantage of the extrusion is that the glass goes through an extra heating cycle above the glass transition temperature (T_g), which can promote glass nucleation and crystallization. Nevertheless, the negative effect of this cycle is limited by the fact that the viscosity range considered is substantially high.

3.4.3.3. Rotational casting

The rotational casting [103] is carried out by casting the molten glass into a cylindrical mold (**Figure 11**), which is then tilted horizontally and rotated at a rotation speed ranging typically from 1000 to 2000 rpm while the glass inside the mold is still liquid. As the liquid cools down, it forms a glass tube inside the mold, which is then loaded into a furnace for glass annealing. Despite being a "manual craft" operation, if processed under the same conditions, the tube

(a)   (b)

Figure 11. Schematic of the rotational casting procedure for manufacturing glass tubes: (a) the molten glass is cast into a mold held in vertical position; (b) the mold is tilted in the horizontal direction and then rotated at high speed. A glass tube forms along the mold internal walls.

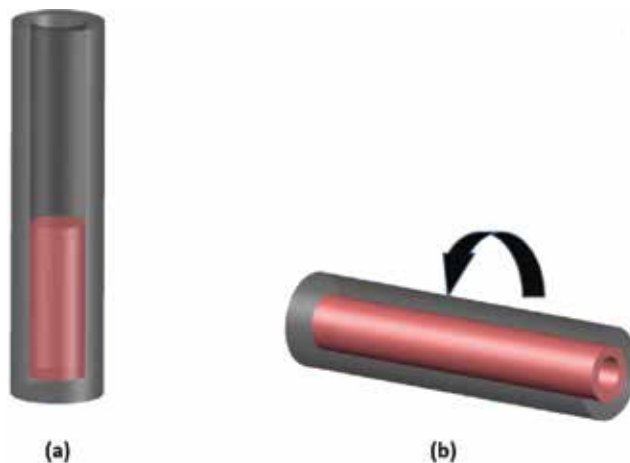inner diameter value is commonly reproducible within $\pm\,5\,\%$. The typical roughness value of the inner tube surface is below 10 nm. Such pristine surface is indeed particularly suitable for the development of optical fibers.

The rotational casting process takes place in a matter of seconds, making it a very fast production technique if compared to the two approaches described above. The main limitation of the rotational casting technique regards the range of inner tube diameter values achievable. Uniform tubes with small or large inner diameters can be difficult to achieve in a reproducible manner. Also, the technique is foremost restricted to glass compositions that display a low viscosity once molten. Silicate glasses, for instance, are unpractical for implementing the rotational casting technique.

3.4.4. Built-in-casting and suction casting approaches

The built-in-casting and suction casting techniques [104, 105] were developed to avoid some of the issues inherent to the rod-in-tube technique, the main purpose being to manufacture a single unit core/cladding structured preform. Both techniques involve the casting of the core material in a liquid state inside a cladding tube for the former approach or on the top of the cooling cladding glass for the latter approach.

These techniques can provide substantially low loss optical fibers and display the advantage to require low processing time. However, the control on the dimension and shape of the core is rather limited with, therefore, a very low reproducibility. Some degree of diffusion process also occurs at the interface between the two glasses. Because of these features, these techniques are being used only at an academic level.

Author details

Daniel Milanese[1,6]*, Joris Lousteau[2], Xiushan Zhu[3], Arturo Chavez-Pirson[4], Diego Pugliese[1], Nadia Giovanna Boetti[5] and Nasser Peyghambarian[3,4]

*Address all correspondence to: daniel.milanese@polito.it

1 Department of Applied Science and Technology and RU INSTM, Politecnico di Torino, Torino, Italy

2 Optoelectronics Research Centre, University of Southampton, Southampton, United Kingdom

3 College of Optical Sciences, University of Arizona, Tucson, AZ, United States of America

4 NP Photonics Inc., Tucson, AZ, United States of America

5 Istituto Superiore Mario Boella, Torino, Italy

6 Consiglio Nazionale delle Ricerche, Istituto di Fotonica e Nanotecnologie, Trento, Italy

References

[1] Rasmussen SC. How Glass Changed the World: The History and Chemistry of Glass from Antiquity to the 13th Century. 1st ed. Berlin: Springer; 2012. 85 p. DOI: 10.1007/978-3-642-28183-9

[2] Varshneya AK. Fundamentals of Inorganic Glasses. 1st ed. New York, USA: Academic Press Inc.; 1994. 570 p

[3] Yamane M, Asahara Y. Glasses for Photonics. 1st ed. Cambridge, UK: Cambridge University Press; 2004. 282 p.

[4] Digonnet MJF, editor. Rare-Earth-Doped Fiber Lasers and Amplifiers. 1st ed. Boca Raton, FL, USA: CRC Press; 2001. 798 p

[5] Brawer SA, White WB. Raman spectroscopic investigation of the structure of silicate glasses. I. The binary alkali silicates. The Journal of Chemical Physics. 1975;**63**:2421-2432. DOI: 10.1063/1.431671

[6] Quimby RS, Miniscalco WJ, Thompson B. Clustering in erbium-doped silica glass fibers analyzed using 980 nm excited-state absorption. Journal of Applied Physics. 1994;**76**:4472-4478. DOI: 10.1063/1.357278

[7] Kitamura R, Pilon L, Jonasz M. Optical constants of silica glass from extreme ultraviolet to far infrared at near room temperature. Applied Optics. 2007;**46**:8118-8133. DOI: 10.1364/AO.46.008118

[8] France PW, editor. Fluoride Glass Optical Fibers. 1st ed. Glasgow and London: Blackie and Sons Ltd; 1990. 280 p.

[9] Seddon AB. Chalcogenide glasses: A review of their preparation, properties and applications. Journal of Non-Crystalline Solids. 1995;**184**:44-50. DOI: 10.1016/0022-3093(94)00686-5

[10] Falconi MC, Palma G, Starecki F, Nazabal V, Troles J, Taccheo S, Ferrari M, Prudenzano F. Design of an efficient pumping scheme for mid-IR $Dy^{3+}:Ga_5Ge_{20}Sb_{10}S_{65}$ PCF fiber laser. IEEE Photonics Technology Letters. 2016;**28**:1984-1987. DOI: 10.1109/LPT.2016.2581022

[11] Jackson SD, Lancaster DG. Fiber lasers that bridge the shortwave to midwave regions of the infrared spectrum. In: Okhotnikov OG, editor. Fiber Lasers. 1st ed. Weinheim: Wiley-VCH; 2012. pp. 233-267. DOI: 10.1002/9783527648641.ch7

[12] Wang JS, Vogel EM, Snitzer E. Tellurite glass: A new candidate for fiber devices. Optical Materials. 1994;**3**:187-203. DOI: 10.1016/0925-3467(94)90004-3

[13] Yiannopoulos YD, Varsamis CPE, Kamitsos EI. Density of alkali germanate glasses related to structure. Journal of Non-Crystalline Solids. 2001;**293–295**:244-249. DOI: 10.1016/S0022-3093(01)00677-9

[14] Veeranna Gowda VC. Physical, thermal, infrared and optical properties of Nd^{3+} doped lithium-lead-germanate glasses. Physica B: Condensed Matter. 2015;**456**:298-305. DOI: 10.1016/j.physb.2014.09.004

[15] Sidek HAA, Bahari HR, Halimah MK, Yunus WMM. Preparation and elastic moduli of germanate glass containing lead and bismuth. International Journal of Molecular Sciences. 2012;**13**:4632-4641. DOI: 10.3390/ijms13044632

[16] Polyanskiy MN. Refractive Index Database [Internet]. 2017. Available from: https://refractiveindex.info/ [Accessed: 2017–11-18]

[17] Jiang X, Lousteau L, Richards B, Jha A. Investigation on germanium oxide-based glasses for infrared optical fibre development. Optical Materials. 2009;**31**:1701-1706. DOI: 10.1016/j.optmat.2009.04.011

[18] Munasinghe HT, Winterstein-Beckmann A, Schiele C, Manzani D, Wondraczek L, Afshar VS, Monro TM, Ebendorff-Heidepriem H. Lead-germanate glasses and fibers: A practical alternative to tellurite for nonlinear fiber applications. Optical Materials Express. 2013;**3**:1488-1503. DOI: 10.1364/OME.3.001488

[19] Rawson H. Properties and Applications of Glass. 1st ed. Amsterdam: Elsevier Science Ltd; 1980. 318 p.

[20] Vogel W. Glass Chemistry. 1st ed. Berlin: Springer Verlag; 1994. 478 p. DOI: 10.1007/978-3-642-78723-2

[21] Baikova LG, Pukh VP, Fedorov YK, Sinani AB, Tikhonova LV, Kireenko MF. Mechanical properties of phosphate glasses as a function of the total bonding energy per unit volume of glass. Glass Physics and Chemistry. 2008;**34**:126-131. DOI: 10.1134/S1087659608020028

[22] Karabulut M, Melnik E, Stefan R, Marasinghe GK, Ray CS, Kurkjian CR, Day DE. Mechanical and structural properties of phosphate glasses. Journal of Non-Crystalline Solids. 2001;**288**:8-17. DOI: 10.1016/S0022-3093(01)00615-9

[23] Fuchs RJ. Method of softening hard water with sodium phosphate glasses. US Patent No. US 3130152 A; 1964

[24] Ahmed I, Lewis M, Olsen I, Knowles JC. Phosphate glasses for tissue engineering: Part 1. Processing and characterisation of a ternary-based P_2O_5-CaO-Na_2O glass system. Biomaterials. 2004;**25**:491-499. DOI: 10.1016/S0142-9612(03)00546-5

[25] Sales BC, Boatner LA. Lead-iron phosphate glass: A stable storage medium for high-level nuclear waste. Science. 1984;**226**:45-48. DOI: 10.1126/science.226.4670.45

[26] Kreidl NJ, Weyl WA. Phosphates in ceramic ware: IV, phosphate glasses. Journal of the American Ceramic Society. 1941;**24**:372-378. DOI: 10.1111/j.1151-2916.1941.tb15444.x

[27] Campbell JH, Hayden JS, Marker A. High-power solid-state lasers: A laser glass perspective. International Journal of Applied Glass Science. 2011;**2**:3-29. DOI: 10.1111/j.2041-1294.2011.00044.x

[28] Brow RK. Review: The structure of simple phosphate glasses. Journal of Non-Crystalline Solids. 2000;**263-264**:1-28. DOI: 10.1016/S0022-3093(99)00620-1

[29] Myers JD, Vollers CS. Laser phosphate glass compositions. US Patent No. US 4248732 A; 1978

[30] Hayden J. Phosphate glass useful in lasers. US Patent No. US 5334559 A; 1994

[31] Brow RK, Click CA, Alam TM. Modifier coordination and phosphate glass networks. Journal of Non-Crystalline Solids. 2000;**274**:9-16. DOI: 10.1016/S0022-3093(00)00178-2

[32] Seneschal K, Smektala F, Bureau B, Le Floch M, Jiang S, Luo T, Lucas J, Peyghambarian N. Properties and structure of high erbium doped phosphate glass for short optical fibers amplifiers. Materials Research Bulletin. 2005;**40**:1433-1442. DOI: 10.1016/j.materresbull.2005.05.004

[33] Harada T, In H, Takebe H, Morinaga K. Effect of B_2O_3 addition on the thermal stability of barium phosphate glasses for optical fiber devices. Journal of the American Ceramic Society. 2004;**87**:408-411. DOI: 10.1111/j.1551-2916.2004.00408.x

[34] Brow RK. Nature of alumina in phosphate glass: I, properties of sodium aluminophosphate glass. Journal of the American Ceramic Society. 1993;**76**:913-918. DOI: 10.1111/j.1151-2916.1993.tb05315.x

[35] Bingham PA, Hand RJ, Hannant OM, Forder SD, Kilcoyne SH. Effects of modifier additions on the thermal properties, chemical durability, oxidation state and structure of iron phosphate glasses. Journal of Non-Crystalline Solids. 2009;**355**:1526-1538. DOI: 10.1016/j.jnoncrysol.2009.03.008

[36] Martin WE, Milam D. Gain saturation in Nd:doped laser materials. IEEE Journal of Quantum Electronics. 1982;**18**:1155-1163. DOI: 10.1109/JQE.1982.1071668

[37] Campbell JH, Wallerstein EP, Hayden JS, Sapak D, Marker AJ. Effects of melting conditions on platinum-inclusion content in phosphate laser glasses. Glass Science and Technology. 1995;**68**:11-21. DOI: 10.4135/9781483327211.n2

[38] Karlsson G, Laurell F, Tellefsen J, Denker B, Galagan B, Osiko V, Sverchkov S. Development and characterization of Yb-Er laser glass for high average power laser diode pumping. Applied Physics B: Lasers and Optics. 2002;**75**:41-46. DOI: 10.1007/s00340-002-0950-4

[39] Lee YW, Sinha S, Digonnet MJF, Byer RL. 20 W single-mode Yb^{3+}-doped phosphate fiber laser. Optics Letters. 2006;**31**:3255-3257. DOI: 10.1364/OL.31.003255

[40] Polynkin A, Polynkin P, Schülzgen A, Mansuripur M, Peyghambarian N. Watts-level, short all-fiber laser at 1.5 μm with a large core and diffraction-limited output via intracavity spatial-mode filtering. Optics Letters. 2005;**30**:403-405. DOI: 10.1364/OL.30.000403

[41] Gapontsev VP, Matitsin SM, Isineev AA, Kravchenko VB. Erbium glass lasers and their applications. Optics and Laser Technology. 1982;**14**:189-196. DOI: 10.1016/0030-3992(82)90095-0

[42] Fermann ME, Hanna DC, Shepherd DP, Suni PJ, Townsend JE. Efficient operation of an Yb-sensitized Er fibre laser at 1.56 μm. Electronics Letters. 1988;**24**:1135-1136. DOI: 10.1049/el:19880772

[43] Barnes WL, Poole SB, Townsend JE, Reekie L, Taylor DJ, Payne DN. Er^{3+}/Yb^{3+} and Er^{3+} doped fiber lasers. Journal of Lightwave Technology. 1989;**7**:1461-1465. DOI: 10.1109/50.39081

[44] Hwang B-C, Jiang S, Luo T, Watson J, Sorbello G, Peyghambarian N. Cooperative upconversion and energy transfer of new high Er^{3+}- and Yb^{3+}–Er^{3+}-doped phosphate glasses. Journal of the Optical Society of America B: Optical Physics. 2000;**17**:833-839. DOI: 10.1364/JOSAB.17.000833

[45] Wu R, Myers JD, Myers MJ, Rapp C. Fluorescence lifetime and 980nm pump energy transfer dynamics in erbium and ytterbium co-doped phosphate laser glasses. In: Proceedings of SPIE 4968, Solid State Lasers XII; 28–30 January 2003; San Jose. Bellingham, WA, USA: SPIE; 2003. pp. 11-17

[46] Margaryan A, Piliavin MA. Germanate Glasses: Structure, Spectroscopy and Properties. 1st ed. Artech House: Boston and London; 1993. 200 p

[47] Sakaguchi S, Todoroki S. Optical properties of GeO_2 glass and optical fibers. Applied Optics. 1997;**36**:6809-6814. DOI: 10.1364/AO.36.006809

[48] Higby PL, Aggarwal ID. Properties of barium gallium germanate glasses. Journal of Non-Crystalline Solids. 1993;**163**:303-308. DOI: 10.1016/0022-3093(93)91308-P

[49] Lezal D, Pedlíková J, Horák J. GeO_2–PbO glassy system for infrared fibers for delivery of Er:YAG laser energy. Journal of Non-Crystalline Solids. 1996;**196**:178-182. DOI: 10.1016/0022-3093(95)00582-X

[50] Cherukuri SC, Pye LD. Faraday rotation of rare earth alkali germanate glasses. In: McCarthy GJ, Silber HB, Rhyne JJ, Kalina FM, editors. The Rare Earths in Modern Science and Technology. 1st ed. Berlin: Springer; 1982. pp. 465-469. DOI: 10.1007/978-1-4613-3406-4_99

[51] Evstropiev KS, Ivanov AO. Physikalisch-chemische eigenschaften von germaniumgläsern. In: Matson FR, Rindone GE, editors. Advances in Glass Technology, Part 2. 1st ed. New York: Plenum Press; 1963. pp. 79-85

[52] Henderson GS. The germanate anomaly: What do we know? Journal of Non-Crystalline Solids. 2007;**353**:1695-1704. DOI: 10.1016/j.jnoncrysol.2007.02.037

[53] Wang J, Lincoln JR, Brocklesby WS, Deol RS, Mackechnie CJ, Pearson A, Tropper AC, Hanna DC, Payne DN. Fabrication and optical properties of lead-germanate glasses and a new class of optical fibers doped with Tm^{3+}. Journal of Applied Physics. 1993;**73**:8066-8075. DOI: 10.1063/1.353922

[54] Xu R, Xu L, Hu L, Zhang J. Structural origin and laser performance of thulium-doped germanate glasses. The Journal of Physical Chemistry. A. 2011;**115**:14163-14167. DOI: 10.1021/jp207574m

[55] Braud A, Girard S, Doualan JL, Thuau M, Moncorgé R. Energy-transfer processes inYb:Tm-doped KY_3F_{10}, $LiYF_4$, and BaY_2F_8 single crystals for laser operation at 1.5 and 2.3 μm. Physical Review B. 2000;**61**:5280-5292. DOI: 10.1103/PhysRevB.61.5280

[56] Fang Y, Zhao G, Xu J, Zhang N, Ma Z, Hu L. Energy transfer and 1.8 μm emission in Yb[3+]/Tm[3+] co-doped bismuth germanate glass. Ceramics International. 2014;**40**:6037-6043. DOI: 10.1016/j.ceramint.2013.11.053

[57] Richards B, Shen S, Jha A, Tsang Y, Binks D. Infrared emission and energy transfer in Tm[3+], Tm[3+]-Ho[3+] and Tm[3+]-Yb[3+]-doped tellurite fibre. Optics Express. 2017;**15**:6546-6551. DOI: 10.1364/OE.15.006546

[58] Wang WC, Yuan J, Chen DD, Zhang JJ, Xu SQ, Zhang QY. Enhanced 1.8 μm emission in Cr^{3+}/Tm[3+] co-doped fluorogermanate glasses for a multi-wavelength pumped near-infrared lasers. AIP Advances. 2014;**4**:107145. DOI: 10.1063/1.4900860

[59] Subramanyam Y, Moorthy LR, Lakshman SVJ. Determination of radiative transitions of Ho[3+] in various ternary sulphate glasses from absorption measurements. Physics and Chemistry of Glasses. 1992;**33**:21-23

[60] Xu R, Pan J, Hu L, Zhang J. 2.0 μm emission properties and energy transfer processes of Yb[3+]/Ho[3+] codoped germanate glass. Journal of Applied Physics. 2010;**108**:043522. DOI: 10.1063/1.3468726

[61] Cai M, Zhou B, Tian Y, Zhou J, Xu S, Zhang J. Broadband mid-infrared 2.8 μm emission in Ho[3+]/Yb[3+]-codoped germanate glasses. Journal of Luminescence. 2016;**171**:143-148. DOI: 10.1016/j.jlumin.2015.11.016

[62] Xu R, Wang M, Tian Y, Hu L, Zhang J. 2.05 μm emission properties and energy transfer mechanism of germanate glass doped with Ho[3+], Tm[3+], and Er[3+]. Journal of Applied Physics. 2011;**109**:053503. DOI: 10.1063/1.3553877

[63] Cai M, Wei T, Zhou B, Tian Y, Zhou J, Xu S, Zhang J. Analysis of energy transfer process based emission spectra of erbium doped germanate glasses for mid-infrared laser materials. Journal of Alloys and Compounds. 2015;**626**:165-172. DOI: 10.1016/j.jallcom.2014.11.077

[64] Cai M, Zhou B, Wang F, Wei T, Tian Y, Zhou J, Xu S, Zhang J. R_2O_3 (R = La, Y) modified erbium activated germanate glasses for mid-infrared 2.7 μm laser materials. Scientific Reports. 2015;**5**:13056. DOI: 10.1038/srep13056

[65] El-Mallawany R. Tellurite glasses. Part 1. Elastic properties. Materials Chemistry and Physics. 1998;**53**:93-120. DOI: 10.1016/S0254-0584(97)02041-5

[66] Naftaly M, Shen S, Jha A. Tm[3+]-doped tellurite glass for a broadband amplifier at 1.47 μm. Applied Optics. 2000;**39**:4979-4984. DOI: 10.1364/AO.39.004979

[67] Wang G, Jiang T, Li C, Yang H, Wang A, Zhang Z. Octave-spanning spectrum of femtosecond Yb:fiber ring laser at 528 MHz repetition rate in microstructured tellurite fiber. Optics Express. 2013;**21**:4703-4708. DOI: 10.1364/OE.21.004703

[68] Shiyu Y, Lousteau J, Olivero M, Merlo M, Boetti N, Abrate S, Chen Q, Chen Q, Milanese D. Analysis of Faraday effect in multimode tellurite glass optical fiber for magneto-optical sensing and monitoring applications. Applied Optics. 2012;**51**:4542-4546. DOI: 10.1364/AO.51.004542

[69] Sakida S, Hayakawa S, Yoko T. Part 2. ^{125}Te NMR study of M_2O-TeO_2 (M = Li, Na, K, Rb and Cs) glasses. Journal of Non-Crystalline Solids. 1999;**243**:13-25. DOI: 10.1016/S0022-3093(98)00812-6

[70] Himei Y, Miura Y, Nanba T, Osaka A. X-ray photoelectron spectroscopy of alkali tellurite glasses. Journal of Non-Crystalline Solids. 1997;**211**:64-71. DOI: 10.1016/S0022-3093(96)00628-X

[71] Suehara S, Hishita S, Inoue S, Nukui A. Cluster calculational approach to tellurite glasses. Physical Review B. 1998;**58**:14124-14126. DOI: 10.1103/PhysRevB.58.14124

[72] McLaughlin JC, Tagg SL, Zwanziger JW, Haeffner DR, Shastri SD. The structure of tellurite glass: A combined NMR, neutron diffraction, and X-ray diffraction study. Journal of Non-Crystalline Solids. 2000;**274**:1-8. DOI: 10.1016/S0022-3093(00)00199-X

[73] Michel JC, Morin D, Auzel F. Propriétés spectroscopiques et effet laser d'un verre tellurite et d'un verre phosphate fortement dopés en néodyme. Rev. Phys. Appl. 1978; **13**:859-866. DOI: 10.1051/rphysap:019780013012085900

[74] Reisfeld R, Jørgensen CK. Excited state phenomena in vitreous materials. In: Gschneidner KA, Eyring L, editors. Handbook on the Physics and Chemistry of Rare Earths. 1st ed. Amsterdam: Elsevier; 1987. pp. 1-90

[75] Jackson SD. Towards high-power mid-infrared emission from a fibre laser. Nature Photonics. 2012;**6**:423-431. DOI: 10.1038/nphoton.2012.149

[76] Richards B, Jha A, Tsang Y, Binks D, Lousteau J, Fusari F, Lagatsky A, Brown C, Sibbett W. Tellurite glass lasers operating close to 2 μm. Laser Physics Letters. 2010;**7**:177-193. DOI: 10.1002/lapl.200910131

[77] Gomes L, Lousteau J, Milanese D, Scarpignato GC, Jackson SD. Energy transfer and energy level decay processes in Tm^{3+}-doped tellurite glass. Journal of Applied Physics. 2012;**111**:063105. DOI: 10.1063/1.3694747

[78] Gomes L, Milanese D, Lousteau J, Boetti N, Jackson SD. Energy level decay processes in Ho^{3+}-doped tellurite glass relevant to the 3 μm transition. Journal of Applied Physics. 2011;**109**:103110. DOI: 10.1063/1.3587476

[79] Balaji S, Sontakke AD, Sen R, Kalyandurg A. Efficient ~2.0 μm emission from Ho^{3+} doped tellurite glass sensitized by Yb^{3+} ions: Judd-Ofelt analysis and energy transfer mechanism. Optical Materials Express. 2011;**1**:138-150. DOI: 10.1364/OME.1.000138

[80] Wang WC, Yuan J, Li LX, Chen DD, Qian Q, Zhang QY. Broadband 2.7 μm amplifed spontaneous emission of Er^{3+} doped tellurite fibers for mid-infrared laser applications. Optical Materials Express. 2015;**5**:2964-2977. DOI: 10.1364/OME.5.002964

[81] Tian Y, Li B, Chen R, Xia J, Jing X, Zhang J, Xu S. Thermal stability and 2.7 μm spectroscopic properties in Er^{3+} doped tellurite glasses. Solid State Sciences. 2016;**60**:17-22. DOI: 10.1016/j.solidstatesciences.2016.07.012

[82] Gomes L, Oermann M, Ebendorff-Heidepriem H, Ottaway D, Monro T, Librantz AFH, Jackson SD. Energy level decay and excited state absorption processes in erbium-doped tellurite glass. Journal of Applied Physics. 2011;**110**:083111. DOI: 10.1063/1.3651399

[83] Pollnau M, Jackson SD. Mid-infrared fiber lasers. In: Sorokina IT, Vodopyanov KL, editors. Solid-State Mid-Infrared Laser Sources. 1st ed. Berlin Heidelberg: Springer-Verlag; 2003. pp. 225-261. DOI: 10.1007/3-540-36491-9

[84] Richards B, Tsang Y, Binks D, Lousteau J, Jha A. Efficient ~2 μm Tm^{3+}-doped tellurite fiber laser. Optics Letters. 2008;**33**:402-404. DOI: 10.1364/OL.33.000402

[85] Gebavi H, Milanese D, Balda R, Chaussedent S, Ferrari M, Fernandez J, Ferraris M. Spectroscopy and optical characterization of thulium doped TZN glasses. Journal of Physics D: Applied Physics. 2010;**43**:135104. DOI: 10.1088/0022-3727/43/13/135104

[86] Percival RM, Szebesta D, Davey ST. Thulium doped terbium sensitised CW fluoride fibre laser operating on the 1.47 μm transition. Electronics Letters. 1993;**29**:1054-1056. DOI: 10.1049/el:19930703

[87] Miniscalco WJ. Optical and electronic properties of rare earth ions in glasses. In: Digonnet MJF, editor. Rare Earth Doped Fiber Lasers and Amplifiers. 2nd ed. New York: Marcel Dekker; 2001. pp. 17-112. DOI: 10.1201/9780203904657

[88] Jackson SD, King TA. Theoretical modeling of tm-doped silica fiber lasers. Journal of Lightwave Technology. 1999;**17**:948-956. DOI: 10.1109/50.762916

[89] Huang L, Shen S, Jha A. Near infrared spectroscopic investigation of Tm^{3+}–Yb^{3+} co-doped tellurite glasses. Journal of Non-Crystalline Solids. 2004;**345-346**:349-353. DOI: 10.1016/j.jnoncrysol.2004.08.042

[90] Richards B, Tsang Y, Binks D, Lousteau J, Jha A. ∼2 μm Tm^{3+}/Yb^{3+}-doped tellurite fibre laser. Journal of Materials Science: Materials in Electronics. 2009;**20**:S317-S320. DOI: 10.1007/s10854-008-9598-0

[91] Milanese D, Gebavi H, Lousteau J, Ferraris M, Schülzgen A, Li L, Peyghambarian N, Taccheo S, Auzel F. Tm^{3+} and Yb^{3+} co-doped tellurite glasses for short cavity optical fiber lasers: Fabrication and optical characterization. Journal of Non-Crystalline Solids. 2010;**356**:2378-2383. DOI: 10.1016/j.jnoncrysol.2010.03.029

[92] Li K, Zhang G, Hu L. Watt-level ∼2 μm laser output in Tm^{3+}- doped tungsten tellurite glass double-cladding fiber. Optics Letters. 2010;**35**:4136-4138. DOI: 10.1364/OL.35.004136

[93] Li LX, Wang WC, Zhang CF, Yuan J, Zhou B, Zhang QY. 2.0 μm Nd^{3+}/Ho^{3+}-doped tungsten tellurite fiber laser. Optical Materials Express. 2016;**6**:2904-2914. DOI: 10.1364/OME.6.002904

[94] Li K, Zhang Q, Fan S, Zhang L, Zhang J, Hu L. Mid-infrared luminescence and energy transfer characteristics of Ho^{3+}/Yb^{3+} codoped lanthanum–tungsten–tellurite glasses. Optical Materials. 2010;**33**:31-35. DOI: 10.1016/j.optmat.2010.07.010

[95] Balaji S, Gupta G, Biswas K, Ghosh D, Annapurna K. Role of Yb^{3+} ions on enhanced ~2.9 μm emission from Ho^{3+} ions in low phonon oxide glass system. Scientific Reports. 2016;**6**:29203. DOI: 10.1038/srep29203

[96] Snyder AW, Love JD. Optical Waveguide Theory. 1st ed. New York: Springer US; 1984. 738 p. DOI: 10.1007/978-1-4613-2813-1

[97] Okamoto K. Fundamentals of Optical Waveguides. 2nd ed. Burlington, MA, USA: Academic Press; 2005. 584 p

[98] Po H, Snitzer E, Tumminelli L, Zenteno L, Hakimi F, Cho NM, Haw T. Double clad high brightness Nd fiber laser pumped by GaAlAs phased array. In: Proceedings of the Optical Fiber Communication Conference; 6-9 February 1989; Houston. OSA; 1989. p. PD7

[99] Akamatsu T. Continuous fabrication of phosphate glass fiber. Journal of Lightwave Technology. 1983;**1**:580-584. DOI: 10.1109/JLT.1983.1072162

[100] Oh K, Paek U-C. Silica Optical Fiber Technology for Devices and Components: Design, Fabrication, and International Standards. 1st ed. Hoboken, NJ, USA: John Wiley & Sons, Inc.; 2012. 472 p.

[101] Roeder E. Extrusion of glass. Journal of Non-Crystalline Solids. 1971;**5**:377-388. DOI: 10.1016/0022-3093(71)90039-1

[102] Roeder E. Flow behaviour of glass during extrusion. Journal of Non-Crystalline Solids. 1972;**7**:203-220. DOI: 10.1016/0022-3093(72)90290-6

[103] Tran DC, Fisher CF, Sigel GH. Fluoride glass preforms prepared by a rotational casting process. Electronics Letters. 1982;**18**:657-658. DOI: 10.1049/el:19820448

[104] Mitachi S, Miyashita T, Kanamori T. Fluoride-glass-cladded optical fibres for mid-infrared ray transmission. Electronics Letters. 1981;**17**:591-592. DOI: 10.1049/el:19810416

[105] Ohishi Y, Sakaguchi S, Takahashi S. Transmission loss characteristics of fluoride glass single-mode fibre. Electronics Letters. 1986;**22**:1034-1035. DOI: 10.1049/el:19860709

Nonsilica Oxide Glass Fiber Laser Sources: Part II

Xiushan Zhu, Arturo Chavez-Pirson,
Daniel Milanese, Joris Lousteau,
Nadia Giovanna Boetti, Diego Pugliese and
Nasser Peyghambarian

Additional information is available at the end of the chapter

Abstract

Nonsilica oxide glasses have been developed and studied for many years as promising alternatives to the most used silica glass for the development of optical fiber lasers with unique characteristics. Their main properties and compositions, alongside the optical fiber fabrication principle, have been previously reviewed in part I. This chapter will review the development of optical fiber lasers operating in the infrared wavelength region based on nonsilica glass fiber materials, either phosphate, germanate or tellurite.

Keywords: nonsilica oxide glass, phosphate glass, germanate glass, tellurite glass, fiber laser, single-frequency fiber laser, mode-locked laser, high energy pulsed fiber laser, nonlinear wavelength conversion, supercontinuum

1. Introduction

The possibility to dope inorganic glasses with rare-earth (RE) ions has allowed the development of glass-based solid state lasers with various configurations, including bulk, microchip and optical fibers [1]. Optical fiber lasers and amplifiers, in particular, found applications in several fields, ranging from telecom (erbium-doped fiber amplifier, EDFA) to remote sensing (light detection and ranging, LIDAR), materials processing (high power lasers for marking, engraving and cutting) and medicine (for diagnosis and therapy of several diseases) [2].

The development of high power fiber lasers, up to 100 kW, did exploit the subsequent advances in engineering and manufacturing high purity silica optical preforms and fibers

originally intended for telecommunication applications [3]. The recent development of a fiber-based supercontinuum (SC) laser source with super high spectral power density was also made possible thanks to the low optical attenuation level achievable in silica glass and new photonic crystal fiber fabrication technology [4].

Despite its success, however, silica glass possesses several intrinsic limits, as detailed in part I, namely: a high phonon energy around 1100 cm^{-1} [5]; a limited rare-earth doping concentration level [6] and a short infrared transmission edge, which restricts its use for numerous high impact applications, such as mid-infrared (mid-IR) lasers, chemical sensing and infrared imaging [7].

The so-called soft glasses are based on alternative glass formers exhibiting different nature and structure, which offer alternative phonon energies and transmission characteristics, high rare-earth ions doping levels (up to 10^{21} ions/cm^3) and high optical nonlinearity (orders of magnitude higher than that exhibited by silica glass). Soft glasses include oxide and nonoxide glasses.

In this chapter, oxide-based soft glass fiber laser sources are reviewed, and the important aspect of soft glass fiber integration with standard optical components is also discussed. Wavelengths above 1400 nm belong to the so-called eye-safe range, where the eye fluids absorb part of the radiation and additionally the cornea cannot effectively focus the beam into the retina: lasers operating in this interval can be used outdoors at higher power levels without compromising the eye safety issue, being the maximum permissible exposure (MPE) higher [8]. Section 2 reports the main examples of phosphate glass fiber lasers, which mainly focus on emission wavelengths ranging from 1 to 1.5 μm. They include the following types of optical fiber laser sources: continuous-wave (CW) lasers, single-frequency lasers, high repetition rate mode-locked lasers and high energy amplifiers. Germanate fiber lasers are reviewed in Section 3, with a focus on emission wavelengths near or above 2 μm, where the glass composition performs at its best. Finally, Section 4 concerns the main types of tellurite fiber lasers, namely rare-earth-doped lasers and nonlinear wavelength conversion lasers.

2. Phosphate glass fiber lasers

As discussed in part I, the most attractive properties of phosphate glass are high solubility of rare-earth ions and low clustering effects. Therefore, highly doped phosphate fibers can be fabricated with low concentration quenching effects and are capable of producing very large unit gain (> 5 dB/cm). In addition, phosphate glass has large phonon energy and thus energy levels have short lifetimes, which enable high energy transfer rates between co-doped ions and reduce detrimental photodarkening effect. Owing to the high gain per unit length, highly Nd^{3+}-, Yb^{3+}- and Er^{3+}-doped phosphate fibers have been extensively used to develop a lot of short-length (from a few cm to tens of cm) lasers and amplifiers, including continuous-wave fiber lasers, single-frequency fiber lasers, high repetition rate mode-locked fiber lasers and high energy pulsed fiber amplifiers.

2.1. Continuous-wave phosphate fiber lasers

Phosphate fiber lasers were first demonstrated with Nd^{3+}- and Er^{3+}-doped phosphate fibers at 1054 and 1366 nm, and 1535 nm, respectively, by Yamashita in 1989 [9]. However, the output

powers of these fiber lasers using 10-mm long single-mode fibers were less than 1 mW. Later, much higher output power was obtained by using Nd^{3+}-doped multimode phosphate glass fibers [10]. In 2011, a watt-level single-mode Nd^{3+}-doped phosphate fiber laser was demonstrated with an output power of 2.87 W at 1053 nm and an efficiency of 44.7% [11]. However, due to the complicated structure of the energy levels, Nd^{3+}-doped fiber lasers are always susceptible to different detrimental effects, such as cross-relaxation, up-conversion, excited state absorption, etc., which constrain their power scaling. Compared to Nd^{3+}-doped fiber lasers, Yb^{3+}-doped fiber lasers are immune from these efficiency-reducing effects due to their simple energy level structure and are characterized by a lower quantum defect. The first 10-W level phosphate glass fiber laser at the 1 μm band was demonstrated with a 12 wt% Yb^{3+}-doped double-cladding phosphate fiber fabricated by NP Photonics [12]. Nearly 20 W output at 1.07 μm with a slope efficiency of 26.5% was obtained with an 86.4-cm long gain fiber pumped at 940 nm. When a 71.6-cm long 26 wt% Yb^{3+}-doped phosphate fiber was pumped at 977.6 nm, 57 W output at 1.06 μm with an efficiency of 50.6% was obtained even with a propagation loss of this fiber as high as 3 dB/m [13]. The output power of CW Yb^{3+}-doped phosphate fiber lasers is only constrained by the thermal issues. A 100-W level CW Yb^{3+}-doped phosphate fiber laser can be achieved by reducing the fiber loss and improving the fiber thermal management.

Compared to highly Nd^{3+}- and Yb^{3+}-doped phosphate fibers that have been generally used for short-length lasers at 1 μm, Er^{3+}-doped phosphate fibers are more attractive because they can provide very high gain per unit length at the 1.5 μm telecommunication window and thus very short length Er^{3+}-doped fiber amplifiers (EDFAs) can be developed for optical communications. A highly Er^{3+}-doped phosphate fiber was first used for laser amplification at NP Photonics in 2001 [14]. A net gain of 21 dB and a gain per unit length of 3 dB/cm were achieved in a 71-mm long 3.5 wt% Er^{3+}-doped phosphate fiber. Super compact gain module very suitable for signal amplification for local area networks (LANs) has been developed with highly Er^{3+}-doped phosphate fiber as shown in **Figure 1(a)**. The length of the pencil-like gain block is less than 10 cm and its diameter is 3–6 mm. Over 22 dB peak gain and over 15 nm of 10 dB bandwidth have been obtained with such a compact gain module as shown in **Figure 1(b)**. Over 40 dB peak gain can be obtained when a dual-end pumping configuration is used.

The gain or output power of a core-pumped Er^{3+}-doped phosphate fiber amplifier is usually limited by the maximum available power of single-mode pump lasers. In order to increase the gain or output power, double-cladding Er^{3+}/Yb^{3+} co-doped phosphate fibers have been fabricated for cladding-pumping with multimode pump diodes. Due to the high rare-earth solubility and large phonon energy typical of the phosphate glass, highly Er^{3+}/Yb^{3+} co-doped phosphate fibers have very high cladding absorption at 980 nm and very efficient energy transfer from Yb^{3+} to Er^{3+}.

In 2015, high concentration Er^{3+}/Yb^{3+} co-doped double-cladding phosphate fibers have been reported with high gain per unit length, specifically 2.3 dB/cm in cladding-pumping configuration and 4.0 dB/cm in core-pumping arrangement [15].

Several watt-level Er^{3+}/Yb^{3+} co-doped phosphate fiber lasers at the 1.5 μm band have been demonstrated [16–18]. As shown in **Figure 2(a)**, more than 9 W CW 1535 nm multimode output was obtained with a 7.0 -cm long 20-μm core Er^{3+}/Yb^{3+} co-doped phosphate fiber, corresponding to a very high output power per unit fiber length of 1.33 W/cm. Diffraction-limited output with
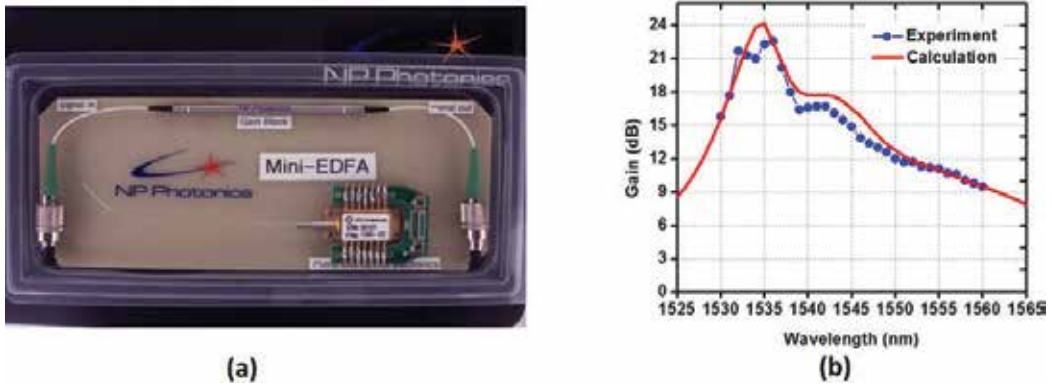
Figure 1. (a) Photograph of a NP photonics mini-EDFA with a pencil-like gain module pumped by a fiber-coupled laser diode; (b) calculated and measured gain of the NP photonics mini-EDFA.
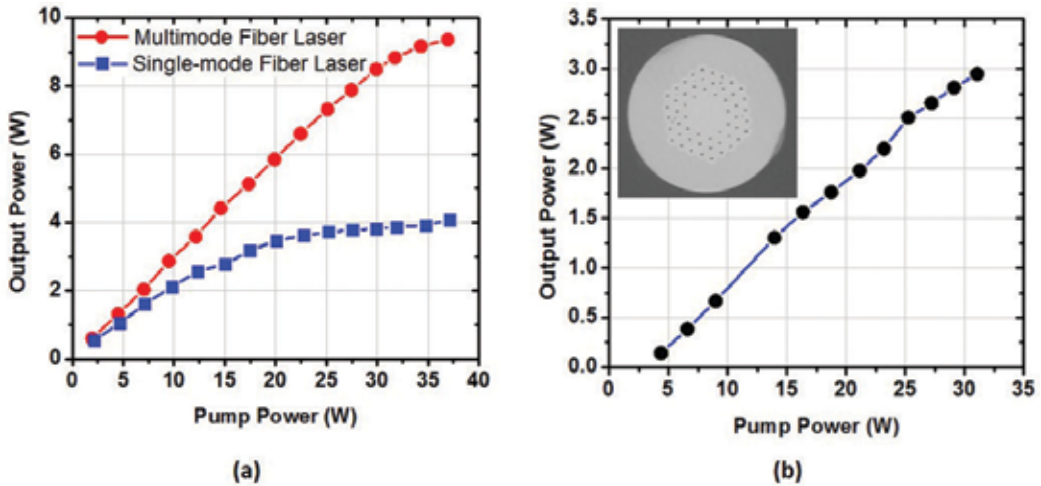
Figure 2. (a) Output power as a function of the pump power for a multimode and a single-mode Er^{3+}/Yb^{3+} co-doped phosphate fiber laser; (b) output power of an Er^{3+}/Yb^{3+} co-doped microstructured phosphate fiber laser as a function of the pump power. Inset: Microscope image of the microstructured phosphate fiber.

an output power of 4 W and $M^2 = 1.1$ was generated with a 7.1-cm long single-mode Er^{3+}-Yb^{3+} co-doped phosphate fiber with a core diameter of 13 μm and core numerical aperture (NA) of 0.08. Phosphate glass microstructured fiber with an active core area larger than 400 mm^2 was also fabricated as shown in **Figure 2(b)** and more than 3 W near diffraction-limited output was obtained with a 11-cm long Er^{3+}/Yb^{3+} co-doped phosphate microstructured fiber.

Although the CW output powers of the highly doped phosphate fiber lasers presented here are much lower than those of the counterpart silica fiber lasers, these experiments have shown the potential and promise of producing high energy single-frequency lasers and ultrashort lasers by using short-length highly doped phosphate fibers, in which the accumulated nonlinearity is significantly reduced.

2.2. Single-frequency phosphate fiber lasers

Single-frequency lasers operating with only a single-longitudinal mode can emit quasi-monochromatic radiation with very narrow linewidth and ultralow noise. Conventional fiber lasers generally consist of meters of fiber with linear cavity configuration and thus cannot generate single-frequency laser output due to the spatial hole burning. Unidirectional ring cavity combined with a narrow-band filter and a very short linear cavity combined with narrow-band fiber Bragg gratings (FBGs) are two major approaches to achieve single-frequency fiber lasers. However, ring cavity single-frequency fiber lasers usually suffer from second mode and mode hopping. Both distributed Bragg reflector (DBR) and distributed feedback (DFB) fiber lasers with a several centimeter long cavity can offer robust single-frequency operation without mode hopping. But the output power of a DFB single-frequency fiber laser is limited due to the very short length of the gain fiber. Moreover, the stability of DFB fiber lasers is low because the FBG is inscribed in the gain fiber where thermal noises will greatly impair the performance of the laser. DBR single-frequency fiber laser can provide robust single-frequency operation at watt-level output power and at sub-kilohertz linewidth. DBR single-frequency fiber lasers also offer easy and convenient way to tune and stabilize the laser wavelength due to their unique configuration. As depicted in **Figure 3(a)**, a DBR single-frequency fiber laser consists of a short piece of gain fiber and two fiber Bragg gratings (FBGs). The free spectral range of a laser cavity is defined as:

$$\Delta v = \frac{c}{2nL} \tag{1}$$

where c is the light speed, n is the refractive index of the optical fiber core and L is the length of the fiber laser cavity. Therefore, robust single-frequency operation of a fiber laser can be obtained only when L is very short and the free spectral range of the laser cavity is so large that only one longitudinal mode is allowed to oscillate within the narrow bandwidth of the
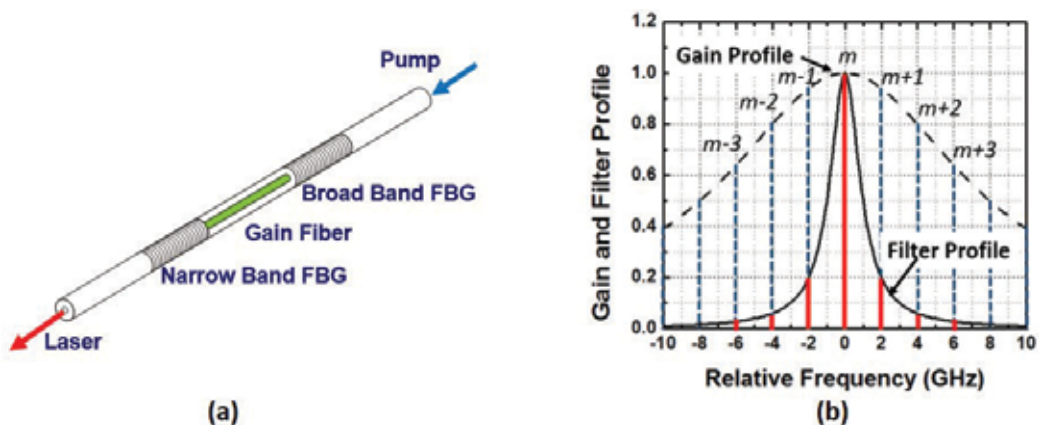

Figure 3. (a) The configuration of a DBR single-frequency fiber laser; (b) single-longitudinal mode operation of a short-length DBR laser ensured by the narrow bandwidth transmission of a FBG.

narrow-band FBG, as depicted in **Figure 3(b)**. Highly doped phosphate glass fibers exhibiting extremely high optical gain per unit length with negligible ion clustering are uniquely suitable for short-length linear cavity single-frequency fiber lasers.

A highly Er^{3+}/Yb^{3+} co-doped phosphate fiber was first used to develop a DBR single-frequency fiber laser at 1560 nm with an output power higher than 200 mW and a very narrow linewidth of less than 2 kHz [19]. Single-frequency fiber lasers exhibit excellent features of low noises, high stability and narrow spectral linewidth, which are usually characterized by optical signal-to-noise ratio (SNR), relative intensity noise (RIN), frequency noise and spectral linewidth. The optical SNR of a single-frequency fiber laser is usually measured with an optical spectrum analyzer using the highest spectral resolution. A typical spectrum of a 1550 nm single-frequency fiber laser is shown in **Figure 4(a)**, exhibiting over 85 dB optical SNR. The RIN is a key parameter to characterize the optical power fluctuation of a laser. The typical RIN of a single-frequency fiber laser is shown in **Figure 4(b)**. The RIN typically has a peak at the relaxation oscillation frequency of the laser and then decreases with the increased frequency until it converges to the shot noise level. The relaxation frequency peak of the RIN can usually be suppressed with a close-loop servo system as shown in the inset of **Figure 4(b)**. The frequency noise is the random fluctuation of the instantaneous frequency of a single-frequency laser. The frequency noise is generally directly measured by frequency discriminators, which convert frequency fluctuation to intensity fluctuation and then measure the power spectral density. The measured frequency noise of DBR single-frequency fiber lasers at 1550 and 1060 nm is shown in **Figure 4(c)**. The frequency noise typically decreases with the increased frequency and exhibits some spikes related to various noises. Due to the various laser noises, a single-frequency laser is not perfectly monochromatic and has finite spectral linewidths. The spectral linewidth of a single-frequency fiber laser is usually measured with heterodyne detection and delayed self-heterodyne detection methods. A linewidth measurement result of a noise-suppressed DBR single-frequency fiber laser at 1550 nm assessed with the delayed self-heterodyne detection method is shown in **Figure 4(d)**. A very narrow spectral linewidth of 500 Hz can be estimated from the −20 dB spectral bandwidth of 10.5 kHz.

The output power of a core-pumped single-frequency fiber laser is limited by the available pump power of single-mode pump diodes and is generally at a level of few hundreds of mW. A higher output power of a single-frequency fiber laser can be achieved with cladding-pumping. A cladding-pumped monolithic all-phosphate glass single-frequency fiber laser was demonstrated by inscribing FBGs directly into heavily Er^{3+}/Yb^{3+} co-doped phosphate glass fiber using femtosecond laser pulses and a phase mask [20]. A robust single-frequency output with power up to 550 mW and a spectral linewidth less than 60 kHz was obtained. In Ref. [21], a 1.6 W single-frequency fiber laser was demonstrated with a double-cladding phosphate fiber with a 18 μm core doped with 1 wt% Er^{3+} and 8 wt% Yb^{3+} ions and a 125 μm cladding.

In addition to single-frequency fiber lasers operating at the 1.5 μm band, several single-frequency fiber lasers at the 1 μm band developed with highly Yb^{3+}-doped phosphate fibers were reported [22–25]. Over 400 mW single-frequency laser output at 1.06 μm was achieved from a 0.8-cm long 15.2 wt% Yb^{3+}-doped phosphate fiber [22]. The measured slope efficiency and estimated quantum efficiency of laser emission are 72.7% and 93%, respectively. In Ref. [23], an all-fiber actively Q-switched single-frequency fiber laser at 1064 nm was developed by using a piezoelectric to
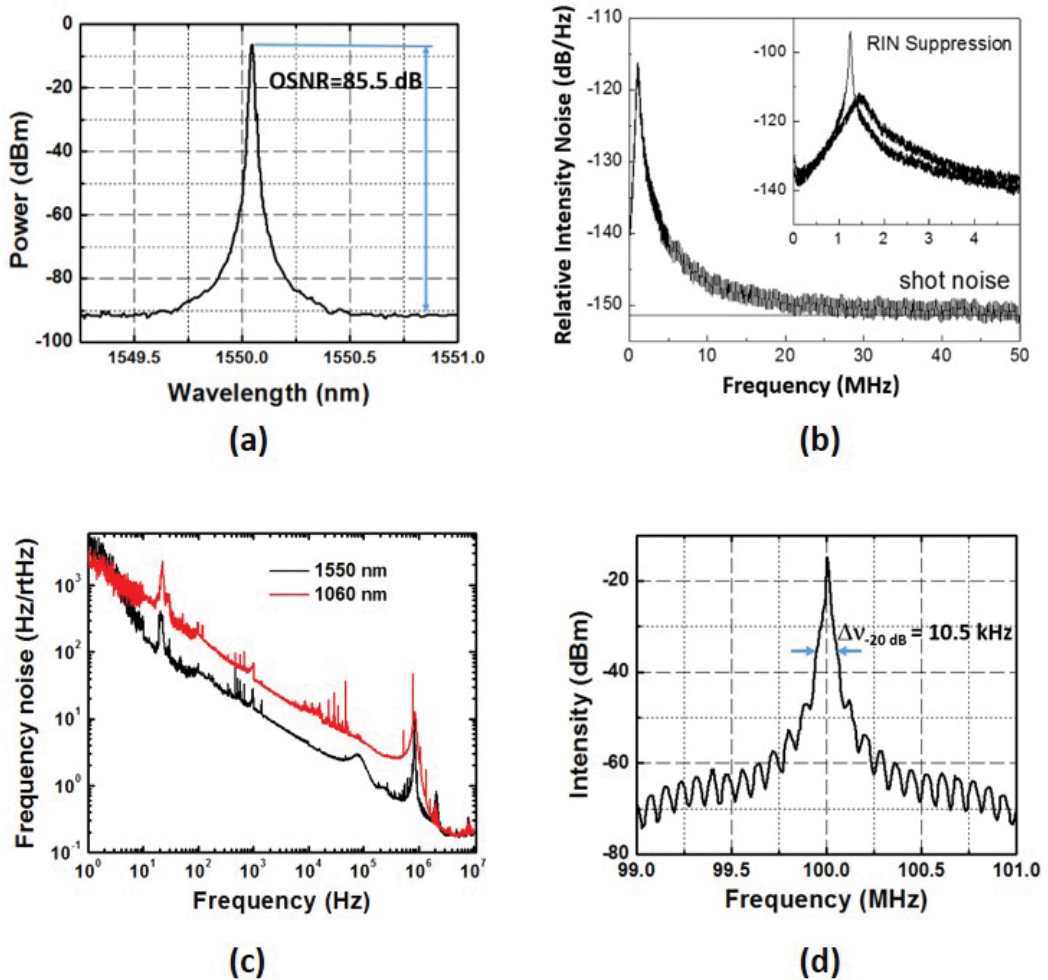
Figure 4. (a) Optical spectrum and (b) RIN of a DBR single-frequency fiber laser at 1550 nm; (c) frequency noises of DBR single-frequency fiber lasers at 1060 and 1550 nm; (d) typical spectral linewidth measurement result of self-delayed heterodyne detection for a DBR single-frequency fiber laser at 1550 nm.

press the fiber and modulate the fiber birefringence. Q-switched single-frequency laser operation at repetition rates tunable from several Hz to up to 700 kHz was demonstrated. In 2016, a single-frequency Yb^{3+} fiber laser operating at a wavelength longer than 1100 nm was demonstrated with a 3.1-cm long 15.2 wt% Yb^{3+}-doped phosphate fiber [24]. More than 62 mW single-frequency laser output with a linewidth of 5.7 kHz was obtained.

Highly Yb^{3+}-doped phosphate fibers have also been used to develop single-frequency laser sources at 976 nm, which are highly demanded for nonlinear wavelength conversion to generate coherent blue light at the 488 nm argon-ion laser wavelength. The energy level diagram of Yb^{3+} ions is shown in **Figure 5(a)**. The ground state absorption of the 915 nm pump corresponds to a transition from the lowest level of the $^2F_{7/2}$ manifold to the upper level of the $^2F_{5/2}$ manifold. The transition from the lowest level of the excited state $^2F_{5/2}$ manifold to the lowest level of the

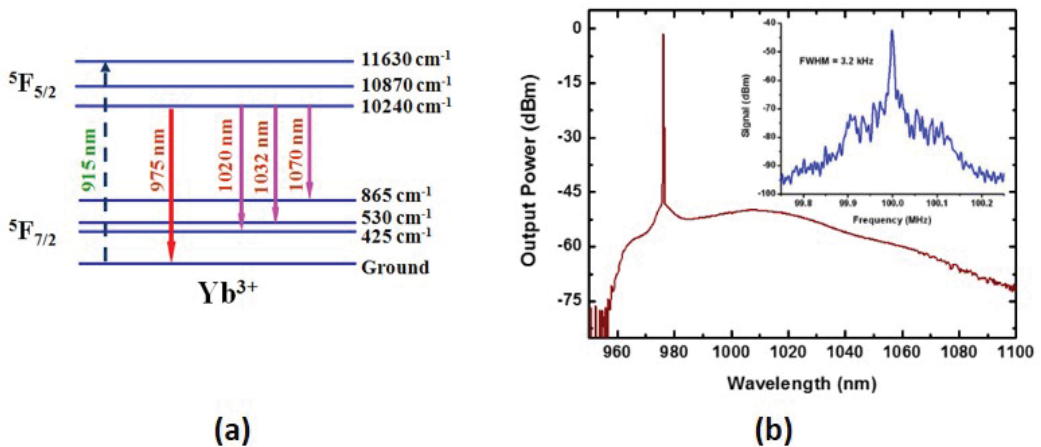**Figure 5.** (a) The energy level diagram of Yb³⁺ ions; (b) optical spectrum of a 976 nm single-frequency fiber laser. Inset: Spectral linewidth measurement result of self-delayed heterodyne detection for the 976 nm single-frequency fiber laser.

ground state $^2F_{7/2}$ manifold produces the laser emission at 976 nm. A DBR single-frequency fiber laser at 976 nm was first developed with a 2-cm long 6 wt% Yb³⁺-doped phosphate fiber and a pair of silica FBGs [25]. More than 100 mW of linearly polarized output were achieved from the all-fiber DBR laser with a linewidth less than 3 kHz. **Figure 5(b)** shows the optical spectrum and the spectral linewidth measurement result of the 976 nm single-frequency fiber laser.

In order to further increase the power level of the 976 nm single-frequency fiber lasers, core- and cladding-pumped highly Yb³⁺-doped phosphate fiber amplifiers have been investigated [25, 26]. A 6 wt% Yb³⁺-doped phosphate polarization maintaining (PM) fiber with a core diameter of 6 μm and a core NA of 0.14 as shown in the inset of **Figure 6(a)** was used for the investigations of core-pumped single-frequency fiber amplifiers [25]. **Figure 6(a)** shows the experimental results, and over 350 mW linearly polarized output with a slope efficiency of 52.5% was obtained from a 4-cm long fiber amplifier. A small signal net gain of 25 dB, corresponding to a unit gain of over 6 dB/cm, was achieved with this fiber. The output power of the core-pumped fiber amplifier is limited by the available single-mode pump power at 915 nm. In order to further increase the 976 nm single-frequency laser output, cladding-pumping with multimode diodes has to be used. The inset of **Figure 6(b)** shows the microscopic image of an Yb³⁺-doped double-cladding phosphate fiber that was used to investigate the power scaling of a 976 nm single-frequency fiber amplifier. This double-cladding phosphate fiber, characterized by a core diameter of 18 μm and a core NA of 0.04, is able to support only the fundamental transverse mode at 976 nm. The inner circular cladding has a diameter of 135 μm and a NA of 0.45. The outer cladding is also made of phosphate glass and its diameter is 150 μm. The core was uniformly doped with 6 wt% Yb³⁺ ions. The output powers of the cladding-pumped fiber amplifiers with different gain fiber lengths (L_f) were measured as shown in **Figure 6(b)**. The output powers of the 6.5, 7, 8 and 10-cm long fiber amplifiers are 2.58, 3.41, 3.14 and 3.12 W, respectively, at the maximum launched pump power of 70 W. The slope efficiencies of the cladding-pumped fiber amplifiers are much lower than those of the core-pumped fiber amplifiers. This is mainly due to the relatively low spatial
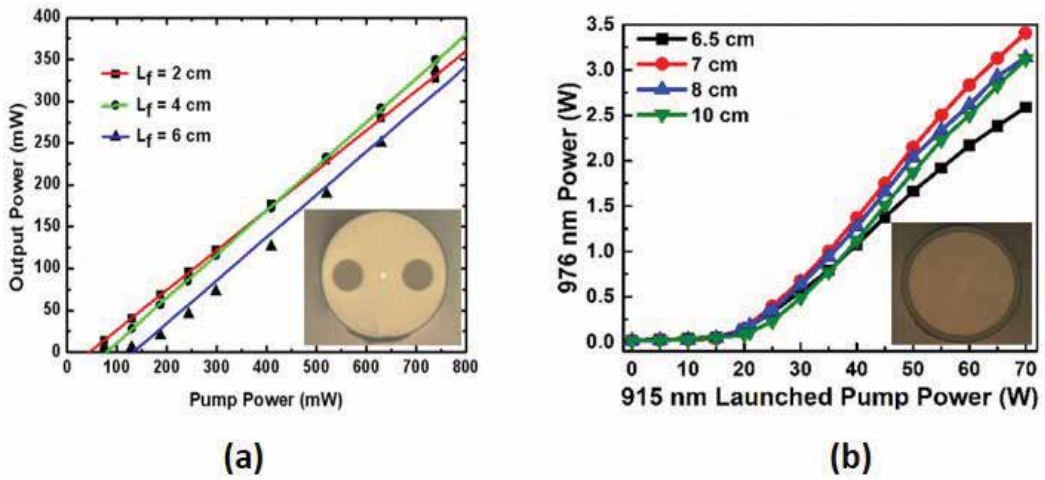
Figure 6. (a) Output power as a function of the pump power of core-pumped single-frequency Yb^{3+}-doped phosphate fiber amplifiers at 976 nm. Inset: Microscopic image of a 6 μm core PM 6 wt% Yb^{3+}-doped phosphate fiber. (b) Output power as a function of the pump power of cladding-pumped single-frequency Yb^{3+}-doped phosphate fiber amplifiers at 976 nm. Inset: Microscopic image of an 18 μm core 6 wt% Yb^{3+}-doped phosphate fiber.

overlap between the pump and the doped fiber core in the cladding-pumping configuration. The output power and the efficiency of the cladding-pumped single-frequency laser fiber amplifier can be significantly improved by using a phosphate fiber with an optimal concentration, a small inner cladding, a large core and a specific waveguide to suppress the long wavelength amplified spontaneous emission (ASE).

2.3. High repetition rate mode-locked phosphate fiber lasers

High repetition rate mode-locked lasers are essentially needed in many fields of science and industry, including material processing, accelerator applications, frequency comb spectroscopy, metrology and coherent control. Passively mode-locked fiber lasers have shown their capability of generating transform-limited pulses in the picosecond regime due to their simplicity and reliability. A drawback of the conventional passively mode-locked fiber lasers is that the pulse repetition rate is at a level of tens of MHz due to the long cavity length (several meters). The repetition rate f_{rep} of a linear cavity fiber laser operating in the fundamental mode locking is expressed as:

$$f_{rep} = \frac{c}{2nL} \tag{2}$$

where L is the cavity length, n is the effective refractive index and c is the velocity of the light in vacuum. To obtain a GHz repetition rate mode-locked fiber laser, the fiber length has to be less than 10 cm. Due to the low absorption coefficient of a conventional silica fiber, which is limited by the low RE solubility of silica glass, it is hard to generate a high-efficiency GHz repetition rate mode-locked laser using conventional silica fiber laser technology. This problem can be solved with highly doped phosphate fiber laser technology.

Because of the extremely high absorption of the highly doped phosphate fibers, mode-locked laser oscillators in all-fiber format with excellent stability and reliability can be developed. As shown in **Figure 7(a)**, an all-fiber mode-locked laser at 1034 nm was made by splicing a 5-cm long 6 wt% Yb^{3+}-doped phosphate fiber to a 3-cm long chirped FBG and the 2-cm long pigtail of a fiber-optic semiconductor saturable absorber mirror (SESAM). The total length of the mode-locked fiber laser cavity is about 10 cm, corresponding to a repetition rate of 1 GHz. The pulse train of this laser was measured by a fast photodetector and is shown in **Figure 7(b)**. The optical spectrum of the 1 GHz repetition rate mode-locked fiber laser is shown in **Figure 7(c)**. The pulse width of this laser was measured by an auto-correlator to be about 16 ps.

The total length of a chirped FBG usually needs to be 3 cm or more so that its bandwidth is sufficiently broad to support the operation of a mode-locked laser. Therefore, a chirped FBG cannot be used to develop an all-fiber mode-locked fiber laser as its repetition rate is larger than 3 GHz. A fiber mirror fabricated by depositing a dichroic thin film onto the fiber end-face can be used as the cavity coupler of a fiber laser. Therefore, the fiber cavity length can be 1 cm or shorter and 10 GHz repetition rate mode-locked fiber lasers can be developed. The first 10 GHz repetition rate mode-locked fiber laser was reported in 2007 [27]. A heavily Er^{3+}/Yb^{3+} co-doped phosphate fiber was used to form 1-cm long cavity with fiber mirrors. Stable mode-locked pulse trains with output power as high as 30 mW at 1535 nm were obtained. In [28], a compact and stable all-fiber fundamentally mode-locked laser system with a repetition rate of 12 GHz was developed with the configuration shown in **Figure 8(a)**. The self-starting mode-locked laser consists of a SESAM with low modulation depth and a high gain per unit length and a polarization maintaining 0.8-cm long Er^{3+}/Yb^{3+} phosphate fiber as gain medium. The optical spectrum of the 12 GHz repetition rate mode-locked fiber laser is shown in **Figure 8(b)**. The 12 GHz repetition rate was confirmed by the modulation of the high resolution (0.01 nm) spectrum. This mode-locked fiber laser has a temporal pulse width of ~2.3 ps and an average power of 5 mW at a pump power of 400 mW. The timing jitter has been measured using an optical cross-correlation method and found to be 44 fs/pulse.
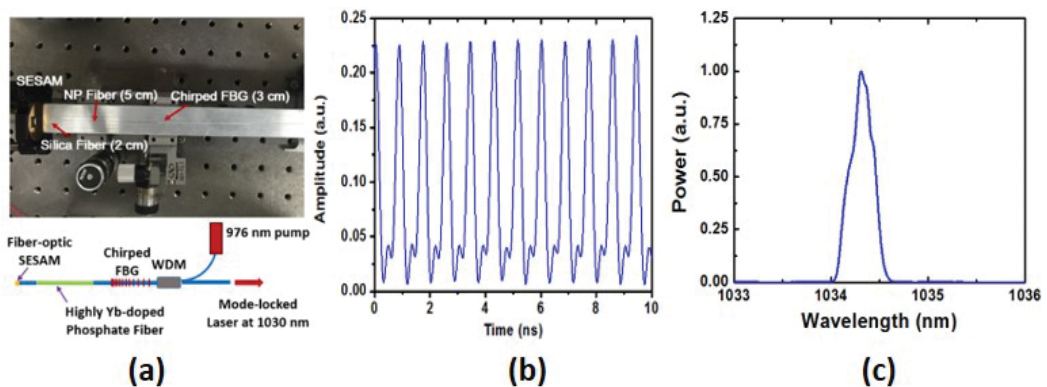

Figure 7. (a) Configuration and setup, (b) pulse train and (c) optical spectrum of a monolithic 1 GHz repetition rate mode-locked Yb^{3+}-doped phosphate laser.
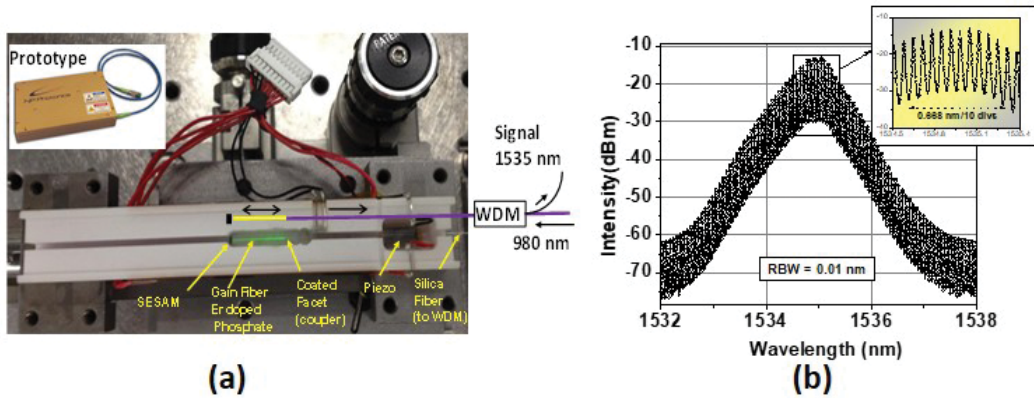
Figure 8. (a) The experimental setup and (b) output optical spectrum of a 12 GHz repetition rate SESAM mode-locked Er^{3+}-doped phosphate fiber laser.

2.4. High energy phosphate fiber amplifiers

The energy of a pulsed laser oscillator is generally much lower than the levels required for the applications. Fiber amplifiers have been extensively used to scale up the power/energy of a laser system because of their high single-pass gains and excellent heat dissipation capability. However, due to the inherent long interaction length of a conventional silica fiber amplifier, its output energy is usually constrained by nonlinear effects including self-phase modulation (SPM), stimulated Raman scattering (SRS), stimulated Brillouin scattering (SBS) and four-wave mixing (FWM), which deform the pulses both in temporal and spectral domains. Highly rare-earth doped phosphate fibers allow the construction of rather short fiber amplifiers enabling high energy pulse amplification less prone to nonlinear distortions. In addition, the nonlinear refractive index of phosphate glass is three times lower and the SBS gain cross-section is 50% weaker than those of silica glass. Moreover, the photodarkening effect in phosphate glass is also much less pronounced than in silica glass [29]. Therefore, highly doped phosphate glass fibers are excellent energy engines for a high energy fiber laser system.

High energy single-frequency laser sources are in great demand for a variety of applications including LIDAR, remote sensing, free-space communication and laboratory research. However, the power scaling of single-frequency lasers has been difficult to obtain in fiber amplifiers due to limitations primarily related to the SBS, which converts a fraction of the desired laser light to a backscattered Stokes-shifted reflection. SBS builds up strongly in the fiber because of the long interaction length and small mode field area. So, it has been difficult to achieve high peak power, single-transverse mode and narrow linewidth operation simultaneously in a fiber laser system, especially for a monolithic all-fiber configuration. The threshold for SBS in an optical fiber is determined by the parameters of the fiber to be:

$$P_{th} = \frac{21\, A_{eff}}{L_{eff}\, g_B} \tag{3}$$

where A_{eff} is the effective mode field area, L_{eff} is the effective length of the optical fiber and g_B is the SBS gain of the glass fiber. Therefore, using short length and large core fiber is a key approach to elevate the peak and average powers for single-frequency lasers. Highly doped phosphate fibers with large mode area have been widely used to achieve nanosecond single-frequency pulses at the 1 and 1.55 μm bands [30–34].

Figure 9(a) shows the output pulse energy and peak power of a highly Yb^{3+}-doped phosphate fiber amplifier for 1064 nm 2 ns pulsed single-frequency laser [33]. The 6 wt% Yb^{3+}-doped phosphate fiber has a core diameter of 25 μm and a cladding of 250 μm, as shown in the inset of **Figure 9(a)**. An average power of 32 W, a pulse energy of 90 μJ and a peak power of 45 kW were obtained with a 45-cm long gain fiber at a pump power of 55 W. **Figure 9(b)** shows the output pulse energy and peak power of a highly Er^{3+}/Yb^{3+} co-doped phosphate fiber amplifier for 1530 nm 105 ns pulsed single-frequency laser [34]. The fiber core is doped with 3 wt% Er^{3+} and 15 wt% Yb^{3+}. The core and cladding diameters of this fiber are 25 and 400 μm, respectively. A single-frequency pulsed laser with a peak power of 1.2 kW at a repetition rate of 8 kHz, corresponding to a pulse energy of 126 μJ, was obtained with a 15 -cm long gain fiber at a pump power of 75 W. When the pulse width of the single-frequency pulses is 10 ns, over 50 kW peak power has also been achieved with a SBS-free highly Er^{3+}/Yb^{3+} co-doped phosphate fiber amplifier [30, 32].

High energy ultrashort pulsed laser sources have enormous impact on many disciplines of science and technology. Solid state mode-locked laser sources, namely Ti:sapphire lasers, have shown their excellence in producing high energy ultrashort pulses. However, Ti:sapphire laser sources usually operate with repetition rates in the kilohertz range, and the output power is still at watt level limited by the thermal issues and low efficiencies. The fast acquisitions and high yields of various applications are currently boosting demands for ultrafast laser sources with high average power and high repetition rate. Fiber amplifiers are high-efficiency energy engine for power scaling of high repetition rate mode-locked lasers. However, the energy
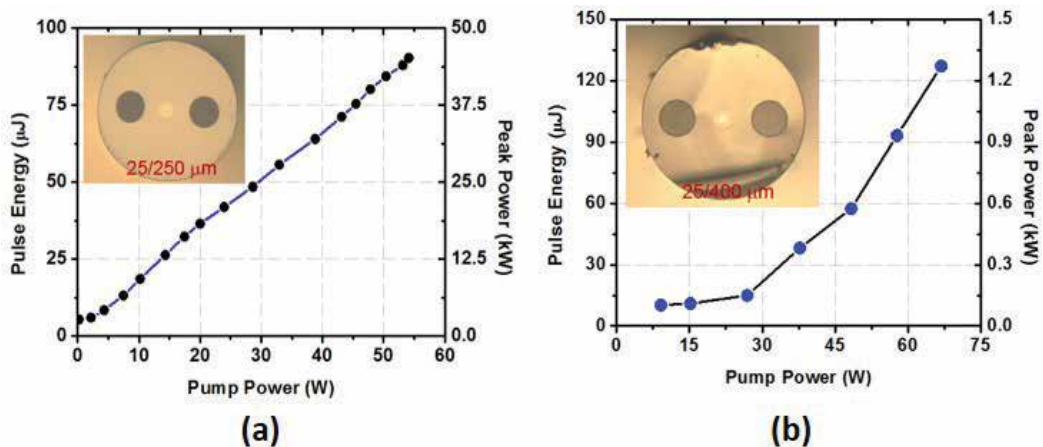

Figure 9. (a) Pulse energy and peak power of a 25/250 μm Yb^{3+}-doped phosphate fiber amplifier for 1064 nm 2 ns single-frequency laser; (b) pulse energy and peak power of a 25/400 μm Er^{3+}/Yb^{3+} co-doped phosphate fiber amplifier for 1530 nm 105 ns single-frequency laser.

scaling of a mode-locked fiber laser system usually suffers from pulse distortion caused by SPM as the pulses propagate through the fiber. The magnitude of the SPM is quantified by the *B*-integral and is proportional to both the beam irradiance inside the amplifier and the propagation length, as shown in the following equation:

$$B = \frac{2\pi}{\lambda} \int_0^L n_2 I(z)dz = \frac{2\pi}{\lambda A_{eff}} \int_0^L n_2 P(z)dz \tag{4}$$

where λ is the laser wavelength, n_2 is the nonlinear refractive index coefficient, $I(z)$ is the pulse peak irradiance along the propagation direction, $P(z)$ is the pulse peak power, L is the total fiber length and A_{eff} is the fiber effective mode area. A *B*-integral of less than π radians is considered linear propagation. Above this value, nonlinear phase accumulation will impose temporally broadened pulses and/or significant pulse pedestal. Therefore, compared to several meters of silica fiber amplifiers, sub-50 cm highly doped phosphate fiber amplifiers are more favorable for mode-locked laser amplification because much less nonlinear distortion is experienced. Highly doped phosphate fiber amplifiers have already been used to demonstrate direct picosecond pulse amplification with low distortion and achieve mJ-level femtosecond laser using the chirped pulse amplification technique [35–37].

Figure 10(a) shows the output average power of a 6 wt% Yb^{3+}-doped phosphate amplifier for direct amplification of 1.86 MHz repetition rate picosecond pulses at 1064 nm. The Yb^{3+}-doped phosphate fiber has a core size of 25 μm and a cladding size of 250 μm. Over 20 W output power was obtained with a 40-cm long gain fiber at a pump power of 40 W. In [35], a 1 wt% Er^{3+} and 8 wt% Yb^{3+} co-doped phosphate fiber amplifier was used to directly amplify picosecond mode-locked pulses at 1.55 μm. An average output power of 1.425 W at a repetition rate of 70 MHz, corresponding to a pulse energy and peak power of 20.4 nJ and 16.6 kW, respectively, was obtained with a 15 cm long fiber with a core size of 14 μm. In [36], a 2 wt% Er^{3+}-doped phosphate
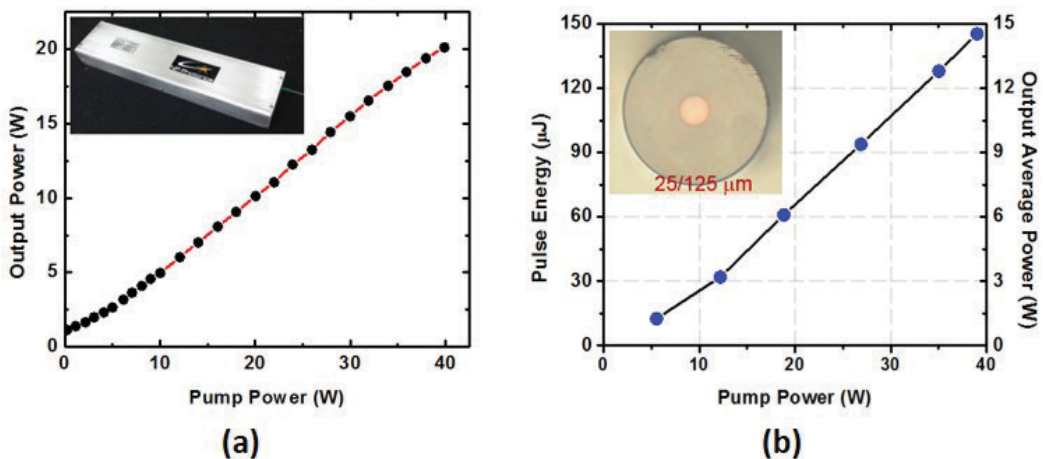

Figure 10. (a) Output average power of an Yb^{3+}-doped phosphate fiber amplifier module (shown in the inset) for 1064 nm 1 MHz 15 ps mode-locked laser; (b) pulse energy and average power of a 25/125 μm Er^{3+}-doped phosphate fiber amplifier for 100 kHz mode-locked laser at 1550 nm.

fiber with a core size of 25 μm and a cladding of 125 μm was fabricated as shown in the inset of **Figure 10(b)** for in-band high-efficiency chirped pulse amplification of a 1.55 μm mode-locked laser. As shown in **Figure 10(b)**, ultrashort pulses with pulse energy >140 μJ and average power of 14 W were obtained with a 20-cm long gain fiber at a 1480 nm pump power of 40 W. A peak power of ~160 MW was obtained with the compressed pulses. This 2 wt% Er^{3+}-doped phosphate fiber yields a gain of 1.443 dB/cm with a slope efficiency >45% for the 100 kHz repetition rate pulses. To further increase the pulse energy, a 1.5 wt% Er-doped phosphate fiber with a core size of 75 μm and a cladding of 250 μm was fabricated [37]. An average output power of 8.5 W at a repetition rate of 4.8 kHz, corresponding to a pulse energy of 1.77 mJ, was obtained with a 28-cm long gain fiber at a pump power of 63 W. Sub-500 fs pulses with a pulse energy of nearly 1 mJ and a peak power of 1.9 GW were obtained after pulse compression.

3. Germanate fiber lasers

Laser sources operating at the 2 μm region are preferred over 1.5 μm Er^{3+} lasers and 1 μm Yb^{3+} and Nd^{3+} lasers for long-range applications, including direct energy laser weapon, LIDAR and sensing systems and direct optical communication, because atmospheric scattering, atmospheric distortion and thermal blooming significantly reduce while increasing the operating wavelength. In addition, 2 μm lasers have found unique applications in nonmetal material processing, especially plastics, highly precise laser surgery and ideal pump sources for high-efficiency mid-infrared or THz laser systems. Although phosphate glasses have shown excellence in making short-length fiber lasers and amplifiers at the 1 μm and 1.55 μm bands, they are not good host material for Tm^{3+} and Ho^{3+} lasers operating at the 2 μm region due to their increased multi-phonon absorption and nonradiative decay. Compared to silica and phosphate glasses, germanate glass has lower phonon energy and longer IR absorption edge. Therefore, Tm^{3+} and Ho^{3+} germanate glass fibers have been fabricated as high-efficiency gain media for fiber laser systems operating at the 2 μm region.

3.1. Single-frequency highly doped germanate fiber lasers

Single-frequency laser sources operating at the 2 μm region are in great demand for various LIDARs. Since germanate glass also displays high RE solubility, highly Tm^{3+}- and Ho^{3+}-doped single-mode germanate glass fibers have been fabricated for the development of DBR single-frequency fiber lasers at 2 μm [38, 39]. A 2-cm long 5 wt% Tm^{3+}-doped germanate fiber with a core diameter of 7 μm and NA of 0.15 was used to develop a single-frequency fiber laser at 1893 nm [38]. As shown in **Figure 11(a)**, this single-frequency fiber laser has a pump threshold of 30 mW, a slope efficiency of 35% and a maximum output power of over 50 mW with respect to the launched power of a single-mode pump laser diode at 805 nm. **Figure 11(b)** shows the output power and optical spectrum (inset) of a 2.05 μm single-frequency fiber laser developed with a 2-cm long 3 wt% Ho^{3+}-doped germanate fiber. This single-frequency Ho^{3+}-doped germanate fiber laser was pumped by a Tm^{3+}-doped fiber laser at 1950 nm. Over 60 mW output power was obtained with the maximum available pump power.
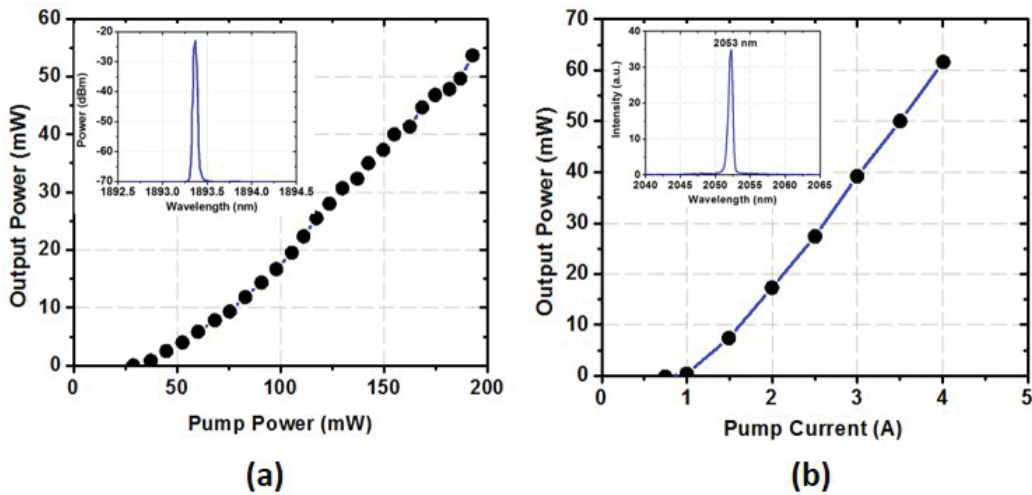
Figure 11. (a) Output power and optical spectrum (inset) of a single-frequency Tm^{3+}-doped germanate fiber laser operating at 1893 nm; (b) output power and optical spectrum (inset) of a single-frequency Ho^{3+}-doped germanate fiber laser operating at 2053 nm.

3.2. High power Tm^{3+}-doped germanate fiber lasers and amplifiers

Tm^{3+} ion is a favorable active element for laser emission at the 2 μm spectral band because of its high quantum efficiency, broad emission band and strong absorption band at 800 nm, where high power and efficiency AlGaAs laser diodes are commercially available. Most importantly, a slope efficiency exceeding the Stokes efficiency can be obtained with Tm^{3+} lasers due to the cross-relaxation energy transfer process ($^3H_6$, $^3H_4 \rightarrow \,^3F_4$, $^3F_4$) between Tm^{3+} ions, which results in a quantum efficiency of 200%. The effect of cross-relaxation energy transfer between Tm^{3+} ions in a germanate glass was verified by the decreased 1.48 μm emission with the increased Tm^{3+} ion concentration [40]. A very high slope efficiency of 58% with respect to the launched power, corresponding to a quantum efficiency of 1.79, was demonstrated with a 4-cm long 4 wt% Tm^{3+}-doped germanate single-mode fiber laser. However, the output power of this single-mode fiber laser is at tens of mW level, which is mainly limited by the available power of single-mode AlGaAs diodes at 800 nm.

In order to develop a high power fiber laser source at 2 μm, highly Tm^{3+}-doped germanate double-cladding fibers with large mode area (LMA) cores were fabricated for cladding-pumping with high power multimode laser diodes [41]. A 64 W fiber laser at 1.9 μm was developed with a 20-cm long 4 wt% Tm^{3+}-doped germanate double-cladding fiber with a core diameter of 50 μm and a NA of 0.02, corresponding to a *V*-number of 1.96. As shown in **Figure 12**, a slope efficiency (SE) of 68% with respect to the launched pump power at 800 nm was demonstrated with single-end pumping configuration, indicating that a quantum efficiency of 1.8 was achieved. As more pump power was launched into the Tm^{3+}-doped germanate fiber by using a dual-end pumping configuration, a 100-W level fiber laser was demonstrated with a 42/200 μm double-cladding fiber, and a slope efficiency of 52.5% was obtained.
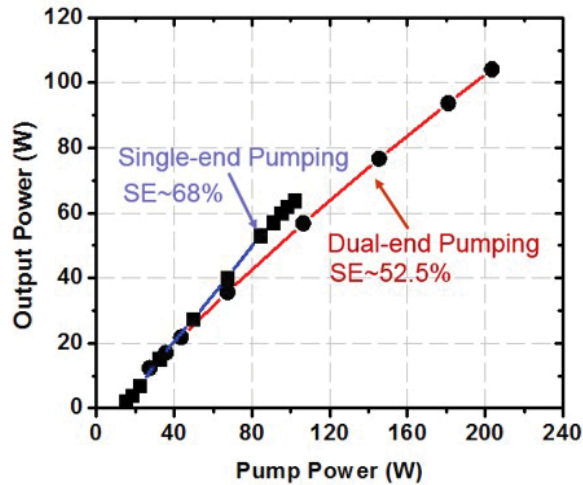
Figure 12. Output power of a single-end pumped 20-cm long 50/200 µm 4 wt% Tm³⁺-doped germanate fiber laser and of a dual-end pumped 40-cm long 42/200 µm 4 wt% Tm³⁺-doped germanate fiber laser.

High energy single-frequency pulsed fiber laser sources have also been demonstrated with highly Tm³⁺-doped germanate fibers [42–44]. In [42], an all-fiber single-frequency Q-switched laser source at 1.92 µm with a pulse energy of 220 µJ was achieved with a monolithic master oscillator and power amplifier (MOPA) configuration. A 2-cm long 5 wt% Tm³⁺-doped germanate fiber was first used to develop an actively Q-switched single-frequency fiber laser oscillator by using a piezo to press the fiber of the DBR cavity. Tens of ns pulses with tunable width from tens of ns to 300 ns and transform-limited linewidths were obtained. Then, two Tm³⁺-doped silica fiber amplifiers were used in cascade to increase the pulse energy to 14 µJ. A 20-cm long 4 wt% Tm³⁺-doped germanate double-cladding fiber with a core diameter of 25 µm and a cladding diameter of 250 µm was used for the last stage of the power amplifier. For 80 ns pulses at a repetition rate of 20 kHz, a pulse energy of 220 µJ, corresponding to a peak power of 2.75 kW, was obtained. **Figure 13(a)** shows the pulse energy and peak power of a power amplifier constituted by a 30-cm long 25/250 µm 4 wt% Tm³⁺-doped germanate fiber and operating at a repetition rate of 5 kHz for 15 ns pulses [43]. Half-mJ pulses with peak power > 33 kW and negligible nonlinear distortions were obtained at a pump power of 18 W. Single-frequency pulsed fiber laser sources at 1.92 µm with much higher average output power and pulse energy were demonstrated with a 41-cm long 4 wt% Tm³⁺-doped germanate fiber with a core diameter of 30 µm and a cladding diameter of 300 µm [44]. An average output power of 16 W for single-frequency transform-limited 2.0 ns pulses at a repetition rate of 500 kHz was achieved. As the repetition rate was reduced to 100 kHz, a maximum peak power of 78.1 kW was obtained for the 2 ns pulses. A maximum pulse energy of nearly 1 mJ was achieved at a power of 33 W for 15 ns pulses with a repetition rate of 1 kHz, as shown in **Figure 13(b)**.

Highly Tm³⁺-doped germanate fibers are also attractive for mode-locked laser power amplifiers with low accumulated nonlinearity because the absorption of such gain fiber is so high and tens of cm long fiber can absorb most of the pump power even with cladding-pumped configurations. A 10 W mode-locked laser source has been developed with a 4 wt% Tm³⁺-doped
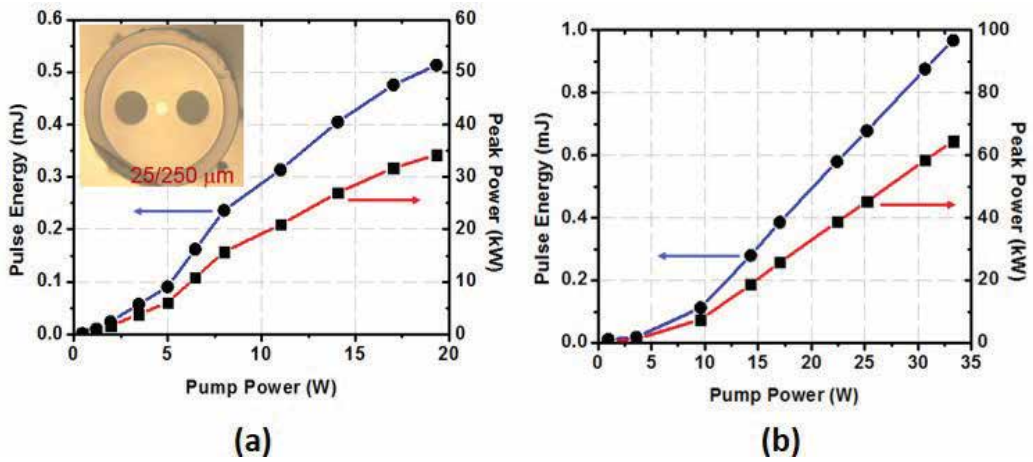
Figure 13. (a) Output pulse energy and peak power of a 25/250 μm 4 wt% Tm-doped germanate fiber amplifier for a 1918.4 nm 5 kHz 15 ns single-frequency laser; (b) output pulse energy and peak power of a 30/300 μm 4 wt% Tm-doped germanate fiber amplifier for a 1918.4 nm 1 kHz 15 ns single-frequency laser.
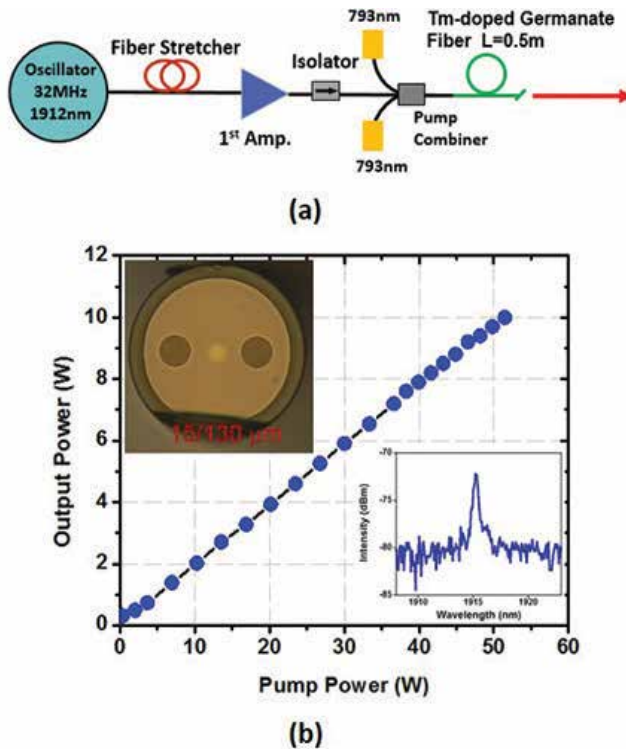
Figure 14. (a) Experimental setup of a 10 W all-fiber mode-locked laser source based on a 15/130 μm 4 wt% Tm³⁺-doped germanate fiber power amplifier; (b) average output power as a function of the 793 nm pump power of a Tm³⁺-doped germanate fiber amplifier for 40 ps mode-locked laser at 1920 nm. Insets: Upper left is the microscopic image of the 15/130 μm 4 wt% Tm³⁺-doped germanate fiber and lower right is the optical spectrum of the mode-locked laser fiber amplifier.

germanate double-cladding fiber with the configuration shown in **Figure 14(a)**. A mode-locked fiber laser oscillator operating at 1912 nm with a repetition rate of 32 MHz was used as the seed laser. The output power of the seed laser was a few mW. A fiber stretcher was used to stretch the pulse width to 40 ps. A core-pumped Tm^{3+}-doped silica fiber amplifier was used to increase the mode-locked laser power to 150 mW first. Then, a 50-cm long Tm^{3+}-doped germanate dou-ble-cladding fiber with a core diameter of 15 μm and a cladding of 130 μm was used for the power amplifier stage. The output power of the Tm^{3+}-doped germanate fiber amplifier as a function of the pump is shown in **Figure 14(b)**. Over 10 W output power with a slope efficiency of 20% was obtained at a pump power of 50 W. The optical spectrum of the 10 W mode-locked laser fiber amplifier is shown in the lower right inset. The spectrum broadening and distor-tion due to the accumulated nonlinear effects are negligible. The efficiency of the Tm^{3+}-doped germanate fiber amplifier is lower than that of a Tm^{3+}-doped silica fiber amplifier. It can be improved by optimizing the composition of the germanate glass to significantly enhance the cross-relaxation process and reduce the fiber propagation loss.

4. Tellurite fiber lasers

Compared to phosphate and germanate glasses, tellurite glass displays a lower maximum phonon energy (800 cm^{-1}) that allows the transmission of light further into the mid-infrared (up to ~5 μm) [45]. In addition, tellurite glass has large rare-earth ion solubility and enhanced absorption and emission cross-sections due to the large refractive index of ~2.0, making rare-earth-doped tellurite glasses very attractive materials for efficient laser emission. So far, various rare-earth-doped fiber lasers at the 1, 1.6 and 2 μm wavelength regions have been reported [46–55]. On the other hand, tellurite glass has large nonlinear refractive index (5.9 × 10^{-19} m^2/W), high thermal stability and strong corrosion resistance, making tellurite fiber an ideal medium for nonlinear wavelength conversion. So far, nonlinear wavelength conversion lasers including SBS lasers, Raman lasers and supercontinuum lasers have been studied and investigated with tellurite fibers [56–66].

4.1. Rare-earth-doped tellurite fiber lasers

The first laser emission with a rare-earth-doped tellurite fiber was demonstrated in 1994 [46]. A single-mode Nd^{3+}-doped tellurite fiber with an elliptical core of 3 μm × 6.5 μm and a NA of 0.21 was fabricated with the rod-in-tube technique. A single-mode laser emission with a lasing threshold of 27 mW was observed at 1061 nm. A slope efficiency of 23% was obtained with 11.9% Fresnel reflection at both ends of the fiber cavity. An Er^{3+}-doped tellurite fiber laser was first reported by Mori et al. in 1997 [47]. A maximum output power of 2.5 mW at 1560 nm with a slope efficiency of 0.65% was obtained at a pump power of 500 mW. Afterwards, Er^{3+}-doped tellurite fiber amplifiers were studied and investigated for the L-band signal amplification for optical communications [48, 49]. Since Er^{3+}-doped tellurite glass has a large emission cross-section due to the electric dipole moment transition with a large refractive index, expressed by $\sigma_e \sim (n^2 + 2)^2/9n$, a small signal gain exceeding 20 dB over a bandwidth as wide as 80 nm includ-ing the 1.55 μm and 1.58 μm bands can be obtained with an Er^{3+}-doped tellurite fiber amplifier. Most importantly, the Er^{3+}-doped tellurite fiber amplifier was found to be very suitable for the

L-band signal amplification especially for signal wavelengths beyond 1600 nm [49]. In addition to the Er^{3+}-doped tellurite fiber for the L-band signal amplification, the S-band signal amplification was demonstrated with a 0.4 mol% Tm^{3+}-doped tellurite fiber by using the transition from $^3H_4$ to $^3F_4$ levels of Tm^{3+} ions [50]. A fiber-to-fiber gain of 11 dB and an internal gain of 35 dB were achieved with a dual-end pumping configuration.

Compared to the S-band signal amplification, the Tm^{3+}-doped tellurite fiber has attracted more attention for laser emission at the 2 μm band. In 2008, Richards et al. reported a high-efficiency Tm^{3+}-doped tellurite fiber laser at 1.88–1.99 μm [51]. An output power of 280 mW with a slope efficiency of 76% was obtained with a 32-cm long 1 wt% Tm^{3+}-doped tellurite fiber core pumped by a silica fiber laser at 1.6 μm. A more powerful output at 2 μm was obtained by cladding-pumping with a multimode laser diode at 800 nm [52]. An output power of 1.12 W with a slope efficiency of 20% was achieved with a 40-cm long 1 wt% Tm^{3+}-doped tellurite double-cladding fiber. Since Ho^{3+} ions are characterized by a larger emission peak than Tm^{3+} ions and Ho^{3+} ions can be excited via an energy transfer process between the Tm^{3+} and Ho^{3+} ions, the sensitization of Ho^{3+} by Tm^{3+} has been usually exploited to achieve laser emission beyond 2 μm by taking advantage of the high absorption of Tm^{3+} ions at 800 nm. In [53], a 2.1 μm fiber laser with an output power of 35 mW was demonstrated with a 7 cm long 1 mol% Tm^{3+} and 0.5 mol% Ho^{3+} co-doped tellurite double-cladding fiber. This fiber was fabricated with the rod-in-tube method and has a core diameter of 9 μm and a NA of 0.14. In [54], a high-efficiency Tm^{3+}/Ho^{3+} co-doped tellurite fiber laser at 2.1 μm was demonstrated with in-band pumping at 1.6 μm. A continuous-wave output power of 160 mW with a slope efficiency of 62% was obtained at a pump power of 350 mW. In addition to Tm^{3+} ions, Yb^{3+} ions were also added as sensitizer to enhance the pump absorption of a Ho^{3+} laser system. A tellurite fiber with a 7.5 μm core doped with 1.5 wt% Yb_2O_3, 1.0 wt% Tm_2O_3 and 1.0 wt% Ho_2O_3 was fabricated [55]. A 60 mW laser output at 2.1 μm with a slope efficiency of 25% was demonstrated with a 17-cm long $Tm^{3+}/Ho^{3+}/Yb^{3+}$ triply-doped tellurite fiber. Although high-efficiency Tm^{3+}-, Tm^{3+}/Ho^{3+}- and $Tm^{3+}/Ho^{3+}/Yb^{3+}$-doped tellurite fiber lasers at 2 μm have been demonstrated, their output is still much lower than that of germanate and silica fiber lasers. Higher output power tellurite fiber lasers can be obtained by reducing the propagation loss of the fiber and improving the thermal management of the fiber laser.

4.2. Nonlinear wavelength conversion tellurite fiber lasers

Because of its broad transmission and large nonlinearity, tellurite glass has been extensively used as a low phonon energy oxide glass in nonlinear photonic devices. Combining the long interaction length and small core size with large nonlinearity, undoped tellurite glass fibers are excellent platforms for nonlinear wavelength conversion lasers with low threshold and high efficiency.

The SBS can convert the incident pump light into lower energy scattered light in counter-propagating direction due to the interaction of the pump light and acoustic phonons. The SBS has found applications in optical amplification, optical fiber sensors, phase conjugation and slow light generation. A SBS laser based on tellurite fiber was first demonstrated with a 200-m long single-mode tellurite fiber with a core diameter of 2.2 μm [56]. A maximum unsaturated power of 54.6 mW at 1550 nm with a slope efficiency of 38.2% was achieved, and the Brillouin gain coefficient of the tellurite fiber was measured to be 1.6989×10^{-10} m/W.

Compared to the Brillouin scattering, the Raman scattering is more attractive for optical amplification and nonlinear wavelength conversion because the Raman gain bandwidth and frequency shift are much larger than those of the Brillouin scattering. By taking advantage of the large Raman gain coefficient (55 W^{-1}/km), broad gain bandwidth (~300 cm^{-1}) and large Raman shift (~750 cm^{-1}) of the tellurite fiber, Mori et al. demonstrated a tellurite fiber Raman amplifier with a gain of over 10 dB and a noise figure below 10 dB from 1490 to 1650 nm [57]. Qin et al. reported a widely tunable ring-cavity tellurite fiber Raman laser with more than 100 nm tunable range (1495–1600 nm) [58]. In [59], Raman tellurite fiber lasers operating at 3–5 μm pumped by readily available CW and Q-switched Er^{3+}-doped fluoride fiber lasers at 2.8 μm were proposed and numerically investigated. The simulation results showed that watt level or even 10-W level fiber laser sources in the 3–5 μm atmospheric transparency window can be achieved by utilizing the first- and second-order Raman scattering in the tellurite fiber. Raman scattering can also be utilized to achieve widely wavelength tunable ultrashort pulses through the soliton self-frequency shift (SSFS), which originates from the intra-pulse stimulated Raman scattering that transfers the high frequency part of the pulse spectrum to the low frequency part. In [60], a widely wavelength tunable 100 fs pulsed laser source in the 1.6–2.65 μm range was achieved with a suspended core microstructured tellurite fiber pumped by a hybrid Er^{3+}/Tm^{3+}-doped silica fiber system.

Supercontinuum (SC) laser sources possessing ultra-broad spectral bandwidth and extremely high spectral brightness have found a variety of applications. Optical fibers have been considered as an inherently excellent candidate for SC generation because they can provide a significant length and guide small beam size for the nonlinear interaction. Because of the large nonlinearity and broad transmission bandwidth, tellurite fibers have shown advantages in SC generation with a low pump power threshold and a very broad spectral bandwidth [61–66]. In 2008, a broadband supercontinuum light spanning over 789–4870 nm was demonstrated with an 8-mm long microstructured tellurite fiber [61]. This tellurite fiber has a core diameter of 2.5 μm, a nonlinear waveguide coefficient of 596 W^{-1}/km and a zero-dispersion wavelength (ZDW) of 1380 nm, allowing anomalous dispersion pumping at 1550 nm. An average power of 70 mW was obtained at a launched pump power of 150 mW. In [62], in order to generate flattened SC light, a microstructured tellurite fiber was tapered to tailor the group velocity dispersion from a small positive value to a large negative one. A flattened SC laser spanning from 843 to 2157 nm with less than 10 dB intensity variation was demonstrated with a 5-cm long and zero-dispersion-decreasing microstructured tellurite fiber. In addition to the SC generation, the second and third harmonic generations in microstructured tellurite fibers were investigated with a 1557 nm femtosecond fiber laser [63]. Supercontinuum light spanning over 470–2400 nm was achieved with a microstructured tellurite fiber with a core diameter of 2.7 μm. This research demonstrated that the chromatic dispersion controlled microstructured tellurite fibers are potential candidates for second harmonic generation, third harmonic generation and SC generation expanding from visible to mid-IR regions. SC generation in highly nonlinear microstructured tellurite fibers pumped by a CW/quasi-CW laser was investigated by Liao et al. [64]. SC with spectral bandwidth broader than one

octave was achieved with a sub-meter fiber and a watt-level peak-power pump. However, these SC laser sources are based on microstructured tellurite fibers, which usually have a very small effective core area and poor heat dissipation capability, and thus their output power scaling is constrained by the breakdown damage of the fiber cores. To achieve a high average power SC laser, solid-cladding tellurite fibers have to be used due to the improved thermal and mechanical properties.

The ZDW of a tellurite glass is typically around 2.3 μm, so the zero dispersion wavelength of a regular step-index tellurite fiber is longer than 2.3 μm. It is worthwhile noting that this value is not compatible with the pump wavelength of the most commonly available high power pump sources, thus making it challenging to achieve high power SC with broad spectral bandwidth. To overcome this constraint, a solid-cladding tellurite fiber with a W-type index profile as the one shown in the inset of **Figure 15(b)** was fabricated by the rod-in-tube method. This fiber has a solid core with a diameter of 3.8 μm and an 11.4 μm inner cladding with index lower than that of the core and the outer cladding. The dispersion of the W-type index fiber was measured and is shown in the inset of **Figure 15(c)**. The first zero-dispersion wavelength is shifted to 2 μm and there is another zero-dispersion wavelength at 3.9 μm. This fiber has been used to demonstrate the first watt-level SC laser source based on a tellurite fiber [65]. More than 1.2 W SC were obtained with conversion efficiency greater than 30% from the 1.9 μm pump wavelength to the 2–5 μm spectral range. Detailed experimental parameters study on mid-IR SC generation in W-type index tellurite fibers is reported in [66]. Soliton SC with a maximum spectral width of over 2000 nm spanning from 2.6 to 4.6 μm and output powers of up to 160 mW was obtained with a 4.2 μm core fiber pumped at 3 μm. The power scaling of the SC generation based on the W-type index tellurite fiber was demonstrated with the all-fiber setup shown in **Figure 15(a)**. A mode-locked fiber laser at 1912 nm with a repetition rate of 32 MHz was used as the seed laser. The pulse width is stretched to 40 ps by a fiber stretcher. The average power of the mode-locked laser was increased to over 10 W by three-stage Tm^{3+}-doped fiber amplifiers. The 10 W mode-locked laser was coupled into the W-type index tellurite fiber via a fiber mode-field adapter. The output power of the all-fiber SC laser source was measured and is shown in **Figure 15(b)**. Nearly 5 W SC were generated at the pump power of 10.6 W. The optical spectrum of the SC laser source is shown in **Figure 15(c)**. The power intensity at long wavelength starts to decrease at about 3.8 μm, which is close to the second zero-dispersion wavelength. Red-shift dispersion waves were measured at wavelengths beyond 4 μm. The long wavelength of the SC can be further extended by using a tellurite fiber with a longer second zero-dispersion wavelength. High power mid-infrared SC laser sources with a high spectral power density in the 3–5 μm atmospheric window are very attractive for long distance applications. Both simulation and experimental results have confirmed that SC with a very high power proportion in the 3–5 μm region can be obtained with a tellurite fiber pumped by ultrafast mid-infrared pulses at a wavelength of around 3 μm [66, 67]. Various Q-switched and mode-locked fiber lasers at 3 μm have already been demonstrated [68, 69]. Therefore, high power all-fiber SC laser sources with >90% power intensity in the atmospheric window can be developed with current fiber laser technology.
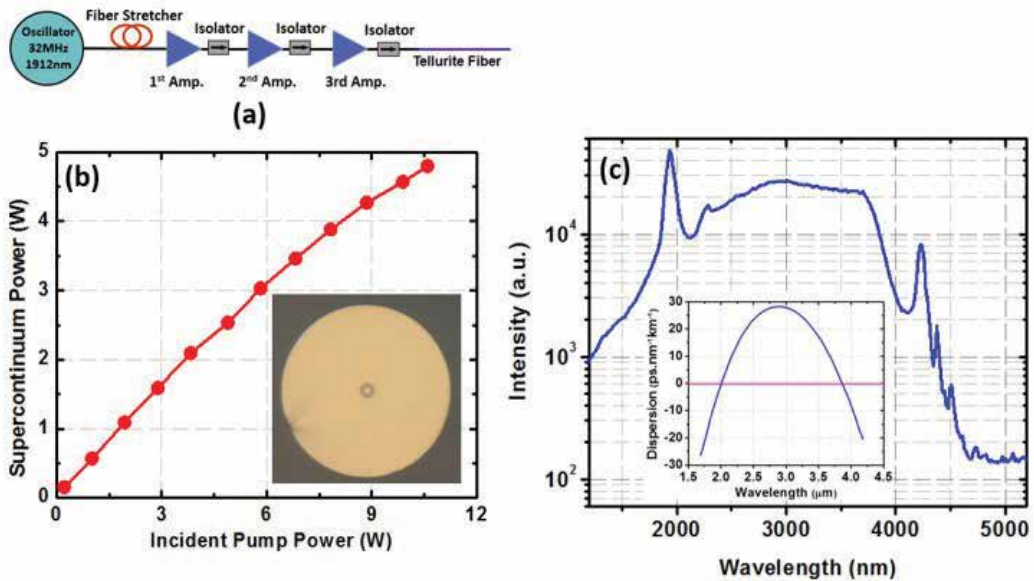
Figure 15. (a) Experimental setup of a 5 W all-fiber SC laser source based on a W-type index tellurite fiber. (b) Average output power of the SC laser source as a function of the mode-locked pump power at 1920 nm. Inset: microscope image of the W-type index tellurite fiber. (c) Optical spectrum of the 5 W all-fiber SC laser source. Inset: Measured dispersion of the W-type index tellurite fiber.

Author details

Xiushan Zhu[1], Arturo Chavez-Pirson[2], Daniel Milanese[3,6]*, Joris Lousteau[4],
Nadia Giovanna Boetti[5], Diego Pugliese[3] and Nasser Peyghambarian[1,2]

*Address all correspondence to: daniel.milanese@polito.it

1 College of Optical Sciences, University of Arizona, Tucson, AZ, United States of America

2 NP Photonics Inc., Tucson, AZ, United States of America

3 Department of Applied Science and Technology and RU INSTM, Politecnico di Torino, Torino, Italy

4 Optoelectronics Research Centre, University of Southampton, Southampton, United Kingdom

5 Istituto Superiore Mario Boella, Torino, Italy

6 Consiglio Nazionale delle Ricerche, Istituto di Fotonica e Nanotecnologie, Trento, Italy

References

[1]   Yamane M, Asahara Y. Glasses for Photonics. 1st ed. Cambridge, UK: Cambridge University Press; 2004. 282 p

[2] Digonnet MJF, editor. Rare-Earth-Doped Fiber Lasers and Amplifiers. 1st ed. Boca Raton, FL, USA: CRC Press; 2001. 798 p

[3] Richardson DJ, Nilsson J, Clarkson WA. High power fiber lasers: Current status and future perspectives. Journal of the Optical Society of America B: Optical Physics. 2010; **27**:B63-B92. DOI: 10.1364/JOSAB.27.000B63

[4] Dudley JM, Taylor JR, editors. Supercontinuum Generation in Optical Fibers. 1st ed. Cambridge, UK: Cambridge University Press; 2010. 419 p. DOI: 10.1017/CBO9780511750465

[5] Brawer SA, White WB. Raman spectroscopic investigation of the structure of silicate glasses. I. The binary alkali silicates. The Journal of Chemical Physics. 1975;**63**:2421-2432. DOI: 10.1063/1.431671

[6] Quimby RS, Miniscalco WJ, Thompson B. Clustering in erbium-doped silica glass fibers analyzed using 980 nm excited-state absorption. Journal of Applied Physics. 1994; **76**:4472-4478. DOI: 10.1063/1.357278

[7] Kitamura R, Pilon L, Jonasz M. Optical constants of silica glass from extreme ultraviolet to far infrared at near room temperature. Applied Optics. 2007;**46**:8118-8133. DOI: 10.1364/AO.46.008118

[8] Charschan SS. In the beginning there was ANSI Z136.1. Journal of Laser Applications. 1997;**9**:189-195. DOI: 10.2351/1.4745459

[9] Yamashita Y. Nd- and Er-doped phosphate glass for fiber laser. In: Proceedings of SPIE 1171, Fiber Laser Sources and Amplifiers; 5-7 September 1989; Boston. Bellingham, WA, USA: SPIE; 1990. pp. 291-297

[10] Griebner U, Koch R, Schönnagel H, Grunwald R. Efficient laser operation with nearly diffraction-limited output from a diode-pumped heavily Nd-doped multimode fiber. Optics Letters. 1996;**21**:266-268. DOI: 10.1364/OL.21.000266

[11] Wu R, Myers JD, Myers MJ, Hardy CR. Nd-doped cladding pumped fiber laser. In: Proceedings of the Fiber Optics and Communication Technologies, Optics in the Southeast; November 4-5, 2001; Charlotte, Washington, USA: OSA; 2001. pp. 1-5

[12] Zhang G, Wang M, Yu C, Zhou Q, Qiu J, Hu L, Chen D. Efficient generation of watt-level output from short-length Nd-doped phosphate fiber lasers. IEEE Photonics Technology Letters. 2011;**23**:350-352. DOI: 10.1109/LPT.2010.2103306

[13] Lee Y-W, Digonnet MJF, Sinha S, Urbanek KE, Byer RL, Jiang S. High-power Yb^{3+}-doped phosphate fiber amplifier. IEEE Journal of Selected Topics in Quantum Electronics. 2009;**15**:93-102. DOI: 10.1109/JSTQE.2008.2010263

[14] Hwang B-C, Jiang S, Luo T, Seneschal K, Sorbello G, Morrell M, Smektala F, Honkanen S, Lucas J, Peyghambarian N. Performance of high-concentration Er^{3+}-doped phosphate fiber amplifiers. IEEE Photonics Technology Letters. 2001;**13**:197-199. DOI: 10.1109/68.914319

[15] Boetti NG, Scarpignato GC, Lousteau J, Pugliese D, Bastard L, Broquin J-E, Milanese D. High concentration Yb-Er co-doped phosphate glass for optical fiber amplification. Journal of Optics. 2015;**17**:065705. DOI: 10.1088/2040-8978/17/6/065705

[16] Qiu T, Li L, Schülzgen A, Temyanko VL, Luo T, Jiang S, Mafi A, Moloney JV, Peyghambarian N. Generation of 9.3-W multimode and 4-W single-mode output from 7-cm short fiber lasers. IEEE Photonics Technology Letters. 2004;**16**:2592-2594. DOI: 10.1109/LPT.2004.836352

[17] Li L, Morrell M, Qiu T, Temyanko VL, Schülzgen A, Mafi A, Kouznetsov D, Moloney JV, Luo T, Jiang S, Peyghambarian N. Short cladding-pumped Er/Yb phosphate fiber laser with 1.5 W output power. Applied Physics Letters. 2004;**85**:2721-2723. DOI: 10.1063/1.1798394

[18] Li L, Schülzgen A, Temyanko VL, Qiu T, Morrell MM, Wang Q, Mafi A, Moloney JV, Peyghambarian N. Short-length microstructured phosphate glass fiber lasers with large mode areas. Optics Letters. 2005;**30**:1141-1143. DOI: 10.1364/OL.30.001141

[19] Spiegelberg C, Geng J, Hu Y, Kaneda Y, Jiang S, Peyghambarian N. Low-noise narrow-linewidth fiber laser at 1550 nm (June 2003). Journal of Lightwave Technology. 2004;**22**:57-62. DOI: 10.1109/JLT.2003.822208

[20] Hofmann P, Voigtländer C, Nolte S, Peyghambarian N, Schülzgen A. 550-mW output power from a narrow linewidth all-phosphate fiber laser. Journal of Lightwave Technology. 2013;**31**:756-760. DOI: 10.1109/JLT.2012.2233392

[21] Qiu T, Suzuki S, Schülzgen A, Li L, Polynkin A, Temyanko VL, Moloney JV, Peyghambarian N. Generation of watt-level single-longitudinal-mode output from cladding-pumped short fiber lasers. Optics Letters. 2005;**30**:2748-2750. DOI: 10.1364/OL.30.002748

[22] Xu S, Yang Z, Zhang W, Wei X, Qian Q, Chen D, Zhang Q, Shen S, Peng M, Qiu J. 400 mW ultrashort cavity low-noise single-frequency Yb^{3+}-doped phosphate fiber laser. Optics Letters. 2011;**36**:3708-3710. DOI: 10.1364/OL.36.003708

[23] Leigh M, Shi W, Zong J, Wang J, Jiang S, Peyghambarian N. Compact, single-frequency all-fiber Q-switched laser at 1 μm. Optics Letters. 2007;**32**:897-899. DOI: 10.1364/OL.32.000897

[24] Yang C, Zhao Q, Feng Z, Peng M, Yang Z, Xu S. 1120 nm kHz-linewidth single-polarization single-frequency Yb-doped phosphate fiber laser. Optics Express. 2016;**24**:29794-29799. DOI: 10.1364/OE.24.029794

[25] Zhu X, Zhu G, Shi W, Zong J, Wiersma K, Nguyen D, Norwood RA, Chavez-Pirson A, Peyghambarian N. 976 nm single-polarization single frequency ytterbium-doped phosphate fiber amplifiers. IEEE Photonics Technology Letters. 2013;**25**:1365-1368. DOI: 10.1109/LPT.2013.2266113

[26] Wu J, Zhu X, Temyanko V, LaComb L, Kotov L, Kiersma K, Zong J, Chavez-Pirson A, Norwood RA, Peyghambarian N. Yb^{3+}-doped double-clad phosphate fiber for 976 nm single-frequency laser amplifiers. Optical Materials Express. 2017;**7**:1310-1316. DOI: 10.1364/OME.7.001310

[27] Yamashita S, Yoshida T, Set SY, Polynkin P, Peyghambarian N. Passively mode-locked short-cavity 10 GHz Er:Yb-codoped phosphate-fiber laser using carbon nanotubes. In:

Proceedings of SPIE 6453, Fiber Lasers IV: Technology, Systems, and Applications; January 20-25, 2007; San Jose. Bellingham, WA, USA: SPIE; 2007. p. 64531Y

[28] Thapa R, Nguyen D, Zong J, Chavez-Pirson A. All-fiber fundamentally mode-locked 12 GHz laser oscillator based on an Er/Yb-doped phosphate glass fiber. Optics Letters. 2014;**39**:1418-1421. DOI: 10.1364/OL.39.001418

[29] Lee YW, Sinha S, Digonnet MJF, Byer RL. 20 W single-mode Yb^{3+}-doped phosphate fiber laser. Optics Letters. 2006;**31**:3255-3257. DOI: 10.1364/OL.31.003255

[30] Leigh M, Shi W, Zong J, Yao Z, Jiang S, Peyghambarian N. High peak power single frequency pulses using a short polarization-maintaining phosphate glass fiber with a large core. Applied Physics Letters. 2008;**92**:181108. DOI: 10.1063/1.2917470

[31] Shi W, Petersen EB, Leigh M, Zong J, Yao Z, Chavez-Pirson A, Peyghambarian N. High SBS-threshold single-mode single-frequency monolithic pulsed fiber laser in the C-band. Optics Express. 2009;**17**:8237-8245. DOI: 10.1364/OE.17.008237

[32] Shi W, Leigh MA, Zong J, Yao Z, Nguyen DT, Chavez-Pirson A, Peyghambarian N. High-power all-fiber-based narrow-linewidth single-mode fiber laser pulses in the C-band and frequency conversion to THz generation. IEEE Journal of Selected Topics in Quantum Electronics. 2009;**15**:377-384. DOI: 10.1109/JSTQE.2008.2010234

[33] Akbulut M, Miller A, Wiersma K, Zong J, Rhonehouse D, Nguyen D, Chavez-Pirson A. High energy, high average and peak power phosphate-glass fiber amplifiers for 1 micron band. In: Proceedings of SPIE 8961, Fiber Lasers XI: Technology, Systems, and Applications; February 1-6, 2014; San Francisco. Bellingham, WA, USA: SPIE; 2014. p. 89611X

[34] Shi W, Peterson EB, Yao Z, Nguyen DT, Zong J, Stephen MA, Chavez-Pirson A, Peyghambarian N. Kilowatt-level stimulated-Brillouin-scattering-threshold monolithic transform-limited 100 ns pulsed fiber laser at 1530 nm. Optics Letters. 2010;**35**:2418-2420. DOI: 10.1364/OL.35.002418

[35] Polynkin P, Polynkin A, Panasenko D, Peyghambarian N, Moloney JV. All-fiber picosecond laser system at 1.5 μm based on amplification in short and heavily doped phosphate-glass fiber. IEEE Photonics Technology Letters. 2006;**18**:2194-2196. DOI: 10.1109/LPT.2006.884242

[36] Peng X, Kim K, Mielke M, Jennings S, Masor G, Stohl D, Chavez-Pirson A, Nguyen DT, Rhonehouse D, Zong J, Churin D, Peyghambarian N. High efficiency, monolithic fiber chirped pulse amplification system for high energy femtosecond pulse generation. Optics Express. 2013;**21**:25440-25451. DOI: 10.1364/OE.21.025440

[37] Peng X, Kim K, Mielke M, Jennings S, Masor G, Stohl D, Chavez-Pirson A, Nguyen DT, Rhonehouse D, Zong J, Churin D, Peyghambarian N. Monolithic fiber chirped pulse amplification system for millijoule femtosecond pulse generation at 1.55 μm. Optics Express 2014;**22**:2459-2464. DOI: 10.1364/OE.22.002459

[38] Geng J, Wu J, Jiang S, Yu J. Efficient operation of diode-pumped single-frequency thulium-doped fiber lasers near 2 μm. Optics Letters. 2007;**32**:355-357. DOI: 10.1364/OL.32.000355

[39] Wu J, Yao Z, Zong J, Chavez-Pirson A, Peyghambarian N, Yu J. Single-frequency fiber laser at 2.05 μm based on Ho-doped germanate glass fiber. In: Proceedings of SPIE 7195, Fiber Lasers VI: Technology, Systems, and Applications; January 24-29, 2009; San Jose. Bellingham, WA, USA: SPIE; 2009. p. 71951K

[40] Wu J, Jiang S, Luo T, Geng J, Peyghambarian N, Barnes NP. Efficient thulium-doped 2-μm germanate fiber laser. IEEE Photonics Technology Letters 2006;**18**:334-336. DOI: 10.1109/LPT.2005.861970

[41] Wu J, Yao Z, Zong J, Jiang S. Highly efficient high-power thulium-doped germanate glass fiber laser. Optics Letters. 2007;**32**:638-640. DOI: 10.1364/OL.32.000638

[42] Shi W, Petersen EB, Nguyen DT, Yao Z, Chavez-Pirson A, Peyghambarian N, Yu J. 220 μJ monolithic single-frequency Q-switched fiber laser at 2 μm by using highly Tm-doped germanate fibers. Optics Letters 2011;**36**:3575-3577. DOI: 10.1364/OL.36.003575

[43] Fang Q, Shi W, Peterson E, Kieu K, Chavez-Pirson A, Peyghambarian N. Half-mJ all-fiber-based single-frequency nanosecond pulsed fiber laser at 2-μm. IEEE Photonics Technology Letters 2012;**24**:353-355. DOI: 10.1109/LPT.2011.2178824

[44] Fang Q, Shi W, Kieu K, Petersen E, Chavez-Pirson A, Peyghambarian N. High power and high energy monolithic single frequency 2 μm nanosecond pulsed fiber laser by using large core Tm-doped germanate fibers: experiment and modeling. Optics Express 2012;**20**:16410-16420. DOI: 10.1364/OE.20.016410

[45] Rhonehouse DL, Zong J, Nguyen D, Thapa R, Wiersma K, Smith C, Chavez-Pirson A. Low loss, wide transparency, robust tellurite glass fibers for mid-IR (2-5 μm) applications. In: Proceedings of SPIE 8898, Technologies for Optical Countermeasures X and High-Power Lasers 2013: Technology and Systems; September 23-26, 2013; Dresden. Bellingham, WA, USA: SPIE; 2013. p. 88980D

[46] Wang JS, Machewirth DP, Wu F, Snitzer E, Vogel EM. Neodymium-doped tellurite single-mode fiber laser. Optics Letters. 1994;**19**:1448-1449. DOI: 10.1364/OL.19.001448

[47] Mori A, Ohishi Y, Sudo S. Erbium-doped tellurite glass fibre laser and amplifier. Electronics Letters. 1997;**33**:863-864. DOI: 10.1049/el:19970585

[48] Mori A, Sakamoto T, Shikano K, Kobayashi K, Hoshino K, Shimizu M. Gain flattened Er^{3+}-doped tellurite fibre amplifier for WDM signals in the 1581-1616 nm wavelength region. Electronics Letters. 2000;**36**:621-622. DOI: 10.1049/el:20000504

[49] Mori A, Sakamoto T, Kobayashi K, Shikano K, Oikawa K, Hoshino K, Kanamori T, Ohishi Y, Shimizu M. 1.58-μm broad-band erbium-doped tellurite fiber amplifier. Journal of Lightwave Technology 2002;**20**:822-827. DOI: 10.1109/JLT.2002.1007935

[50] Taylor ERM, Ng LN, Nilsson J, Caponi R, Pagano A, Potenza M, Sordo B. Thulium-doped tellurite fiber amplifier. IEEE Photonics Technology Letters. 2004;**16**:777-779. DOI: 10.1109/LPT.2004.823733

[51] Richards B, Tsang Y, Binks D, Lousteau J, Jha A. Efficient ~2 μm Tm^{3+}-doped tellurite fiber laser. Optics Letters. 2008;**33**:402-404. DOI: 10.1364/OL.33.000402

[52] Li K, Zhang G, Hu L. Watt-level ~2 μm laser output in Tm^{3+}-doped tungsten tellurite glass double-cladding fiber. Optics Letters 2010;**35**:4136-4138. DOI: 10.1364/OL.35.004136

[53] Li K, Zhang G, Wang X, Hu L, Kuan P, Chen D, Wang M. Tm^{3+} and Tm^{3+}-Ho^{3+} co-doped tungsten tellurite glass single mode fiber laser. Optics Letters. 2012;**20**:10115-10121. DOI: 10.1364/OE.20.010115

[54] Tsang Y, Richards B, Binks D, Lousteau J, Jha A. Tm^{3+}/Ho^{3+} codoped tellurite fiber laser. Optics Letters. 2008;**33**:1282-1284. DOI: 10.1364/OL.33.001282

[55] Tsang Y, Richards B, Binks D, Lousteau J, Jha AA. Yb^{3+}/Tm^{3+}/Ho^{3+} triply-doped tellurite fibre laser. Optics Express. 2008;**16**:10690-10695. DOI: 10.1364/OE.16.010690

[56] Qin G, Mori A, Ohishi Y. Brillouin lasing in a single-mode tellurite fiber. Optics Letters. 2007;**32**:2179-2181. DOI: 10.1364/OL.32.002179

[57] Mori A, Masuda H, Shikano K, Shimizu M. Ultra-wide-band tellurite-based fiber Raman amplifier. Journal of Lightwave Technology. 2003;**21**:1300-1306. DOI: 10.1109/JLT.2003.810917

[58] Qin G, Liao M, Suzuki T, Mori A, Ohishi Y. Widely tunable ring-cavity tellurite fiber Raman laser. Optics Letters. 2008;**33**:2014-2016. DOI: 10.1364/OL.33.002014

[59] Zhu G, Geng L, Zhu X, Li L, Chen Q, Norwood RA, Manzur T, Peyghambarian N. Towards ten-watt-level 3-5 μm Raman lasers using tellurite fiber. Optics Express. 2015;**23**:7559-7573. DOI: 10.1364/OE.23.007559

[60] Koptev MY, Anashkina EA, Andrianov AV, Dorofeev VV, Kosolapov AF, Muravyev SV, Kim AV. Widely tunable mid-infrared fiber laser source based on soliton self-frequency shift in microstructured tellurite fiber. Optics Letters. 2015;**40**:4094-4097. DOI: 10.1364/OL.40.004094

[61] Domachuk P, Wolchover NA, Cronin-Golomb M, Wang A, George AK, Cordeiro CMB, Knight JC, Omenetto FG. Over 4000 nm bandwidth of mid-IR supercontinuum generation in sub-centimeter segments of highly nonlinear tellurite PCFs. Optics Express. 2008;**16**:7161-7168. DOI: 10.1364/OE.16.007161

[62] Qin G, Yan X, Kito C, Liao M, Suzuki T, Mori A, Ohishi Y. Zero-dispersion-wavelength-decreasing tellurite microstructured fiber for wide and flattened supercontinuum generation. Optics Letters. 2010;**35**:136-138. DOI: 10.1364/OL.35.000136

[63] Qin G, Liao M, Chaudhari C, Yan X, Kito C, Suzuki T, Ohishi Y. Second and third harmonics and flattened supercontinuum generation in tellurite microstructured fibers. Optics Letters. 2010;**35**:58-60. DOI: 10.1364/OL.35.000058

[64] Liao M, Gao W, Duan Z, Yan X, Suzuki T, Ohishi Y. Supercontinuum generation in short tellurite microstructured fibers pumped by a quasi-cw laser. Optics Letters. 2012;**37**:2127-2129. DOI: 10.1364/OL.37.002127

[65] Thapa R, Rhonehouse D, Nguyen D, Wiersma K, Smith C, Zong J, Chavez-Pirson A. Mid-IR supercontinuum generation in ultra-low loss, dispersion-zero shifted tellurite glass fiber with extended coverage beyond 4.5 μm. In: Proceedings of SPIE 8898, Technologies for Optical Countermeasures X and High-Power Lasers 2013: Technology and Systems; September 23-26, 2013; Dresden. Bellingham, WA, USA: SPIE; 2013. p. 889808

[66] Kedenburg S, Steinle T, Mörz F, Steinmann A, Nguyen D, Rhonehouse D, Zong J, Chavez-Pirson A, Giessen H. Soliton supercontinuum of femtosecond mid-IR pulses in W-type index tellurite fibers with two zero dispersion wavelengths. APL Photonics. 2016;**1**:086101. DOI: 10.1063/1.4958333

[67] Wei C, Zhu X, Norwood RA, Song F, Peyghambarian N. Numerical investigation on high power mid-infrared supercontinuum fiber lasers pumped at 3 μm. Optics Express. 2013;**21**:29488-29504. DOI: 10.1364/OE.21.029488

[68] Wei C, Zhu X, Norwood RA, Peyghambarian N. Passively continuous-wave mode-locked Er^{3+}-doped ZBLAN fiber laser at 2.8 μm. Optics Letters. 2012;**37**:3849-3851. DOI: 10.1364/OL.37.003849

[69] Zhu X, Zhu G, Wei C, Kotov LV, Wang J, Tong M, Norwood RA, Peyghambarian N. Pulsed fluoride fiber lasers at 3 μm [invited]. Journal of the Optical Society of America B: Optical Physics. 2017;**34**:A15-A28. DOI: 10.1364/JOSAB.34.000A15

Glass Patterning: Technologies and Applications

Nguyen Van Toan, Naoki Inomata,
Masaya Toda and Takahito Ono

Additional information is available at the end of the chapter

Abstract

In this work, we review the progress in recent studies on glass patterning including technologies and applications. Four technologies for glass micromachining including wet etching, sandblasting, reactive ion etching, and glass reflow process are analyzed. Advantages as well as disadvantages of each method are presented and discussed in light of the experiments. Various microsystem applications using the above glass patterning technologies like thermal sensors, hermetically packaged capacitive silicon resonators, optical modulator devices, glass microfluidics, micro-heaters, and vacuum-sealed capacitive micromachined ultrasonic transducer arrays are reported.

Keywords: wet etching, sandblasting, dry etching, glass reflow process, thermal sensors, capacitive silicon resonators, microfluidic, micro-heater, capacitive micromachined ultrasonic transducer

1. Introduction

Nowadays, micro/nano systems play a vital role in innovation in all areas of our life. They are utilized in almost all electrical equipments including cameras, televisions, smartphones, laptop computers, and vehicles, not only to increase the functionality but also to enhance the performance in various operating conditions. Their market is currently dominated by radio frequency (RF) microelectromechanical systems (MEMS), microfluidics, optical MEMS, gyroscopes, accelerometers, microphones, pressure sensors, and inkjet heads. Thus, micro/nano systems are being a mainstream for the electrical equipment.

Silicon and glass are the most commonly used materials in microsystems, employed for the fabrication of a wide range of microdevices [1–5]. Patterning of silicon structures, which has

been studied and developed for years, can be done by both wet (KOH and tetramethyl ammonium hydroxide (TMAH)) [6] and dry (reactive ion etching) etching methods. Forming high aspect ratio silicon structures could be easily achieved by deep RIE (Bosch process) technique [7]. In turn, glass micromachining faces difficulties owing to its components. Tempax glass is one kind of borosilicate glass which is frequently used in the microfabrication owing to low cost, good thermal insulation, excellent optical transparency, and anodic bonding capability. Tempax glass [5] is approximately composed of 75% SiO_2, 13% Na_2O, 10.5% CaO, and other minor additives such as 1.3% Al_2O_3, 0.3% K_2O, etc. Different compositions exhibit a different rate in the etching process so that low aspect ratio structure, etching rate, and mask selectivity are still current issues in glass micromachining. Tempax glass exhibits the excellent mechanical (mechanical strength and stiffness), dielectric (high electric insulation), and optical (high transparency) properties. In addition, it is a bio-compatible material [8]. The thermal expansion coefficient of glass is similar to that of silicon this allowing to produce silicon-on-glass substrates via an anodic bonding technique [4]. High electric insulation becomes a significant point to reduce the signal loss (parasitic capacitances) in RF MEMS, especially in high-frequency ranges and nanomechanical resonant structures [9].

In this work, we review the recent progress in glass micromachining and its applications for the microsystem fabrications. The various glass patterning technologies including wet etching, sandblasting, the reactive ion etching, and glass reflow process are presented together with the microsystem applications including thermal sensors, hermetically packaged capacitive silicon resonators, optical modulator devices, glass microfluidics, micro-heaters, and vacuum-sealed capacitive micromachined ultrasonic transducer (CMUT) arrays.

2. Wet etching and sandblasting

2.1. Description

The wet etching of glass reported in the literature [10, 11] is one of the simple methods for glass patterning; nevertheless, the precisely formed glass structure is difficult owing to its isotropic etching behavior. Advantages and disadvantages of the wet etching method are compared to other methods including sandblasting, RIE, and glass reflow process as shown in **Table 1**. High mask selectivity, low surface roughness, and simple operation are advantages of the wet etching. In turn, wet etching method cannot be used for forming small glass structures, below 1 µm-diameter. Also, created glass structures face a problem of the aspect ratio. Aspect ratio structure of glass patterning via this method is just below 1.

Figure 1 illustrates the wet etching process of glass which begins with a glass substrate of 300-µm-thick (**Figure 1(a)**). Both sides of the glass substrate are coated with 30-nm-thick Cr and 300-nm-thick Au layers (**Figure 1(b)**). Cr-Au layers increase the adhesion of the glass substrate and photoresist. Cr has a good adhesion with glass substrate while Au is an inert material in the diluted HF solution. Next, a photoresist is deposited and patterned by a photolithography process. The back side of the glass substrate is also coated with the photoresist. The Cr-Au layer is then etched out by the wet etchant, as shown in **Figure 1(c)**. Finally, the

Parameters	Wet etching	Sandblasting	RIE	Glass reflow
Feature size				
Minimum size	1 μm	100 μm	<1 μm	<1 μm
Side etching	Yes	No	No	No
Etching profile	U shapes	V shapes	Vertical	Vertical
Aspect ratio	Low	Low	High	High
Surfaces	Smooth	Rough	Smooth	Smooth
Process time	Short	Short	Medium	Long
Mask materials	Metal and photoresist	Dry film resist	Metal mask for high selectivity	Silicon mold
Selectivity between Tempax glass and mask material	High	Low	High	Glass fills into cavity
Etching environment	Liquid	Al_2O_3 particles	Plasma	Atmospheric furnace with a high temperature
Post processes	Good	Particles	Good	Good

Table 1. Summarized advantages and disadvantages of glass micromachining.

wafer is dipped in the diluted HF (**Figure 1(d)**). The wet etching setup is shown in **Figure 1(f)**. The etching rate is a function of the concentration of the diluted HF. Higher etching rate can be achieved by increasing the concentration of the diluted HF; nevertheless, the quality of the photoresist mask becomes poor. In this demonstration, the Tempax glass was etched using the diluted solution of 50% HF:DI (deionized water) = 2:1 for etching time of 10 min. Etching rate and side etching were observed at around 2 μm/min. **Figure 2(a)** and **(b)** show the experimental results of Cr-Au wet etching and glass etching, respectively.

For short patterning glass structures, the wet etching is the preferred way; however, the large depth patterning glass structures face difficulties owing to the high etching rate of the side etching. In order to solve this issue, sandblasting is considered. This is the physical etching method where a particles jet is directed toward a sample (glass substrate) for mechanical erosion via the impingement of high-velocity abrasive particles. Not only glass but also other materials including ceramic and silicon can also be patterned via this method.

Figure 3 describes the sandblasting process which uses thick dry film resist (MS 7050, 50 μm thickness, Mitsubishi paper mills limited., Japan) as a mask material. 300-μm-thick glass substrate is used (**Figure 3(a)**). A dry film resist is pasted, and then photolithography is performed, as shown in **Figure 3(b)**. Next, the glass substrate with a dry film resist patterns is etched via sandblast. **Figure 4** shows a glass patterning with an etching depth of approximately 150 μm. Glass etching surfaces are very rough and etching profiles evolve into V-shapes. Etching through the glass substrate is possible and generally it is employed for microfluidics which need holes for an inlet and outlet of liquid.
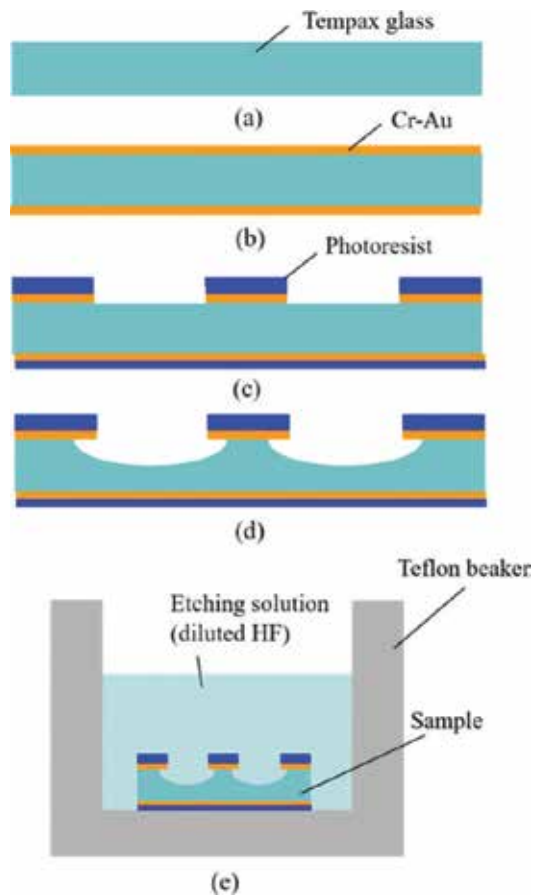
Figure 1. Wet etching process. (a) Tempax glass. (b) Cr-Au sputter. (c) Photolithography and Cr-Au wet etching. (d) Glass wet etching. (e) Wet etching setup.

2.2. Typical applications using wet etching and sandblasting

Generally, wet etching and sandblasting methods are employed for the glass patterning without requiring highly precise structure including large channels for microfluidics, through holes for inlet and outlet liquid in microfluidic, and cavities for microfabricated resonators, as described in the following.

2.2.1. Thermal sensors for heat detection of living cells in liquid

Heat of cells generated by biochemical reactions is one of the critical parameters of living organisms. Monitoring heat of cells is an effective way of investigating cell activities; however, heat production is associated with very small values. It means that the heat losses become a serious problem for heat detection. Low thermal conductivity of glass is one of the good characteristics that make it popular in thermal sensors [12–14]. In this section, we propose and developed heat-detecting silicon resonators which rely on temperature-dependent changes in the resonant frequency of resonators.
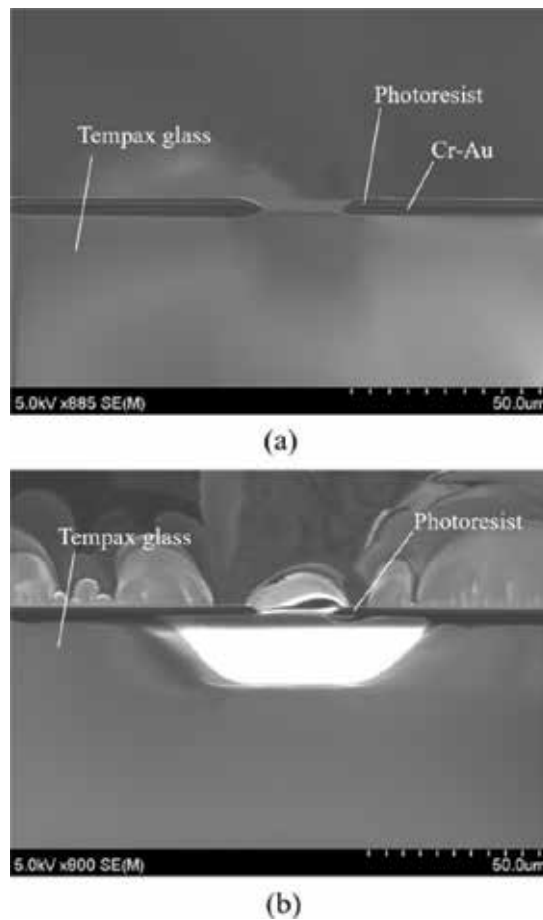
Figure 2. (a) Photolithography and metal etching. (b) Glass etching result.

Figure 5(a) shows the proposed resonant thermal sensor for heat detection of a living cell in a liquid which consists of a glass microfluidic, silicon cantilever, and vacuum chamber. The vacuum chamber and microfluidic are separated by a glass wall. Silicon cantilever is employed as a heat guide from the microfluidic to the vacuum chamber. The heat generated by a cell attached to the silicon cantilever in the microfluidic side is conducted to the silicon resonator in vacuum chamber side and the resulting temperature changes cause a shift in the resonant frequency of the silicon cantilever.

The thermal sensor is fabricated by well-known technologies including photolithography, wet etching, and anodic bonding. Vacuum chamber and microfluidic are formed by the wet etching method and holes for inlet and outlet liquids are patterned by the sandblasting method. **Figure 5(b)** shows the optical image of the completely fabricated device with an attached cell in silicon cantilever in the microfluidic. The details of the experimental processes and evaluation for this device can be found in [12].

In summary, microfluidics, vacuum chambers, and through holes of the glass substrate are successfully patterned by the wet etching and sandblasting methods. The use of resonant
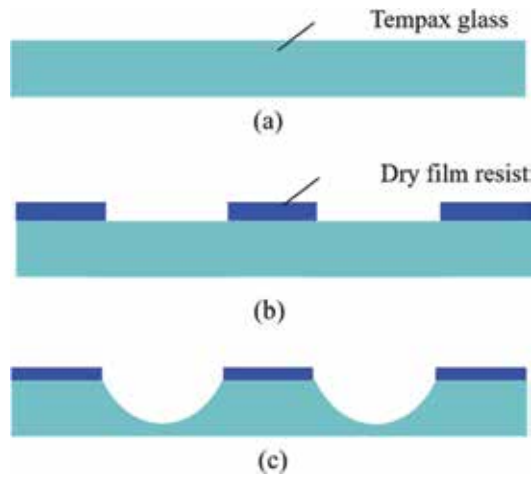
Figure 3. Fabrication process. (a) Tempax glass (b) Photolithography with a dry film resist. (c) Sandblasting.
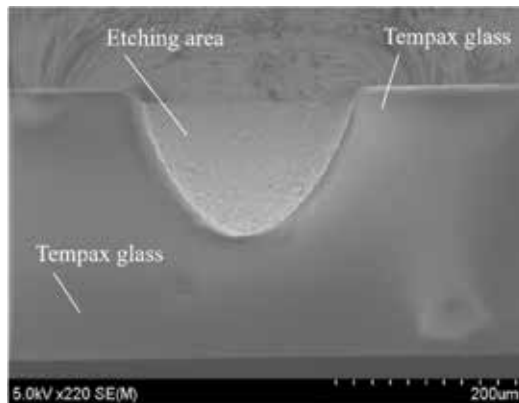

Figure 4. Glass cavity by sandblasting.

thermal sensors to measure the generated heat of a biological cell in a liquid is a clear example. The proposed devices are promising for biochemical reaction monitoring.

2.2.2. Hermetically packaged capacitive silicon resonators

Thermal expansion coefficient of glass is similar to that of silicon which makes them easily bonded together via an anodic bonding method [15]. Silicon-glass bonding becomes a key technology for device integration in various fields including microelectromechanical systems (MEMS), microelectronics, and optoelectronics. Anodic bonding between the glass substrate and silicon was employed in our works including the parasitic capacitance reduction [9, 16] and hermetically packaged device [4]. The structures of the resonator on silicon-on-insulator
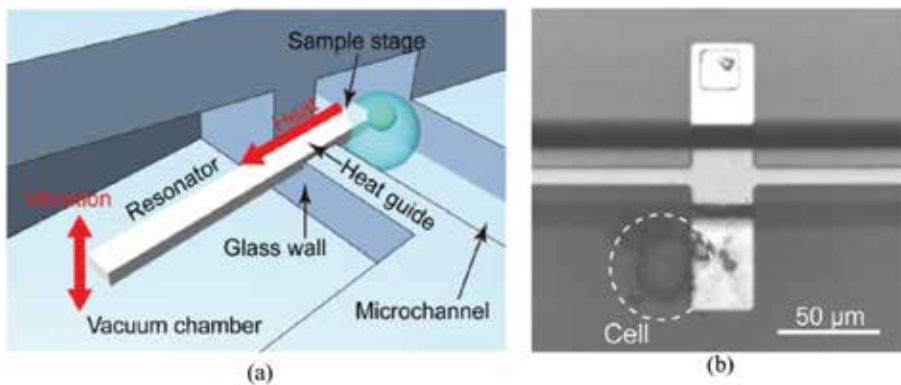
Figure 5. (a) Resonant thermal sensor for heat detection of living cells in liquid. (b) Fabricated device with an attached cell.

(SOI) are transferred to the glass substrate in order to reduce the parasitic capacitances from the handling silicon layer, as presented in [9]. Here, we present the hermetically packaged capacitive silicon resonator based on the anodic bonding.

Capacitive silicon resonators, typically employed for sensing applications and timing references, have been presented in many works [3, 4]. Their output signal is based on the measurement of the change in the capacitance between a sensing electrode and the resonant body. **Figure 6(a)** shows the sketched cross-section image of our proposed capacitive silicon resonator where the resonant bodies are placed between driving/sensing electrodes, supported by two thin beams on the sides and separated by the narrow capacitive gaps (**Figure 6(b)**). The capacitive resonator's operation is described as follows: when an AC voltage V_{AC} is applied to the driving electrode, the resulting electrostatic force induces a bulk acoustic wave in the resonant element. An additional DC voltage V_{DC} is also applied to the driving/sensing electrodes in order to amplify the electrostatic force. Small changes in the size of the sensing gap generate a voltage on the sensing electrode.

The structures of silicon resonator are defined by the deep RIE on SOI wafer and then transferred on to LTCC (low temperature co-fired ceramic) substrate with metal feed-through for electrically connected to silicon electrodes. The device is hermetically packaged by the anodic bonding technique between silicon and glass. **Figure 6(b)** and **(c)** show the optical images of the silicon resonator structure on LTCC substrate and the 2×2 cm^2 glass substrate with patterning obtained by the sandblasting for the packaging step. Front and back sides of the fabricated device after packaged process are shown in **Figure 6(d)** and **(e)**, respectively. The details of the fabrication process and evaluation of the proposal device can be found in [4].

In summary, the glass can be used as a material for the hermetically packaged. Glass and silicon can be well bonded together via the anodic bonding technique. The hermetically packaged capacitive silicon resonators were successfully demonstrated.
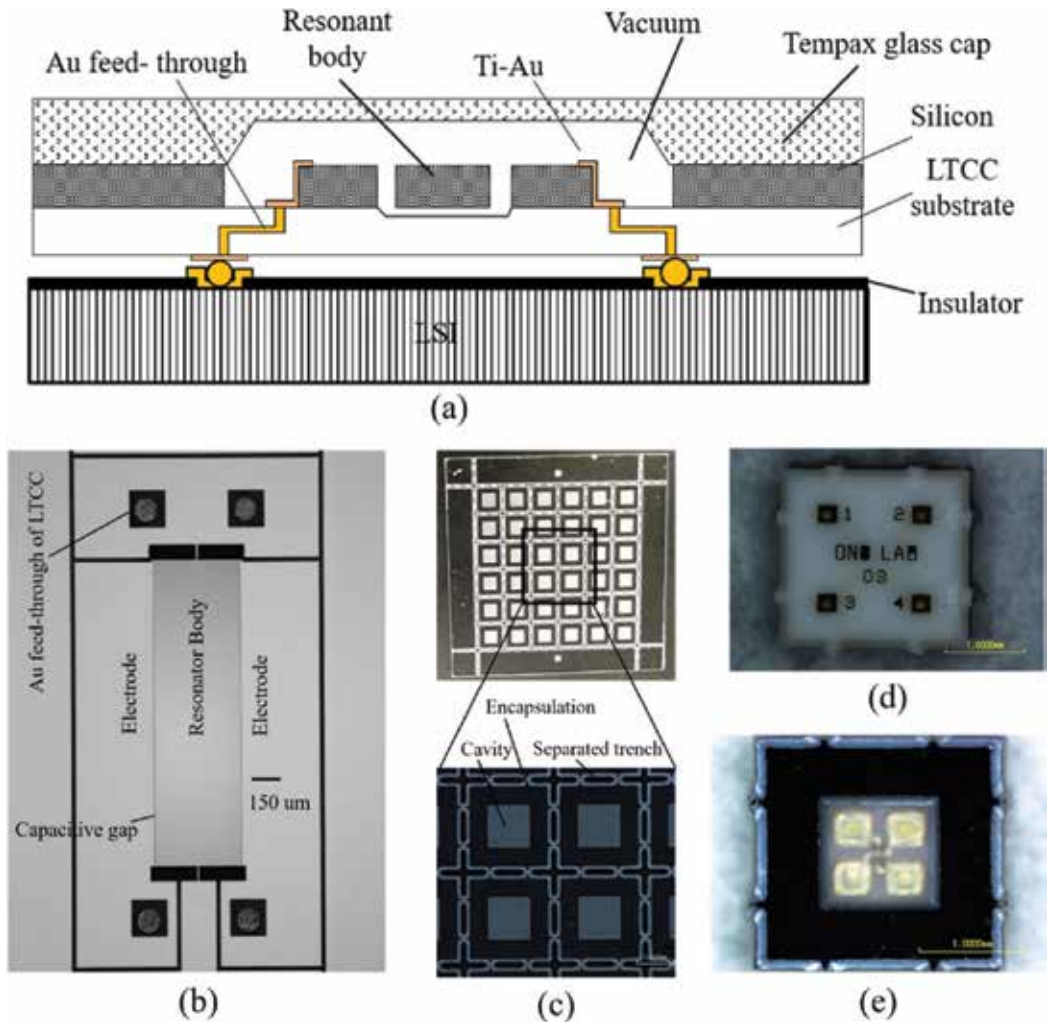
Figure 6. (a) Cross-section of the hermetically packaged silicon capacitive resonator. (b) Micrograph of silicon resonator on LTCC substrate. (c) 2×2 cm glass substrate with sandblasting patterning. (d) Front and (e) back sides of the device after hermetically packaged.

3. Reactive ion etching

3.1. Description

Although wet etching and sandblasting methods for glass patterning are widely used for microsystems, they face problems including small pattern structures and dimension reproducibility. In this section, we present the RIE method which can be potentially used for accurately patterning small glass structures.

Figure 7 shows our laboratory-made RIE equipment for the deep glass etching which is a kind of magnetron-type RIE. A strong permanent magnet (samarium-cobalt (Sm-Co)) is placed

on the top glass cover to enhance plasma density. A small etching chamber with an internal diameter of 145 mm is employed. The distance between the top glass cover and the sample stage is 13 mm. The chamber is evacuated by a turbo-molecular pump with a pumping speed of 300 l/s during the etching process which helps to reduce the deposition of reaction products on the sample surface. Plasma is generated by a 13.56 MHz RF generator and connected to the cathode. The cathode is made by aluminum with 80 mm diameter and isolated from a grounded circular cooling system by a Teflon for stray capacitance reduction. Samples are attached to the cathode stage using silicone grease for heat conduction to the stage.

Figure 8 describes the sample preparation process for the deep etching glass. It starts with a 300 μm-thick Tempax glass substrate (**Figure 8(a)**). After simple cleaning procedures (acetone, ethanol, and piranha), the glass substrate is sputtered by Cr-Au thin films with a thickness of 10 and 40 nm, respectively, as a seed layer for an electroplating of Ni (**Figure 8(b)**). A 600 nm-thick Ni film is formed on the Cr-Au surface with photoresist patterning (**Figure 8(c)** and **(d)**). Finally, the glass substrate is etched out by the above RIE setup mentioned.

The RIE etching result of the above-mentioned process is shown in **Figure 9**. Deep glass pillars with a smooth surface, vertical shapes (base angle ~ 89°) and high aspect ratio (=10) with depth of 10 μm, diameter of 1 μm and pitch of two pillars of 2 μm were achieved. The details of etching conditions and effects of the mask shape profiles can be found in [17].

3.2. Typical applications using reactive ion etching

3.2.1. Optical modulator

High transparency characteristic of glass was employed for many optical systems based on micro-optical-electro-mechanical-systems, as previously reported [17–19]. Optical devices allow manipulation of light including amplitude [20] and phase [21]. In this section, we show an optical modulator device capable of the integration of an image sensor for functional image sensing applications.
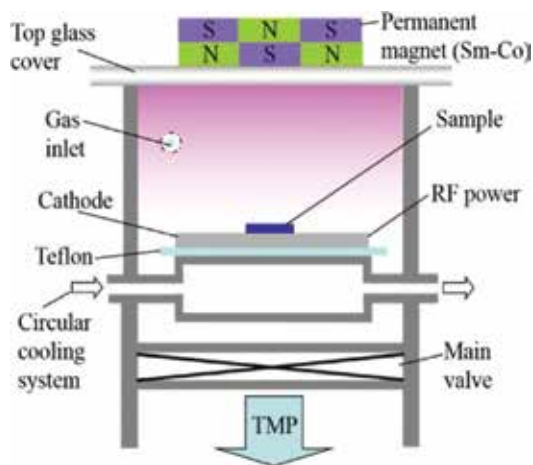

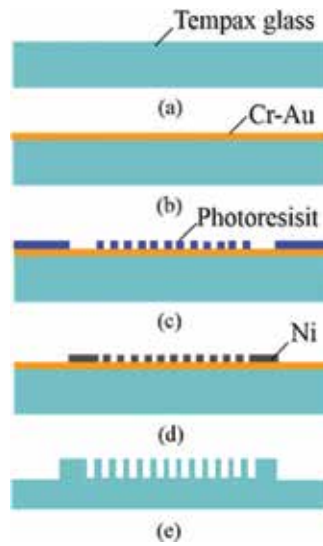**Figure 7.** Reactive ion etching setup.

Figure 8. Glass patterning by RIE. (a) Tempax glass wafer. (b) Cr-Au sputter. (c) Photolithography. (d) Nickel electroplating and photoresist removal. (e) RIE process.
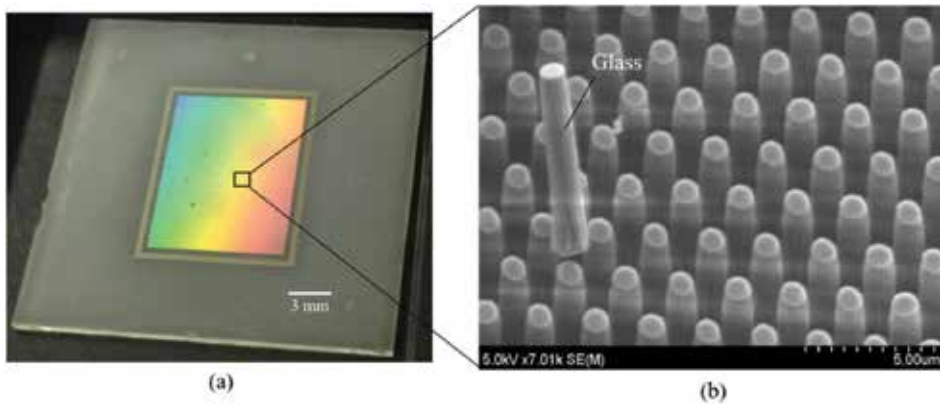

Figure 9. Glass pillar by RIE. (a) Optical image of 2×2 cm glass wafer with pillar patterning at center (colorful area). (b) Close-up scanning electron microscope (SEM) image of the pillar patterning area.

The device structure is illustrated in **Figure 10**. The 7.2×9.6 mm optical window area consists of glass pillar structures assembled with a liquid reservoir. The electrode material of top and bottom electrodes is aluminum-doped zinc oxide (AZO) produced by atomic layer deposition (ALD) method. This device can be directly mounted on an image sensor chip and has a large optical modulation range.

The optical window is operated using a dynamic electrical control of the wetting behavior of liquid on the top of the micropillar surfaces. Device concept was reported in [19, 22, 23]. When a voltage is applied to the structure, the liquid moves into the spaces between the pillars (**Figure 10(b)**). The light reflection at the pillar sidewalls is eliminated because of the

refractive index matching at the interface; therefore, the pillars array gets transparent. Thus, a high optical transmittance is obtained. In the case without liquid between pillars, the light transmittance of the device is lower than that with liquid because of light reflection and scattering by pillar walls and it works ideally as an opaque medium (**Figure 10(a)**). Therefore, by shifting the liquid in and out of the pillar array using electro-wetting, the light transmittance can be electrically controlled.

Glass pillar structures are produced by RIE, as reported before (**Figure 9**). **Figure 10(c)** shows the optical evaluation setup. It contains a cold-cathode fluorescent lamp for illumination, a resolution chart for the optical property evaluation, a focal length and F-number of the camera lens, and an image sensor. A matching oil is inserted into the pillars array just by putting the liquid droplet on the device that immediately penetrates in the whole area of the optical window. **Figure 10(d)** shows a comparison of transmittance with and without liquid penetration by using an image sensor. A low transmittance of the optical window is observed when it is measured without inserting the matching oil for glass pillar structures. The low transmission light, in this case, causes light reflection and scattering by pillar walls. A very high transmitting light of around 90% can be achieved by using matching oil. The possible reason is due to the refractive index matching between glass pillars and matching oil. Thus, the large modulation range of approximately 65% for cases with and without matching oil is achieved.

In summary, glass is a potential material for optical systems owing to its highly transparent property. The optical device based on glass patterning by RIE with the large optical modulation range was demonstrated. This device can be directly mounted on an image sensor chip for functional image sensing applications.
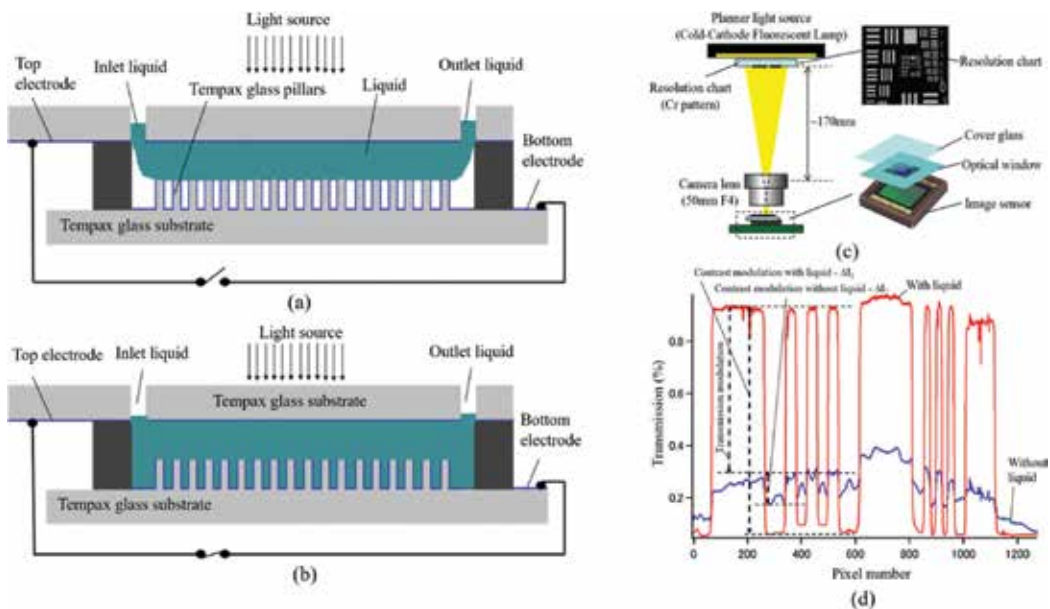

Figure 10. (a) Opaque state (without voltage supply). (b) Transparent state (with voltage supply). (c) Evaluation setup. (d) Optical property evaluation of optical window with and without liquid penetration.

3.2.2. Glass microfluidic integrated with thin silicon layer for observation of biological samples

Microfluidics has huge potential for bio-applications [12–14]. The bio-compatible selection of microfluidic material is important to avoid any effects on biological samples. Thus, a glass material becomes the preferred one for bio-applications [8]. Also, high-resolution observation of living cells helps more understanding of biological functions through the study of cellular dynamics. The surface structure of cancer cells was observed in nanoscale using scanning electron microscopy (SEM) and transmission electron microscopy (TEM), as reported in [24]. A floating particle in the liquid was observed with a TEM system using the microfluidic chamber [25]. In this section, the glass microfluidics integrated with a thin window of silicon layer for the observation of biological samples using a SEM system is described.

Figure 11(a) shows the proposed structure consisting of micro-channels (trapping channel and bypass channel), a thin silicon layer on top of the channels, a trapping pole, an inlet, and an outlet of liquid sample. At first, micro-channels are patterned by reactive ion etching (RIE) with nickel metal as a mask material. Then, SOI wafer with 200 nm-thick device layer is bonded to the patterned glass surface above by anodic bonding method. The handling layer of SOI is partially etched out by deep RIE until reaching the opened insulator layer (SiO$_2$) at the window part. Finally, SiO$_2$ is removed by HF vapors.

Figure 11(b) shows a SEM image of the fabricated device which installed into SEM chamber. DI water is then flowed into microfluidic under SEM observation, as demonstrated in **Figure 11(c)**. The details of the fabrication process, evaluation setup, and measurement results can be found in [26].
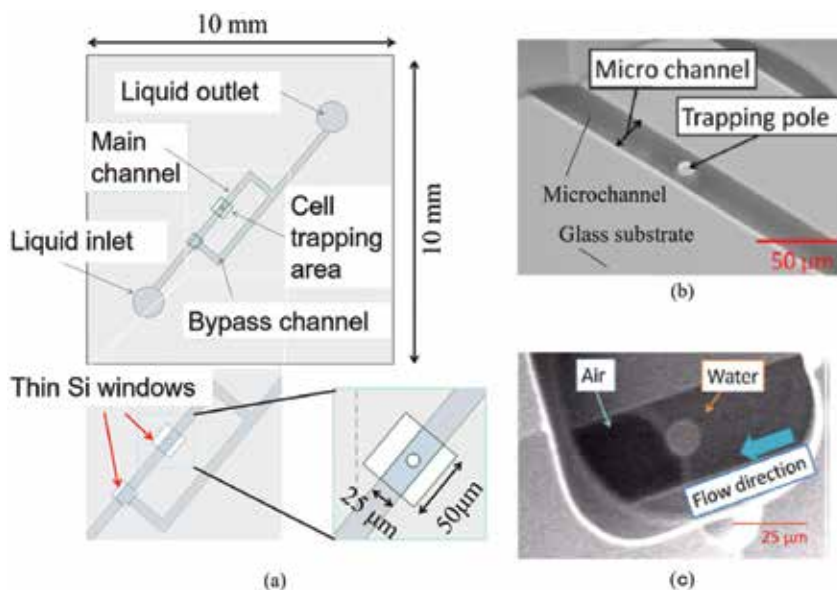

Figure 11. (a) Glass microfluidics integrated with a thin silicon layer for cell observation. (b) Fabricated device. (c) DI water loaded into the microfluidic under SEM observation.

In summary, glass microfluidics, successfully patterned by RIE, integrated with a thin window of silicon layer for the observation of biological samples in vacuum analytical system (ex. SEM) was demonstrated.

4. Glass reflow process

4.1. Description

Precise glass patterning can be achieved by RIE method; however, forming very deep glass structures is a challenge owing to a low etching rate and low selectivity (between the glass and mask material). Also, the reflection of ions [17] at the mask or the edge of the mask and/or mask erosion may contribute to its limited aspect ratio and depth. To overcome the above problems, glass reflow process was investigated in [18, 19] which can create the compounded structures between silicon and glass. In this section, we present glass reflow process and its applications for microsystems.

Figure 12 schematizes glass reflow process which starts with a 300 µm-thick silicon wafer. The silicon structures (silicon mold) are formed by deep RIE based on Bosch process using SF_6 and C_4F_8 (**Figure 12(a)**). Next, anodic bonding of the silicon wafer and the Tempax glass is carried out in a high vacuum chamber with an applied voltage of 800 V at 400°C for 15 min (**Figure 12(b)**). The glass reflow process is performed in a furnace with ambient atmospheric pressure at 750°C for 10 h (**Figure 12(c)**). Tempax glass is melted and poured into cavities of silicon mold during the high-temperature glass reflow process. After that, both sides of the wafer are mechanically lapped and polished by a chemical mechanical polishing process (**Figure 12(d)**).
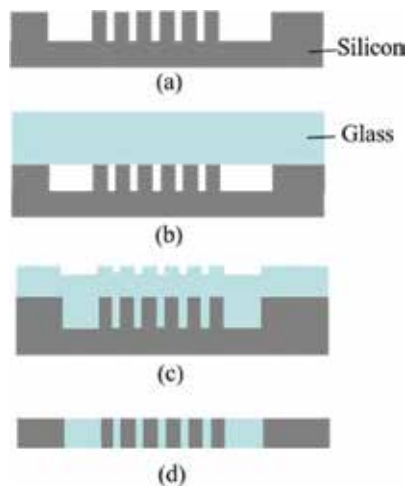

Figure 12. Glass reflow process. (a) Silicon mold. (b) Anodic bonding in a vacuum chamber. (c) Glass reflow process. (d) Lapping and polishing process.

Figure 13(a) and **(b)** show silicon mold formed by deep RIE and the compounded structure between silicon and glass created by glass reflow process, respectively. The complete filling into the cavities was achieved. Thus, the glass structures can be formed by glass reflow process; nevertheless, the process faces difficulties when glass enters into narrow patterns. Glass reflow into narrow trenches was investigated by an additional optimization of the process flow conditions. At higher temperature (1100°C) and with longer time process (20 h), using SiO_2 to enhance surface wettability, the complete filling glass into the narrow trenches was achieved. **Figure 14(a)** and **(b)** show the silicon pillar mold and complete filling glass into narrow trenches, respectively. The details of glass reflow process condition can be found in [18].

In summary, the glass reflow into the large cavities and narrow trenches and deep glass structures compounded with silicon can be achieved. The glass can easily fill large cavities; nevertheless, additional conditions are required for filling into the narrow trenches.

4.2. Typical applications using glass reflow process

The glass reflow process exhibits more advantages than wet etching, sandblasting and RIE methods. We have used it for microsystem applications, as reported in [18, 27]. We have investigated it
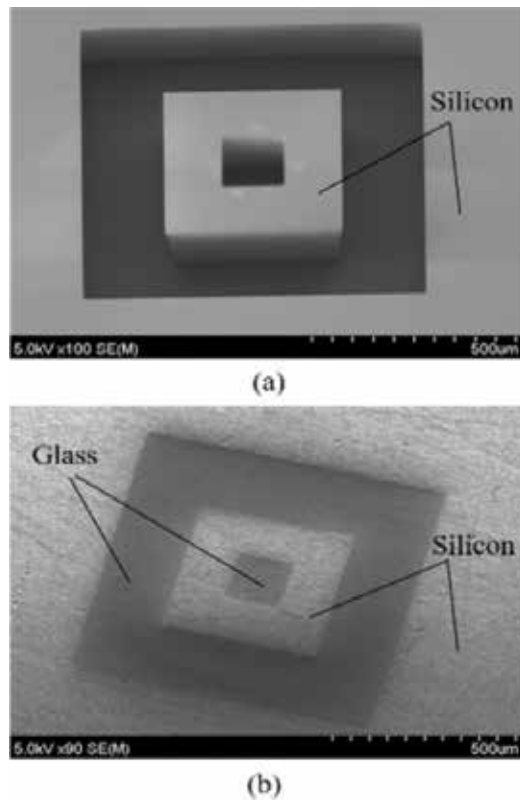

Figure 13. Glass reflow for large pattern size. (a) Silicon mold. (b) Glass reflow into a silicon mold.

in different of microsystems including through-wafer interconnects, thermal isolation, vacuum-sealed capacitive micromachined ultrasonic transducer (CMUT) arrays, and optical modulator devices. The optical modulator device's concept is similar to that in Section 3.2.1. The details of fabrication process and evaluation can be found in [22]. Here, we report thermal isolation and CMUTs, as follows.

4.2.1. Thermal isolation

Micro-heaters are typically used in the gas chemical sensors [28, 29] because the gas chemical reactions in a sensing layer require a high temperature. Micro-heaters are considered as a hot plate which controls the temperature of the sensing layer. Furthermore, they may also be used as an infrared source to analyze the molecular fingerprint of gases using infrared gas sensors [30]. Moreover, several MEMS devices require a good thermal isolation such as infrared detectors [31] and ultrasonic transducers for thermal applications [32]. Thus, the good thermal isolation is very desirable in micro/nano thermal devices. Glasses are suitable materials for this purpose because of their low thermal conductivity, low thermal expansion coefficient
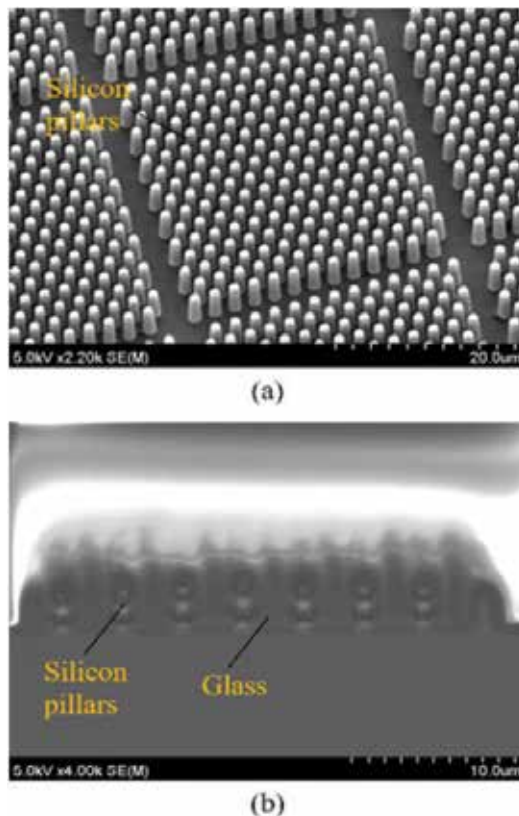

Figure 14. Glass reflow for small pattern size. (a) Silicon mold. (b) Glass reflow into a silicon mold.

and excellent mechanical strength. SiO$_2$ layers of 10–100 μm thickness for thermal isolation was reported in [33], where silicon pillars have formed by deep RIE technique with the high aspect ratio structure which are then oxidized to create the SiO$_2$ layer as thick as the deep RIE patterns. Nevertheless, silicon at bottom areas may be difficult to turn completely to SiO$_2$ and pores may exist inside the SiO$_2$ layer.

A thick glass layer for thermal isolation was proposed in [18]. Silicon micro-heater is compounded by the glass substrate fabricated by the glass reflow process. Top view of the micro-heater is shown in **Figure 15(a)**. The silicon micro-heater has been characterized by the near-infrared imaging as shown in **Figure 15(b)**. The temperature distribution is highly located at the silicon part. The compounded glass can thermally isolate the heated silicon effectively with a temperature difference more than 100°C when the temperature of the silicon part is heated at 140°C at an input power of 200 mW. In addition, a reliability property of the silicon micro-heater is evaluated. The electrical current is supplied to the micro-heater and kept ON state at 140°C for more 2 hours and the response is recorded, as shown in **Figure 15(c)**, which shows highly stable temperature with ±1.5°C tolerance. Thermal cycling is also performed with repetitive ON/OFF cycles for 1.5 hours. ON/OFF states with 1 min/ 1 min cycles are applied and the response is observed which shows a good stability at the heating operation as shown in **Figure 15(d)**.

In summary, the proposed micro-heater fabricated by glass reflow process shows good characteristics that allow possible application to gas chemical sensors.
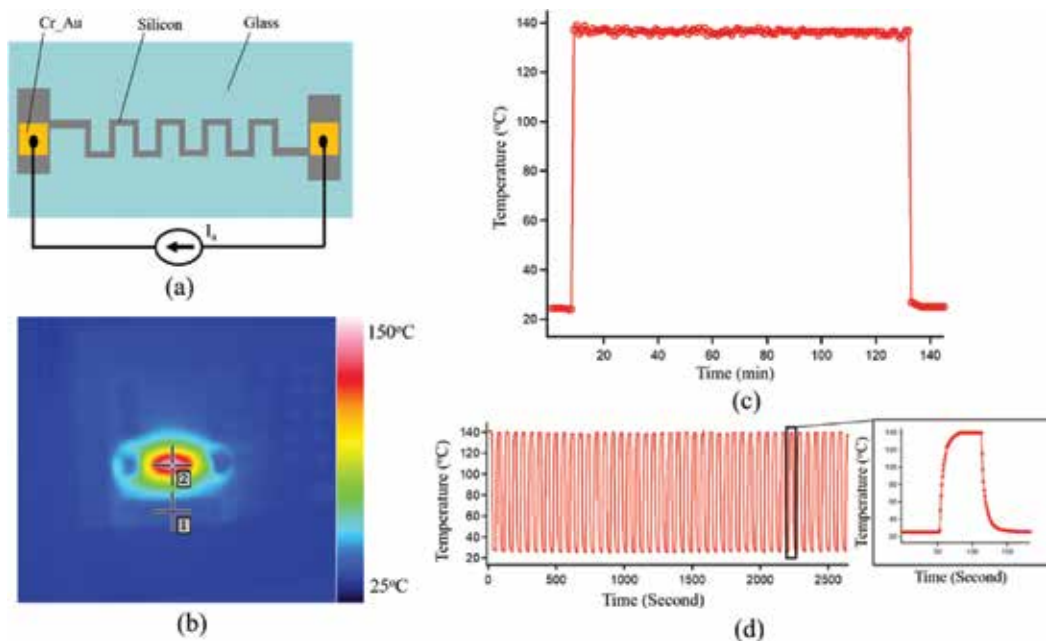

Figure 15. (a) Silicon micro-heater compounded glass. (b) Infracted image of silicon micro-heater. (c) Keep ON at 140°C. (d) ON/OFF cyclic test of the micro-heater.

4.2.2. Vacuum-sealed capacitive micromachined ultrasonic transducer arrays

CMUTs are currently present in many electrical equipment such as medical imaging, nondestructive measurement, and chemical sensing. CMUT array device produced by the glass reflow and anodic bonding reported in our recent work [27]. Firstly, we demonstrate the low resistance of the silicon through-glass wafer via based on the glass reflow process and a low resistivity silicon wafer. Secondly, the anodic bonding between silicon-glass reflow wafer and SOI wafer is successfully performed. Then, the handle and buried oxide layers are etched to release CMUT membranes and electrical connections and pads are subsequently formed via sputter method and using a shadow mask. More information on fabrication process can be found in [27].

Figure 16(a) shows the CMUTs structure which contains silicon through-wafer interconnects and releasing membranes suspended over vacuum gaps. The CMUT cells are separated by the Tempax glass and Cr-Au layers are employed for electrical connections and pads. The CMUT works as a capacitor cell. When a DC voltage is applied to two electrodes, the silicon
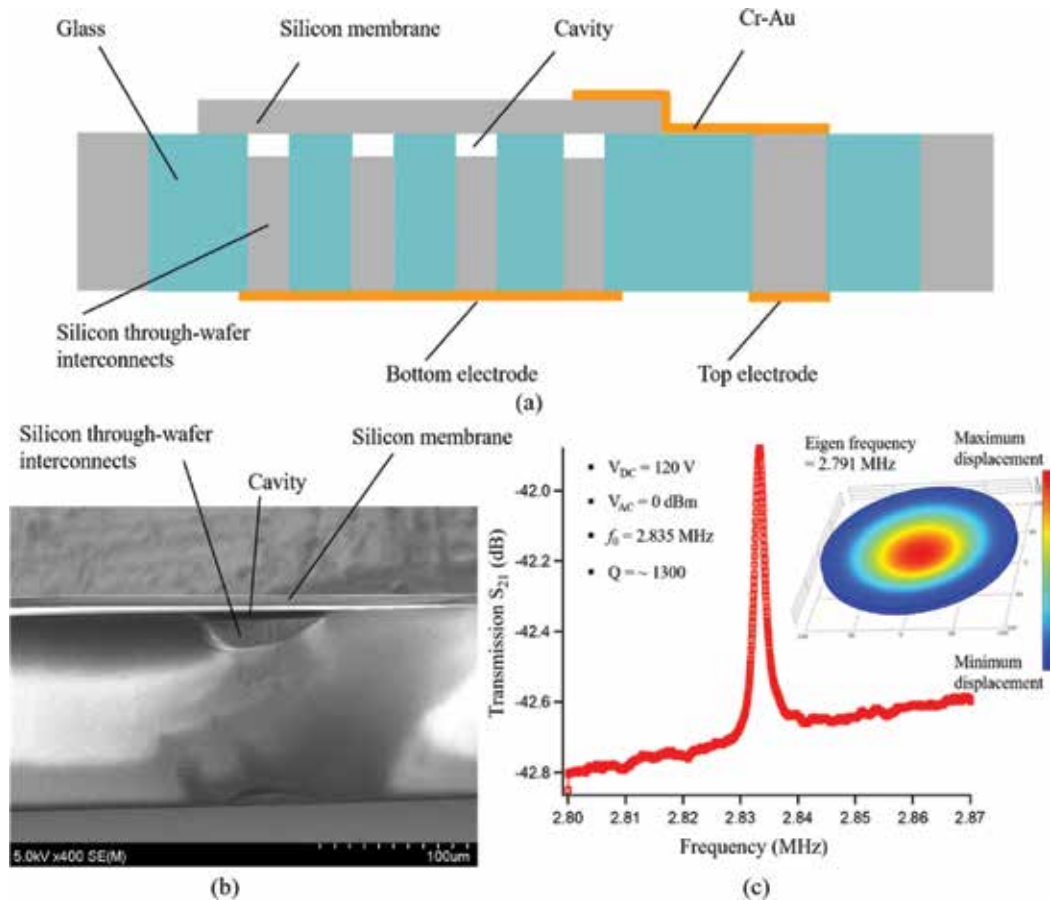

Figure 16. (a) Device structure. (b) Vacuum cavity. (c) Transmission S_{21} of CMUTs device.

membranes are attracted toward the bottom electrode by the electrostatic force. If the AC voltage is supplied to the membrane, driving the capacitor with an alternating voltage generates ultrasound. It works as a transmitter in this case. Otherwise, if the membrane is subjected to ultrasound pressure, the electrical current is created due to the capacitance changes and in this mode, it works as a receiver.

Figure 16(b) shows the SEM image of a vacuum-sealed cavity. The resonance characteristic of CMUT array is evaluated using a network analyzer. Transmission S_{21} is indicated for CMUT array in **Figure 16(c)**. A resonant peak, which is observed under V_{dc} of 120 V, V_{ac} of 0 dBm, is found at 2.83 MHz with the Q factor of approximately 1300 in the vacuum environment of 0.01 Pa. Additionally, the simulation result (FEM – finite element method) is in good agreement with experimental results as shown in **Figure 16(c)**.

In summary, the CMUTs device based on the glass reflow process and anodic bonding was demonstrated. The experiment process may be useful in microsystems including optical devices, microfluidics, packaging with electrical feed-through, and 3D-MEMS devices.

5. Conclusions

In this work, four technologies for glass micromachining including wet etching, sandblasting, RIE, and glass reflow process were reported and discussed. The wet etching and sandblasting technologies are simple process; however, they face problems including small pattern structures and dimension reproducibility. RIE technique exhibits potential for accurately patterning small glass structures, but forming very deep glass structures are a challenge owing to a low etching rate and low selectivity. Glass reflow process which creates compounded structures between silicon and glass is a suitable technology for various microsystem fabrications; nevertheless, some additional conditions are required for filling into the narrow trenches. Typical applications take advantage from the above technologies including thermal sensors, hermetically packaged capacitive silicon resonators, optical modulator devices, glass microfluidics, micro-heaters, and vacuum-sealed capacitive micromachined ultrasonic transducer arrays. It is our hope that this review may be a useful reference for those working in the field of micro/nanosystems.

Acknowledgements

Author details

Nguyen Van Toan*, Naoki Inomata, Masaya Toda and Takahito Ono

*Address all correspondence to: nvtoan@nme.mech.tohoku.ac.jp

Graduate School of Engineering, Tohoku University, Sendai, Japan

References

[1] Ono T, Esashi M. Mass sensing with resonating ultra-thin silicon beams detected by a double-beam laser Doppler vibrometer. Measurement Science and Technology. 2004; **15**:1977-1981

[2] Kim SJ, Ono T, Esashi M. Mass detection using capacitive resonant silicon resonator employing LC resonant circuit technique. The Review of Scientific Instruments. 2007;**78**:085103

[3] Van Beek JTM, Puers R. A review of MEMS oscillations for frequency reference and timing applications. Journal of Micromechanics and Microengineering. 2012;**22**:013001

[4] Toan NV, Miyashita H, Toda M, Kawai Y, Ono T. Fabrication of an hermetically packaged silicon resonator on LTCC substrate. Microsystem Technologies. 2013;**19**:1165-1175

[5] Toan NV, Toda M, Ono T. An investigation on etching techniques for glass micromachining. Micromachining. 2016;**7**:51

[6] Powell O, Harrison HB. Anisotropic etching of {100} and {110} planes in (100) silicon. Journal of Micromechanics and Microengineering. 2001;**11**:217-220

[7] Sammak A, Azimi S, Izadi N, Hosseinieh BK, Mohajerzadeh S. Deep vertical etching of silicon wafers using a hydrogenation-assisted reactive ion etching. Journal of Microelectromechanical Systems. 2007;**16**:912-918

[8] Hossain KMZ, Patel U, Ahmed I. Development of microspheres for biomedical applications: A review. Progress in Biomaterials. 2015;**4**:1-19

[9] Toan NV, Shimazaki T, Ono T. Single and mechanically coupled capacitive silicon nanomechanical resonator. Micro & Nano Letters. 2016;**11**:591-594

[10] Grosse A, Grewe M, Fouckhardt H. Deep wet etching of fused silica glass for hollow capillary optical leaky waveguides in microfluidic devices. Journal of Micromechanics and Microengineering. 2001;**11**:257-262

[11] Iliescu C, Chen B, Miao J. On the wet etching of pyrex glass. Sensor and Actuators Physics: A. 2008;**143**:154-161

[12] Inomata N, Toda M, Sata M, Ishijima A, Ono T. Pico calorimeter for detection of heat produced in an individual brown fat cell. Applied Physics Letters. 2012;**100**:154104

[13] Inomata N, Toda M, Ono T. Highly sensitive thermometer using a vacuum-packed Si resonator in a microfluidic chip for the thermal measurement of single cell. Lab on a Chip. 2016;**16**:3597

[14] Yamada T, Inomata N, Ono T. Sensitive thermal microsensor with pn junction for heat measurement of a single cell. Japanese Journal of Applied Physics. 2016;**55**:027001

[15] Hanneborg A, Nese M, Ohlckers P. Silicon to silicon anodic bonding with a bonrosilicate glass layer. Journal of Micromechanics and Microengineering. 1991;**1**:139-144

[16] Toan NV, Nha NV, Song Y, Ono T. Fabrication and evaluation of capacitive silicon resonators with piezoresistive heat engines. Sensors and Actuators A. 2017;**262**:99-107

[17] Toan NV, Sangu S, Ono T. Fabrication of deep SiO_2 and Tempax glass pillar structures by reactive ion etching for optical modulator. Journal of Microelectromechanical Systems. 2016;**25**:668-674

[18] Toan NV, Sangu S, Ono T. Glass reflow process for microsystem applications. Journal of Micromechanics and Microengineering. 2016;**26**(11):115018 (9 Pages)

[19] Toan NV, Sangu S, Inomata N, Ono T. Glass capillaries based on a glass reflow into nano-trench for controlling light transmission. Microsystem Technologies. 2016;**22**:2835-2840

[20] Mias S, Camon H. A review of active optical devices: I. Amplitude modulation. Journal of Micromechanics and Microengineering. 2008;**18**:083001

[21] Mias S, Camon H. A review of active optical devices: II. Phase modulation. Journal of Micromechanics and Microengineering. 2008;**18**:083002

[22] Toan NV, Sangu S, Saito T, Inomata N, Ono T. Fabrication of a SiO_2 optical window for controlling light transmission. Microsystem Technologies. 2017;**23**:919-927

[23] Toan NV, Sangu S, Ono T. Design and fabrication of large area freestanding compressive stress SiO_2 optical window. Journal of Micromechanics and Microengineering. 2016;**26**:075016

[24] Nishiyama H, Suga M, Ogura T, Maruyama Y, Koizumi M, Mio K, Kitamura S, Sato C. Atmospheric scanning electron microscope observes cells and tissues in open medium through silicon nitride film. Journal of Structural Biology. 2010;**172**:191-202

[25] Evans JE, Jungjohann KL, Wong PCK, Dutrow GH, Arslan I, Browning ND. Visualizing macromolecular complexes within situ liquid scanning transmission electron microscopy. Micro. 2012;**43**:1085-1090

[26] Hayashi H, Toda M, Ono T. Micro fluidic chamber with thin Si windows for observation of biological samples in vacuum. IEEE international conference on Micro Electro Mechanical Systems. 2015:344-347

[27] Toan NV, Hahng S, Song Y, Ono T. Fabrication of vacuum-sealed capacitive micro-machined ultrasonic transducer arrays using glass reflow process. Micromachining. 2016;**7**:76

[28] Tao C, Yin C, He M, Tu S. Thermal analysis and design of a micro-hotplate for silicon substrated micro-structural gas sensor. Proceeding of IEEE-NEMS. 2008:284-287

[29] Partride JG, Field MR, Sadek AZ, Zadeh KK, Plessis JD, Taylor MB, Atanacio A, Prince KE, Mcculloch DG. Fabrication, structural characterization and testing of a nanostructured tin oxide gas sensor. IEEE Sensor Journal. 2009;**9**:563-568

[30] Chen L, Mehregany M. Exploring silicon carbide for thermal infrared radiators. Proceeding of IEEE-Sensors. 2007:620-623

[31] Xu YQ, Wu NJ. Oxide thin film heterostructure IR detector. Proceedings of 17th IEEE-ISAF. 1998:199-202

[32] Mcnab A, Kirk KJ, Cochran A. Ultrasonic transducers for high temperature characterization of micromachined chemical reactions. Proceedings of Tranducers'97. 1997:163-166

[33] Zhang C, Najafi K. Fabrication of thick silicon dioxide layers for thermal isolation. Journal of Micromechanics and Microengineering;**14**:769-774

Application of Glass Beads in Building Exterior Wall Surface Materials

Jihui Yuan

Additional information is available at the end of the chapter

Abstract

Glass beads are solid glass spheres. Because of their high strength, chemical stability, low thermal expansion, and good flowability, they are manufactured from colorless glass for many industrial purposes. In recent years, the urban heat island (UHI) phenomenon has become very serious in urban centers. Heat emitted from exterior walls of buildings accounts for a relatively large proportion of total anthropogenic waste heat. Retroreflective (RR) materials are researched worldwide for the potential in application to building exterior wall surface instead of normal diffuse highly reflective (DHR) materials to resist the UHI. Glass beads are the common main components of these RR materials. Glass beads have different refractive indices and diameters. The classification and reflection principles of glass beads, experimental analysis on the optical properties and thermal performance of glass bead RR materials are elaborated in detail in this chapter. In addition, if these glass bead RR materials are used in building facades, when the incident angle of the sun is very high, the facade will produce a large specular reflection to the road, which may cause adverse effects on pedestrians. Therefore, theoretical and technical aspects of preventing the specular reflection from glass bead RR materials should be studied and implemented.

Keywords: urban heat island, building façade materials, retroreflective materials, glass beads, experimental analysis

1. Introduction

Glass beads are solid glass spheres. Because of their high strength, chemical stability, limited thermal expansion, and good flowability, they are manufactured from colorless glass for several industry purposes and widely used for blasting, filler, and traffic safety.

1.1. Glass bead retroreflective materials

In recent years, the urban heat island (UHI) phenomenon has become serious in urban centers. Among the factors of increasing UHI, the urbanization has been considered as one of the main reasons. Urban constructions are important parts of the urbanization. Heat emitted from exterior walls of buildings accounts for a relatively large proportion of total anthropogenic waste heat. Therefore, many countermeasures of mitigating UHI and saving energy of buildings have been implemented by means of high reflection of the building's exterior wall surface. There are usually three kinds of reflections: diffuse reflection, specular reflection, and retroreflection.

At present, in order to be possibly applied to building exterior wall surface to resist the UHI and save energy consumption of buildings, retroreflective (RR) materials are recommended and researched by scholars worldwide instead of the normal diffuse highly reflective (DHR) materials [1–3]. Glass beads are the common main components of these RR materials. The principle of retroreflection of glass bead is shown in **Figure 1** [4].

Currently, several types of RR materials are commercially available in Japan (as shown in **Figures 2–5** [5, 6]). However, they are employed for various safety and decorative purposes and are useful at nighttime when visibility is important under low-light conditions. As for application to building envelopes, RR materials have not been widely used yet [7]. In order to possibly apply these commercially available RR materials to building the exterior wall surface, their weatherability must be ensured. In the design of buildings, those building materials that are uneasy to maintain won't be considered to be used for the exterior wall surface, since safety is given the highest priority.

Hence, long-term durability of new building's exterior wall surface materials should be verified by a long-term exposure experiment. Afterward, they can be practically applied to exterior wall surface of buildings.
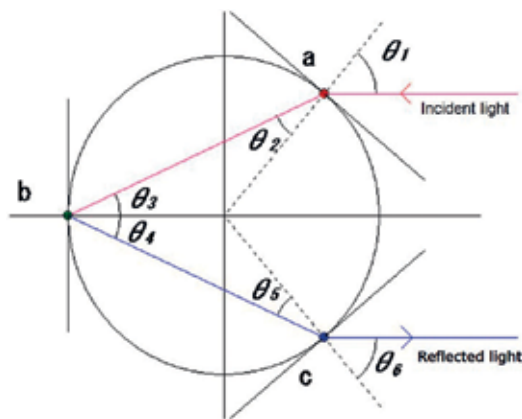

Figure 1. Principle of retroreflection of glass bead.
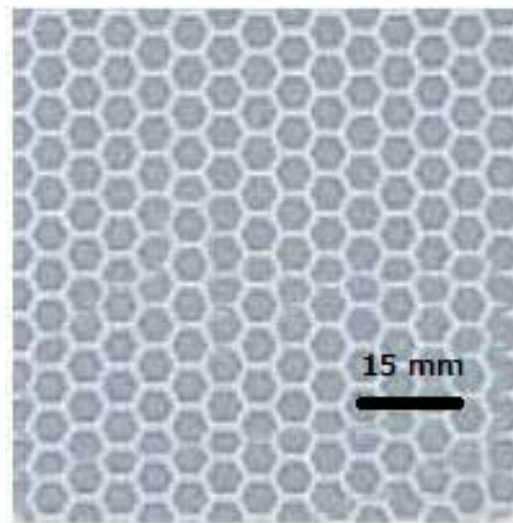
Figure 2. Appearance of lens-type RR material.
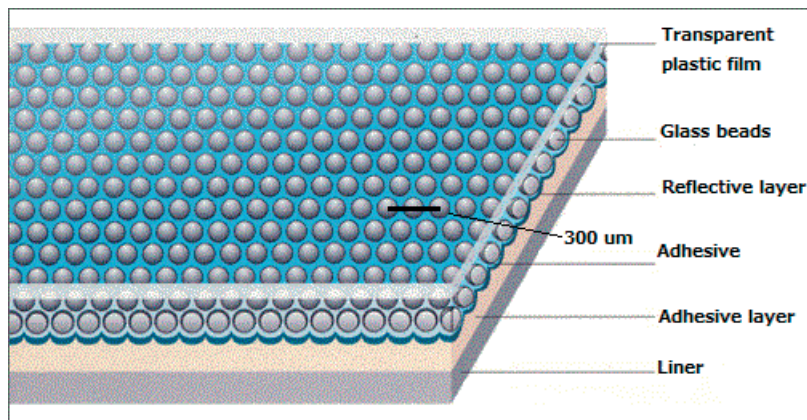
Figure 3. Sectional structure of lens-type RR material.

1.2. Impact on building energy consumption and urban albedo

The same as a DHR material, RR material applied to building facades can decrease the energy consumption of buildings during the cooling period, whereas it can increase the energy consumption of buildings during heating period. Previous research indicated that when comparing the annual thermal load of a simulated building (air-conditioned area = 605 m^2) located in Shanghai, China, with RR facade to that with no RR facade, the yearly cooling load is reduced by about 157 MJ/(m^2-year) (19%). However, the yearly heating load is increased by about 71 MJ/(m^2-year) (6%). In general, the total load of the simulated building is decreased by about 86 MJ/(m^2-year) (4.3%) when the RR façade is
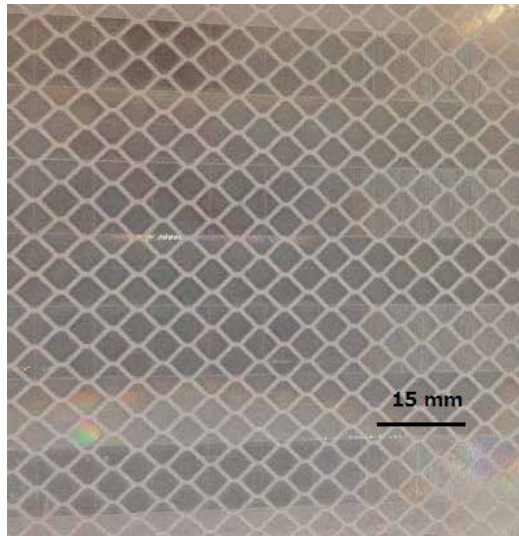
Figure 4. Appearance of prism-type RR material.
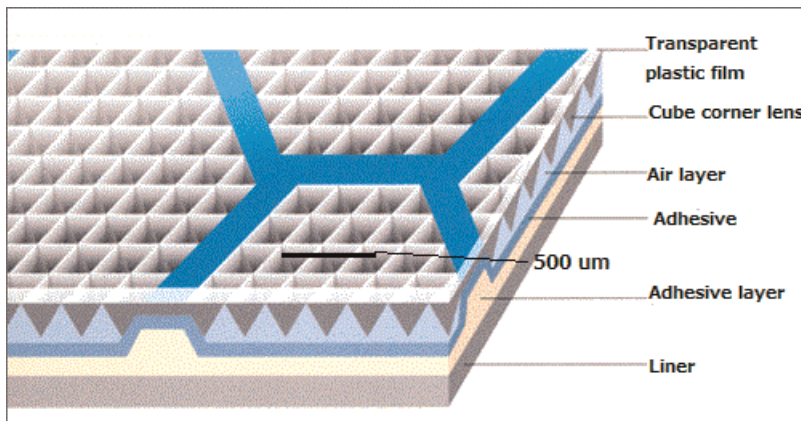
Figure 5. Sectional structure of prism-type RR material.

adopted [8]. A research related to the influence of RR materials on the energy consumption of public buildings in different climatic regions of China showed that the RR coating materials are more effective in the cooling-dominated area (i.e., Guangzhou) than the heating-dominated area (i.e., Harbin) [9]. A research, which is related to the thermal energy impact of RR and DHR envelopes on energy consumptions of buildings in different metropolitan areas of the United States, was analyzed via using the EnergyPlus software [3]. Results showed that the total energy consumption and cooling energy consumption of heating, ventilation and air conditioning (HVAC) are reduced by 8.2 and 9.8%, respectively, under the RR context.

Compared to building exterior wall surface materials with DHR and specular reflective characteristics, a previous research by a two-dimensional urban canyon space model showed that the RR coating of buildings is the most effective to increase the urban albedo [8]. A research showed that the RR materials could be effectively applied to urban pavements and building envelopes to improve the urban albedo [2].

1.3. Motivation and purpose

For possible application of glass bead RR materials to exterior wall surface of buildings, methods of thermal and optical characteristics analysis and durability testing of glass bead RR materials are summarized and elaborated in this study. In addition, if these glass bead RR materials are applied to building facades, when the angle of sunlight incident on the facade surface is high, the facade surface produces a large specular reflection on the road, which may cause adverse effects on pedestrians. Therefore, theoretical and technical aspects of preventing the specular reflection from glass bead RR materials should be studied and implemented. A theoretical possibility of preventing the specular reflection through appropriate design of glass bead RR materials will also be proposed in this study.

2. Methods to derive retroreflectivity of RR materials

There are two main methods to obtain retroreflectivity of RR materials: one is measured by a spectrophotometer system [10] (as shown in **Figure 6**) and the other is determined by a thermal balance principle of surface [11] (as shown in **Figure 7**).
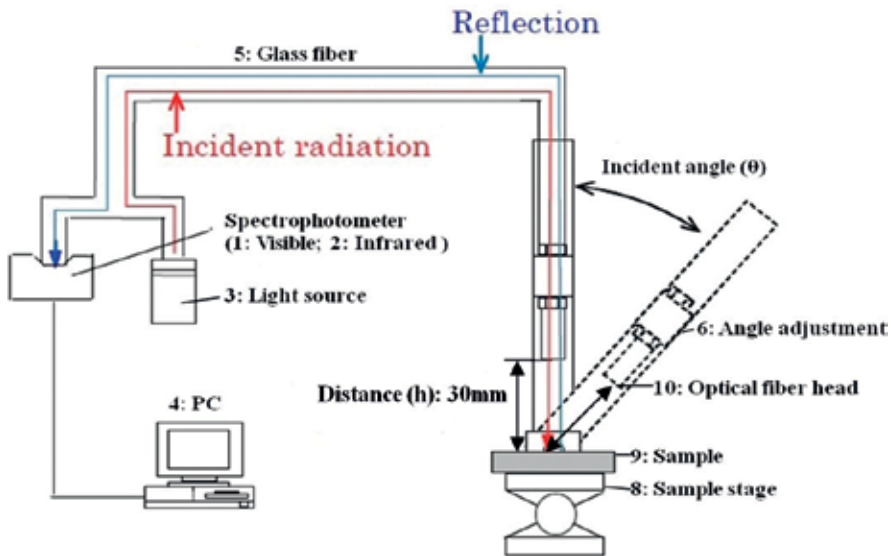

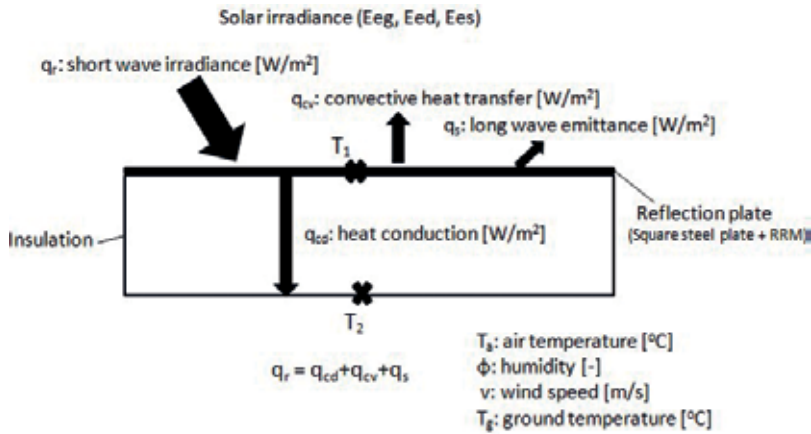**Figure 6.** A diagrammatic general view of the spectrophotometer system.

Figure 7. A conceptual diagram of the thermal balance of RR materials.

2.1. Determination of retroreflectivity by spectrophotometer

The spectrophotometer system is an emitting-receiving optical fiber system, which includes (1) visible spectrophotometer, (2) infrared spectrophotometer, (3) light source, (4) glass fiber, (5) RR sample stage with angle adjustment and angle scale, and (6) computer for processing data.

For the determination of angular retroreflectivity of RR materials using the emitting-receiving optical fiber system, the angular retroreflectivity with incident angle of 7° of the prism RR sample was 0.41, and this was used as the base retroreflectivity. Therefore, the angular retroreflectivity of the other RR materials can be determined through the reflection intensity relative to that of the prism RR sample and the spectral distribution of solar radiation. The function for determining angular retroreflectivity of sample is shown as:

$$\rho_{ret-ang} = \rho_{ret-base} \cdot \int S(\gamma) \cdot E(\gamma) d\gamma \Big/ \int S_{base}(\gamma) \cdot E(\gamma) d\gamma \qquad (1)$$

where $\rho_{ret-ang}$ is the angular retroreflectivity of RR materials [−]; $\rho_{ret-base}$ the retroreflectivity with incident angle of 7° of the base prism RR sample [−]; $S(\gamma)$ the reflection intensity of these RR materials at different incident angles [−]; $S_{base}(\gamma)$ the reflection intensity of the base prism RR sample at incident angle of 7° [−]; and $E(\gamma)$ the spectral distribution of hemispherical solar irradiance specified in ISO 9845-1 of International Organization for Standardization [12].

2.2. Determination of retroreflectivity by thermal balance principle

According to previous research [11], the retroreflectance of RR materials can be derived by subtracting the diffuse solar reflectivity measured with spectrophotometer (incident angle of light source is designed at 7°) from the total solar reflectivity evaluated by the thermal balance principle from temperatures measured outdoors (as shown in **Figure 7**) and is given by:

$$\rho_{ret} = \rho_{tmp} - \rho_{spc} \tag{2}$$

where ρ_{ret} is the retroreflectivity of RR materials [−]; ρ_{tmp} the solar reflectivity evaluated by the thermal balance in the outdoor environment [−]; and ρ_{spc} the solar reflectivity measured by spectrophotometer in the laboratory [−].

ρ_{tmp} can be derived as:

$$\rho_{tmp} = 1 - q_r/E_i \tag{3}$$

where q_r is the amount of shortwave irradiance [W/m^2] and E_i is the global irradiance on the inclined reflecting plate [W/m^2].

$$q_r = q_s + q_{cv} + q_{cd} \tag{4}$$

$$q_s = -F_{sa}\varepsilon_s\varepsilon_a\sigma(T_a)^4 - F_{sw}\varepsilon_s\varepsilon_w\sigma(T_g)^4 + \varepsilon_s\delta(T_1)^4 \tag{5}$$

$$q_{cv} = h(T_1 - T_a) \tag{6}$$

$$q_{cd} = \mu/L(T_1 - T_2) \tag{7}$$

In the previous equations, q_s is the amount of long-wave emittance [W/m^2]; q_{cv} the amount of convective heat transfer [W/m^2], q_{cd} the amount of heat conduction to the insulation [W/m^2]; F_{sa} the form factor from reflecting plate to air [−]; F_{sw} the form factor from reflecting plate to ground [−] (=1−F$_{sa}$); ε_s the emissivity of the reflecting plate surface [−]; ε_a the atmospheric emissivity [−]); ε_w the emissivity of the ground surface [−]; δ the Stefan-Boltzmann constant (=5.67×10^{-8} W/m^2 K^4); h the convective heat transfer coefficient of a flat plate exposed to a stream of air [W/m^{2}K]; T_1 the inner surface temperature of steel mounting plate [°C]; T_a the air temperature [°C]; T_2 the outer surface temperature of steel mounting plate [°C]; T_g the surface temperature of ground [°C]; μ the heat conductivity of the insulation [W/mK]; and L is the thickness of the insulation [m].

The incident irradiance on the reflecting plate can be calculated by the Perez model [13]. The functions for determination of incident irradiance are as follows:

$$E_i = I_s + I_d + I_r \tag{8}$$

$$I_s = E_{es} \times cosi \tag{9}$$

$$I_d = E_{ed} \times (1 + cos\theta)/2 \tag{10}$$

$$I_r = \rho_g \times E_{eg}(1 - cos\theta)/2 \tag{11}$$

where I_s is the direct irradiance on the inclined reflecting plate [W/m^2]; I_d the diffuse irradiance on the inclined reflecting plate [W/m^2]; I_r the irradiance reflected by ground to the inclined reflecting plate [W/m^2]; i the incident angle of solar irradiance on the inclined reflecting plate [deg]; θ the inclination angle of the reflecting plate [deg]; ρ_g the albedo of the ground [−]; E_{es}, the direct irradiance [W/m^2]; E_{ed} the diffuse irradiance [W/m^2]; and E_{eg} is the global irradiance [W/m^2].

3. Development of glass bead RR materials

Eight types of RR samples coated with glass beads with a refractive index of 1.5 or 1.9, added in amounts of 0.15 or 0.30 kg/m^2, on top of a reflective surface of white or silver paint (detailed in **Table 1**), were produced. All glass bead RR samples were 120 mm square plates. Additionally,

Samples	Reflective layer color	Refractive index of glass bead (n)	Diameter of glass bead (μm)	Density of glass beads (kg/m^2)
S1	White	1.5	106–850	0.30
S2	White	1.5	106–850	0.15
S3	White	1.9	106–850	0.30
S4	White	1.9	106–850	0.15
S5	Silver	1.5	106–850	0.30
S6	Silver	1.5	106–850	0.15
S7	Silver	1.9	106–850	0.30
S8	Silver	1.9	106–850	0.15

Table 1. Detailed characteristics of developed glass bead RR samples.
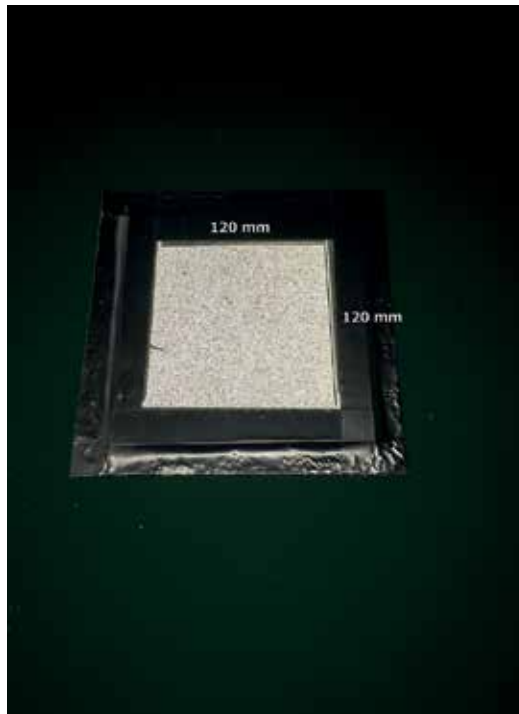
Figure 8. Appearance of developed glass bead RR materials.

because the glass covering could improve the durability of RR material as found in previous research [8], the surface of all glass bead RR samples was designed with a glass sheet covering with high transmittance (visible transmittance 91.3%, UV transmittance 92.5%), a reflectivity of 2%, and high strength. The appearance and structure of the developed glass bead RR sample are shown in **Figures 8** and **9**.
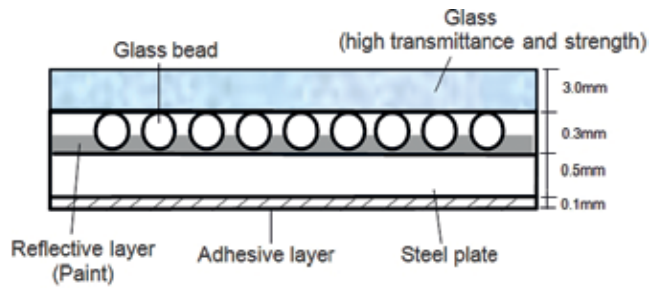
Figure 9. Structure view of developed glass bead RR materials.

Figure 10. Retroreflection effect of developed glass bead RR materials when the artificial light source is incident on their surface.

In addition, for comparison, two types of commercial RR sheet (capsule and prism) samples (KICTEC Corporation) were also produced. The retroreflection effect of all RR samples when the artificial light source is incident on the surface is shown in **Figure 10**.

It is shown that except for the two types of commercial RR sheets, retroreflection intensity of the developed glass bead RR samples with a refractive index of 1.9 and a white reflective layer is much stronger than that with a reflective index of 1.5 and a silver reflective layer.

4. Optical analysis of glass bead RR materials

The reflection intensity of 10 types of RR samples at different incident angles was measured by a specific spectrophotometer system over different incident angles from −85° to 85° with steps
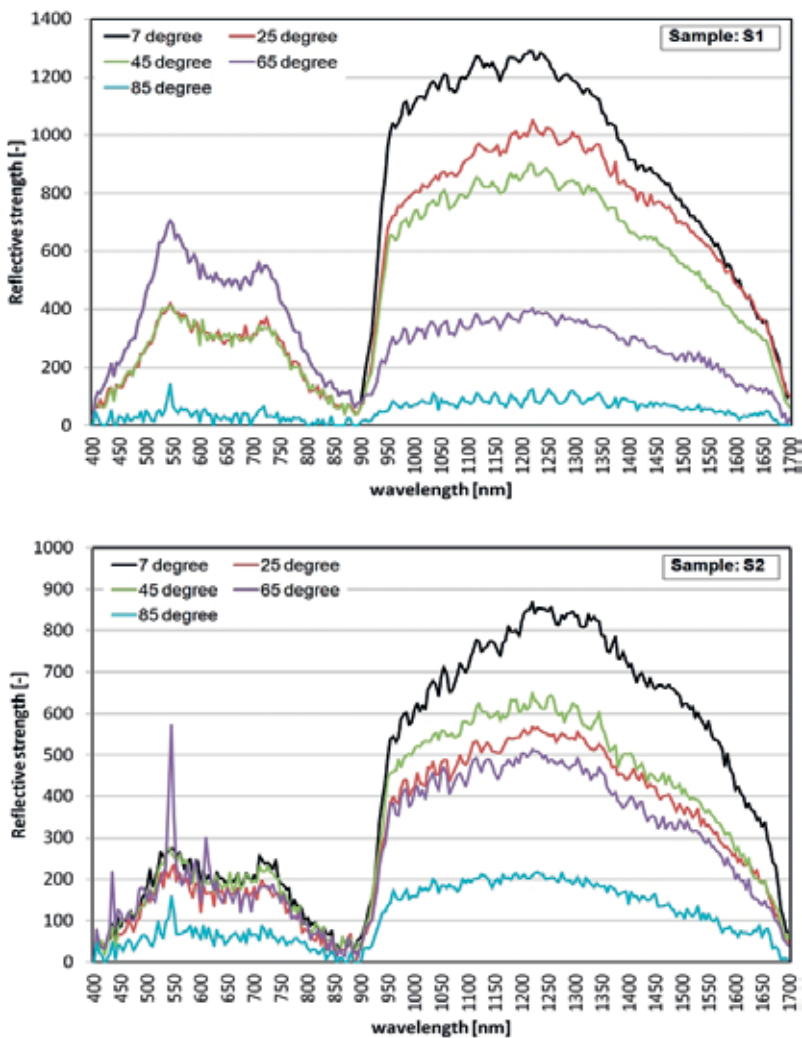
Figure 11. Reflection intensity of RR samples (S1 and S2).

of about 20°. The results are shown in **Figures 11–15**, where the y-axis scale is a raw data output of signal strength for each wavelength with a maximum reading of about 60,000. The graphed values are data from +7° to +85°. The measured values from −7° to −85° were not significantly different.

In addition, the angular retroreflectivity of 10 types of RR samples is calculated by using Eq. (1) and shown in **Table 2**.

For the sake of analyzing the angular distribution of reflection intensity of these developed RR materials, the samples (S1, S3, S5, S7, S9: capsule sheet and S10: prism sheet) are chosen and
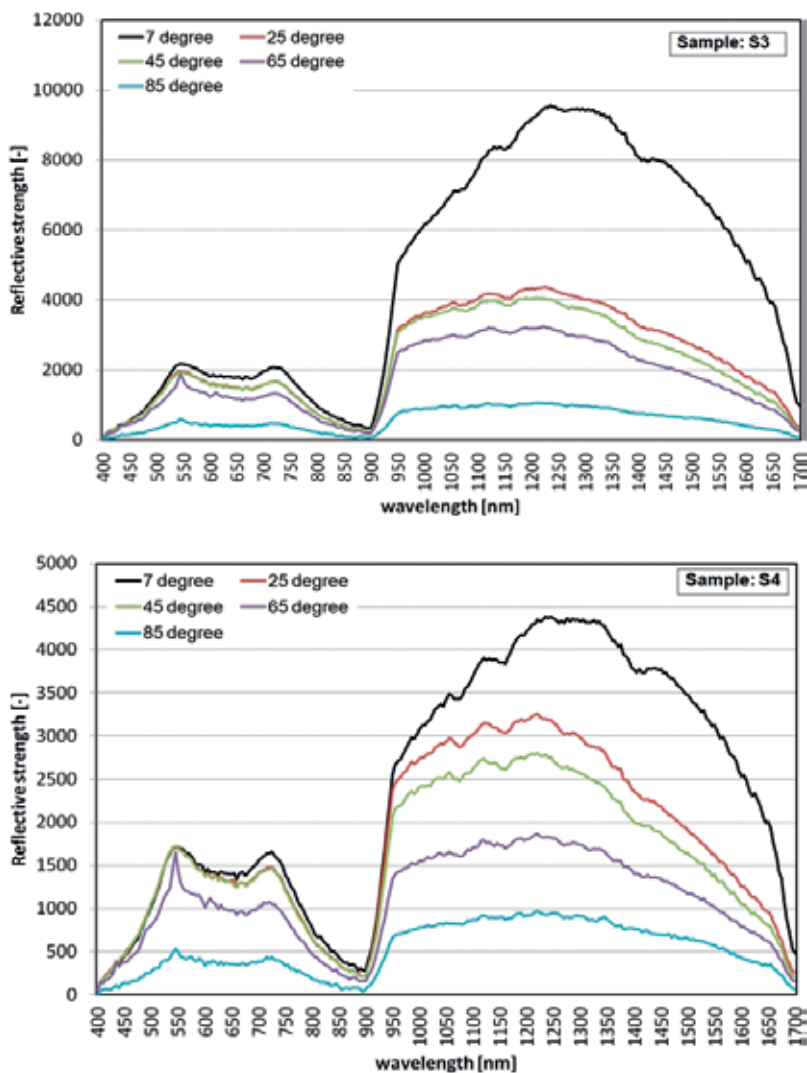
Figure 12. Reflection intensity of RR samples (S3 and S4).
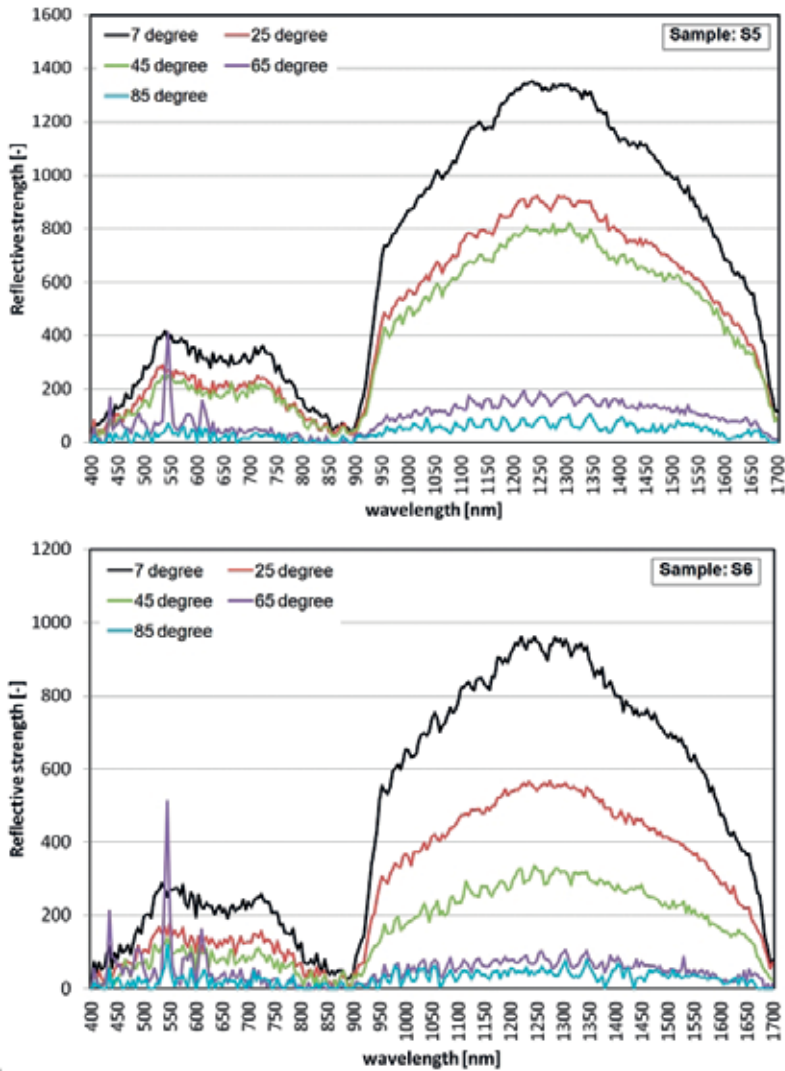
Figure 13. Reflection intensity of RR samples (S5 and S6).

characterized in terms of angular distribution of the reflection intensity ($-80° \sim 80°$) by varying the incident angle of these RR samples from $10°$ to $80°$ with steps of about $20°$ ($10°$, $30°$, $60°$, and $80°$). The detailed angular distribution of reflection intensity of chosen RR samples (S1, S3, S5, S7, S9: capsule sheet and S10: prism sheet) is shown in **Table 3**. Reflection to negative incident angle is the "specular reflection".

It is shown that except for the commercial capsule and prism RR samples, the developed glass bead RR materials with a refractive index of 1.9 are more efficient than those with a
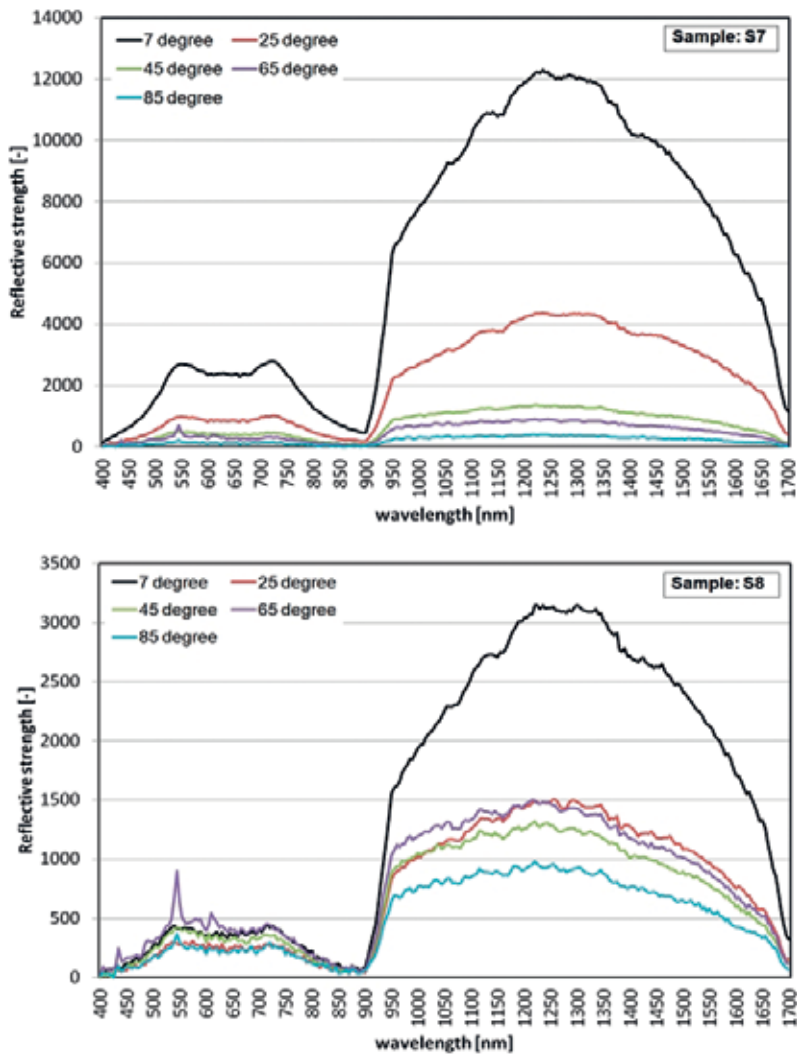
Figure 14. Reflection intensity of RR samples (S7 and S8).

refractive index of 1.5 for application to building coatings at low incident angles of sunlight.

Compared to commercial capsule and prism RR materials, the glass bead RR samples produced in this study are relatively weaker in RR directional characteristics. However, the cost of these developed glass bead RR materials is relatively lower than commercial capsule and prism RR materials. Therefore, as long as the durability of these developed glass bead RR materials can be ensured, it is desirable to develop such low-cost glass bead RR materials and possibly apply to exterior wall surface of buildings.
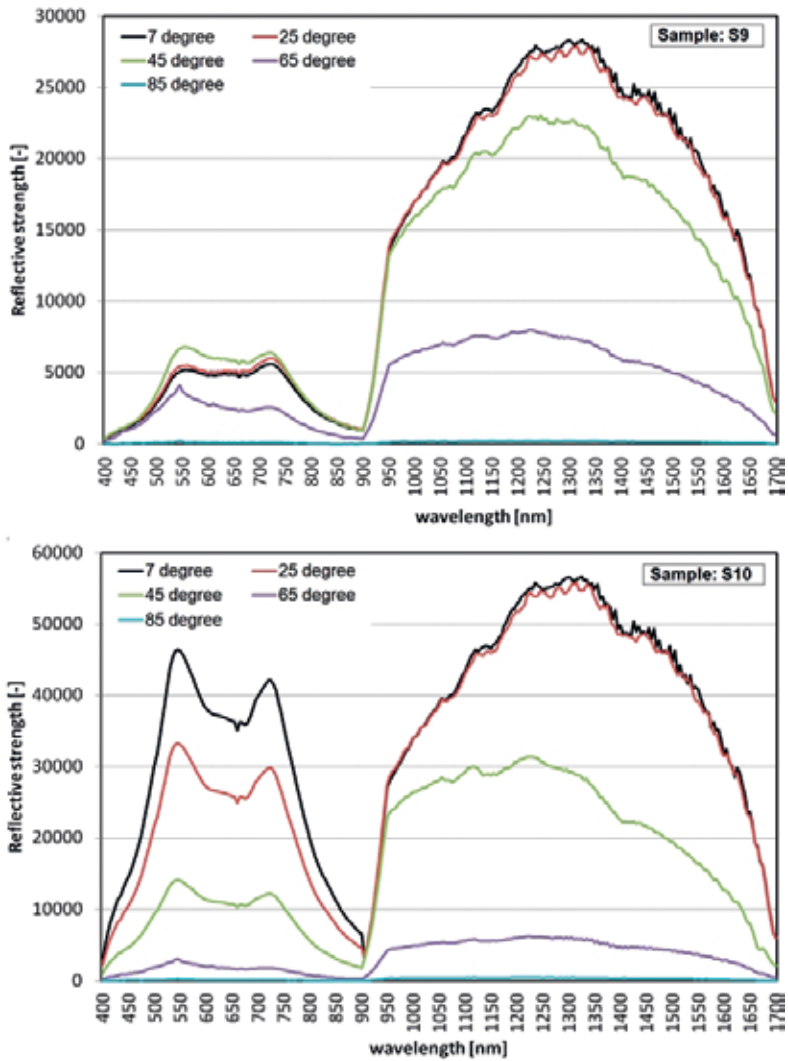
Figure 15. Reflection intensity of RR samples (S9 and S10).

Angle	Sample									
	S1	S2	S3	S4	S5	S6	S7	S8	S9 (capsule)	S10 (prism)
−90°	0.0	0.0	0.0	0.0	0.0	0.0	0.0	0.0	0.0	0.0
−85°	0.1	0.1	0.8	0.7	0.1	0.0	0.3	0.6	0.2	0.2
−65°	0.4	0.4	2.3	1.4	0.1	0.1	0.6	1.0	5.5	3.1
−45°	0.9	0.4	2.8	2.1	0.5	0.2	0.9	0.9	15.2	15.7
−25°	0.6	0.4	3.1	2.3	0.6	0.4	2.8	1.0	17.9	36.9

Angle	Sample									
	S1	S2	S3	S4	S5	S6	S7	S8	S9 (capsule)	S10 (prism)
−7º	0.7	0.6	6.2	3.2	0.9	0.6	7.9	1.9	18.0	41.1
7º	0.7	0.6	6.2	3.2	0.9	0.6	7.9	1.9	18.0	41.1
25º	0.6	0.4	3.1	2.3	0.6	0.4	2.8	1.0	17.9	36.9
45º	0.9	0.4	2.8	2.1	0.5	0.2	0.9	0.9	15.2	15.7
65º	0.4	0.4	2.3	1.4	0.1	0.1	0.6	1.0	5.5	3.1
85º	0.1	0.1	0.8	0.7	0.1	0.0	0.3	0.6	0.2	0.2
90º	0.0	0.0	0.0	0.0	0.0	0.0	0.0	0.0	0.0	0.0

Table 2. Angular retroreflectivity of 10 types of RR samples with different incident angles, $\times 10^{-2}$ [–].

Incidence (°)	10	30	60	80	Incidence (°)	10	30	60	80
S1					S3				
10°	5.1	3.4	2.3	2.0	10°	15.8	3.3	2.4	2.2
30°	3.3	5.0	2.4	2.0	30°	4.3	12.0	2.5	2.2
60°	2.6	2.3	4.6	2.1	60°	2.8	2.9	11.0	2.9
80°	2.0	2.0	2.1	2.5	80°	2.1	2.1	2.2	3.5
0°	4.0	2.5	2.4	2.0	0°	4.8	2.9	2.7	2.2
−80°	2.2	2.0	2.3	12.2	−80°	2.0	2.2	2.5	12.3
−60°	2.4	2.1	8.3	3.1	−60°	2.8	2.6	9.0	3.9
−30°	2.7	8.8	2.6	2.0	−30°	3.7	8.0	2.2	2.0
−10°	7.7	2.5	2.5	2.0	−10°	7.8	2.8	2.6	2.2
S5					S7				
10°	5.8	2.3	2.0	1.9	10°	16.0	2.6	2.3	2.0
30°	2.4	3.6	2.1	1.9	30°	3.4	12.7	2.6	2.1
60°	2.1	2.1	3.2	1.9	60°	2.4	2.1	5.2	2.2
80°	2.0	2.0	2.0	2.6	80°	2.1	2.0	2.0	3.8
0°	4.3	2.3	2.1	1.9	0°	5.7	2.3	1.2	1.1
−80°	2.0	2.0	2.0	8.7	−80°	2.2	2.0	2.2	9.1
−60°	2.1	2.1	7.0	2.4	−60°	2.4	2.1	9.7	3.2
−30°	2.3	5.7	2.2	1.9	−30°	3.7	9.0	2.5	2.3
−10°	5.7	2.7	2.1	1.9	−10°	8.4	2.3	2.3	2.0
S9 (capsule sheet)					S10 (prism sheet)				
10°	35.0	4.4	2.3	2.0	10°	45.0	4.6	3.3	4.3
30°	3.2	32.1	2.3	2.1	30°	4.2	40.0	3.4	5.4

Incidence (°)	10	30	60	80	Incidence (°)	10	30	60	80
60°	2.4	2.5	12.3	2.4	60°	3.8	4.2	7.0	4.0
80°	2.0	2.0	2.2	4.5	80°	2.9	3.1	2.2	3.1
0°	13.0	3.8	1.8	1.2	0°	7.8	4.7	1.9	1.2
−80°	2.2	2.1	2.6	26.7	−80°	2.5	2.6	4.5	24.0
−60°	2.4	2.4	28.0	7.0	−60°	2.6	3.3	21.0	3.2
−30°	4.5	25.4	3.3	2.1	−30°	3.6	15.4	3.5	3.6
−10°	23.4	5.0	2.3	2.0	−10°	10.6	4.1	3.0	3.6

Table 3. Angular distribution of reflection intensity of chosen RR samples, $\times 10^3$ [–].

5. Verification on durability of glass bead RR materials

For possible application of these glass bead RR materials to building facades, the durability of these developed glass bead RR samples should be verified. Therefore, the change in solar reflectivity of these developed glass bead RR samples was evaluated by exposed experiments in the outdoor environment. The experimental stand is shown in **Figure 16**. As an example, the change in solar reflectivity (for incident angle of solar radiation: 5°) of four chosen glass bead RR samples (S1, S3, S5, and S7) for approximately 1 year (about 368 days) exposure to outdoor environments is shown in **Figure 17**.

Figure 16. Experimental stand for deriving retroreflectivity of developed glass bead RR samples.
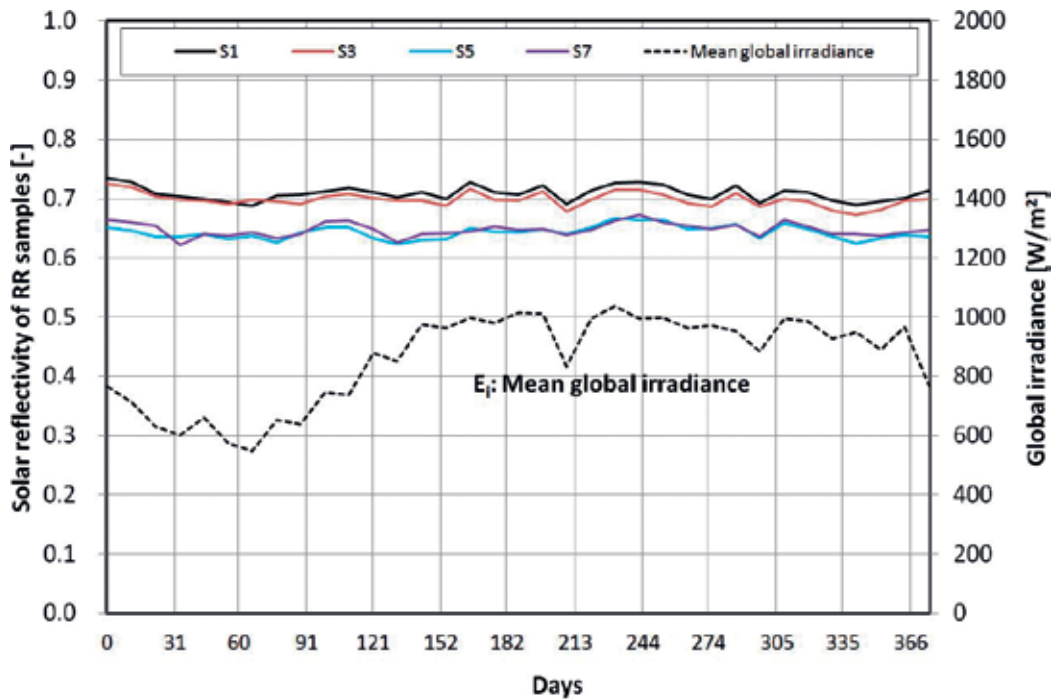
Figure 17. Change in solar reflectivity at incident angle of solar radiation of 5° for four chosen glass bead RR samples (S1, S3, S5, and S7).

The results show that the solar reflectivity of the developed four chosen glass bead RR samples has a limited decrease of only about 0.02 for long-term exposure (about 368 days) in the outdoor environment.

It is considered that the durability of four chosen glass bead RR materials can be ensured during the 368-day exposure in the outdoor environment. In addition, it is also shown that the solar reflectivity of glass bead RR samples (S1 and S3) with white reflective layers is about 0.07 higher than that with silver reflective layers (S5 and S7).

Whether these developed glass bead RR materials meet the durability requirements of building exterior wall surface materials will take longer time to be validated.

6. Influence of glass bead RR façade on pedestrians and proposal of suppression method

According to the research by Takebayashi [14], the effectiveness of applying RR materials to building façades was evaluated in regard to avoiding adverse effects on pedestrians. As shown in **Figure 18**, the result is indicated that the RR materials can be considered for use on building façades below the third floor in order to avoid impacts on pedestrians from the reflection of solar radiation.
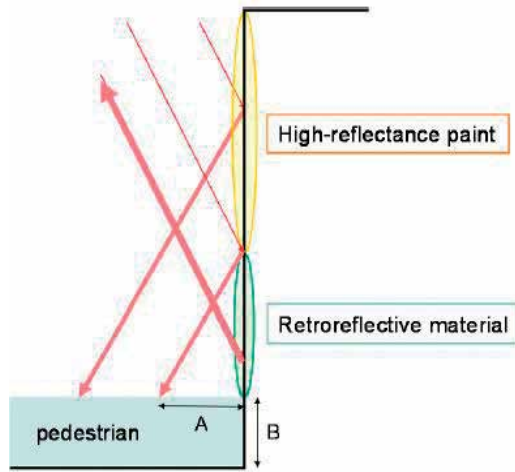
Figure 18. Effect of RR façade on pedestrian [14].

For the glass bead RR material, if it was applied to a building façade, when the solar altitude angle is large such as 60°, the specular reflection component accounts for a relatively large proportion of the whole reflection (as shown in **Figure 19**). Thus, it is essential to suppress the specular reflection which is emitted from a glass bead RR façade by using an appropriate technical method that is described and shown in **Figure 20**.
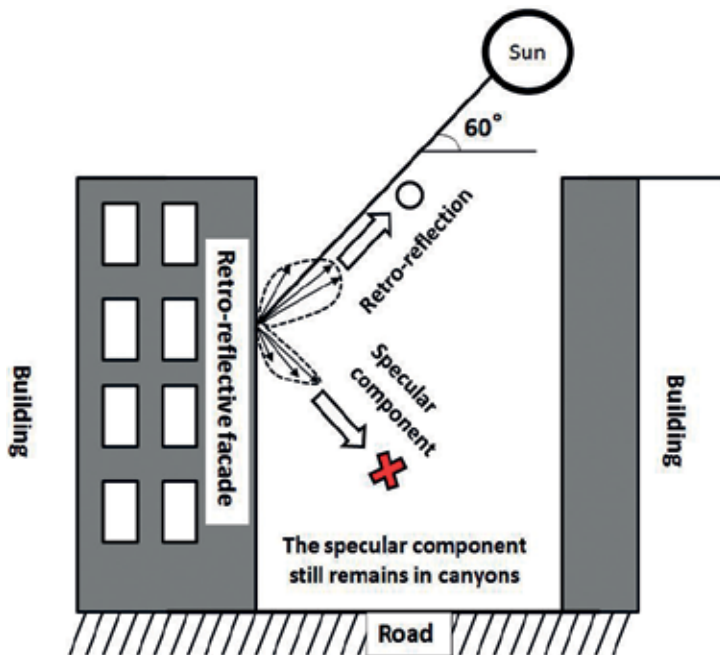
Figure 19. A 2D simulation of the specular reflection component from a glass bead RR façade.
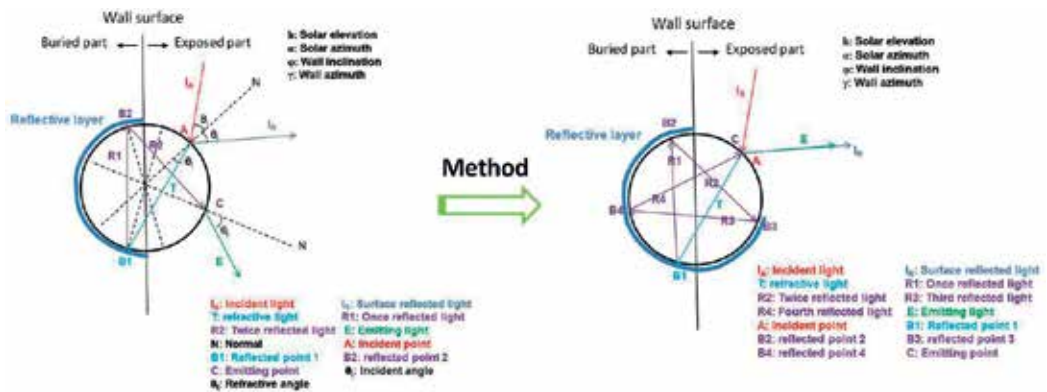
Figure 20. Proposal of avoiding the specular reflection component emitted from a glass bead RR facade.
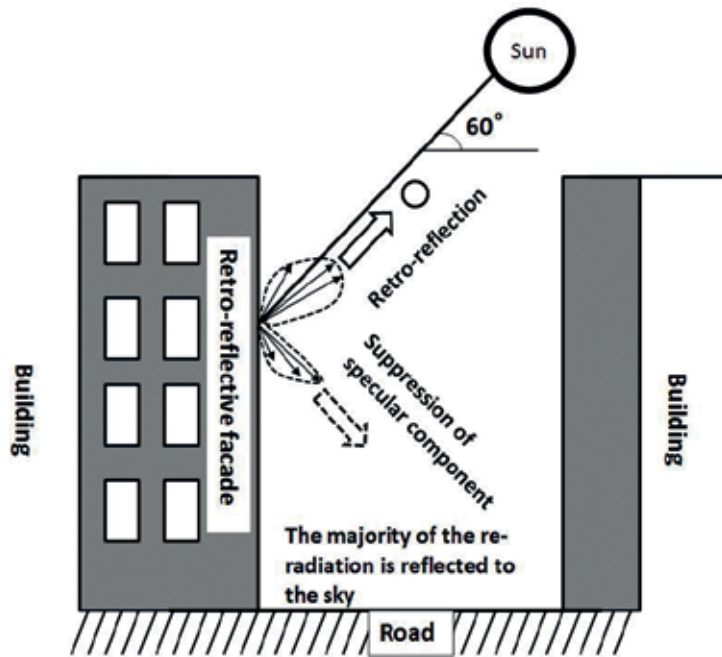
Figure 21. A 2D simulation after the adoption of a proposal to avoid specular reflection effect.

The effect of a newly designed glass bead RR facade on pedestrians and thermal radiation of urban environment could be improved after adopting the method of suppressing the specular reflection emitted from the RR façade of buildings (as shown in **Figure 21**).

7. Summary and conclusions

This chapter shows the application of glass bead materials in building exterior wall surfaces. Two main methods for deriving retroreflectivity of glass bead RR materials were analyzed.

Several types of glass bead RR building coating samples were developed. For possible application of these samples to building coatings and verification of their long-term durability, the optical and durable experiments of these samples were carried out. The theoretical and technical method to prevent the specular reflection which is emitted from glass bead RR façade is proposed in this study.

We can summarize the knowledge as follows:

1. Methods to derive the retroreflectivity of RR materials are proposed and described in this study. One is measured by a spectrophotometer system and the other is determined by a thermal balance principle of surface.

2. Production of glass bead RR samples with low cost that is possibly applied to building coatings is carried out in this study.

3. The reflection directional characteristics of developed glass bead samples were measured by using an emitting-receiving optical fiber system. It is shown that except for commercial capsule and prism RR samples, the developed glass bead RR materials with a refractive index of 1.9 are more efficient than those with a refractive index of 1.5 for application to building coatings as RR materials at low incident angles of sunlight.

4. The long-term durability of the developed glass bead RR samples was verified through exposure experiment in the outdoor environment. It is shown that the durability of the developed glass bead RR materials can be ensured during the 368-day exposure in the outdoor environment, and more time is needed to continue this durability experiment.

5. A proposal of theoretical and technical methods to prevent the specular reflection from the glass bead RR façade is briefly described in this study.

Author details

Jihui Yuan

Address all correspondence to: yuanjihui@hotmail.co.jp

Department of Housing and Environmental Design, Graduate School of Human Life Science, Osaka City University, Osaka, Japan

References

[1] Nishioka M, Inoue S, Sakai K. Retroreflective properties calculating method based on geometrical—Optics analysis performance evaluation of solar retroreflectors. Journal of Environmental Engineering. 2008;**73**(633):1249-1254. DOI: 10.3130/aije.73.1249

[2] Rossi F, Pisello AL, Nicolini A, Filipponi M, Palombo M. Analysis of retro-reflective surfaces for urban heat island mitigation: A new analytical model. Applied Energy. 2014;**114**: 621-631. DOI: 10.1016/j.apenergy.2013.10.038

[3] Han Y, Taylor JE, Pisello AL. Toward mitigating urban heat island effects: Investigating the thermal-energy impact of bio-inspired retro-reflective building envelopes in dense urban settings. Energy and Buildings. 2015;**102**:380-389. DOI: 10.1016/j.enbuild.2015.05.040

[4] Yuan J, Emura K, Farnham C. Geometrical-optics analysis of reflective glass beads applied to building coatings. Solar Energy. 2015;**122**:997-1010. DOI: 10.1016/j.solener.2015.10.015

[5] Yao Sangyo Co., Ltd. 3M™ Enclosed Lens Type Reflective Sheet 1500 Series. Available at: http://www.yao-sangyo.co.jp/sign/envelop_1500.html

[6] Yao Sangyo Co., Ltd. 3M™ Capsule Prism Type High Brightness Reflection Sheet PX 8400 Series. Available at: http://www.yao-sangyo.co.jp/sign/prism_px8400.html

[7] Yuan J, Emura K, Farnham C, Sakai H. Application of glass beads as retro-reflective facades for urban heat island mitigation: Experimental investigation and simulation analysis. Building and Environment. 2016;**105**:140-152. DOI: 10.1016/j.buildenv.2016.05.039

[8] Yuan J, Farnham C, Emura K. Development of a retro-reflective material as building coating and evaluation on albedo of urban canyons and building heat loads. Energy and Buildings. 2015;**103**:107-117. DOI: 10.1016/j.enbuild.2015.06.055

[9] Tao F, Yao J. Influence of retro-reflective material on public buildings energy consumption in different climate regions. Journal of Chemical and Pharmaceutical Research. 2013; **5**(9):447-452. Available at: http://www.jocpr.com

[10] Yuan J, Emura K, Sakai H, Farnham C, Lu S. Optical analysis of glass bead retro-reflective materials for urban heat island mitigation. Solar Energy. 2016;**132**:203-213. DOI: 10.1016/j. solener.2016.03.011

[11] Yuan J, Farnham C, Emura K. A study on the accuracy of determining the retro-reflectance of retro-reflective material by heat balance. Solar Energy. 2015;**122**:419-428. DOI: 10.1016/j. solener.2015.08.040

[12] ISO 9050: Glass in building—Determination of light transmittance, solar direct transmittance, total solar energy transmittance, ultraviolet transmittance and related glazing factors (2003). Available at: http://www.webstore.jsa.or.jp

[13] Perez RR, Ineichen P, Seals R, Michalsky J, Stewart R. Modeling daylight availability and irradiance components from direct and global irradiance. Solar Energy. 1990;**44**(5):271-289. DOI: 10.1016/0038-092X(90)90055-H

[14] Takebayashi H. High-reflectance technology on building façades: Installation guidelines for pedestrian comfort. Sustainability. 2016;**8**(785):1-9. DOI: 10.3390/su8080785

Seal Glass for Solid Oxide Fuel Cells

Montri Suklueng

Additional information is available at the end of the chapter

Abstract

Barium calcium aluminum boro-silicate glass (BCABS) is used as a sealant for Solid Oxide Fuel Cells (SOFCs) to protect against air and hydrogen gas leaking at 800°C. One major problem is the chemical reaction of this glass with barium oxide and other materials in the composition such as Ba-Y-Co-Fe (BYCF) and Ba-Sr-Co-Fe (cathode) used in the fuel cell components, leading to the formation and spreading of barium aluminosilicate glass on the cathode surface in the fuel cell. This investigation indicated that adding 0.4 mol% ZrO_2 to BCABS prevents the formation of barium aluminosilicate glass. Generally, the sealing glass of fuel cells must show high resistivity for no disturbance to electricity from the fuel cell system when generating the electron. The 0.4 mol% ZrO_2 to BCABS is generated with resistivity of 4 MΩ that is useful for SOFCs technology. The thermal expansion coefficient (TEC) in SOFCs is the major condition for producing the cell layers. The thermal expansion coefficient of SOFCs based on each layer (cathode, electrolyte, anode, interconnect and sealant) should be closed to prevent broken cells. The thermal expansion coefficient is 12.40×10^{-6}/°C matched with the TEC of the GDC_{10} electrolyte. Therefore, BCABS glass with 0.4 mol%ZrO_2 generated a novel composite for SOFCs.

Keywords: BCABS sealing glass, SOFCs, electrical stability, thermal expansion coefficient

1. Introduction

Solid oxide fuel cells (SOFCs) are a type of power source conversion device which can transform hydrogen or hydrocarbon gas in fuel into electricity at an intermediate temperature of 600–800°C. SOFCs consist of three layers (cathode/electrolyte/anode) that are designed with a tubular and planer shape [1]. The fuels are often pumped to flow into the SOFC system but it is possible that leaks can occur when using this system. Therefore, excellent sealing is essential to prevent external leaks as well as to contain fuels inside the SOFCs. The sealing composition must provide hermeticity, electronic insulation, and a similar thermal expansion coefficient

(TEC) to match with the SOFC system [2]. Thermal stability is necessary and the operating system should be able to work for long periods in harsh conditions. Furthermore, the sealant must be able to survive the thermal cycles for 40,000 h at intermediate temperatures of 500–800°C [3]. The character of the seal glass should enhance stability and durability in both chemical and mechanical forms [2].

Based on the glass ceramic sealant type, the best is BCABS with the following composition: (mol%) 35BaO, 15CaO, 5Al$_2$O$_3$, 37SiO$_2$, 8B$_2$O$_3$ [4]. This sealant is derived through the chemical reaction with barium compositions on the cathode side of the SOFCs systems; for example, BSCF (Ba-Sr-Co-Fe) [5], or BYCF (Ba-Y-Co-Fe) [6] that leads to the formation of barium aluminosilicate [7, 8] on the surface as shown in **Figure 1**. But how can we stop the barium aluminosilicate which blocks the electricity generation of SOFCs? ZrO$_2$ reveals better thermal shock resistance at 400°C, and improves thermal oxidation resistance [10, 11]. BCABS with added (0.4 mol%) ZrO$_2$ (BCABS-0.4 mol%ZrO$_2$) is shown to be an excellent glass ceramic sealant for operating SOFCs that can also match the required TEC, has high resistivity, and no cracks. The TEC of BCABS-0.4 mol%ZrO$_2$ of 12.17–12.78 $\times$ 10^{-6}/°C also matches with the GDC$_{10}$ electrolyte at 13.08 $\times$ 10^{-6}/°C. BCABS-0.4 mol%ZrO$_2$ showed resistivity of 4 MΩ cm for 100 h. BCABS-0.4 mol%ZrO$_2$ of SEM also exhibited a smooth surface free of cracks, blisters and without barium aluminosilicate [9]. The melting point is 867.25°C [9].

Due to the SOFCs being developed for use at low operating temperatures, this will make the SOFC system highly efficient. Therefore, the development of glass ceramic sealants containing the addition of 0.4 mol%ZrO$_2$ in the BCABS glass composition can be shown to use low cost advanced materials for SOFC technology. This sealing glass can prevent the spread of barium aluminosilicate on the surface of the barium composition on the cathode side of the SOFC system. The melting point of the composition is 867.25°C. The electrical resistivity of this mixture is 4MΩ cm which is 8 times lower than the original BCABS. The TEC is matched with SOFCs based on the GDC$_{10}$ electrolyte that is valued at around 12.17–12.78 $\times$ 10^{-6}/°C [12]. The microstructure between cathode and glass is free of cracks and shows good adherence to both surfaces. These properties of BCABS-0.4 ZrO$_2$ composition can be promoted as a sealant for SOFC low cost technology which has barium oxide content.
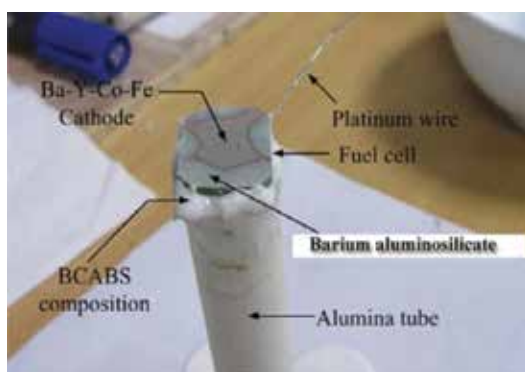

Figure 1. The sealing glass BCABS was sintered at 800°C for 5 h and the barium aluminosilicate coated on the solid oxide fuel cell surface [9].

2. Preparation of materials

The materials for this glass sealant show novel composition with added ZrO_2 in BCABS under a mol% ratio as exhibited in **Table 1**. Commercial powders BaO (99%), CaO (99%), Al_2O_3 (99%), B_2O_3 (99%), SiO_2 (99%) and ZrO_2 (99%) were obtained from Sigma Aldrich GmbH, Germany. Stoichiometric amounts of powder were mixed together to get the glass sealant composite. The powder mixtures were ground for 1 h and mixed with distilled water, generating the high temperature. Thus, for the best safety of preparation, the mixtures were prepared using a stainless steel tray or thermal ceramic tray. It is important not to touch the composition when the distilled water is first mixed with powder because of the high thermal production and dust! The mixture was milled with cylindrical alumina balls using a horizontal rotary ball mill for 24 h and then dried in the oven at 150°C until it became a powder as shown **Figure 1**. The powders were ground again for 4 h in our in-house designed grinding machine and sieved at 150 mesh size, resulting in the fine powder of sealing glass for SOFC technology. The calcinated batch was melted under air ambience in a solid oxide fuel cell system (cathode|electrolyte|anode), with a platinum wire and alumina tube at 1000°C. The melting was then quenched between an alumina tube and fuel cell to obtain the glass frit to be used for electrical stability as shown in **Figure 2**.

Composition	Samples			
	BCABS	**BCABS-1ZrO$_2$**	**BCABS-2ZrO$_2$**	**BCABS-3ZrO$_2$**
BaO	35	35	35	35
CaO	15	15	15	15
Al$_2$O	5	5	5	5
SiO$_2$	37	36.6	36.2	35.9
B$_2$O$_3$	8	8	8	8
ZrO$_2$	0	0.4	0.8	1.1

Table 1. Chemical composition of the of the sealing glass (mol%) [9].

Figure 2. The BCABS-1ZrO$_2$ was prepared after drying in the over at 150°C for 4 h.

However, the preparation of the glass sealant must be practiced because it involves rheology and sintering. Therefore, before using this glass sealant in the real experiments, it is necessary to learn how to control the glass flow at the high temperature for the sealant. For example in SOFCs technique, increasing for 90 min to 1000°C and then stabilizing for 1 min, before then cooling down for 90 min to room temperature.

3. Physical properties

The chemical reactions of the sealing glass BCABS, BCABS doped with ZrO_2, and the solid oxide fuel cells after they were sintered at 1000°C for 1 h are shown in **Figure 3(a)–(d)**. The compositions related appear in **Table 1**. The BCABS composition revealed an excellent connection between the fuel cell and glass; some chemical reactions on the fuel cell due to the barium aluminosilicate are spread on the fuel cell [13], **Figure 4(a)**. BCABS-1ZrO$_2$ glass showed no reaction in the fuel cell with a shiny, high adhesive glass composition deposited on the fuel cell surface in **Figure 4(b)**. BCABS doped 0.4 mol% may affect the chemical glass composition and can be obviously revealed without barium aluminosilicate coated on the fuel cell. The reasons
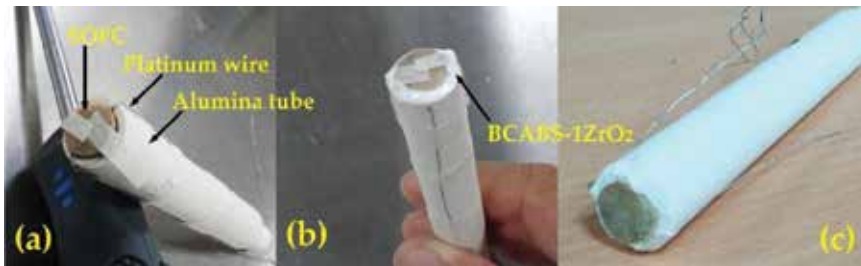
Figure 3. (a) The preparation for measuring power density of the SOFC based on the pellet comprising the SOFC pellet, alumina tube and platinum wire; (b) BCABS-1ZrO$_2$ glass quenched between the SOFC pellet and alumina tube; (c) BCABS-1ZrO$_2$ glass after sintering at 1000°C for 1 min.

Figure 4. Comparison of the chemical reaction between glass ceramic sealant and solid oxide fuel cell: (a) BCABS, (b) BCABS-1ZrO$_2$, (c) BCABS-2ZrO$_2$, and (d) BCABS-3ZrO$_2$. Picture exhibits the comparison of glass ceramic sealants: (e) BCABS and (f) BCABS-1ZrO$_2$ [9].

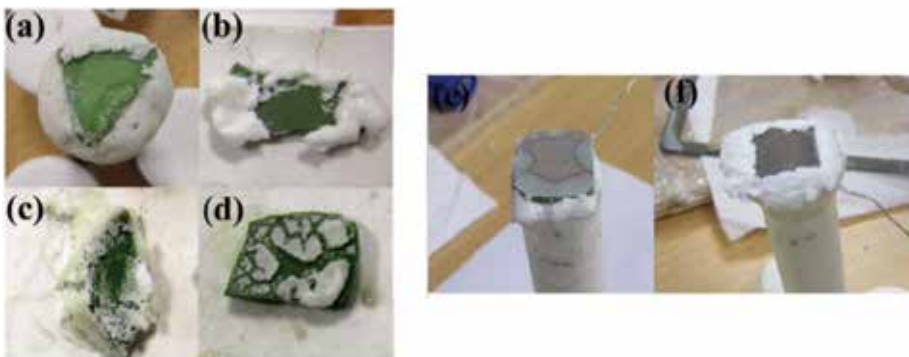for the chemical compound with crystallographic structure are explained in the XRD analysis section. The glass BCABS-2ZrO$_2$ and BCABS-3ZrO$_2$ showed clear cracks on the fuel cell that may be attributed to the high quantity of ZrO$_2$ generating the pin holes and pores in the surface [14, 15]. Therefore, the sealing glass BCABS-1ZrO$_2$ is an excellent sealing material for the investigation of properties leading to no reaction on the fuel cell surface. BCABS and BCABS-1ZrO$_2$ sealing glass were sintered with fuel cells that clearly compared the different sealing glasses as shown in **Figure 4(e)** and **(f)**.

4. Differential thermal analysis (DTA)

The chemical reaction of the glass sealant at high temperatures is very important for application to SOFCs technology for the analysis phase of chemical reactions and melting points that can be designed by time and temperature for coating between the alumina tube and fuel cell. Differential thermal analysis (DTA) is the one instrument for measuring which is based on the peak represented chemical reaction and melting point. DTA plots of the investigated BCABS-1ZrO$_2$ glass are shown in **Figure 5**. An endothermic baseline shift indicates glass transition and an exothermic shift indicates crystallization. The plots show the inflection in the temperature range from room temperature to 1000°C with an intense exothermic peak at 76.82°C (Tp). This range, from 40 to 150°C is associated with the elimination of adsorbed and zeolitic H$_2$O. The coordinated H$_2$O is removed in this heating range. The glass transition temperature T$_g$ exhibits the estimates to be 196.87, 306.13, 427.02 and 867.25°C from this point of intersection of the tangents drawn at the slope change. The peak of T$_g$ at 427.02°C corresponded to the thermal
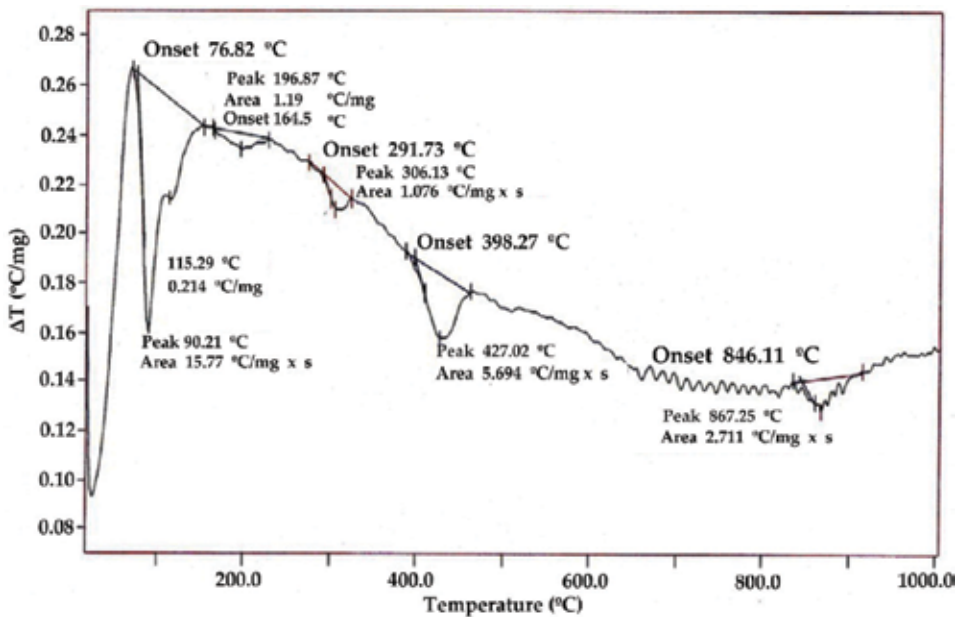

Figure 5. Differential thermal analysis (DTA) curve of investigated BCABS-1ZrO$_2$ glass [9].

expansion curve of BCABS-1ZrO$_2$. The glass transition T_g of 867.25°C is the melting point. However, the glass sealant should be sintered over the melting point for coating the gap between the SOFC and alumina tube without leaks. For example, a temperature at 1000°C for 1 min can reveal the beautiful coating as shown in **Figure 3(c)**.

5. X-ray diffraction (XRD) analysis

X-ray diffraction (XRD) is a versatile, non-destructive, analytical technique that reveals detailed information involving the chemical composition, crystallographic structure and physical properties of materials [16]. In the case of powder diffraction, this technique is used to characterize the crystallographic structure, crystallite size and preferred orientation in polycrystalline or powdered solid samples [17]. Powder diffraction is also commonly used to identify unknown substances by comparing the diffraction data against a database matched by the International Centre for Diffraction Data (ICDD). Based on the BCABS-1ZrO$_2$ glass, XRD indicates the inclusion of many compositions such as Barium Calcium Silicate (Ca$_{0.1}$Ba$_{0.9}$SiO$_3$), Barium Aluminum Silicate (BaAl$_2$Si$_2$O$_8$), Silicon Oxide (SiO$_2$), Silicon (Si), Calcium Aluminum Silicate Hydroxide (Al$_2$Ca$_2$O$_{13}$Si$_3$), Barium Zirconium Silicate (Ba$_2$Zr$_2$Si$_3$O$_{12}$) and Calcium Silicate (CaSiO$_3$). The major peak is Ca$_{0.1}$Ba$_{0.9}$SiO$_3$ leading to BaO, CaO and SiO$_2$ that are the main components. Additionally, Barium Zirconium Silicate (Ba$_2$Zr$_2$Si$_3$O$_{12}$) is very interesting because this compound combined with the Barium Oxide and Zirconium Oxide may stop the Barium Aluminosilicate coating on fuel cell surfaces. This composition may cause decreased resistivity such that the resistance of BCABS-1ZrO$_2$ is generated 8 times lower than BCABS (**Figure 6**).
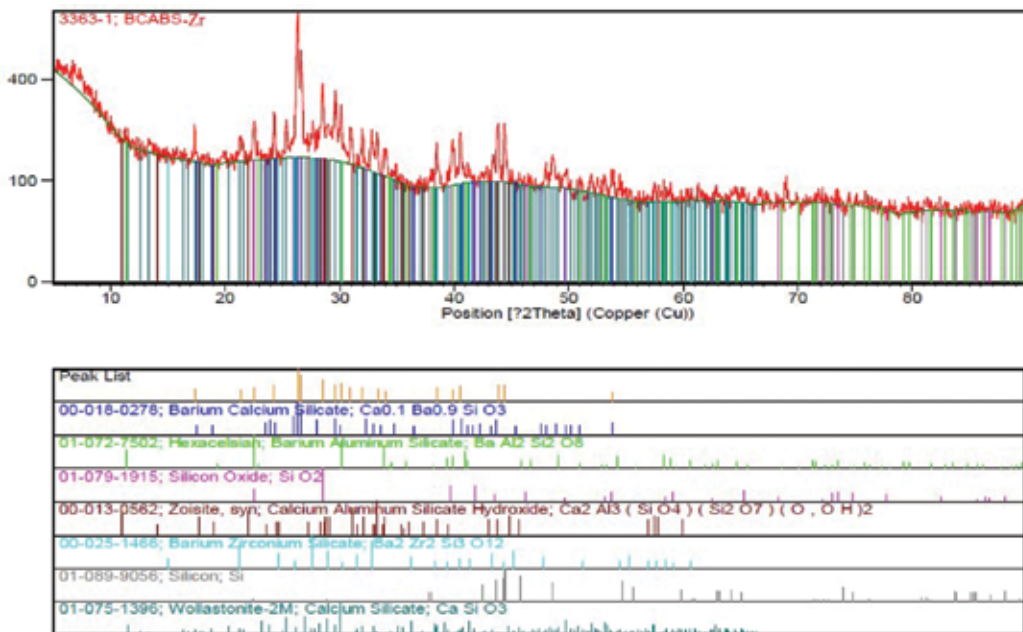

Figure 6. XRD data of the BCABS-1ZrO$_2$ after sintering at 1000°C for 1 min.

6. Thermal expansion

Based on SOFCs technology are contained the cathode, electrolyte and anode layer. All of the three layers must be controlled by the thermal expansion coefficient the same as the electrolyte, while this experiment uses the GDC_{10} electrolyte. Hence, the thermal expansion coefficients (TEC) of the cathode and anode should be close to that of the electrolyte [18]. Because SOFCs are operated at high temperatures of 600–800°C, all the layers are expanded. In cases where the three layers of SOFCs have different thermal expansion coefficients they can easily be broken. For this reason, the thermal expansion coefficient of sealing glass must also be close to that of the GDC_{10} electrolyte. The linear thermal expansion of BCABS and $BCABS-1ZrO_2$ glass is shown in **Table 2**. Thermal expansion of BCABS exhibited linear expansion, with a thermal expansion coefficient of 12.40×10^{-6}/°C. The $BCABS-1ZrO_2$ also showed linear thermal expansion between 34 and 400°C, with a thermal expansion coefficient of 12.78×10^{-6}/°C. The increase in TEC from 34 to 600°C is shown in **Table 2**. Thermal expansion of $BCABS-1ZrO_2$ also matches with the GDC_{10} electrolyte at 13.08×10^{-6}/°C [19].

Compositions	Thermal expansion coefficient ($\times 10^{-6}$/°C)			
	34–200(°C)	34–400(°C)	34–600(°C)	34–800(°C)
$BCABS-1ZrO_2$	12.17	12.78	16.53	11.70
BCABS	12.20	12.81	12.54	12.40

Table 2. Comparison of thermal expansion coefficient properties of sealing glass $BCABS-ZrO_2$ and BCABS [9].

7. Electrical stability analysis

Sealing glass in SOFCs operation is a part which should be an effective electrical insulator to support the fuel cell in highly efficient generation of electricity. However, based on the real experiment, the SOFC technology needs to be interconnected to pass the electricity to the external circuit from the high temperature system. For the purpose of full option of this experiment, $La_{0.08}Sr_{0.20}Cr_{0.92}Co_{0.08}O_3$ was used for the fuel cell interconnect. Investigation by Acchar et al. has shown that this interconnect has the best composition of materials to achieve the ideal features of an interconnect; for example high density, porosity, and high conductivity [20].

Electrical stability analysis was measured with the interconnect $La_{0.08}Sr_{0.20}Cr_{0.92}Co_{0.08}O_3$. Glass was exposed to ambient air on one side and H_2, 2.7% H_2/Ar saturated with 20 or 30 vol% H_2O on the other side. A graphic diagram of the test set-up, detailing the perimeter seal, gas chamber and electrical connection is shown in **Figure 7**. The electrical stability of both glasses BCABS and $BCABS-1ZrO_2$ was investigated in the furnace at a temperature of 800°C for 100 h. Some of the samples were intentionally broken for interfacial characterization of cross-sections using a scanning electron microscope (SEM). **Figure 8** exhibits the electrical conductivity of the interconnect ($La_{0.08}Sr_{0.20}Cr_{0.92}Co_{0.08}O_3$) composite at different temperatures. Using the electrical circuit connection seen in **Figure 7**, the resistance between $BCABS-1ZrO_2$ and the interconnect ($La_{0.08}Sr_{0.20}Cr_{0.92}Co_{0.08}O_3$) composite was measured.
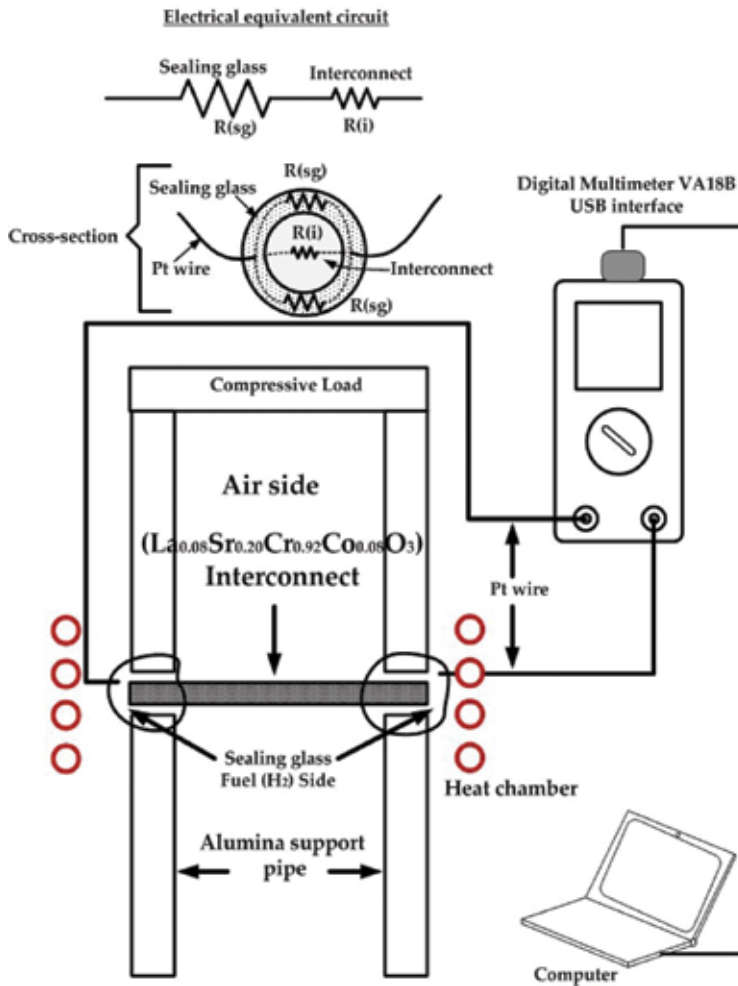
Figure 7. The graphic diagram exhibits the set-up of electrical stability measurement, the glass covered the interconnect and connected with platinum (Pt) wire used for measuring resistivity [9].

However, the interconnect ($La_{0.08}Sr_{0.20}Cr_{0.92}Co_{0.08}O_3$) composite has very low resistivity. Therefore, the major resistivity of BCABS-1ZrO$_2$ was measured, as indicated in **Figure 9(a, b)** [9]. The measurement of the resistivity of sealing glass and interconnect materials can be written in the form of electrical equivalent circuit. The resistance is ($La_{0.08}Sr_{0.20}Cr_{0.92}Co_{0.08}O_3$) interconnect (Ri) and BCABS-1ZrO$_2$ sealing glass (Rsg), while the cross-section is fitted by electrical circuit as shown in **Figure 7** and this cross-section also corresponds to **Figure 3(b)**. All resistances are connected in series circuits as represented in Eq. (1). However, the resistance of ($La_{0.08}Sr_{0.20}Cr_{0.92}Co_{0.08}O_3$) interconnect (Ri) is very low, which must easily release electrons to the external circuit in a real experiment of SOFCs. Therefore, the total resistance from this investigation is BCABS-1ZrO$_2$ sealing glass (Rsg).

$$R_{\text{total\_Realing glass}} = R(rg) + R(i) \qquad (1)$$

The electrical stability was investigated for BCABS and BCABS-1ZrO$_2$ for 100 h at 800°C, as shown in **Figure 9(b)**. The resistance of BCABS is 8 times higher than BCABS-1ZrO$_2$. The trends indicated a gentle step down at 48 h with both stabilized until 100 h. The 0.4 mol% ZrO$_2$ doped in BCABS revealed decreasing electrical resistivity of the sealing glass. The electrical stability of BCABS and BCABS-1ZrO$_2$ sealing glass at different temperatures is shown in **Figure 9** [9]. Both compositions exhibited decreasing resistivity at 520°C. The composition might change phase at 520°C since that is one of the major properties of BCABS sealing glass.

8. Microstructure analysis

It is common sense to study the structure of material with regard to their function. The transforms of macroscopic properties of materials are created by the transforms of its microstructure.
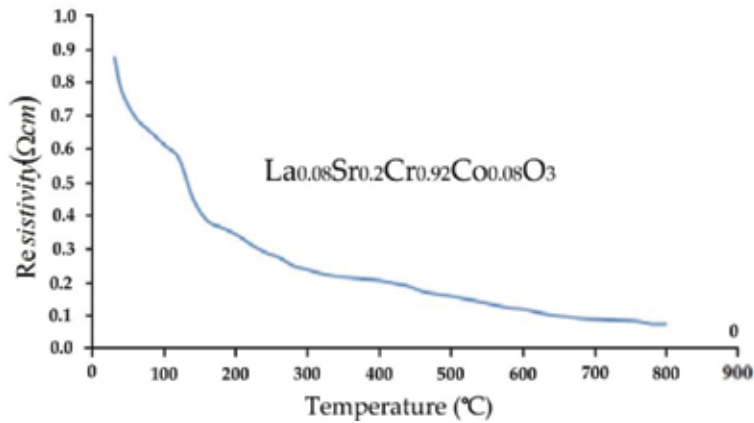

Figure 8. Electrical conductivity of the interconnect (La$_{0.08}$Sr$_{0.20}$Cr$_{0.92}$Co$_{0.08}$O$_3$) composite at different temperatures [9].
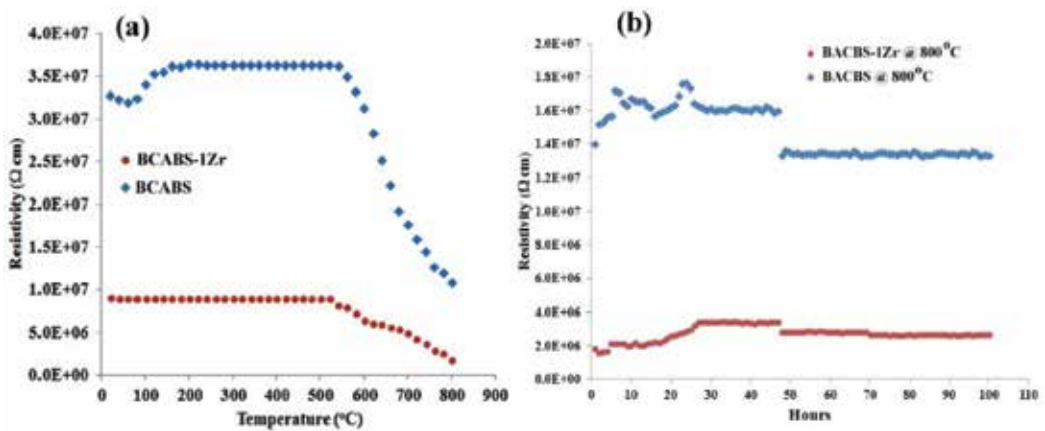

Figure 9. (a) Electrical stability of BCABS and BCABS-1ZrO$_2$ sealing glass at different temperatures; (b) the electrical stability of refractory sealing glass BCABS and BCABS-1ZrO$_2$ at 800°C for 100 h [9].
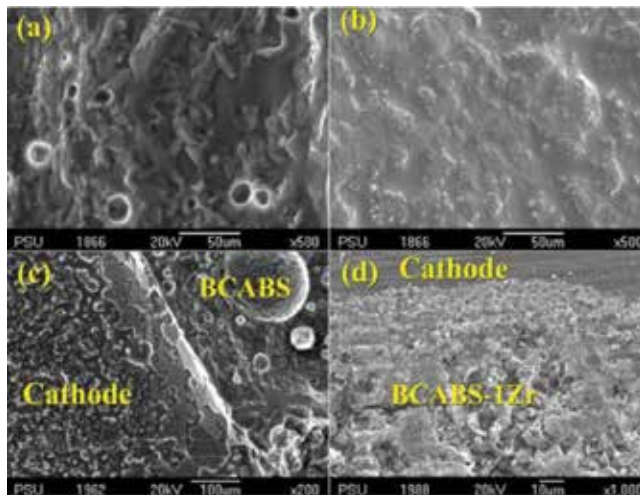
Figure 10. Microstructure of refractory glass: (a) BCABS; (b) BCABS-1ZrO$_2$ on the cathode surface. Microstructure of the cross-section between cathode materials and glass: (c) BCABS sealing glass; (d) BCABS-1ZrO$_2$ sealing glass [9].

For example, porosity, density, grain, and so forth. On the contrary, a highly compact structure or higher density at the surface of the materials can cause slower moisture migration during hot drying or water penetration into the interior during rehydration [21]. In particular images investigating technologies and structures, reconstruction methods have been presented as powerful and reliable tools in fuel cell and component research. The microstructure can allow analysis of the coating of barium aluminosilicate on the fuel cell that is the main problem of BCABS glass when used with the cathode based on the barium oxide (BaO). **Figure 10(a)** reveals the microstructure of refractory glass BCABS with a rough surface free of cracks. Due to both the sealing glass and fuel cell containing barium oxide, they are sintered together as this can combine the phase of barium oxide composition coated on the surface of the fuel cell. **Figure 10(b)** presents the microstructure of refractory glass BCABS-1ZrO$_2$ with a smooth surface free of cracks and blisters, which may be generated from the addition of ZrO$_2$. **Figure 10(c)** shows the microstructure of refractory glass BCABS on a cross-section between glass and cathode, which indicates the formation of barium aluminosilicate and no occurrence of cracks. **Figure 10(d)** reveals the microstructure of refractory glass BCABS-1ZrO$_2$ on the cross-section between glass and cathode, which indicates excellent contact without the formation of barium aluminosilicate or cracks [9].

9. Conclusion

The BCABS sealing glass is easily mixed with the cathode side (containing barium oxide, particularly BSCF and BYCF) of SOFCs at high temperatures. The cathode side of SOFCs receives O$_2$ or air for generating electricity to the external circuit. The cathode is conducted by BCABS sealing glass that can clearly reduce the power density in SOFCs. An improved glass ceramic sealant containing the addition of 0.4 mol% ZrO$_2$ in the BCABS glass composition was developed. The addition of ZrO$_2$ in the sealing glass can prevent the spreading of barium

aluminosilicate on the surface of the SOFCs. The melting point of the mixture is 867.25°C. The electrical resistivity of this mixture is 4 MΩ which is 8 times lower than BCABS, but is very useful for preventing leaks and did not disturb the electricity of the fuel cell. The thermal expansion coefficient reveals a value of 12.40×10^{-6}/°C, which is close to that of the GDC_{10} electrolyte which can protect against the breaking of the cell. The microstructure surface of the mixture exhibits no cracks and is shiny. Therefore, addition of 0.4 mol% ZrO_2 to BCABS can be promoted as a useful sealing technology for SOFCs which contain barium oxide.

Author details

Montri Suklueng

Address all correspondence to: montri.su@psu.ac.th

Energy Systems Research Institute (PERIN), Prince of Songkla University, Songkhla, Thailand

References

[1] Brett DJ, Atkinson A, Brandon NP, Skinner SJ. Intermediate temperature solid oxide fuel cells. Chemical Society Reviews. 2008;**37**:1568-1578

[2] Mahapatra M, Lu K. Seal glass for solid oxide fuel cells. Journal of Power Sources. 2015;**195**:7129-7139

[3] Singh RN. Innovative Self Healing Seals for Solid Oxide Fuel Cells (SOFC). DOE Award DE-09FE001390: University of Cincinnati; 2012

[4] Piao J, Sun K, Zhang N, Chen X, Zhou D. Sealing glass of barium-calcium-aluminosilicate system for solid oxide fuel cells. Journal of Rare Earths. 2007;**25**:434-438

[5] Liu QL, Khor KA, Chan SH. High-performance low-temperature solid oxide fuel cell with novel BSCF cathode. Journal of Power Sources. 2006;**161**:123-128

[6] Suklung M, Yoong VN, Peter H, Ming LC. Optimization of a novel composite cathode for intermediate temperature SOFCs applications. Walailak Journal of Science and Technology (WJST). 2014;**12**:373-381

[7] Fergus JW. Sealants for solid oxide fuel cells. Journal of Power Sources. 2005;**147**:46-57

[8] Ghosh S, Kundu P, Sharma AD, Basu RN, Maiti HS. Microstructure and property evaluation of barium aluminosilicate glass-ceramic sealant for anode-supported solid oxide fuel cell. Journal of the European Ceramic Society. 2008;**28**:69-76

[9] Suklueng M, Voo NY, Lim CM, Razak H, Hing P. The effect of ZrO_2 on the structure of barium calcium aluminium boro-silicate (BCABS) glass. Journal of The Australian Ceramic Society Volume. 2015;**51**:63-68

[10] Becker PF. Transient thermal stress behavior in ZrO_2-toughened Al_2O_3. Journal of the American Ceramic Society. 1981;**64**:37-39

[11] Liang B, Ding C. Thermal shock resistances of nanostructured and conventional zirconia coatings deposited by atmospheric plasma spraying. Surface and Coatings Technology. 2005;**197**:185-192

[12] Lyskov N, Kolchina L, Galin M, Mazo G. Optimization of composite cathode based on praseodymium cuprate for intermediate-temperature solid oxide fuel cells. Russian Journal of Electrochemistry. 2015;**51**:450-457

[13] Ananthanarayanan A, Kothiyal GP, Montagne L, Tricot G, Revel B. The effect of P_2O_5 on the structure, sintering and sealing properties of barium calcium aluminum boro-silicate (BCABS) glasse. Materials Chemistry and Physics. 2011;**130**:880-889

[14] Habibi M, Yang S, Guo S. Phase stability and hot corrosion behavior of ZrO_2-Ta_2O_5 compound in Na_2SO_4-V_2O_5 mixtures at elevated temperatures. Ceramics International. 2014;**40**:4077-4083

[15] Pavlyuchkov D, Savinykh G, Fabrichnaya O. Experimental investigation and thermodynamic modeling of the ZrO_2-MgO-Al_2O_3 system. Journal of the European Ceramic Society. 2014;**34**:1397-1408

[16] Villanova J, Sicardy O, Fortunier R, Micha J-S, Bleuet P. Determination of global and local residual stresses in SOFC by X-ray diffraction. Nuclear Instruments and Methods in Physics Research Section B: Beam Interactions with Materials and Atoms. 2010;**268**:282-286

[17] Liu M, Lynch ME, Blinn K, Alamgir FM, Choi Y. Rational SOFC material design: New advances and tools. Materials Today. 2011;**14**:534-546

[18] Tietz F. Thermal expansion of SOFC materials. Ionics. 1999;**5**:129-139

[19] Guo T, Zhang L, Song X, Dong X, Shirolkar MM, Wang M, Li M, Wang H. Influences of $Gd_2Ti_2O_7$ sintering aid on the densification, ionic conductivity and thermal expansion of $Gd_{0.1}Ce_{0.9}O_{1.95}$ electrolyte for solid oxide fuel cells. Journal of Power Sources. 2014;**262**: 239-244

[20] Acchar W, Sousa C, Mello-Castanho S. Mechanical performance of $LaCrO_3$ doped with strontium and cobalt for SOFC interconnect. Materials Science and Engineering A. 2012; **550**:76-79

[21] Iwai H, Shikazono N, Matsui T, Teshima H, Kishimoto M, Kishida R, Hayashi D, Matsuzaki K, Kanno D, Saito M, Muroyama H, Eguchi K, Kasagi N, Yoshida H. Quantification of SOFC anode microstructure based on dual beam FIB-SEM technique. Journal of Power Sources. 2010;**195**:955-961

Applications of Glass Fibers in 3D Preform Composites

Kadir Bilisik, Gaye Kaya, Huseyin Ozdemir,
Mahmut Korkmaz and Gulhan Erdogan

Additional information is available at the end of the chapter

Abstract

E-glass three dimensional (3D) stitched preform composites have been developed for several industrial applications due to their high mechanical performance and damage tolerance properties. Although some in-plane properties of the stitched E-glass composite structure are slightly lower than in laminated composite, its mode-I delamination failure is improved. This was achieved by using the out-of-plane directional stitched fibers. Recently, some nanoparticles as single-walled nanotubes (SWNT) or multiwalled nanotubes (MWNT) or nanofibers (NF) were added to the glass fabric structure or stitched preform during consolidation process. This further enhances the thermo-mechanical impact properties of the E-glass fiber composites.

Keywords: glass fiber, nanosilicate, nanocarbon, preform, 3D fabric architecture

1. Introduction

Textile fiber composites have been used in various space-aerospace, ballistic, industrial, and medical areas due to their high stiffness to weight ratio and damage tolerance properties [1]. The most important reasons for the increased use of textile structural composites are the increased expectations for product performance and demand for lightweight materials in global markets.

Textile-based composites consist of fibers with high strength and modulus properties, and matrix materials that bond these fibers together to provide load transfer and structural integrity. Fibers provide strength and stiffness to the composite materials, while the resins basically keep the fibers together to transfer stresses between the fibers. Glass fibers are the most common of all reinforcing fibers for polymeric matrix composites, which have low cost, high tensile strength, high chemical resistance, and excellent insulating properties [1–3].

Glass fibers are used as other reinforcement fibers in manufacturing of textile preforms for composites. The textile preform fabrication is done by weaving, braiding, knitting, and stitching and by using nonwoven techniques, and they can be chosen generally based on the end-use requirements. Originally, three dimensional (3D) preforms can be classified according to fiber interlacement types. Simple 3D preform consists of two dimensional (2D) fabrics and is stitched depending on stack sequence. More sophisticated 3D preforms are fabricated by specially designed automated loom and manufactured to near-net shape to reduce scrap [4–6].

In polymeric materials, the use of organic and inorganic fillers has become very common. Polymer composites are used commercially in various areas such as construction and civil engineering, automobile components, and sports equipment. Over the past 20 years, great importance has been attached to the development of polymeric nanocomposites. In nano-composites where at least one of the components is in the nanometer range, the final product is in micro- or macrosize. In addition, advances in computer technology have facilitated the characterization of nanomaterials and their estimation through modeling and simulations [7].

This chapter deals with applications of glass fibers in 3D preform composites. The fabrication, classification, and properties of glass fibers were introduced. Types of matrix and properties of used nanofillers in textile-based polymeric composites in the form of sphere, tubes, and fibers were explained. 2D and 3D fabric forms of glass fibers were reviewed especially considering the 3D stitched composite. Basic fabrication methods of composites were provided. Mechanical properties and failure modes of glass fiber–reinforced 3D composites were discussed by considering the special application areas.

2. Glass fibers, matrix, and nanoadditives

2.1. Glass fibers

Glass can be finely spun into fibers that are pliable to be woven into textiles. Glassy materials, above their glass transition temperature, T_g, show Newtonian viscosity, i.e., the stress is proportional to the strain rate. This property is exploited in the drawing of glass into fiber and planar forms [8]. Glass fibers are used in manufacturing structural composites, printed circuit boards, and a wide range of special-purpose products [9]. Glass fiber manufacturing is the high-temperature conversion of various raw materials, which are predominantly boro-silicate, into a homogeneous melt, followed by the fabrication of this melt into glass fibers [10]. The most important melt properties of fiberglass melts are the fiber-forming viscosity, the temperature at which fibers are formed, and the liquid temperature at which crystals can form within hours and remain in equilibrium with the melt [11]. The basic component of glass fibers is silica (silicon dioxide (SiO_2)) derived from ordinary sand, and the viscous melts can be strong melts typically containing 50–100% SiO_2 and 0–25% Al_2O_3 [12, 13]. The continuous fibers are produced using bushings, which have a few hundred to several thousand small tubes of the bushing. One fiber is produced from each tip. The temperature of the glass exiting tip is typically in the range of 1150–1300°C, depending upon the composition of the glass.

The glass will normally flow out of the bushing under the force of gravity into fibers on the order of 1 mm diameter. The final diameter of the glass fiber is a strong function of the tension applied to the fiber as it is being drawn [14]. **Figure 1** shows the manufacturing of glass fibers and some produced glass fiber tows [15, 16].

The compositions of the glass fibers vary depending on glass types (A-glass, S-glass, or E-glass). More than 99% of continuous glass fibers are spun from an E-glass [17]. The remaining glass fibers are premium special-purpose products [18]. **Table 1** presents the glass fiber types with short explanations [19].

The physical properties of glass fibers are affected by the compositions. The two types of glass fibers commonly used in the fiber-reinforced plastic industry are E-glass and S-glass [2]. Therefore, the physical properties of these fibers are generally discussed. The densities of E-glass and S2-glass fibers are 2.58 g/cm^3 and 2.46 g/cm^3, respectively. The softening points of E-glass and S2-glass are 846°C and 1056°C, respectively. The tensile strengths and modulus are 3345 MPa and 72.3 GPa for E-glass and 4890 MPa and 86.9 GPa for S2-glass, while the elongations are 4.8 and 5.7%, respectively [19]. Scanning electron microscope (SEM) views of E-glass fiber and tow are shown in **Figure 2** [20].

2.2. Matrix

Polymer-based matrix materials are basically classified into two main groups as thermoset and thermoplastic. In general, thermoset polymeric resins have a widespread use in fiber-reinforced composites. The fibers are applied with these resins using the resin transfer molding or recently vacuum-assisted resin transfer molding techniques. During processing, the viscosity of the polymer is low during the interaction of the fiber with the matrix.
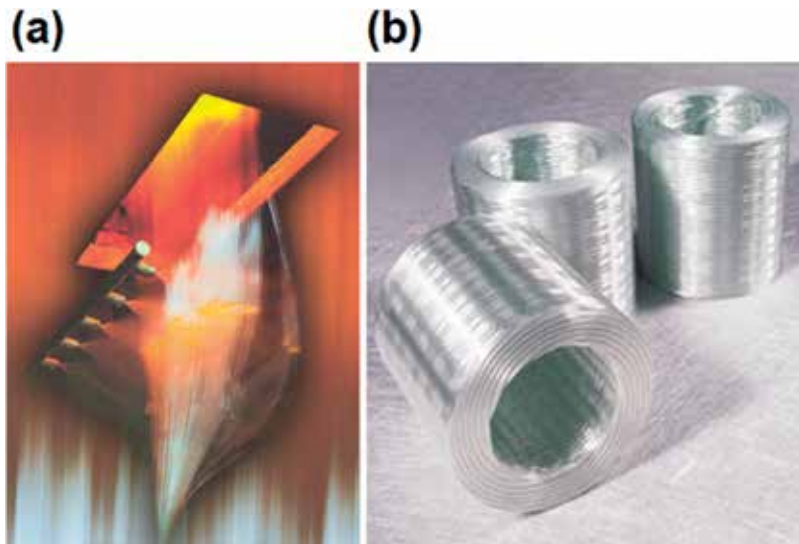

Figure 1. (a) Drawing of glass filaments and (b) glass tows [15, 16].

Type	Description
A glass	High alkali glass—72–75% silica, 0–6 alumina, and 0–6 boron oxide content. Poor resistance to heat. Used for windows, containers, light bulbs, tableware, etc.
C glass	Chemical glass—64–78% silica, 3–5% alumina, and 4–6% boron oxide content. Improved durability and corrosion resistance. Glass staple fibers for making glass mats.
D glass	Dielectric glass—72–75% silica, 0–1 alumina, and 21–24% boron oxide content. Improved dielectric strength and low density. Improved electrical performance.
E glass	Electrically resistant glass—52–56% silica, 12–16% alumina, and 5–10% boron oxide content. Used in glass reinforced plastics as general-purpose fibers where strength and high electrical resistivity are required.
ECR glass	Modified 'E' glass—54–62% silica and 9–15% alumina content. Superior long-term resistance to strain crack corrosion in acid conditions.
AR glass	Alkali-resistant glass—55–75% silica and 1–18% zirconium content. Used in cement substrates and concrete.
R glass	55–60% silica and 23–28% alumina content. High-strength, high-modulus at a lower cost than 'S' glass.
S2 glass	64–66% silica, 24–25% alumina, and 9.5–10% magnesium oxide (40% higher than E-glass) content. Developed for aerospace applications.

Table 1. Glass fiber types and some of their physical and chemical specifications [19].
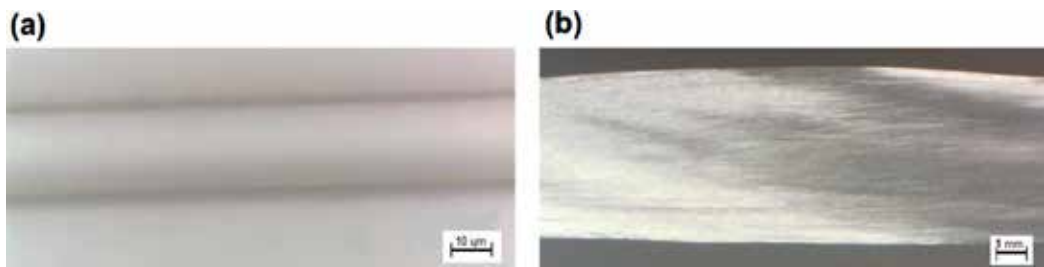

Figure 2. SEM views of E-glass fiber and tow. (a) E-glass fiber and (b) E-glass tow [20].

This provides good wetting properties between the fiber and the matrix without any additional high temperature or pressure. However, the low strain properties of thermoset resins reduce the impact strength of the composites. The most widely used thermoset resins are epoxy, polyester, phenolic, and vinyl ester [1, 2, 21].

There is a growing interest in development and production of the thermoplastic polymer–based composites. The reason of this interest is the ability of thermoplastic composites to form and remold easily in shorter process times compared to thermoset composites. Furthermore, thermoplastic composites provide high fracture toughness, damage tolerance, and microcrack resistance [22, 23]. Thermoplastic resins are about 500–1000 times more viscous than thermoset resins. This restricts the infusion tendency of resins to fibers. In addition, the need for high pressures in thermoplastic composite process is also considered as another limiting factor. Semicrystalline thermoplastic polymers such as polyether ether ketone (PEEK), polyphenylene sulfide (PPS), and liquid-crystal polymers (LCP) are mainly used in aviation due to their

mechanical and chemical resistance at relatively high temperatures. Some other thermoplastic polymers such as polypropylene(PP), acrylonitrile butadiene styrene (ABS), and polyamide (PA) find use in the automotive industry. PP has a very common use in the production of thermoplastic composites due to its low cost, high specific properties, and reusability [24, 25]. The properties of some of the thermoset and thermoplastic resins are presented in **Table 2** [21].

Polyesters are used extensively in continuous and discontinuous composites and they are relatively inexpensive with processing flexibility. They are cured by addition reactions in which unsaturated carbon-carbon double bonds (C═C) are the locations where cross-linking occurs. Typical polyester consists of at least three ingredients: a polyester, a cross-linking agent such as styrene, and an initiator, usually a peroxide, such as methyl ethyl ketone peroxide (MEKP). One of the main advantages of polyesters is that they can be formulated to cure at either room temperature or elevated temperatures, allowing great versatility in their processing. Epoxies are high-performance matrix systems for primarily continuous fiber composites and have better high-temperature performance than polyesters and vinyl esters. Epoxies are used in resin transfer molding, filament winding, pultrusion, hand layup, and other processes with various high-modulus and high-strength fibers. The properties of the resultant resins are strongly dependent on the cross-linking [2, 3]. Vinyl esters are similar to polyesters but are tougher and have better moisture resistance [2, 26].

2.3. Nanoadditives

Nanoparticles have been identified in the last decade as an important class of materials for various emerging applications in optics, electronics, or the biomedical area. Many of the potential applications are based on two major changes when the scale of material structures decreased. These are the high surface-to-volume ratio and the improvement of the electronic properties [27]. Nanocomposites can be described as particle-filled polymers in which at least one of the components is in nanometer dimensions [28]. The investigation of fullerenes (nanosphere) and carbon nanotubes (CNT) has opened a totally new window for the development of polymer matrix composites with novel properties and applications [29]. Nanofillers have a considerable potential in improving the properties of polymeric composites [30, 31]. The stiffness, toughness, and abrasion resistance of nanocomposites depend on the size, shape, ratio, and uniform distribution of the fillers in the polymers [32]. It can be possible to obtain

Polymer	Resin	Density (g/cm³)	Tensile modulus (GPa)	Tensile strength (MPa)
Thermoset	Epoxy	1.2–1.4	2.5–5.0	50–110
	Phenolic	1.2–1.4	2.7–4.1	35–60
	Polyester	1.1–1.4	1.6–4.1	35–95
Thermoplastic	Polyamide	1.1	1.3–3.5	55–90
	PEEK	1.3–1.35	3.5–4.4	100
	PPS	1.3–1.4	3.4	80

Table 2. The specification of thermoset and thermoplastic matrix [21].

materials with high toughness values by producing nanocomposites with high nanoparticle ratio, homogeneous alignment, and high interface strength [33]. Interfacial bond properties between nanoparticle and matrix in the composite are active research subject in the research and development societies [31]. Nanosphere, single-walled, or multiwalled tubes were applied to the composites by dispersing the nanoparticles in the resin using various techniques such as shear mixing, ultrasonication, calendering, ball milling or ultrasonication-extrusion, and transfer-printing. If nanofibers were used, they were attached, grown, or grafted onto fibers or 2D fabrics. Full deagglomeration of CNTs using mixers is difficult to achieve. High flow rates creating high-shear forces cause well distribution of agglomerated CNTs. However, their breakage is not avoided and the presence of CNT agglomerates is usually observed [34]. Various nanosized materials were developed by employing the up-to-date processing as silica is one of the most important and most studied oxide nanoparticle types. Due to its quite simple preparation, its chemical inertness, and the relatively inexpensive precursors, it became a prominent compound in academics and in commercial applications [27]. Because of its high specific component of surface energy, silica has a stronger tendency to agglomerate than carbon black [35]. **Figure 3** shows the SEM (scanning electron microscope) micrograph of nanosilica and nano- and microcarbon spheres [20].

In the past few years, novel materials such as carbon nanotubes (CNTs) and related technologies have posed a strong candidacy for providing an integrated approach toward enhanced structural integrity and multifunctionality [36]. The development of novel glass fiber–reinforced plastics (GFRPs) with electrical conductivity has opened up new opportunities for damage sensing. Adding a small amount of carbon nanotubes to form an electrically conductive network is a promising approach to monitor damage initiation and propagation for glass fiber–reinforced composites [37].

The pre-dispersed overcoating of nanotubes and the process modifications allow improvement of the interface properties of 2D woven E-glass composites since the reinforcement effect of nanotubes on z-direction [38]. The amine functionalized carbon nanotubes had improved tensile strength compared to neat [39]. The modulus of composites is enhanced by the addition of silicon carbide nanoparticles by considering dispersion of these particles in resin, which highly depends on the coupling agents and dispersants [40]. Moreover, the weak
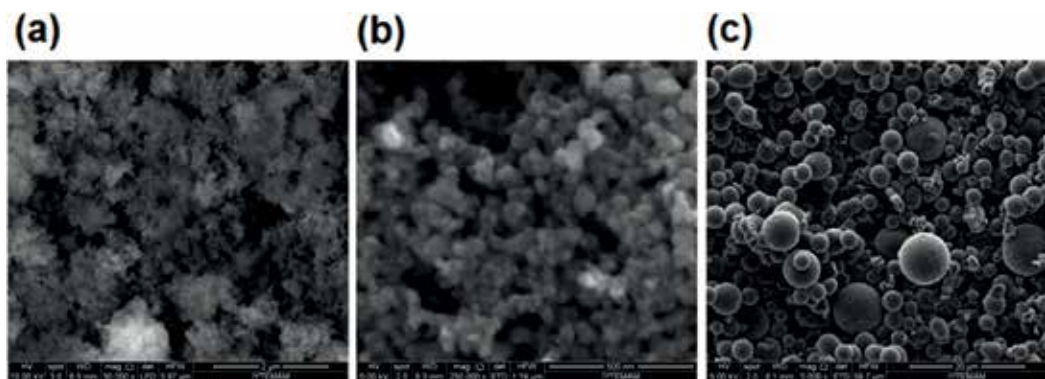

Figure 3. SEM micrograph of some nanofillers. (a) Nanosilica (magnification 50,000×); (b) nanocarbon (magnification 250,000×); and (c) nanocarbon (magnification 5000×) [20].

bonds at the interfaces of silicon carbide nanoparticles and resin lead to stress concentration rely on the particle geometry [41].

3. 2D fabrics and 3D preforms

3.1. Two dimensional (2D) fabrics

The most preferred 2D fabrics in textile structural composites are discussed as 2D woven fabric, triaxial woven fabric, braided fabric and knitted fabric, uniaxial and biaxial knitted fabrics, and nonwoven fabric. The most common fabric used in the textile structural composites is 2D woven fabric due to its more stable property compared to the knitted fabric. To form the 2D woven fabric, there are two yarn sets as warp and weft interlace each other at right angle. 2D woven fabric has three types of main patterns as plain, twill, and satin and also a lot of derivative patterns. Because the plain woven fabric is formed by more interlacement points between warp and weft, its structural characteristics become more rigid, less flexible, and more durable. Twill woven fabric has inclined paths from right to left or from left to right on the fabric surface due to its interlacements of warp and weft. In satin woven fabric, warp has long floats, which are evenly distributed through the fabric. It has low crimp ratio. The schematic views of weaves and microscopic view of E-glass plain woven fabrics are shown in **Figure 4** [20].

The schematic views of triaxial woven fabric and braided fabric are shown in **Figure 5(a)** and **(b)**. As shown in **Figure 5(a)**, triaxial weave has three sets of yarn as +bias, −bias, and weft yarn in which these yarns take in interlacements [42]. This fabric has large gaps in the crossing region of warp and weft due to interlacements and it restricts to make dense fabrics during 2D woven fabric formation [44]. 2D braided fabric has one yarn set as braiders, which have $+\theta°$ and $-\theta°$ orientations. As shown in **Figure 5(b)**, these braider yarns are intertwined with each other to make the 2D braided fabric structure [43].

Figure 6(a–g) shows the schematic views of weft and warp knitted fabrics and uniaxial and biaxial knitted fabrics. The knitted fabric is constituted from yarn loops connected to each other and to the neighboring rows and columns by various techniques. The basic knitting types are weft knitting (**Figure 6a**) and warp knitting (**Figure 6b**) [45].
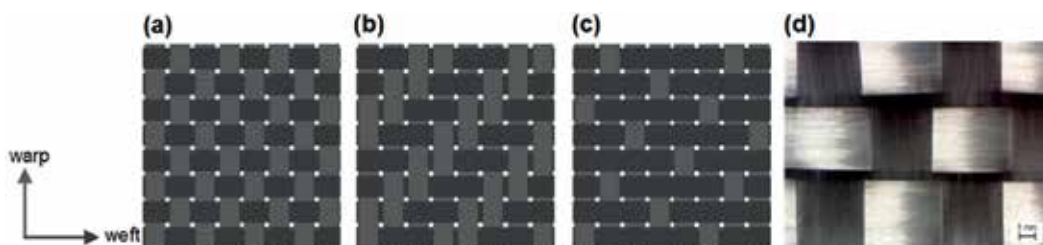

Figure 4. The schematic views of weaves and microscopic view of E-glass plain woven fabrics. (a) plain; (b) twill; (c) satin; and (d) E-glass plain woven fabric [20].
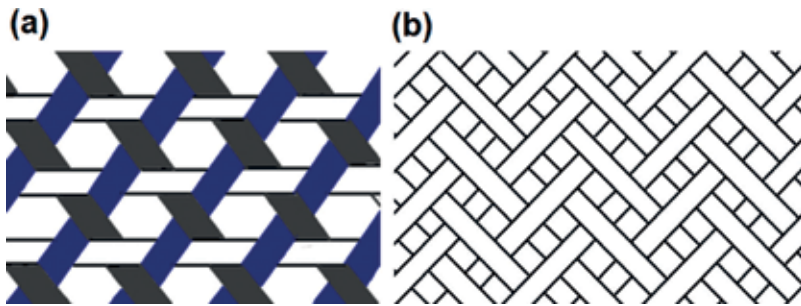
Figure 5. Schematic views of triaxial woven and braided fabrics. (a) Triaxial woven fabric and (b) braided fabric [42, 43].
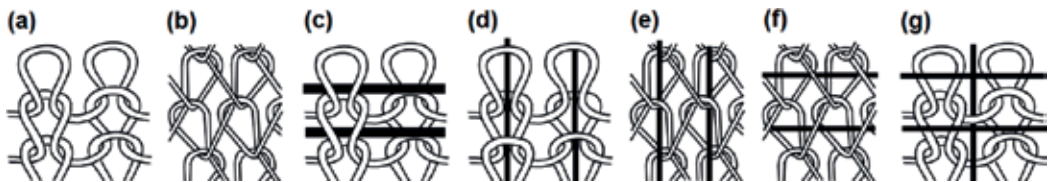

Figure 6. (a) Weft knitted fabric; (b) warp knitted fabric; (c) weft inlaid weft knitted fabric; (d) warp inlaid weft knitted fabric; (e) warp inlaid warp knitted fabric; (f) weft inlaid warp knitted fabric; and (g) 0°/90° inlaid weft knitted fabric [45–47].

The uniaxial knitted fabric is a special type looped knitted fabric. It has big gaps, which lead to low fiber-volume-fractions, high-elongation, and low stiffness. Because of these restrictions, some structural modifications were performed by adding inlay yarns either in fabric length (**Figure 6(d)** and **(e)**) or width (**Figure 6(c)** and **(f)**). The tensile strengths of uniaxial knitted fabric composites improved in the direction of inlaid [46].

Biaxial knitted fabric is manufactured by introducing the warp (0°), weft (90°), or diagonal (±45°) yarns into the weft (**Figure 6(g)**) or warp knitted fabrics, which resulted as the improved mechanical properties of composites at the inlaid directions [48]. Nonwoven fabric is a web structure made up of short fibers that are held together by various techniques [49]. Nonwoven manufacture is that it is generally done in one continuous process directly from the raw material to the finished fabric [50]. **Figure 7** shows the view of nonwoven glass mat [51].

3.2. Three dimensional (3D) fabrics

2D fabric–reinforced composites are a biaxially oriented planar structure. However, unidirectional fiber composite is an axially oriented planar structure. Both suffer from a delamination. 3D fabric preforms have been developed to make the delamination free composite.

Stitching can be used to make 3D fabrics using the 2D woven fabric [52]. 3D stitched fabric is manufactured by stitching 2D fabric layers in thickness direction. It can be stitched at one direction (0°), two directions (0° and 90°), and four directions (0°, 90°, and ±bias) as shown in **Figures 8** and **9**. Stitching can be made by sewing machine. The lock stitching is generally used in stitched preform fabrication for composites [53, 54].
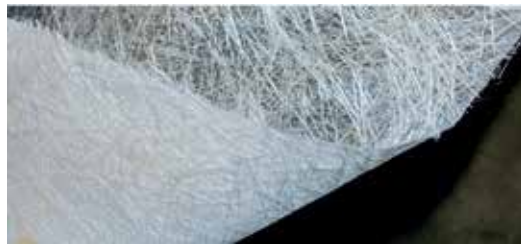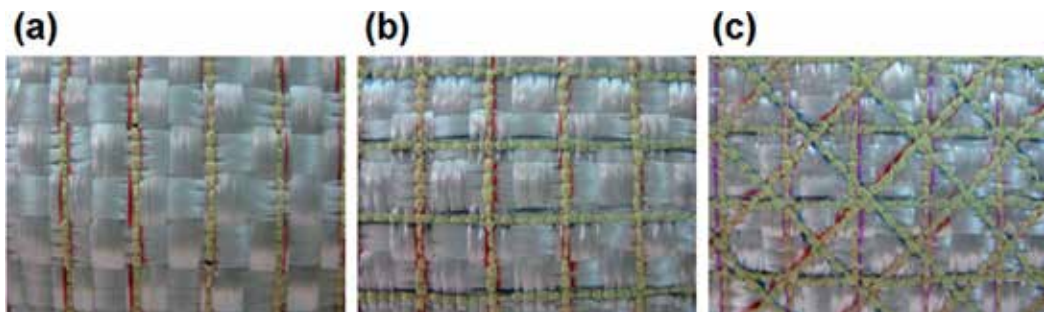
Figure 7. Nonwoven glass mat [51].

Figure 8. Top views of stitched E-glass preforms. (a) One-directional machine stitched; (b) two-directional machine stitched; and (c) four-directional machine stitched [53].
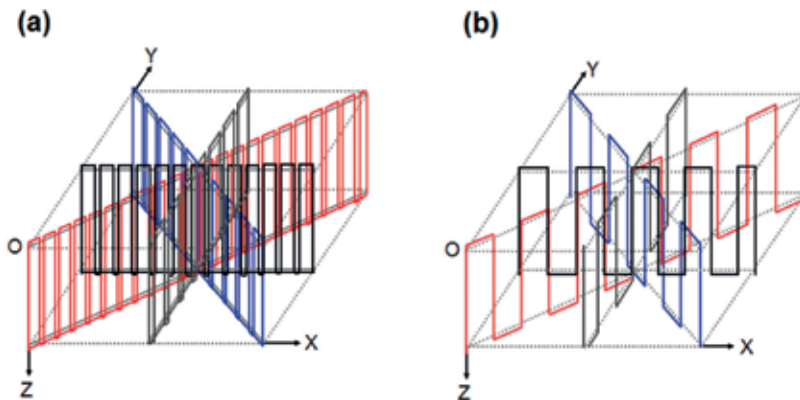
Figure 9. Schematic view of multistitched yarn paths. (a) Machine multistitched yarn path and (b) hand multistitched yarn path [54].

3D orthogonal woven fabric has three yarn sets as warp, weft, and z-yarn (**Figure 10(a)**). These yarn sets are interlaced to one another and oriented in three orthogonal directions to form the fabric [59]. Warp yarns are placed in the direction of the fabric length, while the weft yarns are inserted between the warp layers to form double picks. Z-yarns lock the other two yarn sets and provide structural integrity [48]. **Figure 10(a–d)** shows some of the 3D fabrics [55–58].

Figure 10. Some of the 3D fabrics. (a) 3D woven carbon fabric [55]; (b) multiaxis 3D woven carbon fabric [56]; (c) multiaxis 3D circular woven aramid fabric [57]; and (d) multiaxis 3D braided conical aramid fabric [58].

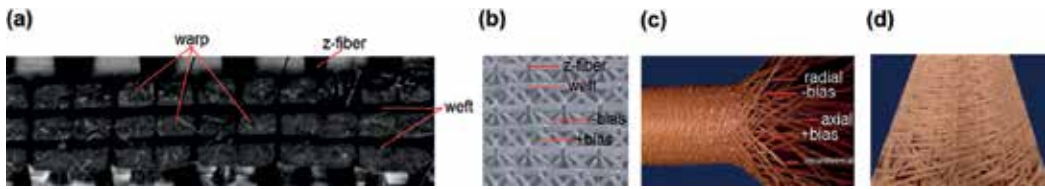A multiaxis 3D woven fabric, method, and machine were developed by Mohamed and Bilisik [60]. The multiaxis 3D woven fabric has five yarn sets as +bias, −bias, warp, weft, and z-yarn. ±Bias yarns are placed on the front face and back face. These yarns are locked to the other yarn sets by the z-yarns (**Figure 10(b)**). Multiaxis 3D circular woven fabric, method, and machine were developed by Bilisik. The 3D circular woven fabric has axial and radial yarns along with circumferential and ±bias yarns (**Figure 10(c)**). Cylindrical preform can be made with thin and thick wall sections depending upon end-use requirements [61]. In multiaxis 3D braided fabric, braider yarns are intertwined with the axial yarns, whereas ±bias yarns are oriented at the surface of the structure and locked by the radial yarns to the other yarn sets (**Figure 10(d)**). The properties of the multiaxial 3D braided structure in the transverse direction can be enhanced and the nonuniformity in the directional Poisson's ratios can be decreased [58, 62].

4. Composite

Several methods are developed in order to make composite based on 2D fabric and 3D preforms. The fiber properties, type of fabric formation and matrix, end-use requirement, and shape/size characteristics of the part influence the composite fabrication processes. **Figure 11** shows the schematic views of some of the composite fabrication techniques [20, 63].

Hand layup is the most commonly used composite fabrication method. It is still preferred because of highly flexible in design and suitable for the production of a wide variety of raw materials. The fabric layers are laid according to the desired thickness, and after each layer is laid, the resin is added by brush to spread the resin to wet the fibers. Then, the part is usually cured at room temperature and removed from the mold (**Figure 11(a)**). Resin transfer mold (RTM) is a recently introduced composite fabrication method to produce near-net shape parts.
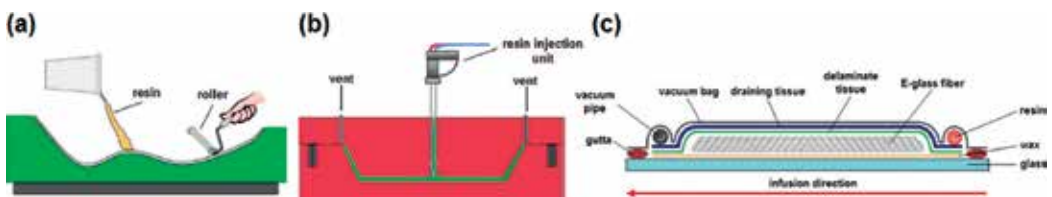

Figure 11. Schematic views of some of the composite fabrication techniques. (a) Hand layup; (b) resin transfer molding [63]; and (c) vacuum-assisted resin transfer molding [20].

The preform is placed in the gap between the molds. Then, the mold is closed and the gaps in the preform are filled by wetting all the fibers with resin. This process usually takes place under high pressure. The part is removed from the molds after curing (**Figure 11(b)**). The vacuum-assisted resin transfer molding (VARTM) method is more cost-effective since it does not require a metallic mold. The preform is placed on the mold and covered with sealing tape with flexible vacuum film. The resin passes through the structure under vacuum and it is possible to produce high performance composite structures with high fiber volume fractions (**Figure 11(c)**) [1–3].

5. Properties of preforms and composites

3D glass woven preforms improve the out-of-plane properties of the composites. 3D stitched woven preforms also enhance the out-of-plane properties without decreasing the in-plane properties of the composite [64]. It is pointed out that the fracture mechanism of the stitched composite plates is affected by the loading direction in tensile test, but the stiffness of the structure is not significantly affected by the stitching [65]. The tensile strengths of stitched composite, in which twisted stitching yarns are utilized, is lower compared to the stitched composite having with untwisted stitching yarns [66]. It is demonstrated that stitching prevents the crack propagation [66, 67]. The stitching causes local irregularities and undulation in the preform, which leads to a nonuniform fiber volume fractions and reduces the in-plane properties of the composite [68, 69]. In unstitched composites, delamination-based cracks are observed as a form of layer separation. However, in stitched composites, mode-I failure is improved and catastrophic delamination is eliminated in which the composite becomes damage tolerance material. It is stated that the tensile strength of stitched composites is dependent on the parameters as stitching yarn type and stitching density. The ±45° directional off-axis tensile strengths of the 2D unstitched woven E-glass/polyester composites are 84.1 MPa and 75.4 MPa, while the ±45° directional off-axis tensile strengths of the 3D stitched woven E-glass/polyester composites vary from 86.5 to 70.0 MPa and from 83.5 to 64.1 MPa. The tensile strengths of four directional densely stitched composite is almost 15 and 6% lower than those of the unstitched composites at +45 and −45 directions, respectively. The similar trend is obtained for the ±45° directional off-axis tensile modulus of composite structures. The ±45° directional off-axis tensile modulus of the 2D unstitched woven E-glass/polyester composites is 5.9 GPa and 6.2 GPa, while the ±45° directional off-axis tensile modulus of the 3D stitched woven E-glass/polyester composites vary from 6.4 to 4.0 GPa and from 6.3 to 3.7 GPa. The tensile modulus of four directional densely stitched composite is almost 32 and 40% lower than those of the unstitched composites at +45 and −45 directions, respectively. These results show that when the stitching direction and stitching density in structures increase, their off-axis tensile strengths and modulus decrease since the multi-stitching process causes more filament breakages [70]. The warp and weft directional specific tensile strengths of the unstitched composites are higher than those in the multistitched composites due to stitching that causes filament breakages during insertion of the z-yarn. The stitching yarn types, stitch directions, and the stitch density generally influence the in-plane tensile properties of the multistitched E-glass/polyester woven composites. The warp-weft directional tensile strengths of the 2D unstitched woven E-glass/polyester composites are

303 MPa and 285 MPa, while the warp-weft directional tensile strengths of the 3D stitched woven E-glass/polyester composites vary from 353 to 229 MPa and from 345 to 209 MPa. The tensile strength of four directional densely stitched composite is almost 25 and 27% lower than those of the unstitched composites at warp and weft directions, respectively. The warp-weft tensile modulus of four directional densely stitched composite is almost 35 and 35% lower than those of the unstitched composites at warp and weft directions, respectively. However, the warp-weft damaged areas of four directional densely stitched composite after tensile failure are almost 70 and 82% lower than those of the unstitched composites at warp and weft directions, respectively. The warp and weft directional damaged areas of multistitched composites decrease when the stitching directions in the out-of-plane of the structure increased. Therefore, the stitching yarns lock the in-plane directional warp and weft yarns in the layered woven structure and confine the damage areas at narrow regions, which considers as damage tolerant materials [71]. Furthermore, the off-axis tensile modulus of the multistitched composites decreases with the increase of the stitching direction and stitching density [70].

The warp and weft direction specific bending strengths and modulus of the unstitched/ nanocomposites are higher than those of the stitched composites since the stitching perhaps causes filament breakages during needle piercing action. The warp-weft specific strengths of four directional densely stitched composite are almost 25 and 31% lower than those of the unstitched composites at warp and weft directions, respectively. On the other hand, the warp and weft directional damaged areas of the unstitched composites are higher than multistitched and multistitched/nanocomposites. The addition of the nanosilica to the stitched structures increases the damage tolerance [72]. One of the critical property of the stitched composite is also through-the-thickness directional shearing. The short-beam strengths of hand-stitched composites in the warp and weft direction increase slightly as the stitching direction increased from two directions to four directions. In addition, the warp and weft directional short-beam strengths of machine-stitched structures with high-modulus stitching yarns (Kevlar® 129) are higher than those of the machine-stitched structures stitched with low-modulus stitching yarns (Nylon 6.6) [73]. The tensile and impact behaviors of stitched E-glass/polypropylene woven composites are studied. The stitching in the through-the-thickness direction increases impact damage tolerance especially at low temperatures. It is claimed that there is a relation between stitching fiber fracture work and energy absorption based on fiber volume fraction in stitched composites [74]. The mechanical properties such as the tensile and compression and compression-after-impact (CAI) strength of noncrimped fabric are not degraded by the stitching parameters, whereas the tensile and compression strength and the tensile fatigue behavior are reduced as a result of pronounced localized fiber undulations due to stitching [68]. Stitched layered composite has slightly higher compression and CAI strengths than the integrally woven composite [75]. In addition, it is found that the strength of overlap joint during preforming is improved by using high-density chain stitching [76]. The damage initiation force for 3D noninterlaced stitched composite is lower than for the 2D unstitched woven composite due to weak resin-rich regions around the stitch loops. Densely stitched composite with more stitched-induced matrix cracks upon impact loading is due to the presence of weak resin-rich pockets around the stitching yarns [77–80]. The noncrimp stitched carbon fabric composite shows a quasi-isotropic behavior, while 2D woven composite demonstrated an anisotropic behavior. Stitching in the noncrimp carbon fabric has only a minor effect on its strength properties. Damage sites are mainly observed in the resin-rich
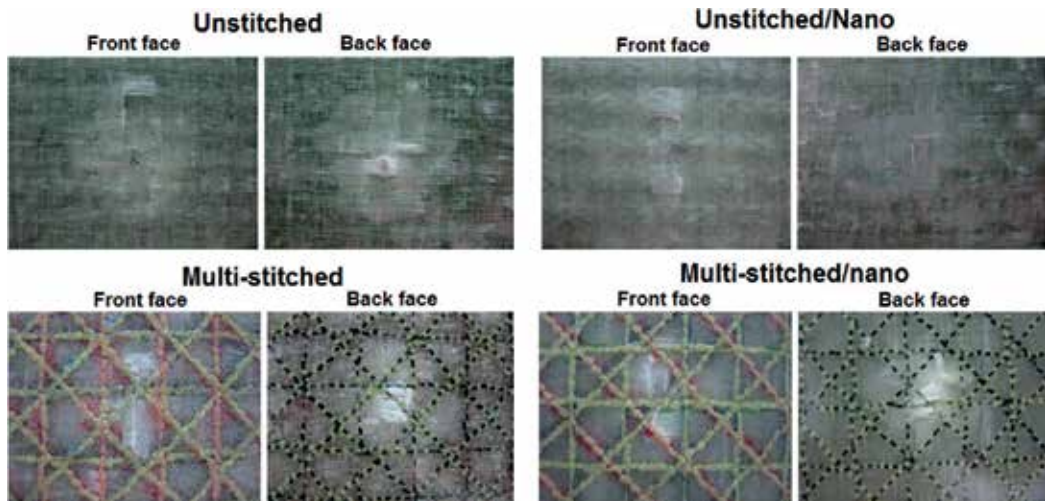
Figure 12. Damaged areas of composite after low-velocity impact test [82].

zones created by the stitching [81]. The low-velocity impact properties of the multistitched/micro-/nano-E-glass/polyester woven composites are studied. It is observed that the material type (silicate or carbon or metal), the material particle size (nano or micro), amount of materials (weight, %), stitching density (step/cm), and stitching type (hand or machine) influence the damaged areas of composites. **Figure 12** shows the damaged areas of composite after low-velocity impact test. The damaged areas of multistitched/nanosilica (5 wt.%) composite after low-velocity impact test are almost 60 and 48% lower than those of the unstitched composites on front and back faces, respectively [82].

The multistitched and multistitched/nano-E-glass/polyester woven composite show a better damage resistance performance compared to those of the unstitched or unstitched/nano-composites. The multistitching suppresses the impact energy relatively at a small area of the composite. In addition, adding the nanomaterial to the multistitched structure can further enhance the damage resistance performance [82].

6. Glass fabric and glass composite applications

The glass fiber–reinforced composites are used in a variety of forms to assure the required properties of usage areas as space, aerospace, automobile, energy, marine, electronic components, and defense-related special areas. The composites are designed according to service environments of usage areas in mechanical, impact, flammability, and electrical properties.

6.1. Aviation and aerospace

Although the volumes of fiber-reinforced polymer composites used for aircraft applications were a relatively small percentage, they found their most advanced applications in the fabrication of civil or military aircrafts [83]. For instance, the Boeing 787 made large use of composite materials in its airframe and primary structure. The use of composites, especially in the highly tension-loaded

part of the fuselage, greatly reduced maintenance labor and cost. **Figure 13** shows the percentages of used composite materials along with metals in commercial civilian airplane (Boeing 787) [84]. Typical glass fiber–reinforced composite applications in aircraft were engine cowlings, luggage racks, instrument enclosures, bulkheads, ducting, storage bins, and antenna enclosures. In addition, it was also widely used in ground-handling equipment [85].

6.2. Automotive

Glass fiber composite used in automotive is primarily driven by the demand for lightweight components, fuel efficiency, and recycling [86]. The two most common types of glass fibers used in automotive composites were the E-glass, which was cost-effective and had good tensile properties. Second one was S-glass, which had 40% higher tensile properties compared to the E-glass. But, it was expensive [87]. All glass fiber–based composites were used in automotive as primary or secondary structural parts of interior headliner, underbody system, and air intake manifold, instrument panel, bumper beam, and engine cover [88]. **Figure 14** shows the glass fiber–based composite panels in car and trucks [63].

6.3. Boats and marine

Glass fiber both continuous TOW or discontinuous short forms has been the main material for the recreational boating industry, which was employed as hulls with a minimum number of assembled parts. Glass fiber–based composites have gained acceptance in pleasure craft because of light weight, vibration damping, corrosion resistance, impact resistance, low construction costs, and ease of fabrication, maintenance, and repair. Current leading-edge manufacturing technologies were driven by racing vessels, both power and sail [85, 89].
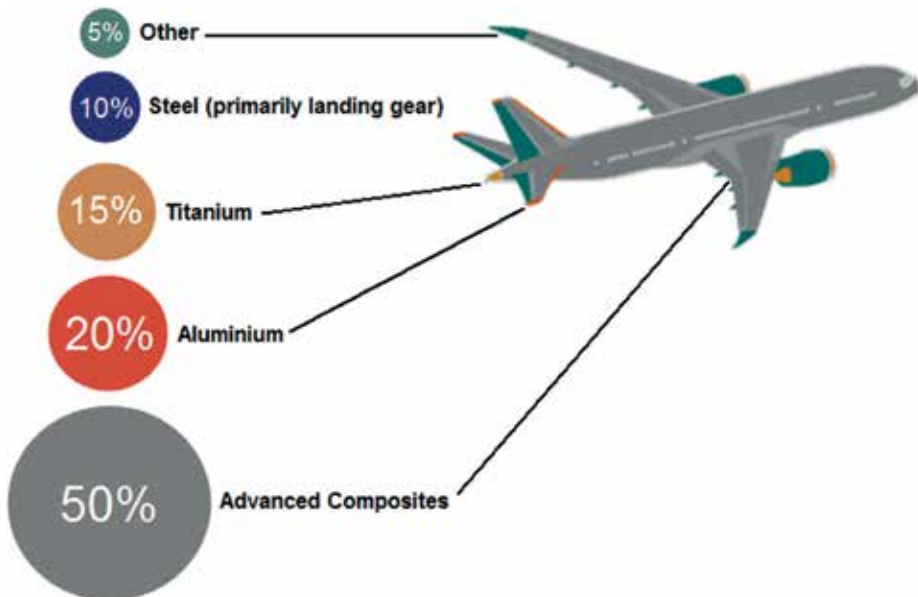

Figure 13. Composite materials used in civilian aircraft (Boeing 787) [84].

Figure 14. Glass fiber–reinforced composite body panels for truck and car [63].

6.4. Electronics

Glass fiber/epoxy composites have been the foundational structural substrate in printed circuit boards since 1980. They supported the transistors, resistors, and integrated circuits at all digital technologies. Glass composite board connected them electrically via conductive pathways etched or printed on their surfaces [90]. They were also used as insulators for high-voltage energy cabin components, a cable, or cable-coated material to transit the electrical energy [91].

6.5. Wind energy

In the sector of energy generation, glass fiber composites were utilized in manufacturing wind generators. The blades of the generators were generally made of epoxy resins reinforced with glass or carbon fibers. Their high mechanical strength and modulus made them attractive material for the wind blade in turbine generators [26]. **Figure 15** shows the wind blades placed in the sea [92].

6.6. Ballistic

2D S2-glass fabric and 3D S2-glass preform composites were employed in ballistic armor. 3D S2-glass ballistic plate has better energy absorption properties due to z-yarn insertion in the through-the-thickness direction. This provided additional energy absorbing as a mechanism of high-strain interlayer deformations. In addition, 2D S2-glass fabric plate with or without

Figure 15. Wind blades placed in the sea [92].

Figure 16. Glass fiber–based ballistic plate and bulletproof jacket [93].

stitching or 3D S2-glass preform composite plate has certain specific energy-absorbing advantages over the ceramic or metal armor plate. **Figure 16** shows the glass fiber–based ballistic plate and bulletproof jacket [26, 93, 94].

7. Future trends

Biaxial 2D woven fabrics have been widely used as simple and complex-shaped structural composite parts in various technical areas. In addition, biaxial weaving methods and techniques are well developed. 3D glass fabrics have multiple layers and show no delamination. 3D woven glass preform as well as multilayered stitched fabrics will be expanded in the field of especially marine and industrial applications as a form of composite structure. However, the multiaxis 3D weaving technique is at an early stage of development and needs to be fully automated. This will be a future technological challenge in the area of multiaxis 3D weaving.

8. Conclusion

In this chapter, two dimensional glass fabric (2D) and three dimensional (3D) glass preforms, fabrication methods, and application areas were reviewed. Glass fabrics were readily available and important, but they were specific segmented basic materials. 2D E-glass fabrics were traditionally employed in various industrial areas. 3D glass fabrics have multiple layers and no delamination due to out-of-plane directional fibers. Various techniques were also developed for 3D glass preforms. 3D orthogonal and stitched as well as multiaxis 3D knitted and 3D braided glass preforms are commercially available. On the other hand, various unit cell base models on 3D glass preform and composites were developed to define their geometrical and mechanical properties. Multiaxis 3D glass fabrics have multiple layers, and their in-plane properties are enhanced due to the bias yarn layers. However, the multiaxis

3D woven preform technique is at an early stage of development. Recently, 3D woven and stitched glass preforms were made by adding single or multiwalled nanotubes and nanofibers to enhance their mechanical, thermal, and electrical properties. This will open up new material classes as well as application areas for near future.

9. Sources of further information and advice

Many studies have been carried out on the characterization and modeling of 2D and 3D glass preform composite structures, but limited information is available on the 3D fabric architecture and nanoadded glass fiber composites. Recent literature and books can be useful for having more information on these areas as indicated in Refs. [95–97].

Author details

Kadir Bilisik[1]*, Gaye Kaya[2], Huseyin Ozdemir[3], Mahmut Korkmaz[4] and Gulhan Erdogan[1]

*Address all correspondence to: kadirbilisik@gmail.com

1 Department of Textile Engineering, Erciyes University, Turkey

2 Department of Textile Engineering, Kahramanmaras Sutcu Imam University, Turkey

3 Vocational School of Technical Sciences, Gaziantep University, Turkey

4 Mustafa Cikrikcioglu Vocational School of Technical Sciences, Erciyes University, Turkey

References

[1] Hoa SV. Principles of the Manufacturing of Composite Materials. Lancaster: DEStech Publications, Inc.; 2009. pp. 3-5

[2] Mallick PK. Fiber Reinforced Composites Materials, Manufacturing and Design. 2nd ed. Florida: CRC Press; 2007. pp. 60-116

[3] Campbell FC. Manufacturing Processes for Advanced Composites. Oxford: Elsevier; 2003. pp. 39-62

[4] Bilisik K. Multiaxis three dimensional (3D) woven fabric. In: Vassiliadis S, editor. Advances in Modern Woven Fabrics Technology. Zagreb, Croatia: InTech; 2011. pp. 80-106

[5] Brandt J, Drechsler K, Filsinger J. Advanced textile technologies for the cost effective manufacturing of high performance composites. RTO AVT Specialist Meeting on Low Cost Composite Structures; 7-11 May 2001; Loen, Norway

[6] Mohamed M. Three dimensional textiles. American Scientist. 1990;**78**:530-541

[7] Hussain F, Hojjati M, Okamoto M, Gorga RE. Review article: Polymer-matrix nanocomposites, processing, manufacturing, and application: An overview. Journal of Composite Materials. 2006;**40**:1511-1575

[8] Chawla K. Fibrous Materials. Cambridge: Cambridge University Press; 2016. pp. 199-229

[9] Wallenberger FT. Melt viscosity and modulus of bulk glasses and fibers: Challenges for the next decade, in present state and future prospects of glass science and technology. In: Proceedings of the Norbert Kreidl Symposium; 3-8 July 1994; Liechtenstein; 1994. p. 63-78

[10] Glass Fiber Manufacturing: United States Environmental Protection Agency (EPA) [Internet]. 2017. Available from: https://www3.epa.gov/ttnchie1/ap42/ch11/final/c11s13.pdf. [Accessed: 2017-06-10]

[11] Wallenberger FT. Commercial and experimental glass fibers. In: Wallenberger FT, Bingham PA editors. Fiberglass and Glass Technology: Energy-Friendly Compositions and Applications. US: Springer; 2010. p. 3-90

[12] Gonterman JR, Weinstein MA. Plasma melting technology and applications. In: Wallenberger FT, Bingham PA editors. Fiberglass and Glass Technology: Energy-Friendly Compositions and Applications. US: Springer; 2010. p. 431-451

[13] Hausrath RL, Longobardo AV. High-strength glass Fibers and markets. In: Wallenberger FT, Bingham PA editors. Fiberglass and Glass Technology: Energy-Friendly Compositions and Applications. US: Springer; 2010. p. 197-225

[14] Jones FR, Huff NT. Structure and Properties of Glass Fibres. In: A.R. Bunsell editor. Handbook of Tensile Properties of Textile and Technical Fibres. Cambridge: Woodhead Publishing; 2009. p. 529-573

[15] Sisecam, Turkey: Products [Internet]. 2017. Available from: http://www.sisecamkimyasallar.com/tr/faaliyet-alanlarimiz/cam-elyaf/sisecam-tek-uclu-fitil [Accessed: 2017-08-16]

[16] Fiberglass News: The Making of Glass Fiber [Internet]. 2017. Available from: https://fiberglassnews.wordpress.com/tag/glass/ [Accessed: 2017-08-17]

[17] Jones JR. Glass fibres. In: Hearle JWS, editor. High-Performance Fibres. Cambridge: Woodhead Publishing Ltd.; 2001. pp. 197-238

[18] Wallenberger FT, Watson JC, Li H. Glass Fibers. ASM Handbook. 21: Composites. Ohio: American Technical Publishers Ltd; 2001. pp. 27-34

[19] High Strength Glass Fibers: AGY [Internet]. 2017. Available from: http://www.agy.com/wp-content/uploads/2014/03/High_Strength_Glass_Fibers-Technical.pdf. [Accessed: 2017-06-05]

[20] Yolacan G. Experimentally determination of the mechanical properties of stitched and containing nano-particle multilayered E-glass/polyester woven fabric composites (thesis). Kayseri: Erciyes University; 2013

[21] Mazumdar SK. Composites Manufacturing, Materials, Product and Process Engineering. Florida: CRC Press; 2002. pp. 46-154

[22] Offringa AR. Thermoplastic composites-rapid processing applications. Composites Part A: Applied Science and Manufacturing. 1996;**27**:329-336

[23] Iyer SR, Drzal LT. Manufacture of powder-impregnated thermoplastic composites. Journal of Thermoplastic Composite Materials. 1990;**3**:325-355

[24] Brandrup J, Immergut H, Grulke A. Polymer Handbook. 4th ed. New York: John Willey & Sons, Inc.; 1999. p. 171

[25] Choi BD, Diestel O, Offermann P. Commingled CF/PEEK hybrid yarns for use in textile reinforced high performance rotors. In: 19th International Conference on Composite Materials (ICCM); 28 July-2 August 2013; Montreal; 2013. p. 1-10

[26] Loos M. Composites. In: Loos M, editor. Carbon Nanotube Reinforced Composites. Oxford: Elsevier; 2015. pp. 38-63

[27] Kickelbick G. Nanoparticles and composites. In: Levy D, Zayat M, editors. The Sol-Gel Handbook: Synthesis, Characterization and Applications. Weinheim: Wiley-VCH; 2015. pp. 227-244

[28] Chandradass J, Kumar MR, Velmurugan R. Effect of clay dispersion on mechanical, thermal and vibration properties of glass fiber-reinforced vinyl ester composites. Journal of Reinforced Plastics and Composites. 2008;**27**:1585-1601

[29] Friedrich K, Fakirov S, Zhang Z. Polymer Composites from Nano- to Macro-Scale. New York: Springer; 2005. pp. 3-23

[30] Gojny FH, Wichmann MHG, Fiedler B, Schulte K. Influence of different carbon nanotubes on the mechanical properties of epoxy matrix composites—A comparative study. Composites Science and Technology. 2005;**65**:2300-2313

[31] Thostenson ET, Li C, Chou TW. Nanocomposites in context. Composites Science and Technology. 2005;**65**:491-516

[32] Wetzel B, Haupeiit F, Friedrich K, Zhang MQ, Rong MZ. Impact and wear resistance of polymer nanocomposites at low filler content. Polymer Engineering and Science. 2002;**42**:1919-1927

[33] Wichmann MHG, Schulte K, Wagner HD. On nanocomposite toughness. Composites Science and Technology. 2008;**68**:329-331

[34] Grishchuk S, Schledjewski R. Mechanical dispersion methods for carbon nanotubes in aerospace composite matrix systems. In: Paipetis AS, Kostopoulos V, editors. Carbon Nanotube Enhanced Aerospace Composite Materials: A New Generation of Multifunctional Hybrid Structural Composites. New York: Springer; 2013. pp. 100-132

[35] Vilgis T, Heinrich G, Klüppel M. Reinforcement of Polymer Nano-Composites: Theory, Experiments and Applications. Cambridge: Cambridge University Press; 2009. pp. 75-100

[36] Paipetis AS, Kostopoulos V. Carbon nanotubes for novel hybrid structural composites with enhanced damage tolerance and self-sensing/actuating abilities. In: Paipetis AS, Kostopoulos V, editors. Carbon Nanotube Enhanced Aerospace Composite Materials: A New Generation of Multifunctional Hybrid Structural Composites. New York: Springer; 2013. pp. 2-16

[37] Vavouliotis AI, Kostopoulos V. On the use of electrical conductivity for the assessment of damage in carbon nanotubes enhanced aerospace composites. In: Paipetis AS, Kostopoulos V, editors. Carbon Nanotube Enhanced Aerospace Composite Materials: A New Generation of Multifunctional Hybrid Structural Composites. New York: Springer; 2013. pp. 22-52

[38] Zhu J, Imam A, Crane R, Lozano K, Khabashesku VN, Barrera EV. Processing a glass fiber reinforced vinyl ester composite with nanotube enhancement of interlaminar shear strength. Composites Science and Technology. 2007;**67**:1509-1517

[39] Seyhan AT, Gojny FH, Tanoglu M, Schulte K. Critical aspects related to processing of carbon nanotube/unsaturated thermoset polyester nanocomposites. European Polymer Journal. 2007;**43**:374-379

[40] Yong V, Hahn HT. Processing and properties of SiC/vinyl ester nanocomposites. Nanotechnology. 2004;**15**:1338-1343

[41] Patnaik A, Satapathy A, Mahapatra SS, Dash RR. A comparative study on different ceramic fillers affecting mechanical properties of glass-polyester composites. Journal of Reinforced Plastics and Composites. 2009;**28**:1305-1318

[42] Dow NF. Triaxial fabric. US Patent 3446251, 27 May 1969

[43] Brunnschweiler D. Braids and braiding. Journal of the Textile Institute. 1953;**44**:666-686

[44] Lida S, Ohmori C, Ito T. Multiaxial fabric with triaxial and quartaxial portions. US Patent 5472020, 5 Dec 1995

[45] Hamada H, Ramakrishna S, Huang ZM. Knitted fabric composites, 3-D textile reinforcements in composite materials. In: Miravete A, editor. 3-D Textile Reinforcements in Composite Materials. Cambridge: Woodhead Publishing Ltd; 1999. pp. 180-216

[46] Padaki NV, Alagirusamy R, Sugun BS. Knitted preforms for composite applications. Journal of Industrial Textiles. 2006;**35**:295-321

[47] Technische Universitat Dresden [Internet]. 2017. Available from: http://tu-dresden.de/die_tu_dresden/fakultaeten/fakultaet_maschinenwesen/itm/forschung/forschungsthemen/gl_gestrick [Accessed: 2017-05-29]

[48] Bilisik K, Karaduman NS, Bilisik NE. 3D fabrics for technical textile applications. In: Jeon HY, editor. Non-woven Fabrics. Intech; 2016. pp. 81-141

[49] Grafe T, Graham K. Polymeric nanofibers and nanofiber webs: A new class of nonwovens. International Nonwovens Journal. 2003;**12**:51-55

[50] Anand SC. Technical fabric structures-knitted fabrics. In: Horrocks AR, Anand SC, editors. Handbook of Technical Textiles. 2nd ed. Cambridge: Woodhead Publishing Ltd.; 2016. pp. 107-162

[51] Advanced packaging Technologies [Internet]. 2017. Available from: http://advancepac.com/wordpress/markets/adhesive-specialty-films/glass-film/ [Accessed: 2017-08-05]

[52] Bilisik K, Yolacan G. Experimental characterization of multistitched two dimensional (2D) woven E-glass/polyester composites under low velocity impact load. Journal of Composite Materials. 2014;**48**:2145-2162

[53] Bilisik K, Yolacan G. Experimental determination of bending behavior of multilayered and multidirectionally-stitched E-glass fabric structures for composites. Textile Research Journal. 2012;**82**:1038-1049

[54] Bilisik K. Characterization of multi-stitched woven nano composites under compression after low velocity impact (CALVI) load. Polymer Composites. 2017:1-11. DOI: 10.1002/pc.24406, (on line)

[55] Bilisik K. Multiaxis 3D woven preform and properties of multiaxis 3D woven and 3D orthogonal woven carbon/epoxy composites. Journal of Reinforced Plastics and Composites. 2010;**29**:1173-1186

[56] Bilisik K. Dimensional stability of multiaxis 3D woven carbon preform. Journal of the Textile Institute. 2010;**101**:380-388

[57] Bilisik K. Multiaxis three dimensional (3D) circular woven preforms-"radial crossing weaving" and "radial in-out weaving": Preliminary investigation of feasibility of weaving and methods. Journal of the Textile Institute. 2010;**101**:967-987

[58] Bilisik K. Three dimensional (3D) axial braided preforms: Experimental determination of effects of structure-process parameters on unit cell. Textile Research Journal. 2011;**81**:2095-2116

[59] Bilisik K, Karaduman NS, Bilisik NE, Bilisik HE. Three dimensional (3D) fully interlaced woven preforms for composites. Textile Research Journal. 2013;**83**:2060-2084

[60] Mohamed MH, Bilisik K. Multilayered 3D fabric and method for producing. US Patent 5465760, 14 Nov 1995

[61] Bilisik AK. Multiaxial three dimensional (3D) circular woven fabric. US Patent 6129122, 10 Dec 2000

[62] Bilisik K, Karaduman NS, Bilisik NE. Fiber architectures for composite applications. In: Sohel R, Raul F. editors. Fibrous and Textile Materials for Composite Applications. US: Springer; 2016. p. 75-95

[63] Technical Design Guide for FRP Composite Products and Parts [Internet]. 2017. Available from: http://www.moldedfiberglass.com/sites/default/files/docs/MFG_Technical_Design_Guide_FRP_Composite_0.pdf [Accessed: 2017-07-25]

[64] Mouritz AP, Leong KH, Herszberg I. A review of the effect of stitching on the in-plane mechanical properties of fibre-reinforced polymer composites. Composites Part A: Applied Science and Manufacturing. 1997;**28A**:979-991

[65] Wu E, Wang J. Behavior of stitched laminates under in-plane tensile and transverse impact loading. Journal of Composite Materials. 1995;**29**:2254-2279

[66] Velmurugan R, Solaimurugan S. Improvements in mode I interlaminar fracture toughness and in-plane mechanical properties of stitched glass/polyester composites. Composites Science and Technology. 2007;**67**:61-69

[67] Aymerich F, Priolo P, Sun CT. Static and fatigue behaviour of stitched graphite/epoxy composite laminates. Composites Science and Technology. 2003;**63**:907-917

[68] Beier U, Fischer F, Sandler JKV, Altstadt V, Weimer C, Buchs W. Mechanical performance of carbon fibre-reinforced composites based on stitched preforms. Composites Part A: Applied Science and Manufacturing. 2007;**38**:1655-1663

[69] Wei Y, Zhang J. Characterization of microstructure in stitched unidirectional composite laminates. Composites Part A: Applied Science and Manufacturing. 2008;**39**:815-824

[70] Bilisik K, Yolacan G. Off-axis tensile properties of multistitched plain woven E-glass/polyester composites. Fibers and Polymers. 2014;**15**:589-598

[71] Bilisik K, Yolacan G. Warp and weft directional tensile properties of multistitched biaxial woven E-glass/polyester composites. Journal of the Textile Institute. 2014;**105**:1014-1028

[72] Bilisik K, Yolacan G. Warp-weft directional bending properties of multistitched biaxial woven E-glass/polyester nano composites. Journal of Industrial Textiles. 2015;**45**:66-100

[73] Bilisik K, Yolacan G. Short beam strength properties of multistitched biaxial woven E-glass/polyester nano composites. Journal of Industrial Textiles. 2015;**45**:199-221

[74] Zhao N, Rodel H, Herzberg C, Gao SL, Krzywinsky S. Stitched glass/PP composite. Part I: Tensile and impact properties. Composites Part A: Applied Science and Manufacturing. 2009;**40**:635-643

[75] Farley GL. A mechanism responsible for reducing compression strength of through-the-thickness reinforced composite material. Journal of Composite Materials. 1992;**26**:1784-1795

[76] Lee C, Liu D. Tensile strength of stitching joint in woven glass fabrics. Journal of Engineering Materials and Technology. 1990;**112**:125-130

[77] Tan KT, Watanabe N, Iwahori Y. Impact damage resistance, response, and mechanisms of laminated composites reinforced by through-thickness stitching. International Journal of Damage Mechanics. 2012;**21**:51-80

[78] Tan KT, Watanabe N, Iwahori Y. X-ray radiography and micro-computed tomography examination of damage characteristics in stitched composites subjected to impact loading. Composites Part B: Engineering. 2012;**42**:874-884

[79] Chen G, Li Z, Kou C, Gui L. Finite element analysis of low-velocity impact damage of stitched laminates. Journal of Reinforced Plastics and Composites. 2004;**23**:987-995

[80] Xiaoquan C, Al-Mansour AM, Zhengneng L, Chenghe K. Compression strength of stitched laminates after low-velocity impact. Journal of Reinforced Plastics and Composites. 2005;**24**:935-947

[81] Truong TC, Vettori M, Lomov S, Verpoest I. Carbon composites based on multi-axial multi-ply stitched preforms. Part 4. Mechanical properties of composites and damage observation. Composites Part A: Applied Science and Manufacturing. 2005;**36**:1207-1221

[82] Bilisik K, Yolacan G. Low-velocity impact characterization of multistitched woven E-glass/polyester nano/micro composites. Textile Research Journal. 2014;**84**:1411-1427

[83] Use of Composite Materials in Aerospace [Internet]. 2017. Available from: https://compositesuk.co.uk/composite-materials/applications/aerospace [Accessed: 2017-07-03]

[84] Composites in the Airframe and Primary Structure. 2017. Available from: http://www.boeing.com/commercial/aeromagazine/articles/qtr_4_06/article_04_2.html   [Accessed: 2017-08-17]

[85] Uses of Fiberglass [Internet]. 2017. Available from: https://www.thoughtco.com/uses-of-fiberglass-820412 [Accessed: 2017-07-05]

[86] Automotive Glass Fiber Composites Market—Growth Trends and Forecasts (2015-2020) [Internet]. 2015. Available from: https://www.mordorintelligence.com/industry-reports/automotive-glass-fiber-composites-market [Accessed: 2017-08-20]

[87] Composites: On good form [Internet]. 2014. Available from: https://automotivemanufacturingsolutions.com/process-materials/on-good-form composite-materials [Accessed: 2017-08-21]

[88] Market reports [Internet]. 2017. Available from: http://www.lucintel.com/lucintelbrief/lucintel-brief-opportunity-and-challenges-in automotive-composites-industry.pdf [Accessed: 2017-08-21]

[89] Technical Report of Ship Structure Committee, SSC-360. Use of Fiber Reinforced Plastics in the Marine Industry. September 1990

[90] Printed Circuit Boards: A Mobile Market [Internet]. 2017. Available from: http://www.compositesworld.com/articles/printed-circuit-boards-a-mobile-market [Accessed: 2017-08-21]

[91] Paulson JA, Mesbah A, Zhu X, Molaro MC, Braatz RD. Control of self-assembly in micro and nano-scale systems. Journal of Process Control. 2015;**27**:38-49

[92] Fiberglass News [Internet]. 2017. Available from: https://fiberglassnews.wordpress.com/tag/glass/ [Accessed: 2017-08-16]

[93] Glass Armor Systems: AGY [Internet]. 2017. Available from: http://www.agy.com/wp-content/uploads/2014/03/S-2_Glass_Armor_Systems-Defense.pdf [Accessed: 2017-08-22]

[94] Bhatnagar A. Lightweight Ballistic Composites: Military and Law-Enforcement Applications. Florida: CRC Press; 2006. pp. 400-408

[95] Wallenberger FT. Energy-friendly compositions and applications. In: Wallenberger FT, Bingham PA, editors. Fiberglass and Glass Technology. New York: Springer Science+Business Media; 2010

[96] Kadir Bilisik, Nesrin Karaduman, Nedim Erman Bilisik, Fiber architectures for composite applications. In: Raul Fangueiro, Sohel Rana, editors. Fibrous and Textile Materials for Composite Applications. Singapore: Springer Science+Business Media; 2016. pp. 75-134

[97] Bilisik K. Impact resistant fabrics. In: Miao M, Xin J, editors. Engineering of High Performance Textiles. New York: Elsevier Limited-Woodhead Publishing; 2017

Edited by Vincenzo M. Sglavo

In this book, some recent advances in glass science and technology are collected. In the first part, the structure and crystallization of innovative glass compositions are analysed. In the second part, innovative applications are described from the use of glass in optical devices and lasers to fibres in composites, micropatterned components in sensors and microdevices, beads in building walls and sealing in solid oxide fuel cells.

IntechOpen